



**HAL**  
open science

# Theoretical Study of Excited-state Processes in the Condensed Phase

Liam Wilbraham

► **To cite this version:**

Liam Wilbraham. Theoretical Study of Excited-state Processes in the Condensed Phase. Theoretical and/or physical chemistry. Université Paris sciences et lettres, 2017. English. NNT : 2017PSLECO01 . tel-01730939

**HAL Id: tel-01730939**

**<https://pastel.hal.science/tel-01730939>**

Submitted on 13 Mar 2018

**HAL** is a multi-disciplinary open access archive for the deposit and dissemination of scientific research documents, whether they are published or not. The documents may come from teaching and research institutions in France or abroad, or from public or private research centers.

L'archive ouverte pluridisciplinaire **HAL**, est destinée au dépôt et à la diffusion de documents scientifiques de niveau recherche, publiés ou non, émanant des établissements d'enseignement et de recherche français ou étrangers, des laboratoires publics ou privés.

# THÈSE DE DOCTORAT

de l'Université de recherche Paris Sciences et Lettres  
PSL Research University

Préparé à Chimie ParisTech

## Theoretical Study of Excited State Processes in the Condensed Phase

Ecole doctorale n°388

CHIMIE PHYSIQUE ET CHIMIE ANALYTIQUE DE PARIS CENTRE

Spécialité CHIMIE THEORIQUE

Soutenu par Liam WILBRAHAM  
le 19 Septembre 2017

Dirigée par Dr. Ilaria CIOFINI  
et Dr. François-Xavier COUDERT

### COMPOSITION DU JURY :

Pr. STENER Mauro  
Università di Trieste, Rapporteur

Dr. DANIEL Chantal  
Université de Strasbourg, Rapporteur

Pr. Maurel François  
Université Paris Diderot, Président du jury

Pr. PUNTORIERO Fausto  
Università degli Studi di Messina, Membre du jury

Dr. CIOFINI Ilaria,  
Chimie ParisTech, Directeur de thèse

Dr. COUDERT François-Xavier  
Chimie ParisTech, Co-Directeur de thèse



# Contents

|          |   |          |
|----------|---|----------|
| <b>1</b> | <b>Introduction and Thesis Framework</b>                                | <b>1</b> |
| <b>2</b> | <b>Theoretical Background</b>   | <b>5</b> |
| 2.1      | The Schrodinger Equation . . . . .                                      | 5        |
| 2.2      | The Hartree-Fock Method . . . . .                                       | 7        |
| 2.2.1    | Spin-Orbital Approximation . . . . .                                    | 7        |
| 2.2.2    | Slater Determinants . . . . .   | 7        |
| 2.2.3    | Computing the Hartree-Fock Energy . . . . .                             | 8        |
| 2.2.4    | Linear Combinations of Atomic Orbitals (LCAO) . . . . .                 | 9        |
| 2.2.5    | The Secular Equation . . . . .  | 10       |
| 2.2.6    | The Self-Consistent Field . . . . .                                     | 11       |
| 2.2.7    | Electron Correlation . . . . .  | 13       |
| 2.3      | Density Functional Theory . . . . .                                     | 13       |
| 2.3.1    | Hohenberg-Kohn Existence Theorem . . . . .                              | 14       |
| 2.3.2    | Hohenberg-Kohn Variational Theorem . . . . .                            | 14       |
| 2.3.3    | The Exchange-Correlation Approximation . . . . .                        | 15       |
|          | Local Density Approximation . . . . .                                   | 15       |
|          | Generalized Gradient Approximation and Kinetic Energy Density . . . . . | 16       |
|          | The Adiabatic Connection and Hybrid Density Functionals . . . . .       | 16       |
| 2.4      | Time-Dependent Density Functional Theory . . . . .                      | 18       |
| 2.4.1    | Runge-Gross Theorem . . . . .   | 18       |
| 2.4.2    | Van-Leeuwen Theorem . . . . .   | 19       |
| 2.4.3    | Linear Response Formalism . . . . .                                     | 19       |
| 2.4.4    | Calculating Excitation Energies with TDDFT . . . . .                    | 21       |
| 2.4.5    | The Adiabatic Approximation in TDDFT . . . . .                          | 24       |
| 2.4.6    | Charge Transfer Excitations . . . . .                                   | 25       |

---

|  |           |
|--|-----------|
| Range-Separated Hybrid Functionals . . . . .                                     | 26        |
| 2.5 Recovering Static Correlation . . . . .                                      | 27        |
| 2.5.1 Multi-Configuration Self-Consistent Field . . . . .                        | 28        |
| 2.5.2 Complete Active Space Self-Consistent Field . . . . .                      | 30        |
| 2.5.3 Perturbation Theory and CASSCF . . . . .                                   | 30        |
| 2.5.4 Multi-Configuration Pair-Density Functional Theory . . . . .               | 32        |
| On-Top Density Functionals . . . . .   | 32        |
| 2.6 Modeling Solvent Effects . . . . .   | 33        |
| 2.6.1 The Polarizable Continuum Model . . . . .                                  | 33        |
| <b>3 Modeling the Crystalline Phase</b> . . . . .                                | <b>37</b> |
| 3.1 Periodic Boundary Conditions . . . . .                                       | 37        |
| 3.1.1 Bloch Functions and Crystalline Orbitals . . . . .                         | 38        |
| 3.1.2 Periodic Boundary Conditions and Excited-State Properties . . . . .        | 39        |
| 3.2 Cluster Modeling . . . . .   | 39        |
| 3.2.1 Hybrid Energy Schemes . . . . .  | 40        |
| ONIOM . . . . .  | 40        |
| Frozen Density Embedding . . . . .   | 43        |
| Periodic Electrostatic Embedded Cluster Method . . . . .                         | 44        |
| 3.2.2 Cluster Modeling vs. Periodic Boundary Conditions . . . . .                | 45        |
| <b>4 SC-Ewald: A Self-Consistent Excited-State Embedding Potential</b> . . . . . | <b>47</b> |
| 4.1 The Infinite Electrostatic Potential . . . . .                               | 47        |
| 4.2 The Ewald Embedding Approach . . . . .                                       | 49        |
| 4.3 Extension of Ewald Embedding to the Excited-State . . . . .                  | 52        |
| 4.3.1 The SC-Ewald Algorithm . . . . .   | 52        |
| 4.3.2 SC-Ewald Algorithm and User Manual . . . . .                               | 53        |
| 4.3.3 Limitations of the Current Implementation . . . . .                        | 54        |
| Loss of Crystalline Symmetry . . . . .   | 54        |
| Neglect of Quantum Effects on Potential . . . . .                                | 55        |
| The Cluster-Point Charge Boundary . . . . .                                      | 55        |
| Crystalline Networks . . . . .   | 55        |

---

|   |           |
|---|-----------|
| Lower-Dimensional Periodicity . . . . .   | 56        |
| <b>5 Excited-State Intramolecular Proton Transfer in the Solid-State</b>            | <b>57</b> |
| 5.1 Introduction . . . . .  | 57        |
| 5.2 Computational Details . . . . .   | 60        |
| 5.3 Results and Discussion . . . . .  | 63        |
| 5.3.1 Computed Emission Energies . . . . .  | 63        |
| 5.3.2 Emission Dependence on Environment: QM:QM' and Ewald . . . . .                | 64        |
| 5.3.3 Effect of the Environment on Reaction Thermodynamics . . . . .                | 66        |
| 5.3.4 Emission Dependence on Environment: SC-Ewald . . . . .                        | 68        |
| 5.4 Conclusions . . . . .   | 71        |
| <b>6 Aggregation-Induced Emission:<br/>The case of Diphenyl Fluoronone</b>          | <b>73</b> |
| 6.1 Introduction . . . . .  | 73        |
| 6.2 Computational Details . . . . .   | 76        |
| 6.3 Results and Discussion . . . . .  | 77        |
| 6.3.1 Assessment of Dimer Coupling at the Excited State . . . . .                   | 77        |
| 6.3.2 Assignment of Spectral Absorption Bands . . . . .                             | 78        |
| 6.3.3 Solvated and Aggregated Fluorescence of DPF . . . . .                         | 80        |
| 6.4 Conclusions . . . . .   | 83        |
| <b>7 Mechanochromic Fluorescence:<br/>Extending SC-Ewald to the Amorphous Phase</b> | <b>85</b> |
| 7.1 Introduction . . . . .  | 85        |
| 7.2 Computational Details . . . . .   | 86        |
| 7.2.1 Crystalline-Phase Emission . . . . .  | 87        |
| 7.2.2 Amorphous-Phase Emission . . . . .  | 88        |
| 7.2.3 Emission in Solvent . . . . .   | 89        |
| 7.3 Results and Discussion . . . . .  | 89        |
| 7.3.1 Emission in DFB-X Crystalline Polymorphs . . . . .                            | 90        |
| 7.3.2 Emission in Amorphized DFB-X . . . . .  | 92        |
| 7.4 Conclusions . . . . .   | 99        |

---

|           |   |            |
|-----------|---|------------|
| <b>8</b>  | <b>Cluster Modeling of Luminescent Metal-Organic Frameworks</b>   | <b>101</b> |
| 8.1       | Introduction . . . . .  | 101        |
| 8.2       | Computational Details . . . . .   | 103        |
| 8.3       | Results and Discussion . . . . .  | 105        |
| 8.3.1     | Density Functional Performance . . . . .  | 105        |
| 8.3.2     | Absorption and Fluorescence . . . . .   | 108        |
| 8.3.3     | Phosphorescence in Zn[DMPMB] . . . . .  | 111        |
| 8.4       | Conclusions . . . . .   | 114        |
| <b>9</b>  | <b>Additional Concerns in Condensed-Phase Modeling:<br/>Spin-State Ordering in Transition Metal Complexes</b> | <b>115</b> |
| 9.1       | Introduction . . . . .  | 115        |
| 9.2       | Computational Details . . . . .   | 117        |
| 9.3       | Results and Discussion . . . . .  | 119        |
| 9.3.1     | A Representative Benchmark with DFT . . . . .   | 119        |
| 9.3.2     | Performance of Wave Function Theory-Based Approaches . . . . .  | 123        |
| 9.4       | Conclusions and Perspectives . . . . .  | 127        |
| <b>10</b> | <b>General Conclusions and Perspectives</b>   | <b>129</b> |
| <b>11</b> | <b>Résumé en français</b>   | <b>131</b> |
| 11.1      | Introduction . . . . .  | 131        |
| 11.2      | Embedding à l'état excité: SC-Ewald . . . . .   | 132        |
| 11.3      | Application au transfert de protons à l'état excité . . . . .   | 134        |
| 11.4      | Application aux agrégats émissifs . . . . .   | 138        |
| 11.5      | Extension aux matériaux amorphes . . . . .  | 141        |
| <b>12</b> | <b>Appendix to Chapter 4</b>  | <b>145</b> |
|           | Input Files . . . . .   | 145        |
|           | Output Files . . . . .  | 149        |
|           | Launching SC-Ewald Modes of Use . . . . .   | 150        |
| <b>13</b> | <b>Appendix to Chapter 5</b>  | <b>153</b> |
| <b>14</b> | <b>Appendix to Chapter 6</b>  | <b>155</b> |

|                                 |            |
|---------------------------------|------------|
| <b>15 Appendix to Chapter 7</b> | <b>157</b> |
| <b>16 Appendix to Chapter 8</b> | <b>161</b> |
| <b>17 Appendix to Chapter 9</b> | <b>163</b> |



## Chapter 1

# Introduction and Thesis Framework

Materials which may be considered “photoactive” are those from which an observable response may be elicited from interaction with light. The observable response in question may be, for instance, an induced chemical reaction, change in colour or luminescence, an alteration of magnetic properties, or a combination of several of these.

From these responsive materials, devices may be fabricated which harness their intrinsic properties for a particular application. The constant development of new photoactive materials for use in areas such as light emitting, [1,2] medical, [3,4] and catalytic devices [5,6] is driven by the need for greater efficiency, improved performance and reduced cost. However, innovation currently relies on incremental progress, trial-and-error, and accidental discovery with reduced emphasis on pre-synthesis materials design.

With currently available hardware and recent developments in theoretical methods such as time-dependent density functional theory, theory is well-positioned to provide a route towards pre-synthetic design. There is a caveat, however, that changes in the excited-state properties of said materials induced by the inherent condensed-phase environment of a given device must be properly accounted for. In the context of modeling photophysical processes at a molecular level, “condensed-phase” effects are those induced by surrounding solvent molecules, in the case of solution, or other photoactive molecules in the case of crystalline or amorphous-phase materials.

It is well known that photophysical properties of a given molecular system can be strongly influenced, and are often predicated, by phase-sensitive interactions [7,8]. For this reason, considerable resources have been dedicated to the study of environmental influence in order to gain insight into, and control over, different excited state processes which can give rise to potentially useful photophysical traits to be applied within optoelectronic devices.

From both an experimental and theoretical perspective, methods for studying the photophysical properties of photoactive molecules in solution are very well developed to the extent that theory-led molecular design is becoming feasible to exploit target properties. Unfortunately, the state of the art in solid-state modeling lies far behind that which can be applied to solutions. Additionally, in the solid-state, photophysical processes are more difficult to characterize experimentally and reports of interesting photophysical behavior in periodic systems, which can often be small and subtle, are far rarer when compared with

solution. Describing complex photochemistry in the solid phase, therefore, represents a significant and ongoing challenge for computational chemists. Models of sufficient quality - able to both understand and predict the influence of a given environment on optical properties, as well as how they are altered by changing the environment - are a necessary component for the understanding and design of functional molecules and materials.

This problem forms the central task of this thesis, in which we seek to develop and apply a relatively low-cost embedding model – SC-Ewald – capable of modeling crucial electrostatic interactions with the solid-state environment, accounting for those at both short- and long-range. SC-Ewald, which is essentially an embedded cluster approach and is described in chapter 4, improves upon some aspects of current cluster embedding methods such as ONIOM, which is demonstrated in several proof-of-concept studies throughout this thesis.

Chapter 5 represents the conception and first application of SC-Ewald, where it has been used to study an excited-state double proton transfer reaction in a dual-emissive molecular crystal. The initial application of a ground-state embedding potential, while providing an adequate description of the excited-state reaction mechanism, lead to an unsatisfactory prediction of the dual-emission properties, which prompted the reformation of the embedding potential, via a self-consistent adjustment procedure, to an excited-state embedding potential. From this change in embedding strategy, we observed an excellent recovery of the dual-emissive properties. The application of this self-consistent charge-adjustment procedure, later referred to as SC-Ewald, to other photo-active materials is then described in subsequent chapters.

In chapter 6, SC-Ewald is used to understand the photophysical behavior of an organic molecule which is non-emissive in solution, yet exhibits bright luminescence in the solid-state. Though different mechanisms are often cited for such behavior, known as aggregation-induced emission, we suggest that the solid-state luminescence is a result of a brightening of otherwise poorly-emissive states by the electrostatic potential induced by surrounding molecules in the solid-state.

Chapter 7 extends the application of SC-Ewald to the study of a family of organic molecules which exhibit mechanically- and structurally-sensitive fluorescence properties. Generally, this property is known as mechanochromic fluorescence and is induced by mechanical grinding of a given crystalline sample under irradiation. The amorphous nature of the resulting ground sample introduces an additional problem for computational approaches due to the many possible molecular configurations present. Using a hybrid approach rooted in classical molecular dynamics and SC-Ewald, we demonstrate that an intelligent sampling of molecular configurations near to the excited-state crystalline geometry results in remarkable reproduction of the mechanochromic properties, which, when combined with steady-state and time-resolved experimental data, provides unprecedented insight into the mechanisms behind mechanochromic fluorescence and indeed the interpretation of amorphous-phase optical properties in general.

A step away from SC-Ewald, chapter 8 contains a study of the photophysical properties

of metal-organic frameworks (MOFs), using an example of two isostructural MOFs (based on Cd and Zn) with strikingly different luminescent properties to discriminate between potential sources of their respective luminescence. Using a mixed periodic and cluster-based approach, a perhaps counter-intuitive conclusion was drawn – that luminescence from the Zn- and Cd-based MOFs is a result of radiative decay from the lowest lying triplet and singlet ligand-centered excited states, respectively.

Serving as an illustrative study into other issues related to condensed-phase modeling besides interaction with the environment, chapter 9 raises the question of modeling spin-state ordering in iron complexes, highlighting the somewhat arbitrary performance of density functional theory with respect to functional choice. Using wave function based approaches CASSCF and CASPT2, it is shown that different components of a given density functional approximation – for instance the inclusion of Hartree-Fock exchange and dependence on the kinetic energy density – respond differently, and in a systematic fashion, to changes in ligand-field strength. As a preliminary study into how the flexibility of density functional theory through functional formulation and the multi-reference capabilities of CASSCF may be applied to study these properties, the recently-developed MC-PDFT approach has also been applied, providing results in agreement with CASPT2, with an even treatment of complexes containing both strong- and weak-field ligands.



## Chapter 2

# Theoretical Background

In this chapter, we outline the theoretical approaches used throughout this work. The first section explores the root of most modern quantum chemistry: the Hartree-Fock approach, along with its limitations. The second and third sections explore Density Functional Theory and its extension to the excited state, Time-Dependent DFT. Finally, we look at how both Hartree-Fock and DFT fail in modeling systems with significant multi-reference character, and how this can be overcome by the way of wave-function based methods.

### 2.1 The Schrodinger Equation

To solve for a many-body wave function, one usually must obtain solutions to the time-independent Schrodinger equation:

$$\hat{H}\Psi = E\Psi \quad (2.1)$$

where  $\hat{H}$  is the Hamiltonian operator,  $\Psi$  is the many-body wave function, which contains all information on the quantum state of the system, and  $E$  is the total system energy. For a system of  $N$  nuclei and  $n$  electrons, the non-relativistic Hamiltonian is written as a sum of kinetic and potential energies:

$$\hat{H} = \hat{T}_e + \hat{T}_N + \hat{V}_{Ne} + \hat{V}_{ee} + \hat{V}_{NN} \quad (2.2)$$

$$\hat{H} = \sum_i^n \frac{-\hbar}{2m_e} \nabla_i^2 + \sum_\alpha^N \frac{-\hbar}{2M_\alpha} \nabla_\alpha^2 + \sum_\alpha^N \sum_i^n \frac{q_i Z_\alpha}{4\pi\epsilon_0 r_{i\alpha}} + \sum_i^n \sum_{j>i}^n \frac{q_i q_j}{4\pi\epsilon_0 r_{ij}} + \sum_\alpha^N \sum_{\beta>\alpha}^N \frac{Z_\alpha Z_\beta}{4\pi\epsilon_0 r_{\alpha\beta}}, \quad (2.3)$$

where indexes  $i$  and  $j$  ( $\alpha$  and  $\beta$ ) run over all electrons (nuclei);  $q$  and  $m$  ( $Z$  and  $M$ ) are the charge and mass of an electron (nucleus);  $r$  is the inter-particle distance;  $\hbar$  is the reduced Planck's constant and  $\nabla^2$  is the Laplacian. The wave function is then defined as a function of  $3(n + N)$  coordinates. The two terms denoted by  $\hat{T}$  are the kinetic energies of the electrons  $\hat{T}_e$  and nuclei  $\hat{T}_N$ . Terms denoted by  $\hat{V}$  are the electrostatic attraction between electrons and nuclei  $\hat{V}_{Ne}$ , electron-electron electrostatic repulsion  $\hat{V}_{ee}$  and inter-nucleus repulsion  $\hat{V}_{NN}$ . Noting that  $q_i = -e$ ,  $Z_\alpha = eZ_\alpha$  and using atomic units ( $m_e = 1$ ,  $\hbar = 1$ ,  $\frac{e^2}{4\pi\epsilon_0} = 1$ ), the

Hamiltonian can be rewritten in a more condensed form:

$$\hat{H} = \sum_i^n \frac{1}{2} \nabla_i^2 + \sum_\alpha^N \frac{1}{2M_\alpha} \nabla_\alpha^2 + \sum_\alpha^N \sum_i^n \frac{q_i Z_\alpha}{r_{i\alpha}} + \sum_i^n \sum_{j>i}^n \frac{q_i q_j}{r_{ij}} + \sum_\alpha^N \sum_{\beta>\alpha}^N \frac{Z_\alpha Z_\beta}{r_{\alpha\beta}}, \quad (2.4)$$

As the mass of any given nuclei is far greater than that of the electrons, we may make the approximation that the contribution of the kinetic energy of the nuclei to the total energy is negligible. In this way, the movement of nuclei and electrons are decoupled and the electronic properties of the system are calculated at a fixed nuclear geometry. This approximation is known as the Born-Oppenheimer approximation. [9] An additional effect of this approximation is that the nuclear repulsion term is a fixed quantity and thus is effectively eliminated from the many-body problem. The remaining terms constitute what we shall refer to as the electronic Hamiltonian  $\hat{H}_{el}$ :

$$\hat{H}_{el} \Psi_{el} = E_{el} \Psi_{el} \quad (2.5)$$

where  $\hat{H}_{el}$  is given by:

$$\hat{H} = \sum_i^n \frac{1}{2} \nabla_i^2 + \sum_\alpha^N \sum_i^n \frac{q_i Z_\alpha}{r_{i\alpha}} + \sum_i^n \sum_{j>i}^n \frac{q_i q_j}{r_{ij}} \quad (2.6)$$

Equation 2.5 is an eigenvalue equation, whose solutions give the electronic wave function  $\Psi_{el}$  and total system energy  $E_{el}$ . We may further rewrite this Hamiltonian as the sum of mono- and bi-electronic terms:

$$\hat{H}_{el} = \sum_i^n \left( \hat{h}_1(i) + \sum_{j>i}^n \hat{h}_{12}(i, j) \right). \quad (2.7)$$

Now, the total energy of the system may be expressed as the sum of the electronic energy and the nuclear repulsion constant:

$$E_{tot} = E_{el} + E_{NN} \quad (2.8)$$

Where  $E_{NN}$  is given by the final term in equation 2.4. Because of the bi-electronic term, the Schrodinger equation cannot be solved analytically for systems with more complexity than those containing a single electron (e.g. the hydrogen). In order to study more complex systems of chemical relevance, we must develop approximations which render the Schrodinger equation readily solvable.

## 2.2 The Hartree-Fock Method

### 2.2.1 Spin-Orbital Approximation

If we assume that the overall many-electron problem may be decomposed into a series of non-interacting entities, the electronic Hamiltonian may be written as a sum of mono-electronic operators:

$$\hat{h}(i)\phi(r_i) = \epsilon_i\phi(r_i), \quad (2.9)$$

where  $r_i$  is the position vector of electron  $i$ . The overall electronic wave function  $\Psi_{el}$  is then written as the (Hartree) product of the mono-electronic eigenfunctions, or orbitals [10,11]:

$$\Psi_{el} = \phi(r_1)\phi(r_2)\dots\phi(r_n). \quad (2.10)$$

Thus the total electronic energy of the system is written as a sum of the orbital energies  $\epsilon_i$ :

$$E_{el} = \sum_i^n \epsilon_i. \quad (2.11)$$

Taking into account the property of electron spin, we may define our orbitals as a product of space and spin functions, yielding so-called spin-orbitals. As our Hamiltonian is non-relativistic in nature, there is no coupling between these spin and space functions comprising a given spin-orbital. Such orbitals can then be written as a product of space  $\phi_i$  and spin  $\sigma_i$  functions:

$$\phi_i(r_i; s_i) = \phi(r_i)\sigma(s_i). \quad (2.12)$$

Where the spin function describes the intrinsic angular momentum of an electron, which may take two values:  $\pm\frac{1}{2}$ , generally denoted by  $\alpha$  and  $\beta$ .

### 2.2.2 Slater Determinants

As electrons are fermions, the resulting wave function must possess certain properties. For instance, it must be anti-symmetric with respect to the permutation of two electrons. In other words, the sign of the wave function must be inverted when exchanging the coordinates of two electrons. As a simple product of spin-orbitals does not fulfill this criterion, we rely on a mathematical object known as a Slater Determinant,  $\Phi_K$ :

$$\Phi_K = \frac{1}{\sqrt{n!}} \begin{vmatrix} \phi_1(r_1)\sigma(s_1) & \phi_2(r_1)\sigma(s_1) & \dots & \phi_n(r_1)\sigma(s_1) \\ \phi_1(r_2)\sigma(s_2) & \phi_2(r_2)\sigma(s_2) & \dots & \phi_n(r_2)\sigma(s_2) \\ \vdots & \vdots & \ddots & \vdots \\ \phi_1(r_n)\sigma(s_n) & \phi_2(r_n)\sigma(s_n) & \dots & \phi_n(r_n)\sigma(s_n) \end{vmatrix}. \quad (2.13)$$

The pre-factor is a normalization constant of the wave function and the the space functions of the spin-orbitals are orthonormal:

$$\langle \phi_i | \phi_j \rangle = \delta_{ij}, \quad (2.14)$$

where we use Dirac notation to describe the overlap of two space functions and  $\delta_{ij}$  is the Kronecker delta. For discussion in subsequent sections of this chapter, it is important to note that the HF determinant is composed from a single Slater Determinant, meaning that a single electronic configuration may be considered when solving for the overall wave function.

### 2.2.3 Computing the Hartree-Fock Energy

Using the variational theorem, we may calculate the HF energy  $E_0^{HF}$  according to:

$$E_0^{HF} = \frac{\langle \Phi_0 | \hat{H}_{el} | \Phi_0 \rangle}{\langle \Phi_0 | \Phi_0 \rangle} \geq E_0^{exact}, \quad (2.15)$$

meaning that the electronic energy computed via HF is at least greater than or equal to the lowest possible energy of the system. With a given set of space functions  $\{\phi_i\}$ , the minimal energy for a given nuclear configuration can be found by varying the form of each space function under the orthonormality constraint. For a closed-shell system, in which all electrons of opposite spin are paired and all orbitals doubly occupied, the HF energy is a sum of mono- and bi-electronic operators:

$$E_0^{HF} = \langle \Phi_0 | \hat{H}_{el} | \Phi_0 \rangle = 2 \sum_i^{n/2} h_{ii} + \sum_i^{n/2} \sum_j^{n/2} (2J_{ij} - K_{ij}), \quad (2.16)$$

where each operator is given by the following integrals:

$$h_{ii} = \int \phi_i^*(1) \hat{h}_1 \phi_i(1) dr_1 = \langle i | \hat{h}_1 | i \rangle \quad (2.17)$$

$$J_{ij} = \iint \phi_i^*(1) \phi_j^*(2) \hat{h}_{12} \phi_i(1) \phi_j(2) dr_1 dr_2 = (ij | ij) \quad (2.18)$$

$$K_{ij} = \iint \phi_i^*(1) \phi_j^*(2) \hat{h}_{12} \phi_j(1) \phi_i(2) dr_1 dr_2 = (ij | ji). \quad (2.19)$$

$J_{ij}$  and  $K_{ij}$  are called, respectively, the coulomb and exchange integrals. The latter is a direct result of the anti-symmetric nature of the wave function described by the Slater Determinant. Each integral is performed over a finite volume element  $r_i$  in three dimensions. Note the factor of 2 preceding the coulomb interaction energy - a product of the concept that only electrons of the same spin may experience exchange repulsion, as only electrons of the same spin may be exchanged directly. In order to obtain the set of orbitals  $\{\phi_i\}$  which construct the HF wave function, we must consider both the interaction between electrons and nuclei as well as between electrons. To do so, we approximate the potential felt by a given electron as a mean-field of those remaining. In this framework, each orbital is then an

eigenfunction of an effective operator, known as the Fock operator,  $\hat{F}$ . The  $i$  corresponding eigenvalue equations are known as the Hartree-Fock equations:

$$\hat{F}\phi_i = \epsilon_i\phi_i. \quad (2.20)$$

The minimization of the energy associated with the determinant describing the wave function  $\Phi_0$  represents a series of eigenvalue problems, one for each of the  $n/2$  molecular orbitals present in the system. The expression of the Fock operator is given by the following equation:

$$\hat{F}(1) = \hat{h}_1(1) + \sum_j^{n/2} [2\hat{J}_j(1) - \hat{K}_j(1)], \quad (2.21)$$

where:

$$\hat{J}_j(1)\phi_i(1) = \int \phi_j^*(2)\hat{h}_{12}\phi_j dr_2 \phi_i(1) \quad (2.22)$$

$$\hat{K}_j(1)\phi_i(1) = \int \phi_j^*(2)\hat{h}_{12}\phi_j dr_2 \phi_j(1). \quad (2.23)$$

For a given orbital  $i$ , the HF potential is given by:

$$v_i^{HF} = \sum_j^{n/2} [2\hat{J}_j - \hat{K}_j], \quad (2.24)$$

which represents the average potential - produced by all other electrons and nuclei in the system - felt by electron  $i$  occupying molecular orbital  $i$ .

### 2.2.4 Linear Combinations of Atomic Orbitals (LCAO)

In order to solve the HF equations, it is necessary to introduce a set of variable functions, or basis set, which defines the space that our wave function can occupy. To do so, molecular orbitals are usually defined using a linear combination of basis functions - or atomic orbitals  $\{\chi_i\}$  - centered on each atom [12]:

$$\phi_i = \sum_{\mu} c_{\mu i} \chi_{\mu i}. \quad (2.25)$$

Where  $c_{\mu i}$  are the coefficients that may be varied when optimizing the wave function. Within this approximation, the electronic Schrodinger equation becomes a system of algebraic equations, solvable by standard matrix algebra techniques. Generally in calculations within the field of quantum chemistry, the functions which constitute the basis set are of one of two types: Slater-type orbitals (STO) and Gaussian-type orbitals (GTO). The former have the following form:

$$\chi^{STO} = \frac{[2\zeta]^{n+1/2}}{[(2n)!]^{1/2}} r^{n-1} e^{-\zeta r} Y_l^m(\theta, \Pi), \quad (2.26)$$

with  $n$ ,  $l$  and  $m$  as quantum numbers,  $Y_l^m(\theta, \Pi)$  spherical harmonics as a function of radial coordinates and  $\zeta$  as the exponent of the function which controls its overall 'diffuseness'

with respect to the nuclear center. STOs have the advantage that they closely resemble the orbital of the hydrogen atom, though, in practice, the calculation of their integrals is difficult.

As a result, it is far more common to use a linear combination of GTOs - which are far simpler to integrate - to try to reproduce the overall form of a given STO. The general form of a GTO is given by:

$$\chi^{GTO} = \left(\frac{2\alpha}{\pi}\right)^{3/4} \left[\frac{(8\alpha)^{i+j+k} i! j! k!}{(2i)!(2j)!(2k)!}\right]^{1/2} x^i y^j z^k e^{-\alpha r^2} \quad (2.27)$$

where the reduced likeness to the hydrogen 1s orbital stems from the more rapidly-decaying exponential term,  $x$ ,  $y$  and  $z$  are the Cartesian coordinates and  $\alpha$  controls the width of the Gaussian function. As stated above, new *contracted* Gaussian functions (CGTO) are formed as a linear combination of so-called *primitive* functions of the form in equation 2.27:

$$\chi^{CGTO} = \sum_{\mu} d_{\mu r} \chi_{\mu}^{GTO} \quad (2.28)$$

where  $d_{\mu r}$  are the coefficients preceding each primitive function which control the overall shape of the CGTO. Each primitive function possesses the same overall character ( $i, j, k$  are identical) and differ in the exponent  $\alpha$ . Additionally, for a given contraction, the coefficients are held constant and the weight of each contraction is controlled by an external coefficient, reducing the number of coefficients to be determined during the optimization of the overall wave function. It is with this genre of basis functions that all work in this thesis is carried out.

## 2.2.5 The Secular Equation

Using the development of LCAO in the preceding section, the Hartree-Fock eigenvalue problem may be rewritten in matrix form [12]:

$$\sum_{\mu} F_{\mu\nu} c_{\nu i} = \epsilon_i \sum_{\mu} S_{\mu\nu} c_{\nu i} \quad (2.29)$$

$$\mathbf{FC} = \mathbf{SC}\epsilon, \quad (2.30)$$

where we have assumed that our basis functions are normalized but not orthogonal, leading to the overlap matrix  $\mathbf{S}$  with elements:

$$S_{\mu\nu} = \int \chi_{\mu}^*(1) \chi_{\nu}(1) dr_1 \quad (2.31)$$

The Fock matrix elements  $\mathbf{F}$  are given by the following:

$$F_{\mu\nu} = H_{\mu\nu} + \sum_{\rho} \sum_{\sigma} P_{\rho\sigma} [(\mu\nu|\rho\sigma) - \frac{1}{2}(\mu\sigma|\rho\nu)], \quad (2.32)$$

where  $(\mu\nu|\rho\sigma)$  and  $(\mu\sigma|\rho\nu)$  are the coulomb and exchange integrals respectively,  $P_{\rho\sigma}$  are elements of the density matrix given by

$$P_{\rho\sigma} = 2 \sum_i^{n/2} c_{\rho i} c_{\sigma i}, \quad (2.33)$$

and  $H_{\mu\nu}$  are the mono-electronic integrals of the form

$$H_{\mu\nu} = \int \chi_{\mu}^*(1) \hat{h}_1 \chi_{\nu}(1) dr_1, \quad (2.34)$$

which remain fixed for a given basis set. With this information, it can be seen that the matrix  $\mathbf{F}$  depends on the density matrix  $\mathbf{P}$ , which depends on the values of the molecular orbital coefficients in  $\mathbf{C}$ . Thus, the eigenvalue problem in equation 2.30 is non-linear and requires an iterative process to be solved, beginning with a density matrix guess. This iterative process, known as the *Self Consistent Field* (SCF) procedure, is discussed in the next section.

### 2.2.6 The Self-Consistent Field

The eigenvalue problem in equation 2.30 is solved using an iterative process. This *Self Consistent Field* (SCF) procedure is outlined in figure 2.1.

In the first SCF cycle, one estimates  $\mathbf{P}$ , calculates the interaction integrals and diagonalizes the Fock matrix to obtain energy eigenvalues and renewed basis function coefficients. Using these new parameters, the same procedure is performed until the density matrix elements of the  $n^{\text{th}}$  and  $n-1^{\text{th}}$  cycles differ by less than a pre-defined threshold.

From a physical point of view, the HF approach constitutes multiple evaluation and refinement of the Hartree-Fock potential. That is to say, until the mean-field produced by a given charge density is identical to the field produced from the same density.

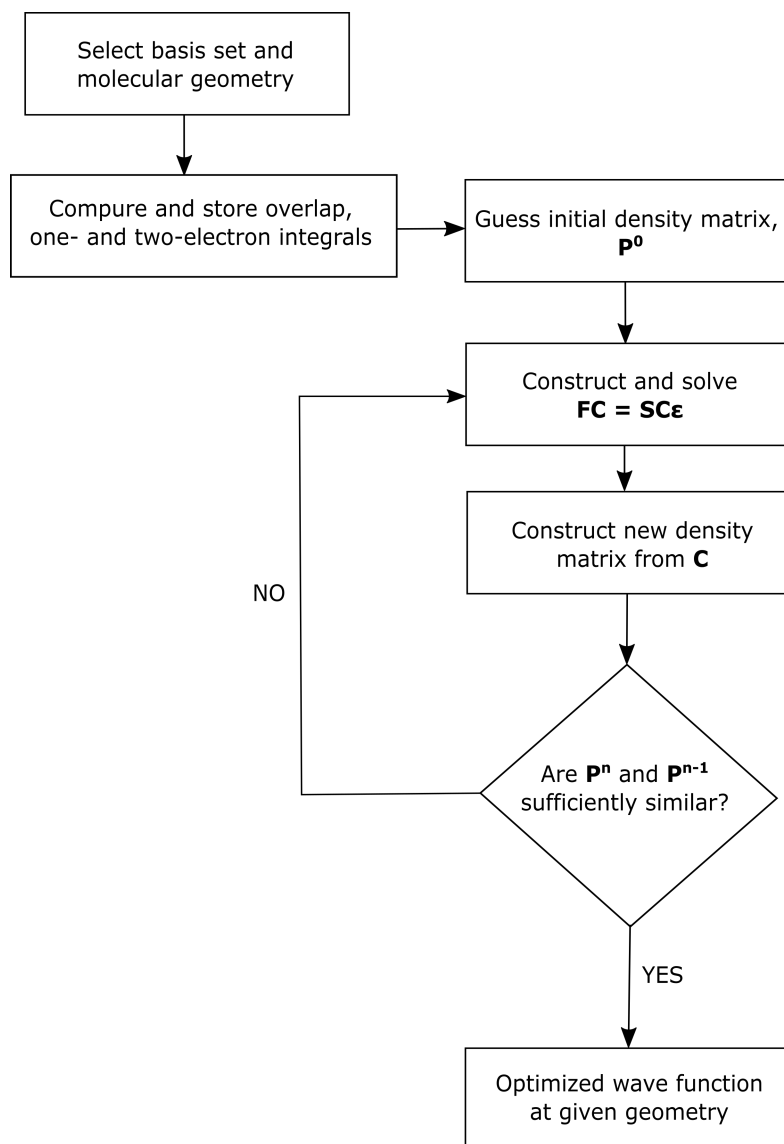


FIGURE 2.1: Flowchart of the SCF procedure within the HF approach.

### 2.2.7 Electron Correlation

The mean-field nature of Hartree–Fock theory imposes the fundamental approximation that each electron moves in a static electric field of all the other electrons. When operating on the resulting wave function with the Hamiltonian operator, we obtain the lowest possible energy for that wave function, which is described by a single Slater determinant. As there is a crucial difference between the Fock operator  $\hat{F}$  and the Hamiltonian  $\hat{H}$  - the latter returns the electronic energy for a many-body system of electrons and the former is a set of interdependent one-electron operators - one might consider how the HF wave function may be modified to return a lower total energy when applying the Hamiltonian. Naturally, from the variational principle, such a wave function would serve as a better approximation of the true wave function.

Within the limit of a complete basis set, the discrepancy between the energy produced by the exact wave function and that produced by HF after the application of the Hamiltonian is known as the *correlation energy*,  $E_{corr}$ :

$$E_{corr} = E_{exact} - E_0^{HF} < 0. \quad (2.35)$$

In the following sections, we discuss different approaches to recover  $E_{corr}$ , such as Density Functional Theory (section 2.3) and post-HF approaches section (2.5)

## 2.3 Density Functional Theory

Rather than center the discussion of molecular electronic structure around a complex mathematical object (the wave function) defined by  $3(n + N)$  coordinates, Density Functional Theory (DFT) focuses on a simplified, more intuitive observable that can be defined in three dimensions: the electron density  $\rho(r)$ , [13] which is linked to the wave function by the following relation:

$$\rho(r) = \Psi^*(r)\Psi(r) = |\Psi^2(r)| \quad (2.36)$$

This idea is attractive in that it permits the simplification of the overall electronic problem and introduces scope for the inclusion of the correlation energy discussed in section 2.2.7. The central idea of DFT is that the ground state of a given system is a functional (a function of a function) of the electronic density. Integrating the density  $\rho$  over all space yields the total number of electrons  $n$ :

$$\int \rho(r) dr = n \quad (2.37)$$

Within the Born-Oppenheimer approximation, the expression for the electronic Hamiltonian reduces from:

$$\hat{H}_{el} = \hat{T}_e + \hat{V}_{Ne} + \hat{V}_{ee} = -\frac{1}{2} \sum_i^n \nabla_i^2 - \sum_\alpha^n \sum_i^n \frac{Z_\alpha}{r_{i\alpha}} + \sum_{j>i} \frac{1}{r_{ij}} \quad (2.38)$$

to

$$\hat{H}_{el} = -\frac{1}{2} \sum_i^n \nabla_i^2 + v_{ext}(r) + \sum_{j>i} \frac{1}{r_{ij}} \quad (2.39)$$

However, the rigorous foundation for such a focus was not provided until 1964, when Hohenberg and Kohn proved two theorems [14] critical to the establishment of DFT as a legitimate methodology. These theorems, along with their application in quantum chemistry, shall be introduced in the subsequent sections.

### 2.3.1 Hohenberg-Kohn Existence Theorem

The first theorem demonstrates that, in a given, finite  $n$ -electron system with a given particle interaction, there exists a one-to-one correspondence between the external potential  $v_{ext}(r)$  and the ground-state density  $\rho_0(r)$ . In other words, the external potential is a unique functional of the ground-state density  $v[\rho_0](r)$  within an arbitrary additive constant. As a consequence, all observables - including the energy - can be written as a functional of the electronic density. The total energy can thus be expressed as:

$$E[\rho] = T[\rho] + V_{ee}[\rho] + \int \rho(r)v_{ext}(r) dr \quad (2.40)$$

The first two terms of the above equation are a universal functional, meaning that they are defined independently from the external potential.  $T[\rho]$  is the kinetic energy functional while  $V_{ee}[\rho]$  is the electron-electron repulsion potential.

### 2.3.2 Hohenberg-Kohn Variational Theorem

In their second theorem, Hohenberg and Kohn demonstrated that the electronic density of the ground state can be calculated using the variational method. [15–17] In a similar vein to the HF approach, the expectation value of the Hamiltonian is such that:

$$E[\rho] = \langle \Psi[\rho] | \hat{H} | \Psi[\rho] \rangle \geq E_0, \quad (2.41)$$

meaning that the exact ground state energy is a lower bound to what can be obtained with DFT.

Although these theorems demonstrate a link between the electronic density and the system wave function, they do not provide a means of obtaining  $\rho$  without first determining  $\Psi$ . We are then confronted with the same problem as for HF insofar as the direct solution of the Schrodinger equation is impossible due to the presence of the inter-electron repulsion term  $\hat{V}_{ee}$ .

In order to resolve this problem, the real Hamiltonian - describing a system of  $n$  interacting particles - is substituted with a fictitious Hamiltonian describing a system of non-interacting particles with the same density as the fully-interacting system. [18] The resulting

mono-electronic operator, the Kohn-Sham operator  $\hat{H}_{KS}$  is:

$$\hat{H}_{KS} = T_s + \int \frac{\rho(r)\rho(r')}{|r-r'|} dr' + v_{xc}[\rho] + v_{ext}(r) \quad (2.42)$$

where the first and second terms are the non-interacting kinetic and classic coulomb energies. The third term, known as the exchange-correlation potential, is defined as:

$$v_{xc}[\rho] = \frac{\partial E_{xc}[\rho(r)]}{\partial \rho(r)}. \quad (2.43)$$

$E_{xc}$  is the exchange-correlation energy and contains all other interactions - including electron exchange, static and dynamic correlation and changes to the kinetic energy brought by inter-electron interactions - and is discussed in the following section. In principle,  $E_{xc}$  not only accounts for the difference between the classical and quantum mechanical electron-electron interactions, but also includes the difference in kinetic energy between the real and fictitious non-interacting systems.

### 2.3.3 The Exchange-Correlation Approximation

At this point it is important to state that, in the formalism described above, DFT is formally exact. [13] This means that, as long as we know the precise form of the exchange correlation potential, DFT produces the exact energy of the system in question. The inherent complexity of the exchange-correlation functional, however, means that its exact form is unknown. As a consequence, we must make approximations as to its form and properties. A distinct and fundamental disadvantage of DFT is that the method by which we approximate  $v_{xc}[\rho]$  is not obvious and, although some exact properties of the potential are known, there is no clear hierarchical approach to systematically improve its formulation. In this section, various approximations to  $v_{xc}[\rho]$  are discussed along with their justification and implications on the calculated energy of the system.

#### Local Density Approximation

We shall discuss the formulation of various functionals in terms of the functional dependence of  $E_{xc}$  on the electron density. This is expressed as an interaction between the electron density and a so-called *energy density*  $\varepsilon_{xc}$  that depends explicitly on the electron density:

$$E_{xc}[\rho] = \int \rho(r)\varepsilon_{xc}[\rho(r)] dr. \quad (2.44)$$

Here, the energy density is a sum of individual exchange and correlation contributions.

In the Local Density Approximation, [19] the energy density at some position  $r$  is computed exclusively using the value of  $\rho$  at that same position - the local value of  $\rho$ :

$$E_{xc}^{LDA}[\rho(r)] = \int \rho(r) \varepsilon_{xc}[\rho(r)] dr. \quad (2.45)$$

In practice, the only functionals which conform to such a definition that are regularly applied are those that derive from the uniform electron gas, [20] for which the density has an identical value at every position. In this respect, for a given point in the system with an associated density, the contribution to the exchange-correlation energy is computed with the rest of the system described locally by a uniform electron gas with the given density.

### Generalized Gradient Approximation and Kinetic Energy Density

Since the electron density is typically rather far from spatially uniform, it is reasonable to believe that the LDA approach will have limitations. An obvious way to improve the exchange-correlation functional is to make it depend not only on the local value of the density, but on the extent to which the density is locally changing, for example by introducing the gradient of the density into its formulation. Usually, gradient corrected functionals are obtained by adding a correction term to the LDA functional:

$$\varepsilon_{xc}^{GGA}[\rho(r)] = \varepsilon_{xc}^{LDA}[\rho(r)] + \Delta \varepsilon_{xc} \left[ \frac{|\nabla \rho(r)|}{\rho^{4/3}(r)} \right] \quad (2.46)$$

Where the correction depends on the dimensionless reduced gradient. This is generally referred to as the Generalized Gradient Approximation (GGA). [21]

If including the gradient of the density constitutes an improvement over LDA, a logical next step - in the same vein as a Taylor expansion - is to include a dependence on the second derivative of the density (the Laplacian). Such functionals are called meta-GGA functionals and go beyond the gradient-corrected approximation. However, due to numerical issues with with the Laplacian of the density, an alternative and frequently-used meta-GGA formalism is to include the dependence on the kinetic-energy density  $\tau$ :

$$\tau(r) = \sum_i^{occupied} \frac{1}{2} |\nabla \phi_i(r)|^2 \quad (2.47)$$

where  $\phi_i$  are the self-consistently determined Kohn-Sham orbitals.

### The Adiabatic Connection and Hybrid Density Functionals

DFT assumes a fully non-interacting reference system of particles, but imagine if one could control the extent of electron-electron interaction with a given parameter. Using the Hellman-Feynman theorem, it can be shown that the exchange-correlation energy can be computed

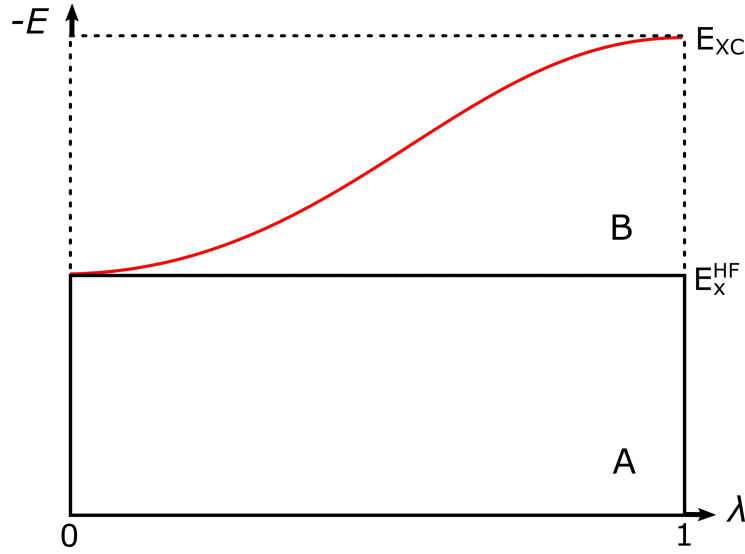


FIGURE 2.2: Pictorial analogy describing the adiabatic connection method. Rectangle  $A$  represents the fully non-interacting system, for which we only have exchange interaction. The full exchange-correlation energy is represented by the area in rectangle  $A$  plus that under the red curve in rectangle  $B$ , i.e. some fraction  $x$  of rectangle  $B$ .

as [13]:

$$E_{xc} = \int_0^1 \langle \Psi(\lambda) | v_{xc}(\lambda) | \Psi(\lambda) \rangle \quad (2.48)$$

where the parameter  $\lambda$  controls the extent of electron-electron interaction, with a range from 0 (none at all) to 1 (exact). It is useful to adopt a geometric picture to describe this integral. In figure 2.2, we partition the electron-electron interaction into two portions - a lower rectangle,  $A$ , and a fraction of another rectangle sitting on top,  $B$ . The lower rectangle represents the fully non-interacting system - in which the only inter-electron interaction is exchange - deriving from the antisymmetry of the wave function described by the Slater determinant. As the breadth of this rectangle is 1, the total interaction energy represented by this portion is thus just 1 times the exact exchange (HF) energy:  $E_x^{HF}$ . The only real difference between  $E_x^{HF}$  for HF and DFT is that the Kohn-Sham orbitals are used. The remaining interaction energy, therefore, is represented by the area under the curve in rectangle  $B$ , i.e. some fraction  $x$  of rectangle  $B$ . As we do not know  $x$ , nor the expectation value of the fully interacting exchange-correlation potential, we may only regard  $x$  as some parameter to be optimized. In this case, the only option is to approximate the fully interacting system (at the upper right corner of  $B$ ) by some choice of DFT functional (for instance, one that relies on the GGA approximation). In this regime, the total area under the curve ( $A + xB$ ) can be approximated as:

$$E_{xc} = E_x^{HF} + x(E_{xc}^{DFT} - E_x^{HF}) \quad (2.49)$$

It is convention to express  $E_{xc}$  in terms of an alternative parameter,  $a$ , defined as  $1 - x$ , giving:

$$E_{xc} = (1 - a)E_{xc}^{DFT} + aE_x^{HF} \quad (2.50)$$

Drawing this connection between the interacting and non-interacting systems is known as the Adiabatic Connection Method, and forms the basis for what are known as Hybrid Density Functionals.

One such Hybrid Functional, widely known as PBE0, [22] takes a value of  $a = 0.25$  (i.e. 25% HF exchange):

$$E_{xc} = E_{xc}^{PBE} + \frac{1}{4}(E_x^{HF} - E_x^{PBE}), \quad (2.51)$$

Where the exchange and correlation functional used to approximate the fully-interacting system is that of Perdew, Burke and Ernzerhoff - known as PBE. Note that, for PBE0, the exchange and correlation portions of the fully interacting system are separated and the adiabatic connection method is applied only to the exchange part. Additionally, as the value of  $a$  in PBE0 derives from perturbation theory arguments, and the underlying GGA functional (PBE) contains no empirical parameters, it is considered a parameter-free hybrid functional.

## 2.4 Time-Dependent Density Functional Theory

Now that we have established ground state DFT, we discuss how it can be extended to calculation of excited-state properties using what is known as Time-Dependent Density Functional Theory (TDDFT). In the following, we introduce the formal justification for TDDFT, how it can be used to calculate excitation energies for molecules, its weaknesses and how these may be overcome.

Introducing the time-dependent Schrodinger equation:

$$\hat{H}_{el}(r, t)\Psi_{el}(r, t) = i\frac{\partial}{\partial t}\Psi_{el}(r, t), \quad (2.52)$$

where:

$$\hat{H}_{el}(r, t) = \hat{T}_e(r) + \hat{V}_{ee}(r, t) + V(r, t). \quad (2.53)$$

As before, the first two terms are the kinetic and electron-electron repulsion terms. The final term is an external potential, although in this case it is time-dependent. For times  $t \leq 0$ , the external potential is constant and therefore reduces to what we find in the previous sections for the time-independent Schrodinger equation. At times  $t > 0$ , the system is now interacting with the same field, though the field is time-dependent.

### 2.4.1 Runge-Gross Theorem

From the time-dependent Schrodinger equation, we have a formally-defined map by which a given external potential  $V(t)$  produces a time dependent wave function  $\Psi(t)$ , evolved from a given initial state  $\Psi_0$ . This wave function can then be used to map a time-dependent density  $\rho(r, t)$ :

$$V(t) \rightarrow \Psi(t) \rightarrow \rho(r, t) \quad (2.54)$$

In order to validate TDDFT, this map must be inverted - we must know that the time dependent density is a valid variable which can completely determine the system dynamics as the wave function does. This was demonstrated in a theorem by Runge and Gross in 1984, [23] which shows that two densities  $\rho(r, t)$  and  $\rho'(r, t)$  that evolve from a common initial many-body state  $\Psi_0$  under two *different* time-dependent external potentials  $V(t)$  and  $V'(t)$  become different at times infinitesimally greater than  $t_0$ . In this way, there is a one-to-one correspondence between densities in potentials that evolve from a fixed initial state. This is the fundamental existence theorem of TDDFT as, from this one-to-one correspondence, it follows that time-dependent density is a unique functional of the potential and vice-versa - that the external potential is a unique functional of the time-dependent density. In turn, the many-body Hamiltonian and thus the many-body wave function are functionals of  $\rho(r, t)$  as well.

### 2.4.2 Van-Leeuwen Theorem

As we have seen previously in DFT and HF theories, the difficulties associated with the inter-electronic repulsion term of the time-dependent Hamiltonian are naturally present in TDDFT. Therefore, in practice, it would be useful to have a scheme analogous to the Kohn-Sham formalism of DFT, in which we replace the fully interacting system with a fictitious non-interacting system which possesses the same density. With just the Runge-Gross theorem, however, we are not explicitly allowed to do this.

In 1999, the theorem of van Leeuwen provided a solid foundation for such an approximation, stating that for a time-dependent density  $\rho(r, t)$  associated with a many-body system with particle-particle interaction  $\omega(r, r')$ , initial state  $\Psi_0$  and external time-dependent potential  $V(t)$ , there exists a different many-body system with interaction  $\omega'(r, r')$  and a unique external potential  $V'(t)$  which reproduces the same time-dependent density. Note that the initial state  $\Psi_0$  must possess the correct initial density and its time-derivative at  $t_0$ .

Interestingly, imposing the condition  $\omega(r, r') = \omega'(r, r')$  (i.e. the interaction of the real and fictitious systems is identical) and choosing  $\Psi_0 = \Psi'_0$ , it is proved that there is a unique potential  $V'(t)$  that produces the density of the interacting system  $\rho(r, t)$ . This is exactly the statement provided by the Runge-Gross theorem, revealing the Runge-Gross theorem to be a special case of the Van-Leeuwen theorem.

### 2.4.3 Linear Response Formalism

TDDFT is able to capture the dynamical nature of an excitation process. During a transition between the ground and a given excited state, periodic charge-density fluctuations are induced, accompanied by dynamical many-body effects and mixing of Kohn-Sham eigenstates. Together, this leads to a correction to the raw Kohn-Sham eigenvalue spectrum (i.e. if one were to construct an absorption spectrum using only the differences in the Kohn-Sham

energy eigenvalues) towards the true spectrum. These dynamical many-body effects are embedded in the so-called exchange-correlation kernel ( $f_{xc}$ ), the key component of TDDFT in the same sense that the exchange-correlation functional is the key component of Kohn-Sham DFT.

Up until now, we have spoken only in terms of the time-dependent Schrodinger equation. In practice, its full solution is often not required or, indeed, desirable. One can imagine that, in cases where the system does not deviate much from the ground state (or, more generally, equilibrium), calculating the full time-dependent wave function only to extract small deviations from it would be inefficient, not to mention numerically challenging. An alternative approach might be to attempt to calculate these differences directly, which can be accomplished through response theory. [24]

Response theory, more specifically linear response theory, is a widely used method one can apply to study how a system responds to weak perturbations. In the context of optical spectroscopy techniques, the weak perturbation is the probing of the ground state by an electric field and the linear response of the system to this field contains all of the information about its optical spectrum.

The Van-Leeuwen theorem was discussed in section 2.4.2, which stated that the time dependent density  $\rho(r, t)$  corresponding to the external potential can also be reproduced in a non-interacting time-dependent Kohn-Sham system with time-dependent external potential:

$$v_{ks}[\rho](r, t) = V(r, t) + \int \frac{\rho(r', t)}{|r - r'|} dr' + v_{xc}[\rho](r, t). \quad (2.55)$$

This can be formally inverted, giving the time-dependent density as a function of the Kohn-Sham potential:

$$\rho(r, t) = \rho[v_{ks}](r, t) \quad (2.56)$$

If we were to expand the time-dependent density in orders of the effective potential, we would obtain the first order term:

$$\rho_1(r, t) = \iint \chi_{ks}(r, t, r', t') v_{ks1}(r', t') dr' dt' \quad (2.57)$$

$$\chi_{ks} = \left. \frac{\delta \rho[v_{ks}](r, t)}{\delta v_{ks}(r', t')} \right|_{v_{ks}[\rho_0](r)} \quad (2.58)$$

This is the linear response equation in TDDFT, which is the density-density response function for non-interacting Kohn-Sham particles and yields the same response as the fully interacting, many-body response equation. The resulting linearized effective potential is:

$$v_{ks}[\rho](r, t) = V_1(r, t) + \int \frac{\rho_1(r', t)}{|r - r'|} dr' + v_{xc1}[\rho](r, t). \quad (2.59)$$

While the first two terms - the external perturbation and the linearized time-dependent

Hartree potential - can actually be written down, the last term - the linearized exchange-correlation potential - can be written explicitly only via a functional Taylor expansion:

$$v_{xc1} = \iint \frac{\delta v_{xc}[\rho](r, t)}{\rho(r', t')} dr' dt' \Big|_{\rho_0(r)} \rho(r', t') \quad (2.60)$$

which features the so-called time dependent exchange-correlation kernel:

$$f_{xc}(r, t, r', t') = \frac{\delta v_{xc}[\rho](r, t)}{\rho(r', t')} \Big|_{\rho_0(r)} \quad (2.61)$$

which is a functional of the ground state density. As previously alluded to, the kernel is the key quantity of TDDFT in the linear response regime. Now that we have an idea of the linearized potential  $v_{xc1}$  let us substitute it into the TDDFT linear response equation 2.57:

$$\begin{aligned} \rho_1(r, t) = & \iint \chi_{ks}(r, t, r', t') dr' dt' \left[ V_1(r, t) \right. \\ & \left. + \iint \left\{ \frac{\delta(t' - \tau)}{|r' - x|} + f_{xc}(r', t', x, \tau) \right\} dx d\tau \rho_1(x, \tau) \right] \end{aligned} \quad (2.62)$$

where we have introduced two dummy variables,  $x$  and  $\tau$ , to emphasize the different double integrals. This expression highlights the dependency of the linearized potential on  $\rho(r, t)$ , and thus demonstrates that the overall linear density response must be solved self-consistently.

#### 2.4.4 Calculating Excitation Energies with TDDFT

In this section we shall introduce how excitation energies are usually calculated within the TDDFT framework. To do so, it is convenient to work in the frequency domain. Performing a Fourier transformation of equation 2.62:

$$\rho_1(r, \omega) = \int \chi_{ks}(r, r', \omega) dr' \left[ V_1(r, \omega) + \int \left\{ \frac{1}{|r' - x|} + f_{xc}(r', x, \omega) \right\} dx \rho_1(x, \omega) \right] \quad (2.63)$$

With the frequency-dependent, non-interacting Kohn-Sham response function:

$$\chi_{ks}(r, r', \omega) = \sum_{i=1}^{\infty} \sum_{j=1}^{\infty} (f_i - f_j) \frac{\phi_i^0(r) \phi_j^{0*}(r) \phi_i^{0*}(r') \phi_j^0(r')}{\omega - \omega_{ij}} \quad (2.64)$$

where  $f_i$  and  $f_j$  are the occupation numbers of the Kohn-Sham ground state and

$$\omega_{ij} = \varepsilon_i - \varepsilon_j \quad (2.65)$$

are the differences between the Kohn-Sham energy eigenvalues for pairs of given molecular orbitals. The above double sum is written so as to include only contributions that involve one occupied ( $f = 1$ ) and one unoccupied ( $f = 0$ ) molecular orbital. The denominator is

such that the non-interacting response function has poles at the excitation energies of the Kohn-Sham system.

At this point, we summarize that the exact excitation energies are given by the poles of the density-density response function, which diverges if the system is subjected to any perturbation at such a frequency and has an eigenmode character. [24] Moreover, inspecting equation 2.62 reveals that an external perturbation is not even required, as a system can provide a finite response at its excitation frequencies even without external perturbation. From here, the idea is to produce a method of calculating these modes directly, for which the starting point is equation 2.63 with the external potential term dropped:

$$\rho_1(r, \omega) = \int \chi_{ks}(r, r', \omega) dr' \left[ \int \left\{ \frac{1}{|r' - x|} + f_{xc}(r', x, \omega) \right\} dx \rho_1(x, \omega) \right] \quad (2.66)$$

Multiplying by the terms in square brackets and integrating over  $r$  we obtain:

$$F_{Hxc}(x, \omega) = \sum_{i=1}^{\infty} \sum_{j=1}^{\infty} \frac{(f_i - f_j)}{\omega - \omega_{ij}} \int dr \left\{ \frac{1}{|x - r|} + f_{xc}(x, r, \omega) \right\} \phi_i^0(r) \phi_j^{0*}(r) \times \int dr' \phi_i^{0*}(r') \phi_j^0(r') F_{Hxc}(r', \omega) \quad (2.67)$$

where:

$$F_{Hxc}(r, \omega) = \int dr' \left\{ \frac{1}{|r - r'|} + f_{xc}(r', x, \omega) \right\} \rho_1(r', \omega) \quad (2.68)$$

For brevity, we have not included spin explicitly, but it is sufficient to mention that, in absence of spin-orbit coupling terms, excitations are only allowed between orbitals of like spin. In any case, within a closed shell formalism, there is no distinction in space between a given orbital pair of opposite spin. Next, after multiplying by  $\phi_i^{0*}(r') \phi_j^0(r')$  and integrating by  $r$  once more, we may rewrite equation 2.67 to give:

$$\int dr \phi_i^{0*}(r) \phi_j^0(r) F_{Hxc}(r, \omega) = \sum_{i=1}^{\infty} \sum_{j=1}^{\infty} \frac{(f_i - f_j)}{\omega - \omega_{ij}} K_{ij, i'j'}(\omega) \int dr \phi_i^{0*}(r') \phi_j^0(r') F_{Hxc}(r', \omega) \quad (2.69)$$

Where we have defined what are known as the coupling matrix elements,  $K(\omega)$ :

$$K_{ij, i'j'}(\omega) = \int dr \int dr' \phi_i^{0*}(r) \phi_j^0(r) \left\{ \frac{1}{|r - r'|} + f_{xc}(r, r', \omega) \right\} \phi_{i'}^0(r') \phi_{j'}^{0*}(r') \quad (2.70)$$

Introducing a final auxiliary quantity:

$$\beta_{ij}(\omega) = \frac{1}{\omega - \omega_{ij}} \int dr \phi_i^{0*}(r) \phi_j^0(r) F_{Hxc}(r, \omega) \quad (2.71)$$

We obtain the final expression:

$$\sum_{i=1}^{\infty} \sum_{j=1}^{\infty} [\delta_{ii'} \delta_{jj'} \omega_{ij} + (f_i - f_j) K_{ij, i'j'}(\omega)] \beta_{i'j'}(\omega) = \omega \beta_{ij}(\omega) \quad (2.72)$$

Which has the form of an eigenvalue equation where the eigenvalues are the exact excitation energies of the system. Note that the equation is of infinite dimension since the sums run over all bound states in the Kohn-Sham regime. Naturally, the above equation is only defined where  $f_i - f_j \neq 0$ , which means that we must only consider transitions from unoccupied to occupied Kohn-Sham states (and vice-versa). In turn, we can rewrite equation 2.72 as two coupled equations:

$$\sum_{i=1}^{\infty} \sum_{j=1}^{\infty} [\delta_{pi'} \delta_{qj'} \omega_{ij} + (f_i - f_j) K_{pq, i'j'}(\omega)] \beta_{i'j'}(\omega) = \omega \beta_{pq}(\omega) \quad (2.73)$$

$$\sum_{i=1}^{\infty} \sum_{j=1}^{\infty} [\delta_{qi'} \delta_{pj'} \omega_{ij} + (f_i - f_j) K_{qp, i'j'}(\omega)] \beta_{i'j'}(\omega) = \omega \beta_{qp}(\omega) \quad (2.74)$$

where we have used the notation  $p, p'$  for occupied states and  $q, q'$  for unoccupied states. If we explicitly introduce the occupation numbers in each case, we can rewrite the coupled equations in more detail:

$$\sum_{i=1}^{\infty} \sum_{j=1}^{\infty} \left\{ [\delta_{pp'} \delta_{qq'} \omega_{pq} - K_{pq, p'q'}(\omega)] \beta_{p'q'}(\omega) + K_{pq, q'p'}(\omega) \beta_{q'p'}(\omega) \right\} = \omega \beta_{pq}(\omega) \quad (2.75)$$

$$\sum_{i=1}^{\infty} \sum_{j=1}^{\infty} \left\{ -K_{qp, p'q'}(\omega) \beta_{p'q'}(\omega) + [\delta_{qq'} \delta_{pp'} \omega_{qp} + K_{qp, p'q'}(\omega)] \beta_{q'p'}(\omega) \right\} = \omega \beta_{qp}(\omega) \quad (2.76)$$

If we let:

$$X_{pq} = -\beta_{pq}, \quad Y_{pq} = \beta_{qp}, \quad (2.77)$$

We obtain the final expression for the direct computation of the exact excitation energies of a given non-interacting Kohn-Sham system of particles:

$$\sum_{i=1}^{\infty} \sum_{j=1}^{\infty} \left\{ [\delta_{pp'} \delta_{qq'} \omega_{pq} + K_{pq, p'q'}] X_{p'q'} + K_{pq, q'p'} Y_{p'q'} \right\} = \omega X_{pq} \quad (2.78)$$

$$\sum_{i=1}^{\infty} \sum_{j=1}^{\infty} \left\{ K_{qp, p'q'} X_{p'q'} + [\delta_{qq'} \delta_{pp'} \omega_{qp} + K_{qp, p'q'}] Y_{p'q'} \right\} = \omega Y_{pq}. \quad (2.79)$$

If we assume that the Kohn-Sham orbitals are real, we can write the coupled equation set in compact matrix form, sometimes known as the Casida Equation [25]:

$$\begin{pmatrix} \mathbb{A} & \mathbb{B} \\ \mathbb{B} & \mathbb{A} \end{pmatrix} \begin{pmatrix} \mathbf{X} \\ \mathbf{Y} \end{pmatrix} = \omega \begin{pmatrix} -\mathbb{1} & 0 \\ 0 & \mathbb{1} \end{pmatrix} \begin{pmatrix} \mathbf{X} \\ \mathbf{Y} \end{pmatrix} \quad (2.80)$$

Where matrix elements of  $\mathbb{A}$  and  $\mathbb{B}$  are:

$$A_{pq,p'q'}(\omega) = \delta_{pp'}\delta_{qq'}\omega_{q'p'} + K_{pq,p'q'}(\omega) \quad (2.81)$$

$$B_{pq,p'q'}(\omega) = K_{pq,p'q'}(\omega) \quad (2.82)$$

Which are sometimes referred to as the orbital rotation Hessians. [24] Again, this matrix pseudo-eigenvalue equation has infinite dimension, so in practice we only solve for a set number of excitation energies (i.e. a pre-defined number of eigenvalues). Generally, the accuracy of an eigenvalue associated with a given excitation energy increases with the number of higher-energy eigenvalues computed, meaning that one should usually consider a greater number of excited states than explicitly required.

In general, the Casida equation returns the exact excitation energies of any many-body system. In order to obtain exact excitation energies however, certain conditions must be met. Firstly, the exact Kohn-Sham ground state of the system must be obtained, which requires an exact Kohn-Sham density functional. Secondly, we require the exact, frequency-dependent exchange-correlation kernel,  $f_{xc}$ , and the infinite eigenvalue problem must be solved. Since matrix elements  $\mathbb{A}$  and  $\mathbb{B}$  explicitly depend on the frequency via the exchange-correlation kernel, this must be done in a self-consistent fashion. It is not necessary to say that, in practice, none of these conditions can be met exactly. Therefore, varying degrees of approximation must be made.

It is also important to note that setting the coupling matrix elements to zero simply yields the Kohn-Sham excitation energies  $w_{ij}$  as eigenvalues which are single excitations - no double or multiple excitations are accounted for. On the other hand, if we were to possess an exact, frequency-dependent kernel, we would obtain poles of the many-body response function  $\omega$  with multiple-excitation character. Unfortunately, this is never true in practice as we shall discuss now.

### 2.4.5 The Adiabatic Approximation in TDDFT

As outlined above, the key quantity in TDDFT is the frequency dependent exchange correlation kernel, which describes the frequency dependent exchange-correlation potential  $v_{xc}[\rho](r, \omega)$ . In analogy to ground-state DFT, application of TDDFT requires an approximation of this potential. The simplest approximation to make here would be to transfer exchange-correlation functionals used in ground-state DFT (e.g. GGA, Hybrid Functionals) to the excited state, where we substitute the frequency-dependent density for the ground state density:

$$v_{xc}^A(r, \omega) = v_{xc}^{GS}[\rho(r, \omega)](r). \quad (2.83)$$

In TDDFT, this is known as the adiabatic approximation. [24] The term 'adiabatic' indicates that  $v_{xc}^A(r, \omega)$  becomes exact where a perturbation acting on the system is sufficiently slow. In reality, this condition is rarely realized, however the adiabatic approximation is used in

almost all applications of TD-DFT in chemistry. A consequence of this is the lack of frequency dependence of  $f_{xc}$ , meaning that only singly-excited states may be accessed within the adiabatic approximation.

### 2.4.6 Charge Transfer Excitations

A well known weakness of TDDFT is the computation of excitation energies where the hole and electron are separated by a large distance. [26] In this section, we outline how this arises and how the choice of density functional within the adiabatic approximation can alleviate this weakness. [24]

Let us begin by considering a case where the donor and acceptor moieties are separated by a large distance  $R$ . In this limit, we can use elementary concepts to obtain the excitation energy, assuming that we have some way of clearly defining  $R$ . The minimum energy required to remove an electron from the donor is given by the ionization potential of the donor,  $I_d$ . When the electron arrives at the acceptor, some of that energy is recovered by the acceptor's electron affinity,  $A_a$ . Once this event has occurred, the two sub-systems feel the electrostatic interaction energy of the resulting electron hole pair, given by  $\frac{-1}{R}$ . For  $R \rightarrow \infty$ :

$$\omega_{ct}^{exact} = I_d - A_a - \frac{1}{R} \quad (2.84)$$

Note that, in principle, this is the exact limit. Comparing with what we would obtain from TDDFT assuming that the charge-transfer excitation lies sufficiently far from any other excitation:

$$\omega_{ct}^{TDDFT} = \varepsilon_a^{DFT} - \varepsilon_d^{DFT} + 2 \iint \phi_a(r)\phi_d(r) \left\{ \frac{1}{|r' - x|} + f_{xc}(r', x, \omega) \right\} \phi_a(r')\phi_d(r') dr dr', \quad (2.85)$$

where the orbitals in question are the highest occupied  $\phi_d(r)$  and lowest unoccupied  $\phi_a(r)$  orbitals of the donor and acceptor moieties, respectively. Since  $\phi_d(r)$  and  $\phi_a(r)$  have an exponentially vanishing overlap, at large distances the final term tends to zero. As a result, the excitation energy computed at TDDFT level collapses to the difference in the Kohn-Sham orbital eigenvalues:

$$\omega_{ct}^{TDDFT} \rightarrow \varepsilon_a - \varepsilon_d. \quad (2.86)$$

This result is insufficient in two ways. Firstly, we clearly lack the  $\frac{-1}{R}$  component from equation 2.84. Secondly, in the limit of the exact exchange-correlation functional:

$$I_d = -\varepsilon_d^{DFT}, \quad A_a = -\varepsilon_a^{DFT}. \quad (2.87)$$

As has been mentioned several times previously, however, we do not possess the exact exchange-correlation functional. Within standard approximations (i.e. GGA), DFT tends to provide excitation energies which are significantly underestimated, explaining why TDDFT can often drastically fail when computing charge-transfer phenomena.

Next, let us consider the same model, only this time we apply a time-dependent Hartree-Fock (TDHF) approach:

$$\omega_{ct}^{TDHF} = \varepsilon_a^{HF} - \varepsilon_d^{HF} - \iint \frac{\phi_a(r)\phi_d(r)\phi_a(r')\phi_d(r')}{|r-r'|} dr dr', \quad (2.88)$$

which becomes, in the limit of large separation:

$$\omega_{ct}^{TDHF} = \varepsilon_a^{HF} - \varepsilon_d^{HF} - \frac{1}{R} \quad (2.89)$$

This demonstrates that the exact-exchange integral is responsible for the  $\frac{-1}{R}$  behavior. Additionally, from Koopman's theorem, [27] we know that the difference in orbital eigenvalues computed with Hartree-Fock is approximately equal to the difference between the ionization potential of the donor and the electron affinity of the acceptor. As a result, TDHF produces charge-transfer excitation energies at least qualitatively correctly.

From here, it is unsurprising that if exact exchange were to somehow be incorporated into the exchange-correlation functional (i.e. Hybrid functionals), we would achieve an improved description of charge-transfer excitations. Functionals which contain a low to moderate amount of exact exchange, such as PBE0 [22] which contains 25% HF exchange, perform well when the distance between the donor and acceptor moieties is not too large. In larger systems, however, where  $R$  becomes large, even hybrid functionals with a reduced amount of exchange fail to cure the underestimation of charge-transfer excitation energies. One might assume that we can just increase the amount of exchange to 100% to completely nullify this problem, though in practice this is not the case as we in turn sacrifice the short-range qualities of a given functional. This apparent trade-off problem has been tackled by a class of functionals known as *range-separated hybrids*, which are discussed in the next section.

### Range-Separated Hybrid Functionals

The basic idea of a range-separated hybrid is to separate the Coulomb interaction into short range (SR) and long range (LR) parts, which are connected by some kind of function  $f$  [28]:

$$\frac{1}{|r-r'|} = \frac{f(\eta, r)}{|r-r'|} + \frac{1-f(\eta, r)}{|r-r'|}, \quad (2.90)$$

where typical choices for function  $f$  are:

$$f(\eta, r) = e^{-\eta|r-r'|}, \quad f(\eta, r) = \text{erf}(\eta r) = \frac{1}{\sqrt{\pi}} \int_r^\infty e^{-r'^2} dr' \quad (2.91)$$

where the separation parameter  $\eta$  can be defined either empirically or using some physical arguments. The resulting general formula for a range-separated hybrid (RSH) is then:

$$E_{xc}^{RSH} = E_x^{SR-DFA} + E_x^{LR-HF} + E_c^{DFA} \quad (2.92)$$

where DFA stands for ‘density functional approximation’, meaning any standard approximation to the exchange-correlation energy within DFT. Since the separation function forces the exact-exchange contribution to  $E_{xc}$  to be 100% at large distances, range-separated hybrids have the correct asymptotic behavior ( $\frac{-1}{R}$ ) while at short distances they make use of the full density functional approximation. Needless to say, these properties mean that range-separated hybrids perform well in the calculation of excitations with significant charge-transfer character, as has been outlined in several benchmark studies. It is for this reason that, at several points throughout this thesis, they have been employed for the study of charge-transfer processes in the condensed phase.

## 2.5 Recovering Static Correlation

In section 2.2.7, we introduced the main deficiency of Hartree-Fock theory - its neglect of electron correlation. Generally, electron correlation is broadly divided into two types: ‘dynamic’ and ‘static’. [13] Dynamic correlation is intuitive, and arises from the correlated motion of each electron with respect to the others. In most cases, dynamic correlation is the dominant contributor to the overall electronic correlation energy  $E_{corr}$  and, up until now, we have discussed how this might be recovered using a system of non-interacting particles that experience an exchange-correlation potential in the framework of DFT. Slightly more opaque, static correlation might arise in situations where we have (near-)degenerate frontier orbitals. Using an illustrative example, if we consider a given molecule whose molecular orbitals are filled until we arrive at (in this example) two degenerate frontier orbitals with only one electron left to place, we must choose one of the two orbitals in which to place it. Let’s say we choose orbital 1 and optimize the wave function using HF theory. We now have a wave function which has been optimized where all other electrons and nuclei feel the electrostatic potential of the electron in orbital 1. However, we could have equally chosen a different initial electron configuration by placing the electron in orbital 2, from which we would have obtained a different wave function. The restriction of only being able to place our electron in one of the two orbitals comes from how we have constructed our wave function - using a single Slater determinant. As, within HF and DFT, we cannot do better than our single Slater determinant, a logical next step would be to construct the wave function using a linear combination of determinants:

$$\Psi = \sum_i c_i \psi_i, \quad (2.93)$$

where the coefficients  $c_i$  reflect the weight of a given electron configuration  $\psi_i$ , known as a configuration state function (CSF), to the overall wave function  $\Psi$ . The first determinant is usually chosen as the HF determinant, however this does not have to be the case in general. To obtain such a wave function, not only must we optimize the coefficients  $c_i$ , but the coefficients that lie within each determinant (i.e. those which constitute the basis set). In the next section, we introduce how this is done via the Multi-Configuration Self-Consistent

Field (MCSCF) approach. [13] Not that, as DFT is formally exact, if one were to be in possession of the exact exchange-correlation functional, DFT is capable of recovering all of what is described above. Unfortunately, this is never the case, and DFT is in practice a single-reference method. As a result, it is necessary to explore other methods capable of recovering the multi-reference character, some of which are outlined below.

### 2.5.1 Multi-Configuration Self-Consistent Field

From the expression in equation 2.93, the total energy may be written as follows:

$$E = \sum_{ij} c_i^* c_j \langle \psi_i | \hat{H} | \psi_j \rangle \quad (2.94)$$

Where  $\hat{H}$  is the electronic Hamiltonian. In the context of MCSCF, it is useful to introduce the unitary group generators (also called shift operators):

$$\hat{E}_{pq} = a_{p\alpha}^\dagger a_{q\alpha} + a_{p\beta}^\dagger a_{q\beta}, \quad (2.95)$$

where  $a_{p\alpha}^\dagger$  is a creation operator for an electron in orbital  $p$  with spin  $\alpha$ , while  $a_{q\alpha}$  is an annihilation operator for an electron in orbital  $q$  with spin  $\alpha$ . In other words, the overall operator  $\hat{E}_{pq}$  serves to generate electron configurations by 'exciting' electrons from occupied to unoccupied orbitals. The Hamiltonian can be expressed in terms of these operators:

$$\hat{H} = \sum_{pq} (p|\hat{h}_1|q) \hat{E}_{pq} + \frac{1}{2} \sum_{pqrs} (pq|rs) (\hat{E}_{pq} \hat{E}_{rs} - \delta_{qr} \hat{E}_{ps}). \quad (2.96)$$

With this, the matrix elements from equation 2.94 become:

$$\langle \psi_i | \hat{H} | \psi_j \rangle = \sum_{pq} \gamma_{pq}^{ij} h_{pq} + \frac{1}{2} \sum_{pqrs} \Gamma_{pqrs}^{ij} (pq|rs), \quad (2.97)$$

where the coefficients in front of the one- and two-electron integrals for each matrix element are called the coupling coefficients, written as follows:

$$\gamma_{pq}^{ij} = \langle \psi_i | \hat{E}_{pq} | \psi_j \rangle \quad (2.98)$$

$$\Gamma_{pqrs}^{ij} = \langle \psi_i | \hat{E}_{pq} \hat{E}_{rs} - \delta_{qr} \hat{E}_{ps} | \psi_j \rangle. \quad (2.99)$$

We now have the following expression for the energy, in terms of the one- and two-electron integrals and the coupling coefficients:

$$E = \sum_{ij} c_i^* c_j \left[ \sum_{pq} \gamma_{pq}^{ij} h_{pq} + \frac{1}{2} \sum_{pqrs} \Gamma_{pqrs}^{ij} (pq|rs) \right] \quad (2.100)$$

Moving the sums over the determinant coefficients inside the inner loops, we arrive at the most compact form:

$$E = \sum_{pq} \gamma_{pq} h_{pq} + \frac{1}{2} \sum_{pqrs} \Gamma_{pqrs} (pq|rs) \quad (2.101)$$

where the coupling coefficients have become:

$$\gamma_{pq} = \sum_{ij} c_i^* c_j \gamma_{pqrs}^{ij}, \quad (2.102)$$

$$\Gamma_{pq} = \sum_{ij} c_i^* c_j \Gamma_{pqrs}^{ij}. \quad (2.103)$$

Respectively, these are known as the one- and two-particle density matrices. Now that we have an expression for the energy, we need to be able to minimize this energy with respect to the orbital coefficients. Here, the final, optimized orbitals may be written as some unitary transformation  $\mathbf{U}$  of the original orbital coefficients  $\mathbf{C}^0$ :

$$\mathbf{C} = \mathbf{C}^0 \mathbf{U} \quad (2.104)$$

where, as in Hartree-Fock,  $\mathbf{C}$  and  $\mathbf{C}^0$  are matrices of the molecular-orbital coefficients with a number of rows (columns) equal to the number of atomic orbitals (molecular orbitals). While there are several approaches to parameterizing  $\mathbf{U}$ , a common approach is to write it as the exponential of an anti-Hermitian matrix:

$$\mathbf{U} = e^{\mathbf{R}} \quad (2.105)$$

and expanding it to the second order in  $\mathbf{R}$  using the power series expansion of the exponential. This yields an expression for the new molecular orbitals:

$$\phi_p \approx \phi_p^0 + \sum_q \phi_q^0 \left( R_{qp} + \frac{1}{2} \sum_r R_{qr} R_{rp} \right). \quad (2.106)$$

From what we have outlined so far, in order to calculate an MCSCF wave function, one must consider all electrons and all orbitals and all of the possible ways in which these can be arranged to form our linear combination of CSFs. Within the choice of basis set, this approach, referred to as 'Full CI', yields an *exact* solution of the time-independent Schrodinger equation (within the Born-Oppenheimer approximation and neglecting relativistic effects). Having said this, the number of CSFs ( $N_{CSF}$ ) for even very small systems can be enormous, as is illustrated by the following equation:

$$N_{CSF} = \frac{n!(n+1)!}{\left(\frac{m}{2}\right)! \left(\frac{m}{2}+1\right)! \left(n-\frac{m}{2}\right)! \left(n-\frac{m}{2}+1\right)!} \quad (2.107)$$

where  $n$  and  $m$  are the number of orbitals and electrons, respectively. As a result, full CI calculations are only performed on the smallest of systems. This does not represent the extent of the application of MCSCF in computational chemistry, however. One can imagine

that the CSFs that are dominant contributors to the overall static correlation energy can be pinpointed using chemical intuition. If we were to restrict the number of electrons and orbitals that may be exchanged to form our total number of CSFs, the result would be a significant saving of computational effort and the ability to extend the MCSCF approach to larger systems. This approach, known as the Complete Active Space Self-Consistent Field (CASSCF) method, is introduced in the next section.

### 2.5.2 Complete Active Space Self-Consistent Field

CASSCF [29] limits the full CI calculations by dividing the one-electron orbital space into three sub-spaces: (i) *inactive*, orbitals which are always kept doubly occupied; (ii) *secondary*, orbitals which are always kept unoccupied and (iii) *active*, a set of orbitals which is partially occupied - known as the *active space*. Within the active space, a full CI calculation is essentially carried out, meaning that CSFs are generated from every possible configuration of electrons and orbitals. Naturally, only the active space needs to be chosen and from there the inactive and secondary orbital sub-spaces are inferred. An aspect - and, in some respects, weakness - of CASSCF is that the active space must be chosen by the user, using chemical intuition and, as a result, CASSCF calculations can require far more expertise to conduct in comparison with HF or DFT calculations. Typical considerations for choosing the active space might be to include orbitals which are involved in bond-breaking, bond-formation or in electronic transitions. With the scaling of the CI expansion outlined in equation 2.107, the size of the active space that can be feasibly used is limited to around sixteen electrons in sixteen orbitals. The setup for a given CASSCF calculation is outlined schematically in figure 2.3.

### 2.5.3 Perturbation Theory and CASSCF

A drawback of CASSCF, when used in isolation, is that - unlike in a full CI calculation - not all dynamic correlation is included due to the restriction on the number of CSFs that are generated. As a result, some dynamic correlation is only recovered within the active space. Fortunately, the majority of the remaining dynamic correlation can be recovered with methods which act as an on-top correction to the CASSCF energy - known as a post-SCF procedure. The most popular of these approaches relies on second-order perturbation theory to account for the remaining correlation energy and is known commonly as CASPT2. Naturally, the core difference between CASPT2 and, for instance, Moller-Plesset second-order perturbation theory (MP2) is that CASPT2 uses the multireference wave function  $\Psi_{CASSCF}$  instead of a single reference HF wave function as the unperturbed system. Generally, CASPT2 represents a non-negligible addition to the overall computational cost of a CASSCF calculation, and can often represent the true bottleneck for medium- to large-sized systems.

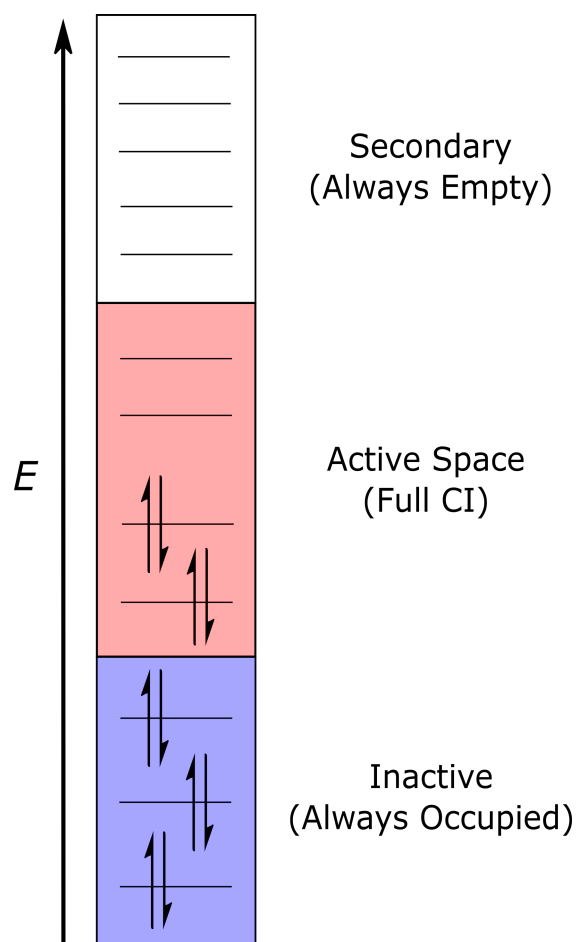


FIGURE 2.3: Schematic of how the orbital space is partitioned in CASSCF calculations. Within the active space, all possible electron configurations are allowed, while in the inactive and secondary sub-spaces orbitals are forced doubly occupied and unoccupied, respectively.

## 2.5.4 Multi-Configuration Pair-Density Functional Theory

The more-recently-developed multiconfiguration pair-density functional theory (MC-PDFT) [30] seeks to combine the explicitly multiconfigurational CASSCF wave function with the low cost of KS-DFT; and it provides a promising alternative to CASPT2 in terms of the required computational resources. The formulation of MC-PDFT has two key differences from Kohn-Sham DFT: (i) the reference wave function is multiconfigurational, and (ii) the density functional employed (called the on-top density functional) depends on the total density and the on-top pair density (in contrast to the exchange-correlation density functionals of Kohn-Sham DFT, which depend on the up-spin and the down-spin densities).

Essentially, MC-PDFT involves two steps: (1) a MCSCF calculation and (2) a post-SCF calculation with an on-top density functional. The MC-PDFT energy is given by:

$$E[\rho, \Pi] = \sum_{pq} h_{pq} \gamma_{pq} + \sum_{pqrs} g_{pqrs} \gamma_{pq} \gamma_{rs} + E_{ot}[\rho, \Pi] + V_{NN} \quad (2.108)$$

where  $\rho$  is the MCSCF density;  $\Pi$  is the MCSCF on-top pair density;  $p, q, r,$  and  $s$  are orbital indices;  $h_{pq}$  are the one-electron kinetic energy, nuclear attraction, and effective core potential integrals,  $\gamma_{pq}$  is an element of the MCSCF one-electron density matrix,  $g_{pqrs}$  are the two-electron integrals,  $E_{ot}$  is the on-top energy, and  $V_{NN}$  is the inter-nuclear repulsion. The on-top energy, akin to the exchange-correlation energy in KS-DFT, includes a correction to the MCSCF one-electron terms plus the exchange and correlation corrections to the MCSCF classical coulomb energy (which is given by the four-index sum in equation 2.108).

Here, it is necessary to discuss the concept of ‘double-counting’ of dynamic electron correlation as, naturally, any attempt to include static correlation energy via a wave function method invariably involves the inclusion of some dynamic correlation energy. In MC-PDFT, this issue is circumvented by only extracting the Coulomb energy and a multi-configurational portion of the kinetic energy from the MCSCF wave function, with the remainder of the energy calculated using an ‘on-top’ density functional, [31] which are described in the next section. In doing so, there is no double-counting of electron correlation within MC-PDFT.

### On-Top Density Functionals

In order to calculate MC-PDFT energies, we need a density functional. While the ultimate goal would be to develop new density functionals to be used specifically with MC-PDFT, the first step that has been taken is to ‘translate’ standard exchange-correlation functionals into what have been termed ‘on-top functionals’ - introducing a dependence on the on-top pair density  $\Pi$ . [32]

To outline how these functionals are formed, it is necessary to recall that if we approximate an exchange-correlation functional using only local densities and their gradients (i.e. GGA), the exchange-correlation functional for a given spin-polarized system may be written as a functional of the total density  $\rho$  and the difference in densities of different spin  $m$ .

From here, Becke suggested that the dependence on  $m$  could instead be substituted for a dependence on the on-top pair density  $\Pi$ . For a single-determinant wave function,  $m$  can be related to  $\Pi$  and  $\rho$  by:

$$m = \rho[1 - R]^{1/2} \quad (2.109)$$

where

$$R = \frac{4\Pi}{\rho^2} \quad (2.110)$$

with  $R \leq 1$  at all points in space. When it comes to multi-determinant wave functions, however,  $R$  can have values greater than 1. Given that  $E(\rho, m, \rho', m)$ , the current general prescription for the translation procedure is given by:

$$E_{ot}[\rho, \Pi] = E_{xc} \left( \rho, \left\{ \begin{array}{ll} \rho(1 - R)^{1/2} & \text{if } R \leq 1 \\ 0 & \text{if } R > 1 \end{array} \right\}, \rho', \left\{ \begin{array}{ll} \rho'(1 - R)^{1/2} & \text{if } R \leq 1 \\ 0 & \text{if } R > 1 \end{array} \right\} \right) \quad (2.111)$$

Essentially, we now have an on-top density functional which has been translated from a given standard GGA functional.

## 2.6 Modeling Solvent Effects

Whether analyzing the absorption properties or excited state lifetime of a molecular system, the majority of photophysical measurements take place in solution. Accurate modeling of the solvation environment, therefore, is paramount from a computational point of view. [33] Here, two main schools of modeling exist [33]: *explicit* solvation, where solvent molecules are accounted for either classically or quantum mechanically, and *implicit* solvation, where interactions with the solvent are accounted for using a reaction field - more commonly referred to as a continuum model. The latter is by far the most commonly employed for modeling solute-solvent interactions and it is this method that we have employed throughout this work. In the following, we outline the main concepts behind common solvation techniques in theoretical chemistry.

### 2.6.1 The Polarizable Continuum Model

In some form or another, the polarizable continuum model (PCM), [34] represents the most frequently used reaction field method. Therein, molecule and solvent are separated by means of a predefined cavity into which the quantum mechanically treated molecule is placed. This cavity can be constructed via, for instance, a superposition of spheres centered on each atom, with smoothing functions applied to prevent discontinuities in the resulting surface or on the iso-density surface of a given molecule. At the surface, the cavity is divided into small, triangular regions by projecting polyhedra from the center of each atomic sphere. This projection produces triangular regions, or *tesseræ*, at the center of which point charges are placed that represent the electrostatic polarisation of the solute electronic density by the solvent. The contribution of the reaction field to the solute free energy can then be expressed

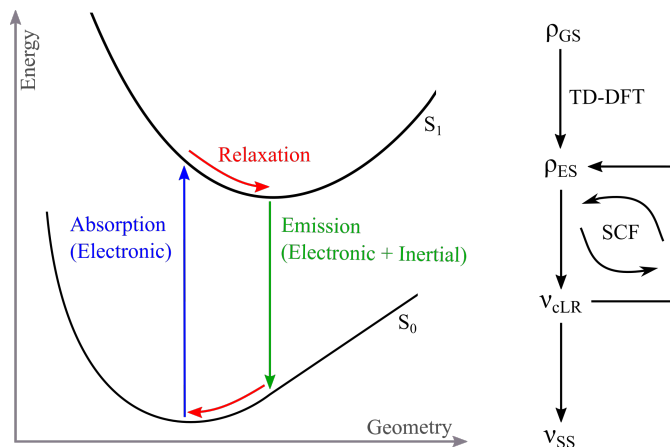


FIGURE 2.4: Left: Arbitrary ground ( $S_0$ ) and excited ( $S_1$ ) potential energy surfaces. Arrows corresponding to absorption (blue) and emission (green) electronic transitions are shown, as well as the ideal equilibrium state of the solvent with respect to the solute used in their calculation. Right: Procedure for obtaining the corrected linear response (cLR) and state specific (SS) solutions for excited-state equilibrium of the solvent.

as:

$$G = \frac{1}{2} \mathbf{V}^\dagger \mathbf{q}, \quad (2.112)$$

where vector quantity  $\mathbf{V}$  represents the values of the solute electrostatic potential and  $\mathbf{q}$  are the charges on the cavity surface centered at each of the tesserae. Though several different models exist for determining the surface charge values, a general relationship, which depends on the solvents electrostatic potential (and therefore, density) can be expressed as:

$$\mathbf{q} = -\mathbf{D}\mathbf{V}, \quad (2.113)$$

where  $\mathbf{D}$  is a square matrix defined by the inverse of the matrix defining the PCM linear system of equations and is related to the geometrical parameters of the cavity and the solvent dielectric constant  $\epsilon$ . The relative polarity of a given solvent is introduced by this dielectric constant, where  $\epsilon = 1$  (i.e. vacuum) within the cavity and  $\epsilon = \epsilon_{solvent}$  elsewhere.

Electrostatic solute-solvent interactions are introduced as a perturbation of the solute Hamiltonian. In the context of TD-DFT, the solute-solvent interaction is expressed as a response operator  $Q$ , resulting in a dielectric-dependent perturbative term being added to the coupling matrix elements  $K$ :

$$K_{\mu\nu,\sigma\tau} = K_{\mu\nu,\sigma\tau}^0 + \sum_{IJ}^{tesserae} \phi_{\mu\nu}(\mathbf{r}) Q_{IJ}(\epsilon) \phi_{\sigma\tau}(\mathbf{r}) \quad (2.114)$$

Where  $K_{\mu\nu,\sigma\tau}^0$  is the coupling matrix element for an isolated system. The second term is the solute-solvent interaction free energy where we have assumed that the solute-solvent interaction surface is approximated by a series of point charges, centered on each of the

tesserae. In this formulation, known as Linear Response PCM (LR-PCM) due to the linear-response formalism of the solute-solvent interaction, the electronic degrees of freedom of the solvent remain in equilibrium with the ground state. This, naturally, is an approximation which may be justifiable in situations where differences in the ground and excited state densities are small. When this is not the case, such as for electronic excitations with significant charge-transfer character, the electrostatic potential produced by the solvent charges can be brought into equilibrium with the density of the excited state of interest in an approach known as Corrected Linear Response (cLR-PCM). [35] The cLR-PCM can be taken as-is or can be seen as the first iteration of a self-consistent determination of the excited state density and associated solvent electrostatic potential, known as State-Specific PCM (SS-PCM, see Figure 2.4). [36] The solute degrees of freedom that we consider to be in equilibrium (or not) with the solute can be divided into two broad terms: electronic and inertial. In physical terms, the former corresponds to the degrees of freedom available to the solvent electronic density, whereas the latter corresponds to the implicit nuclear degrees of freedom of the solvent. Which of these terms we desire to be in equilibrium with our solute (and at which electronic state) depends on the properties we wish to calculate. Figure 2.4 shows an arbitrary representation of a ground and excited-state potential energy surface, onto which we have indicated the ideal equilibrium state of the solute with respect to the solvent for a given property (absorption or emission).

In this thesis, we are primarily interested in assessing the performance of the electrostatic embedding model outlined in chapter 4 for various applications. A core aspect of its assessment is the consideration of system behavior upon changing environment (e.g. fluorescence changes from solution to solid-state) as an explicit observable. For everything that concerns the calculation of optical properties in solution, we make use of PCM using, where appropriate, its various implementations.



## Chapter 3

# Modeling the Crystalline Phase

It is well known that photophysical properties of a given molecular system can be strongly influenced, and are often predicated, by interactions with the surrounding environment, whether it be surrounding solvent [7] or indeed other surrounding molecules within a molecular crystal. [8] For this reason, considerable resources have been dedicated to the study of environmental influence in order to gain insight into, and control over, different excited state processes which can give rise to potentially useful photophysical traits to be applied within optoelectronic devices.

From both an experimental and theoretical perspective, methods for studying photophysical properties in solvents are very well developed to the extent that it is becoming possible to gain control over and tune excited state processes in solution. In the solid state, such processes are more difficult to characterize experimentally and reports of interesting photophysical behavior in periodic systems, which can often be small and subtle, are far rarer when compared with solution. Describing complex photochemistry in the crystalline phase represents a significant and ongoing challenge for computational chemists. Models of sufficient quality - able to both understand and predict the influence of a given environment on optical properties, as well as how they are altered by changing the environment - are a necessary component in the design-process of functional molecules and materials. This chapter outlines what is considered when constructing a given model and constitutes an outline of current computational techniques for approximating the crystalline phase in the context of excited-state modeling.

### 3.1 Periodic Boundary Conditions

If one wishes to study crystalline systems - which are inherently periodic - with quantum chemical methods, a logical step is to extend the approaches outlined in chapter 2 to such periodic systems. In this section, we outline how this is generally achieved by introducing the concept of Bloch functions [37] and how these are applied in solving the Schrodinger Equation for periodic systems.

### 3.1.1 Bloch Functions and Crystalline Orbitals

Let us consider a translation operator  $\hat{T}$ , associated with a given lattice vector  $T$ , applied to the Hamiltonian operator discussed previously for HF and Kohn-Sham theory:

$$\hat{T}\hat{H}(r)\psi(r) = \hat{H}(r+T)\psi(r+T) = \hat{H}(r)\hat{T}\psi(r). \quad (3.1)$$

Due to the periodic nature of the crystal, the Hamiltonian operator itself is also periodic and is associated with a periodic potential. The commutation relation between  $\hat{T}$  and  $\hat{H}$  means that the wave function is an eigenfunction of both the translation operator and the Hamiltonian. Now introducing the Bloch theorem, which states that such eigenfunctions  $\psi(r)$  satisfy the relation:

$$\hat{T}\psi(r) = e^{i\mathbf{k}\cdot\hat{T}}\psi(r) \quad (3.2)$$

(where  $\mathbf{k}$  is a lattice vector defined in reciprocal space) and imposing appropriate periodic boundaries defined by a given crystalline unit cell, we may now in principle model the electronic properties of the crystal using a three-dimensional, periodic array of identical unit cells which are repeated indefinitely. In this way, we are said to be applying ‘periodic boundary conditions’ (PBC) [38] to our system. In analogy with molecular systems, a given mono-electronic wave function may be built using a linear combination of Bloch functions which form what we may now refer to as ‘crystalline orbitals’  $\psi^k$ :

$$\psi^k(r) = \sum_{\mu} c_{\mu}^k \phi_{\mu}^k(r) \quad (3.3)$$

Using these Bloch functions, methods previously outlined in chapter 2 (HF, DFT) may be used to variationally solve for the crystalline orbital coefficients. At this stage, it is important to highlight that, due to the periodic properties of Bloch functions in reciprocal space, the resolution of the HF or Kohn-Sham equations can be limited to the first ‘Irreducible Brillouin Zone’ (IBZ, the unit cell of the symmetrically-reduced reciprocal lattice). As such, the complete set of Bloch eigenfunctions  $\{\psi(r)\}$  can be found for a predefined number of points  $\mathbf{k}$  (k-points) in the IBZ, at each of which the given system of equations are independently solved.

To construct our Bloch functions, we require a basis set. A direct extension of what is discussed in 2, these are made up of local functions  $\chi_{\mu}$  centered on atoms within the crystalline unit cell which are replicated in three-dimensions so as to obtain periodic Bloch functions of the form:

$$\phi_{\mu}^k = \frac{1}{\sqrt{N}} \sum_T e^{i\mathbf{k}\cdot\hat{T}} \chi_{\mu}^T(r - r_{\mu}) \quad (3.4)$$

indicating the inherent periodicity of the underlying basis set. In this thesis, calculations conducted using periodic boundary are performed exclusively using localized basis sets.

### 3.1.2 Periodic Boundary Conditions and Excited-State Properties

While the extension of, for example, DFT to excited states (TDDFT) for molecular systems is nowadays well developed, this is not the case for periodic calculations of crystalline systems. One frequently-used approximation in the literature is to interpret differences between electronic bands in periodic systems directly from Kohn-Sham eigenvalues. [24] Though this approximation can yield surprisingly accurate results, it has no formal justification and neglects potentially significant particle-hole interactions at the excited state. [24] Additionally, agreement with experimental observables is often conditional on the application of empirical shifts. The next step, as for molecular systems, might be to extend ground state methods to the excited state in periodic systems (i.e. TDDFT, TDHF), though in practice this approach suffers from two major drawbacks. [24] As discussed in chapter 2, such methods have been found to be sufficiently accurate for many molecular systems, however this accuracy is not transferred to infinite periodic systems, yielding results of far lower quality. This so-called ‘scale-up catastrophe’ has been attributed (in TDDFT) to the increased dominance of the exchange-correlation kernel over the Hartree response kernel in periodic systems, while the opposite is true for molecular systems. The second drawback is related to the Bloch theorem, as it has been demonstrated that the coupling matrix terms derived from linear-response theory depend simultaneously on more than one k-point in the IBZ. As was outlined in the previous section, Kohn-Sham/HF equations at given k-points in periodic calculations are solved for independently. For infinite three-dimensional systems, the simultaneous dependence on multiple k-points renders the eigenvalue problem restrictively large, though this can be alleviated using TDDFT-style methods that do not construct large matrices explicitly.

In the following, we discuss how the problem of crystalline systems being periodic can be somewhat circumvented using clusters, which are essentially a representative portion of the bulk solid which has been extracted from the periodic system. Naturally, as clusters are inherently ‘molecular’, well-developed methods for molecular systems can be, in principle, ported over and applied to a given cluster model. However, there can be serious consequences of approximating fully periodic systems with finite clusters - specifically when it comes to accounting for the bulk environment - and cluster methods can not be applied for the study of all solid-state properties. Different approaches to cluster modeling of periodic systems are discussed in the next section, along with their respective applicability and drawbacks.

## 3.2 Cluster Modeling

For a number of years, traditional quantum chemistry methods have been used to study the energetics of periodic systems using cluster-based approaches, where the total system is approximated using a finite volume of the bulk. Although cluster-modeling is not appropriate for the calculation of all bulk-phase properties, it can be applied in situations where a bulk property can be described by a well-defined portion of the overall material. [39] This can be

the case, for example, for point defects in periodic solids, surface adsorption of molecules, and heterogeneous catalysis. [40] This same concept can easily be extended to study excited-state processes, as the change in electronic structure brought by photon absorption is usually confined to a given photoactive center.

The quantum chemical methods which underpin cluster modeling, however, can only be applied when studying small fragments of the overall system due to their nonlinear scaling properties, forcing one to neglect often crucial interactions with the surrounding environment. This section is dedicated to a discussion on how recent developments in cluster modeling permit the inclusion of these interactions, their underlying assumptions, and how these affect their applicability in both ground- and excited-state modeling.

### 3.2.1 Hybrid Energy Schemes

In situations where we have a well-defined area of interest within a given cluster, a clear option is to use a more expensive computational method for that portion of the cluster, while approximating the surrounding, less important, environment using a less expensive approach. Of the various advancements in recent years within this paradigm, hybrid energy techniques [39] represent the most popular development. The starting point for such models is to divide the system into at least two regions (I and II), where the total energy of the system is given, generally, by:

$$E = E_I^{high} + E_{II}^{low} + E_{interaction} \quad (3.5)$$

These regions are treated with different levels of theory, applying varying degrees of approximation with associated varying computational cost to each. Typically, the most accurate, and computationally expensive, theory (high level) is reserved for the chemically interesting region (I) where, for example, bond breaking, bond formation or photon absorption is occurring. The remainder of the system (II) is treated with a more approximate, yet cost effective, theory (low). Generally, the material difference between hybrid energy models lies in the interaction term, for which different approximations have been explored. While the underlying formalism and objectives are similar for most hybrid energy schemes, there are key distinctions which lead to differences in model accuracy, applicability, and computational investment. The next section outlines currently available hybrid energy schemes that can be used to compute excited state properties of crystalline systems.

#### ONIOM

The ONIOM approach, [41] in its various implementations, represents the most popular of these hybrid energy schemes. In cases where the studied system is split into two regions, the general form of the hybrid energy is:

$$E_{ONIOM} = E(R)^{low} + E(M)^{high} - E(M)^{low} \quad (3.6)$$

Where *low* and *high* indicate the relative level of theory applied to each of the *real* (R) and *model* (M) subsystems, and R and M signify the entire cluster and the high-level portion respectively (see figure 3.1). We can draw a direct analogy with equation 3.5 by adding and subtracting the low-level energy of the model system:

$$E_{ONIOM} = (E(R)^{low} - E(M)^{low}) + E(M)^{low} + (E(M)^{high} - E(M)^{low}) \quad (3.7)$$

In keeping with equation 3.5, the first term in brackets is the energy of the region *II*, the second term is the energy of region *I*, and the third term is the interaction energy - described by the difference in energy between the high and low levels of theory for the model system. The level of theory we choose for each layer is strongly dependent on the properties of interest. The vast majority of ONIOM-type calculations are performed in the QM:MM formalism, where the high-level layer is treated quantum mechanically (usually with DFT) and the low-level layer is treated classically, with a molecular mechanics force-field. However, molecular mechanics is often inadequate as the low-level method, especially when electronic effects between the regions are important. [42] In such cases, QM:QM' approaches can be employed, for which the low-level region, while also treated quantum mechanically, takes on a reduced basis-set size or a lower-cost QM method.

Electrostatic interactions between the low- and high-level layers are approximated entirely at the low-level, using a simple, classical point charge model:

$$E_{elec} = \sum_i \sum_j \frac{q_i q_j}{R_{ij}} \quad (3.8)$$

Where *i* and *j* are charges located in the high- and low-level subsystems, respectively, and  $R_{ij}$  is the distance between two atomic centers. Charges correspond either to those of the molecular mechanics force-field (QM:MM) [43] or Mulliken charges derived from the QM' electron density (QM:QM'). [42] Here, as the interaction between the two regions is treated entirely by the low-level theory, the high-level wave function is still effectively optimized in isolation, and the interaction energy is included as an additive term to the total energy -

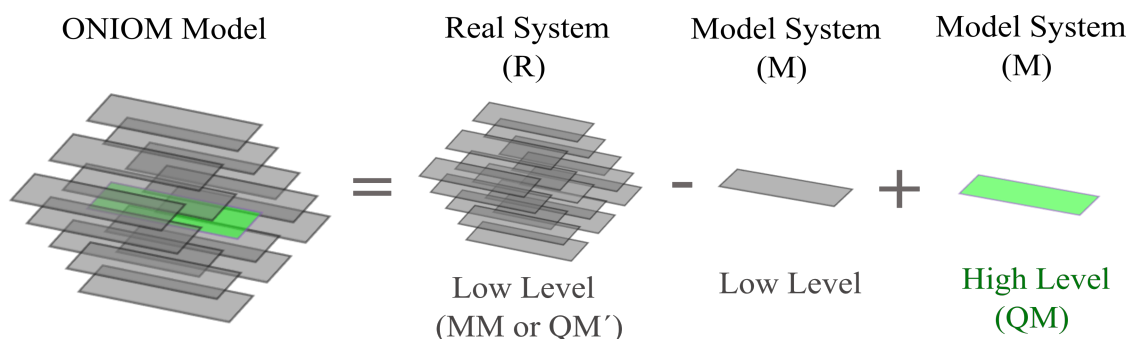


FIGURE 3.1: Schematic representation of equation 3.6, describing how an ONIOM model of a periodic, crystalline system might be constructed.

known as mechanical or classical embedding. The lack of direct coupling between the low-level region the high-level wave function can lead to serious errors in cases which involve significant charge transfer in the high-level region. To improve upon this approximation, introduce direct coupling between layers, and allow for the polarization of the high-level wave function by the low-level layer, this interaction term - in a process known as electronic embedding [42] - can be included explicitly in the quantum-level Hamiltonian as a perturbation:

$$\hat{H} = \hat{H}^0 - \sum_i \sum_j \frac{q_i q_j}{R_{ij}} \quad (3.9)$$

Which, in the LCAO approximation, yields perturbed matrix elements of the core Hamiltonian:

$$h_{\mu\nu} = h_{\mu\nu}^0 - \sum_j q_j V_{\mu\nu} \quad (3.10)$$

Within the SCF procedure, this results in a perturbed density matrix and a subsequent alteration of the final SCF energy. The resulting density can be rationalized as the polarized electronic density of the high-level region by the electrostatic potential of the low-level region.

An as-yet unsolved issue lies in the polarization of the low-level subsystem. [42] In principle, the high- and low-level systems will undergo a mutual polarization until a self-consistency is reached in their charge distributions. In the context of QM:MM, this relies on a polarizable force-field [44] and the introduction of an additional, external self-consistency to equilibrate the excited-state density of the high-level layer with the ground-state density of the low-level layer.

With ONIOM, one can describe the short-range electrostatic potential of the environment and even include the polarizing effect of the environment on a given quantum-mechanical cluster. More recently, the mutual polarization of the QM cluster and the environment has been accounted for using polarizable force-fields for the low-level layer. While not every variation of ONIOM discussed above has been applied to study excited states in crystalline systems, it is important to note that all of these approaches could feasibly be used, with varying degrees of approximation. Generally, ONIOM relies on the confinement of the exciton to the high-level system and, in all cases that do not use non-polarizable force-fields, assumes that the low-level density is reasonably approximated by that of the unpolarized ground state. Naturally, this assumption breaks down if there is a significant change in the low-level wave function between ground and excited states through charge transfer - often an integral part of photochemical processes. For reasons that shall be further discussed in section 4.1, another drawback of ONIOM is its applicability to infinite, periodic systems due to the discrepancy between long-range electrostatic potentials computed for finite and infinite systems.

### Frozen Density Embedding

Frozen Density Embedding (FDE) [45] represents another hybrid energy formalism. Applicable for both three-dimensional periodic systems and surface calculations, the interaction term is described via an embedding potential obtained by partitioning the electron density into two subsystems:

$$\rho_{tot}(r) = \rho_I(r) + \rho_{II}(r) \quad (3.11)$$

Region I is the area of interest while region II is the periodically infinite background. With this partitioning, the total energy  $E_{tot}$  is defined:

$$E_{tot} = E_I + E_{II} + E_{INT} = \langle \Psi_{tot} | \hat{H}_I + \hat{H}_{II} + \hat{H}_{INT} | \Psi_{tot} \rangle \quad (3.12)$$

Where  $\hat{H}_{INT}$  and  $E_{INT}$  denote the Hamiltonian and interaction energy between regions  $I$  and  $II$ , and where  $H_I$ ,  $H_{II}$  and  $E_I$ ,  $E_{II}$  refer to the Hamiltonian and energy for regions  $I$  and  $II$ , respectively. As region  $II$  influences region  $I$  only through the interaction Hamiltonian, the interaction energy represents the key quantity and can equally be expressed as:

$$E_{INT} = E_{tot}[\rho_{tot}] - E_I[\rho_I] - E_{II}[\rho_{II}] \quad (3.13)$$

Where each energy functional contains terms analogous to that found in the conventional DFT framework. The total density  $\rho_{tot}$  is obtained from a periodic DFT calculation and is held constant, therefore making the assumption that the level of theory used for this step already produces a good approximation of the electronic density. From this, the embedding potential is expressed as the functional derivative of the interaction energy with respect to the density in region  $I$ :

$$\hat{v}_{emb} = \frac{\delta E_{INT}}{\delta \rho_I} \quad (3.14)$$

In the Hartree-Fock representation, this potential is added to the Fock operator  $\hat{F}_{\mu\nu}$  as a one-electron operator. Solving for the region  $I$  density matrix in the cluster molecular-orbital basis according to

$$\sum_{\nu} (\hat{F}_{\mu\nu} + \langle \phi_{\mu}(\mathbf{r}) | \hat{v}_{emb}(\mathbf{r}) | \phi_{\nu}(\mathbf{r}) \rangle) C_{\nu,i} = \epsilon_i \sum_{\nu} S_{\mu\nu} C_{\nu,i} \quad (3.15)$$

produces a renewed density matrix for region  $I$ . As the embedding potential itself depends on  $\rho_I$ , a self-consistent procedure is used to obtain a corrected embedding potential. Following this procedure, the total energy of the system is approximated as:

$$E_{tot} \approx E_{tot}^{emb} = E_I + E_{II}^{DFT} + E_{INT}^{DFT} \quad (3.16)$$

Where the energy of region  $I$  is obtained at some higher level of theory than that of both region  $II$  and the interaction energy. Adding and subtracting the DFT energy of region  $I$

( $E_I^{DFT}$ ) allows the total energy to be rewritten:

$$E_{tot}^{emb} = E_{tot}^{DFT} + E_I^{ab} - E_I^{DFT} \quad (3.17)$$

This is reminiscent of the total energy expression for ONIOM, where the total energy of the system is written as the total energy computed at some lower level of theory plus a correction term. Unlike ONIOM, FDE accounts explicitly for the long-range electrostatic interactions of the periodic system through the initial, periodically-derived embedding potential. In the context of excited-state modeling, FDE assumes that the ground state wavefunction of the periodic environment is sufficient when deriving the embedding potential. As discussed for ONIOM, this may not always be justified, particularly in cases where charge-transfer excitations play a key role in the photochemistry of interest.

### Periodic Electrostatic Embedded Cluster Method

Another hybrid energy approach, the Periodic Electrostatic Embedded Cluster Method (PEECM) [46] makes use of a periodic system of point charges to describe the electrostatic interaction between the quantum-mechanically treated fragment and its environment. In this case, the periodic system is split into three sections: (i) the quantum mechanical region, (ii) an isolating layer of point charges where cations are replaced by all-electron effective core potentials (ECPs), (iii) an array of point charges. As this approach is intended for the study of point defects ionic solids, where the magnitude of a given point charge can be relatively large, the isolating shell serves to prevent over-polarization of the central region by nearby, positive point charges. In an analogous fashion to ONIOM electrostatic embedding, interaction between the QM cluster and the surrounding periodic array of point charges is expressed by a perturbation term in the Fock matrix,  $\hat{F}_{emb}$ :

$$\hat{F}_{emb} = - \sum_L \sum_j q_j \int \frac{\mu(\mathbf{r} - \mathbf{R}_\mu) \nu(\mathbf{r} - \mathbf{R}_\nu) \delta(\mathbf{r}' - \mathbf{R}_J + L)}{|\mathbf{r} - \mathbf{r}'|} d\mathbf{r} d\mathbf{r}' \quad (3.18)$$

Where  $\mathbf{L}$  is a lattice vector in direct space,  $q_j$  is a point charge at position  $\mathbf{R}_j - \mathbf{L}$  outside the quantum cluster. This means that this infinite sum includes all periodic point charge images except those that lie inside the quantum cluster or ECP regions. Gaussian functions  $\mu$  and  $\nu$  at positions  $\mathbf{R}_\mu$  and  $\mathbf{R}_\nu$  belong to the QM cluster itself. In practice, the embedding perturbation is split into the so-called "near-field" (NF) and "far-field" (FF) contributions:

$$\hat{F}_{\mu\nu}^{emb} = \hat{F}_{\mu\nu}^{NF} + \hat{F}_{\mu\nu}^{FF} \quad (3.19)$$

Coulomb interactions between the cluster and NF point charges are calculated as a direct sum, with the FF contributions solved using multipole expansions - specifically an approach known as the periodic fast multipole method (PFMM). [47] In contrast to the more precise Ewald approach (discussed in the next chapter), PFMM is conducted entirely in real space

and results in a systematic shift in the electrostatic potential with respect to the Ewald potential. As one is generally only interested in differences in potentials, however, this shift is not significant.

PEECM has been principally developed for the study of ionic crystalline systems, where the charge density at a given site is usually well defined. In principle, it could be extended to study other crystalline systems, provided that a reasonable guess for the point charges which make up the environment could be obtained. Although, to our knowledge, PEECM has not been used for the calculation of excited state properties, it would suffer from the same drawback as both conventional ONIOM methods and FDE, in the sense that the ground state density of the environment may not always be appropriate when describing the embedding potential.

### 3.2.2 Cluster Modeling vs. Periodic Boundary Conditions

It is useful to give additional context to cluster models by discussing their advantages and disadvantages with respect to periodic calculations. Firstly, cluster approaches usually represent a reduced computational cost - particularly when a given property of interest is rather local in nature, leading to a reduced required cluster size. Secondly, a larger number of non-periodic quantum chemical programs are generally available to use. Aside from economical aspects, a larger variety of quantum-chemical models are available to cluster models (for instance, explicitly correlated *ab initio* methods necessary for systems with large contributions from static correlation). Furthermore, there are a larger number of implemented property analyses - for example a large variety of charge fitting processes. Lastly, the modeling of non-ideal crystalline properties - such as point defects, disorder and impurities - is easily achieved.

Although these advantages are substantial, there are also some significant disadvantages of cluster-based methods. Approximating the bulk system as a cluster automatically removes all translational symmetry of the wave function and can lead to the loss of local point group symmetry. The finite nature of the model can lead to an approximate treatment or even full neglect of long-range interactions and a lack of strict boundary constraints such as the total system charge. Cluster models are also conceptually less simple as there are usually a larger number of parameters that need to be set prior to calculation, such as the cluster size, boundary and associated level(s) of theory.

Through the methods outlined above, we have seen how some of these disadvantages may be mitigated by applying various approximations to the crystalline environment. In the next chapter, we introduce the method developed in this thesis which, like those previously discussed, serves as an approximation to the crystalline environment. However, the major difference between this method and those discussed above is that it allows one to generate an *excited-state* embedding potential, rather than that of the ground state.



## Chapter 4

# SC-Ewald: A Self-Consistent Excited-State Embedding Potential

Within the context of the cluster-based techniques in Chapter 3, we have outlined different approaches and considerations for modeling excited-state properties in crystalline media, underlined requirements for the electrostatic potential produced by the environment and how these requirements are, and can be, achieved. We now introduce the electrostatic embedding approach which lays the foundation for the majority of work presented later in this thesis. In essence, this approach counters the problem of long-range electrostatics in infinite periodic systems using the Ewald summation technique. Coupled with a self-consistent procedure, this approach produces an embedding potential derived from the excited-state density of the quantum-mechanical cluster. This chapter first introduces the problem of long-range electrostatics in infinite systems and how this was solved by Ewald, before introducing the original Ewald embedding method for the calculation of ground state properties. Lastly, we outline the self-consistent procedure which yields the excited state embedding potential.

### 4.1 The Infinite Electrostatic Potential

Using the cluster-based approaches discussed in Chapter 3, one seeks to reproduce the electrostatic potential of the surrounding - for our purposes crystalline - environment. While FDE and PEECM explicitly account for long-range electrostatic interactions through, respectively, the embedding operator and fast multipole methods, ONIOM - by far the most frequently used embedding approach - neglects interaction with any of the surrounding bulk crystalline atoms not explicitly included in the chosen cluster. One might assume that these interactions are negligible if the atoms concerned lie sufficiently far from the quantum mechanical cluster. However, in this section, we discuss how this is almost always not the case and how this assumption can lead to significant error in the ground state potential.

The electrostatic potential felt by an atom at a given point within a periodic lattice, known as the Madelung potential, [48] represents that of the surrounding infinite medium. For a periodic system of point-charges, the interaction energy between a given point-charge

$q_i$  and the remaining lattice - represented by charges  $q_j$  - is:

$$E = \frac{1}{2} \sum_{\mathbf{n}} \sum_j \frac{q_i q_j}{|\mathbf{r}_{ij} + \mathbf{n}L|} \quad (4.1)$$

Where the sum is conducted over integer values of  $\mathbf{n} = (n_x L, n_y L, n_z L)$ , resulting in a sum over all points on the lattice. Naturally, computing the electrostatic interaction between a given point and an infinite, periodic system requires an infinite summation - unfeasible in practical terms. A logical assumption would be that, if we were to take a large enough array of charges surrounding our point  $q_i$ , it would serve as an accurate approximation of the infinite electrostatic potential. In reality, due to the slow and conditional nature of the direct summation, approximating the Madelung potential with a finite charge array - however large - can lead to serious errors. [49] The only exception is where the dipole moment of the crystallographic unit cell is exactly zero and where higher electrostatic moments are very small, however in the vast majority of cases these conditions are not met. [49]

A clever solution to this computational problem was given by Ewald in 1921, [50] using an approach which allows one to circumvent the conditional convergence properties of the direct sum. We shall now outline how Ewald summation is performed. Computing the energy  $E_i$  of a point-charge  $q_i$  at position  $\mathbf{r}_i$  within an infinite periodic lattice requires three quantities. The first quantity is the binding energy  $E_i^r$  of charge  $q_i$  due to the infinite array of other charges  $q_j$  with position  $\mathbf{r}_j$ , each of which is shielded by a fictitious Gaussian charge distribution with total charge  $-q_j$ . Crucially, the shielding function allows this summation to converge rapidly in real (direct) space. The second quantity  $E_i^f$  is represented by the binding energy of the charge  $q_i$ , due to the infinite array of Gaussian charge distributions described above, plus an additional Gaussian distribution with total charge  $-q_i$  centered at  $\mathbf{r}_i$ . This sum is conducted over a complete, periodic array of identical Gaussian distributions and, as such, is rapidly convergent when solved in Fourier (reciprocal) space. The third term  $E_i^c$  is effectively the binding energy of charge  $q_i$  due to the additional Gaussian function centered at  $\mathbf{r}_i$  described previously. The terms are combined to compute the binding energy of point-charge  $q_i$ :

$$E_i = E_i^r - E_i^f + E_i^c \quad (4.2)$$

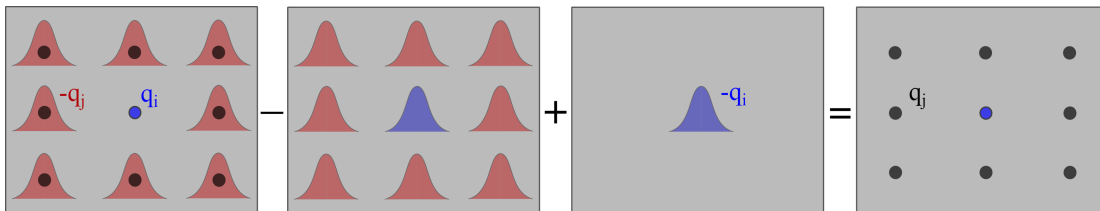


FIGURE 4.1: Schematic representation of equation 4.2 - how the terms computed in the Ewald summation approach are combined to give the electrostatic potential at site  $q_i$  produced by all other atoms  $q_j$  in a periodic lattice.

A schematic of how this combination yields the interaction energy of  $q_i$  with the periodic lattice is given in Figure 11.1. The real space Ewald sum  $E_i^r$  is given by:

$$E_i^r = q_i \sum_j q_j \sum_{\mathbf{n}} \frac{\text{erfc}(\alpha|\mathbf{r}_i + \mathbf{n}L|)}{\alpha|\mathbf{r}_i + \mathbf{n}L|} \quad (4.3)$$

Where

$$\text{erfc}(x) = \frac{2}{\sqrt{\pi}} \int_x^\infty e^{-t^2} dt \quad (4.4)$$

The reciprocal lattice Ewald sum is given by:

$$E_i^f = \frac{-q_k}{\pi V} \sum_j q_j \sum_{\mathbf{m}} \frac{\exp(-\pi^2|\mathbf{f}_m|^2/\alpha^2)}{\mathbf{f}_m} \cos[2\pi \mathbf{f}_m(\mathbf{r}_i - \mathbf{r}_j)] \quad (4.5)$$

Where  $V$  is the unit cell volume and  $\mathbf{f}_m$  are the coordinates in inverse lattice space. The Ewald term for the interaction energy of  $q_i$  with its own Gaussian function  $E_i^c$  is:

$$E_i^c = \frac{-\alpha q_k^2}{\sqrt{\pi}} \quad (4.6)$$

The term  $\alpha$  used throughout governs the relative convergence rates for the real and reciprocal based sums. Large values of  $\alpha$  result in a narrow Gaussian distribution and reciprocal lattice sums which are slow to converge, while small values of  $\alpha$  lead to wider Gaussian functions and real space sums which converge more rapidly. Importantly, the overall sum  $E_j$  is independent of the chosen value of  $\alpha$  when the summation limits for each sum are sufficiently large.

From the above discussion, it is easy to comprehend how this long-range electrostatics problem carries over to any treatment of quantum-mechanical clusters, where the surrounding medium is usually represented as a finite set of point charges designed to reproduce the electrostatic field of the rest of the crystal. Where we have a quantum-mechanically treated cluster embedded within a finite charge array, the embedding potential is given by:

$$V_{\mu\nu}(\mathbf{r}) = \sum_j \langle \phi_\mu | \frac{q_j}{|\mathbf{r} - \mathbf{r}_j|} | \phi_\nu \rangle \quad (4.7)$$

Where  $q_j$  are point charges representing the electrostatic potential of the environment and  $\phi_\mu$  and  $\phi_\nu$  are basis functions located on the quantum-mechanical cluster. This potential represents a direct sum over a finite volume of charges and therefore is subject to the same errors discussed above for direct sum approaches.

## 4.2 The Ewald Embedding Approach

In this section, we introduce a method [51, 52] - originally conceived by Klintonberg and co-workers in 1999 - which seeks to solve some of the problems related to the long-range

electrostatic potential in crystalline environments, without the explicit use of quantum-level periodic calculations. This approach - and its extension to excited state potentials - lays the foundation for the majority of this thesis. In summary, this approach couples point-charge embedding with a charge fitting process, automatically producing a point-charge array which accurately reproduces the Madelung potential for an arbitrary crystalline system, and was originally applied to produce ionic crystal fields for the study of point-defects in periodic systems. A five-step algorithm, outlined schematically in Figure 11.2, is used to generate the array.

### Step 1 - Setting up the Charge Array.

The total charge array volume is given by a  $2N \times 2N \times 2N$  supercell, produced trivially from the crystallographic unit cell of the chosen system, where the volume of the unit cell array is centered at the origin.

### Step 2 - Dividing up the Array.

The charge array produced in step 1 is split into three "Zones". Zone 1 is the central region containing the  $N_1$  atoms for the quantum-mechanical cluster. Zone 2 is a spherical volume of  $N_2$  charges, centered at the origin and encasing the cluster in Zone 1, that do not change throughout the procedure. Zone 3 is the  $N_3$  charges in the remainder of the array that undergo a fitting procedure.

### Step 3 - Computing the Ewald potentials.

Using the Ewald summation method (Section 4.1), the site potentials in Zones 1 and 2 are computed.

### Step 4 - Fitting the Zone 3 Charges.

This step seeks to alter the values of the point-charges in Zone 3 to make the site potentials computed via the direct sum approach  $V(\mathbf{r}_k)$  equal to that of the Ewald potential  $V_E(\mathbf{r}_k)$  for all sites in Zones 1 and 2. An additional goal of the procedure is to reduce the charge and electric dipole moment of the total array equal to zero. A set of linear equations is solved, comprising the  $N_C = N_1 + N_2$  equations that make the site potentials  $V(\mathbf{r}_k)$  of the charges in Zones 1 and 2 equal to their Ewald values

$$\sum_{i \neq k}^{N_T} \frac{q_i + \Delta q_i}{|\mathbf{r}_k - \mathbf{r}_i|} = V_E(\mathbf{r}_k) \quad k = 1 \quad \text{to} \quad N_1 + N_2, \quad (4.8)$$

the charge neutrality equation

$$\sum_{i=N_c+1}^{N_T} \Delta q_i = 0, \quad (4.9)$$

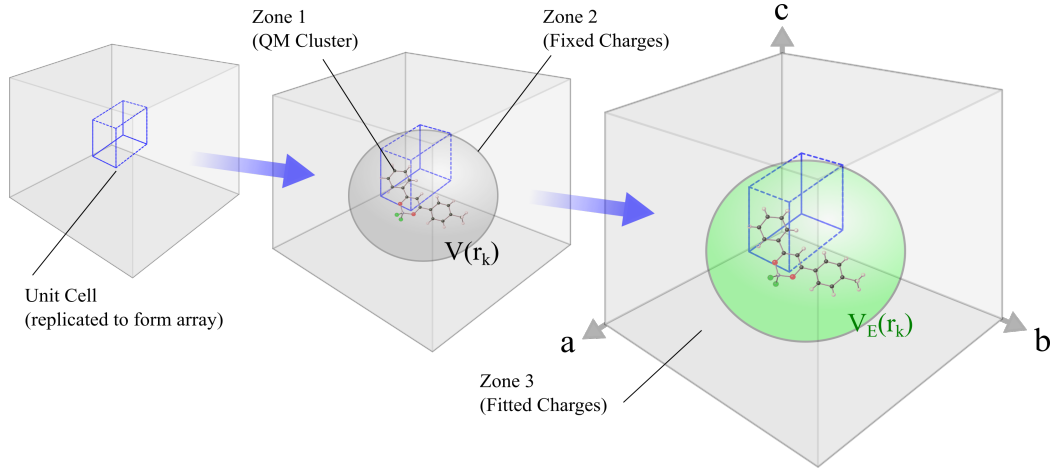


FIGURE 4.2: Schematic of the Ewald embedding procedure. Formation of the array as a supercell of the crystallographic unit cell (left), partitioning of the array into 3 Zones (center), after completion of Zone 3 charge fitting procedure, Ewald electrostatic potential is reproduced at all sites within Zones 1 and 2 (inside green sphere) (right).

and the three dipole equations

$$\sum_{i=N_c+1}^{N_T} \Delta q_i(r)_i = 0. \quad (4.10)$$

The resulting  $N_1 + N_2 + 4$  equations are solved for the changes to the  $N_3$  charge values  $\Delta q_i$ . As the index  $i$  runs over all sites from  $N_1 + N_2 + 1$  to  $N_1 + N_2 + N_3$  and  $N_3 > N_1 + N_2 + 4$ , (there are more parameters to be solved for than equations) the minimum norm solution is chosen. The resulting charge array corresponds to the initial array generated in step 1 with the point-charges in Zone 3 modified by  $\Delta q_i$ .

#### Step 5 - Checking the Quality of the Potential.

The solution is checked calculating the average and rms deviations between the direct sum and Ewald potentials at 1000 randomly chosen points within Zone 1, producing the combined rms deviation between  $V(\mathbf{r}_k)$  and  $V_E(\mathbf{r}_k)$ :

$$V_{rms} = \sqrt{\Delta_{ave}^2 + \Delta_{rms}^2} = \sqrt{\frac{1}{1000} \sum_{k=1}^{1000} [V(\mathbf{r}_k) - V_E(\mathbf{r}_k)]^2} \quad (4.11)$$

This quality check, assuming an appropriate values have been chosen for the volume of the charge array and the diameter of Zone 2, typically returns rms errors between the direct and Ewald sum potentials on the order of micro-Volts. This error can be reduced systematically by increasing the array volume and/or Zone 2 diameter.

As the electrostatic potential, computed via a direct sum, at sites within the quantum-mechanical cluster is now equal to that of the precise Ewald sum approach, the issue of

erroneous long-range electrostatic potentials in finite cluster methods is circumvented. Recalling equation 4.7,

$$V_{\mu\nu}(\mathbf{r}) = \sum_j \langle \phi_\mu | \frac{q_i + \Delta q_i}{|\mathbf{r} - \mathbf{r}_j|} | \phi_\nu \rangle \quad (4.12)$$

the total summation is now finite, though the electrostatic potential it produces is accurately derived from Ewald summation. Although the issue of the long-range electrostatic potential is resolved, we still face similar challenges to those described for ONIOM, PEECM and FDE. Namely, in the Ewald embedding scheme, the charge background is able to polarize the ground-state wave function of the quantum cluster, though the charge background itself is held fixed. Therefore, the effects of mutual polarization between the central cluster in Zone 1 and the rest of the array is not accounted for, resulting in potentially serious consequences when studying excited state - and in particular charge-transfer - phenomena. In the next section, we introduce an extension of the Ewald embedding scheme, able to produce an excited state embedding potential in full electronic equilibrium with the quantum mechanical cluster.

## 4.3 Extension of Ewald Embedding to the Excited-State

### 4.3.1 The SC-Ewald Algorithm

We will now introduce the approach we have developed to extend the Ewald embedding approach to the excited state. In doing so, we use Ewald as a starting point to produce an excited-state embedding potential generated by Mulliken point charges. The steps involved in this process are outlined below and are shown schematically in Figure 11.3.

#### Step 1 - Producing the Ground-State Embedding Potential.

In contrast to the Ewald embedding approach, from this point forward we do not explicitly consider the lattice to be made up of point charges with formal values, as are found in an ionic crystalline system (e.g. NaCl). This means that we require an initial periodic calculation to obtain values to attribute to the atoms in the crystallographic unit cell. These are obtained at the quantum level using CRYSTAL - a program which makes use of localized Gaussian basis sets and is therefore ideal for use in conjunction with finite cluster approaches. After calculating the ground-state electron density of the periodic system, a Mulliken population analysis is performed to obtain the initial charge values  $q_i$  for use in the Ewald charge-fitting scheme. At this point, with an appropriate quantum mechanical cluster (Zone 1) defined, the Ewald embedding algorithm is employed as described in Section 4.2. It is also useful to note that the charge-fitting algorithm used to produce the Ewald potential is usually associated with a negligible computational cost compared with the quantum-level calculations.

#### Step 2 - Calculating the Excited-State Density.

From Step 1, we now have a quantum-mechanically treated cluster embedded inside a charge array which produces an accurate electrostatic potential of the surrounding crystalline system. Here, we use TD-DFT - or, in principle, any method which allows access to excited states - to determine the excited-state density of the cluster in Zone 1. As before, a Mulliken population analysis is performed to obtain charges corresponding to the quantum-mechanical cluster atoms. If one wishes only to compute the absorption properties of the central cluster, it can be appropriate to stop at this stage, as it makes the most physical sense to compute vertical absorption properties in the presence of the ground-state crystalline environment. If, however, emission properties are desired, it is necessary to follow the subsequent steps.

### **Step 3 - Producing the Excited-State Embedding Potential.**

At this point, we take advantage of the crystalline nature of our medium to extrapolate the excited-state charges obtained in Step 2 and create the excited-state embedding charge array. To do this, assuming that the central cluster contains at least one of all the unique atoms in the unit cell, we make use of the symmetry operators available to the space group of the given system. In doing so, we produce the point charges corresponding to each atom in the full crystallographic unit cell, corresponding to those of the excited state density of the central cluster. This unit cell is subsequently used to reform the charge array used in the Ewald algorithm, and the charge fitting process, outlined in Section 4.2, begins anew. Steps 2 and 3 are iterated in a self consistent manner until mean-average deviation in the charges computed for the  $n^{th}$  and  $n - 1^{th}$  iterations does not exceed  $0.001 |e^-|$ . At this point, we consider the excited-state electrostatic potential produced by the charge environment - as well as the excited-state electronic density of the central cluster - to be equilibrated.

### **Step 4 - Optimizing the Excited-State Geometry.**

With the central cluster now situated within the excited-state field of the crystal, we perform a geometry optimization just as one would for an isolated cluster. It is necessary to perform Steps 2 and 3 once more to re-equilibrate the charge array with the newly-acquired excited-state geometry and density. It is worth noting that it is then possible to iterate these steps as well, so as to obtain not only a fully equilibrated embedding potential and density, but a fully equilibrated central cluster (and charge array) geometry. This last step, however, represents a substantial computational investment.

## **4.3.2 SC-Ewald Algorithm and User Manual**

In the appendix to this chapter, an outline of how to perform calculations with SC-Ewald is given, along with a detailed discussion of input and output files.

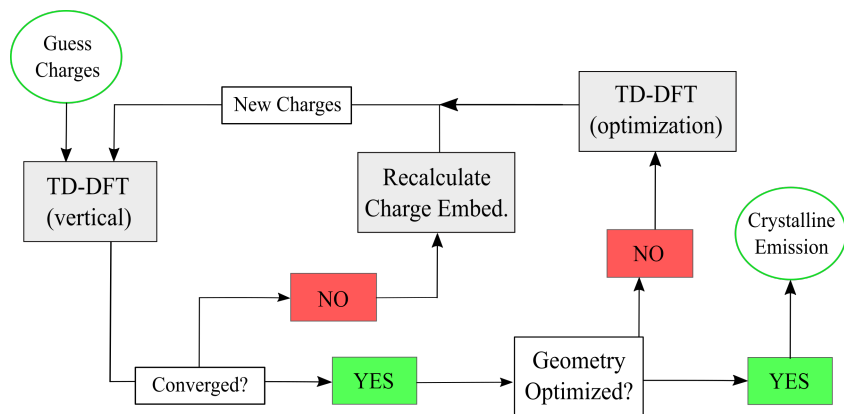


FIGURE 4.3: Self-consistent procedure used to obtain the excited-state embedding potential of the crystalline environment, and optimize the central cluster geometry at the excited state to obtain crystalline emission properties.

### 4.3.3 Limitations of the Current Implementation

Here we discuss limitations of the current implementation of SC-Ewald, covering potential numerical issues, practical problems as well as how some of these have been overcome.

#### Loss of Crystalline Symmetry

The first point is related to how the charge values computed within the quantum cluster are transferred to the Ewald charge array. The number of electrons in the quantum cluster region is usually restrained to integer values. The total charge of the array, however, may take any value and is restricted only by the requirement that the charge array should produce an accurate Ewald potential in the central region. The result is that symmetry breaking can occur with respect to the charge values produced by the central region, resulting in differing charges on atoms which should be identical by symmetry. To circumvent this, charges are averaged according to symmetry:

$$q_{\sigma_j} = \frac{1}{n} \sum_{i \in \sigma_j}^n q_i \quad (4.13)$$

Where  $\sigma_j$  is a group of atoms in the quantum cluster which are equivalent by symmetry and  $n$  is the total number of atoms in this group. In this way, divergent solutions of the self-consistent procedure in SC-Ewald are avoided. The averaging procedure can lead to an undesired consequence, however. If the average charge produced causes the sum of all charges in the quantum region to be slightly greater than zero (due to rounding), this carries through to the creation of the newly formed charge array. As a condition for the Ewald summation is that the total charge of the unit cell (and therefore, array) is zero, this causes spurious errors in the charge fitting process - even if the deviation from zero is very small. There is a simple fix to this however, which is to spread the (extremely small) additional charge over the atoms in the QM cluster, leading to a negligible change in each atom's individual charge but preserving the neutrality requirement of the unit cell.

### Neglect of Quantum Effects on Potential

A drawback of this method - and of all charge-embedding methods - is that the potential of the environment is modeled through classical electrostatics and other electronic effects, such as exchange interaction, are neglected. The only way of improving this conventionally is to increase the size of the quantum cluster so as to include such interactions around an area of interest, which rapidly becomes infeasible as the total number of basis functions in the quantum cluster increases. A potential solution to mitigate this would be to couple the SC-Ewald approach with ONIOM in the QM:QM' variation. In this way, these interactions are at least accounted for in the low-level portion of the hybrid energy formalism.

### The Cluster-Point Charge Boundary

The abrupt change from fully QM treatment of the central cluster to point-charge treatment of the environment could pose problems, as has been discussed previously in the context of over-polarization of the central cluster when modeling ionic solids. [46] For this reason, one must take care when constructing the boundary of the central QM cluster. In cases where the nearest point charges to the cluster are relatively far away and the magnitude of the point charges is generally small (e.g. in the vast majority of organic molecular crystalline materials) this may not pose any problems. However, even when charges are situated relatively far from the cluster, the choice of basis set can be crucial in the context of the SC-Ewald procedure. Generally, diffuse functions should always be avoided when calculating the embedding potential itself, as they tend to reach out towards nearby, positive point-charges. Generally, this does not pose any issue as (i) we expect to achieve better quality Mulliken charges with more local basis sets and (ii) the periodic calculation providing the initial guess charges will almost certainly have not made use of diffuse functions. In cases where the user requires diffuse functions for the calculation of a given property, these may be restored later and used in a single-point calculation (or geometry optimization) within the embedding potential obtained with the reduced basis set. In contrast, densely packed solids with significant ionic character and highly charged atomic centers require additional treatment, at least ensuring that the QM cluster is sufficiently large to mitigate the effects of over-polarization.

### Crystalline Networks

The issue of close-range point-charges can be extended to encompass cases where chemical bonding is important - for example in networked solids with no obvious, discrete sub-units. In these cases, error is naturally introduced at the cluster boundary where a covalent bond has to be broken. If this defect is located far enough from the nuclei of interest, however, its effect on computed properties will be small. This relies on being able to use a QM cluster of sufficient size to realize this constraint and could also be accomplished by coupling the SC-Ewald approach with an ONIOM QM:QM' calculation to minimize the extra computational cost.

### Lower-Dimensional Periodicity

Although the current form of SC-Ewald is only applicable to solids with 3D periodicity, it could be interesting to investigate its potential for studying systems of lower-dimensional periodicity as well. Indeed, 2D [53] and 1D [54] Ewald summation techniques are available, and coupling this with the charge-fitting strategy first outlined by Kintenberg and co-workers [51] as well as the self-consistent procedure outlined in this thesis could see applications in surface and polymer chemistry, for application in - for instance - dye sensitized solar cell or photo-catalytic water splitting technology.

Now that we have introduced the necessary theoretical background and the SC-Ewald approach itself, most of the remainder of this thesis concerns the application of SC-Ewald to the calculation of various excited-state phenomena occurring in the crystalline phase. These include a proof-of-concept study on excited state proton transfer in the solid state (chapter 5), aggregation-induced emission (chapter 6), and mechanochromic fluorescence (Chapter 7). Aside from this, we also explore situations where periodic boundary conditions and large clusters can be used to study the photophysical properties of metal-organic frameworks (Chapter 8) and, finally, we present a perspective concerning how interactions with the environment are not always the key issue in condensed-phase modeling (Chapter 9).

## Chapter 5

# Excited-State Intramolecular Proton Transfer in the Solid-State

### 5.1 Introduction

Proton coupled electron transfer (PCET) refers to the concerted intermolecular or intramolecular transfer of a single proton and electron, a reaction which is pervasive in biology. [55–57] Though this process can occur at the ground state between proton donor and acceptor sites, recent attention has been focused on proton transfer reaction induced by light irradiation, or excited state proton transfer (ESPT). [58] The driving force for such a reaction stems from the reorganization of molecular electronic density upon excitation, resulting in the increased acidity of the proton donor and its spontaneous deprotonation. [59] As for PCET, this process can occur at both an inter- and intramolecular level. The case of intramolecular excited state proton transfer (ESIPT) can be described as a four-level photo-cycle, shown in figure 11.4, where, after the absorption of a photon, proton transfer is thermodynamically favored at the excited state between the proton donor (Y) and acceptor (X) sites. Conversely, radiative decay to the ground state drives the reverse reaction, and the original form (Y–H) is recovered. The pre-requisite for the four-level cycle at the heart of ESIPT is the presence of an intramolecular hydrogen bond (H-bond) between close-range proton donor and proton acceptor groups. [60] The inherent speed of the ESIPT process ( $k_{ESIPT} > 10^{12} s^{-1}$ ) is such that it is able to proceed even at very low temperature, [61] though the rate itself depends on the given donor/acceptor groups involved and the surrounding medium - be it solvent or other ESIPT chromophores in a molecular crystalline form.

Signature properties of ESIPT fluorophores include large Stokes shifts, dual emission, and a sensitivity of optical properties to the surrounding medium. [62,63] The dual-emissive nature of these chromophores stems from the shorter (longer) emission wavelength of the reactant (product). [64,65] Thanks to the dual-emissive properties of ESIPT chromophores and the resulting broad emission bands capable of covering the whole visible domain, such systems have garnered significant interest for the production of white light. [62,66,67] As well as this, ESIPT chromophores have been applied in various fields as molecular logic gates, [68] fluorescence imaging devices, [69] and UV-absorbers. [70]

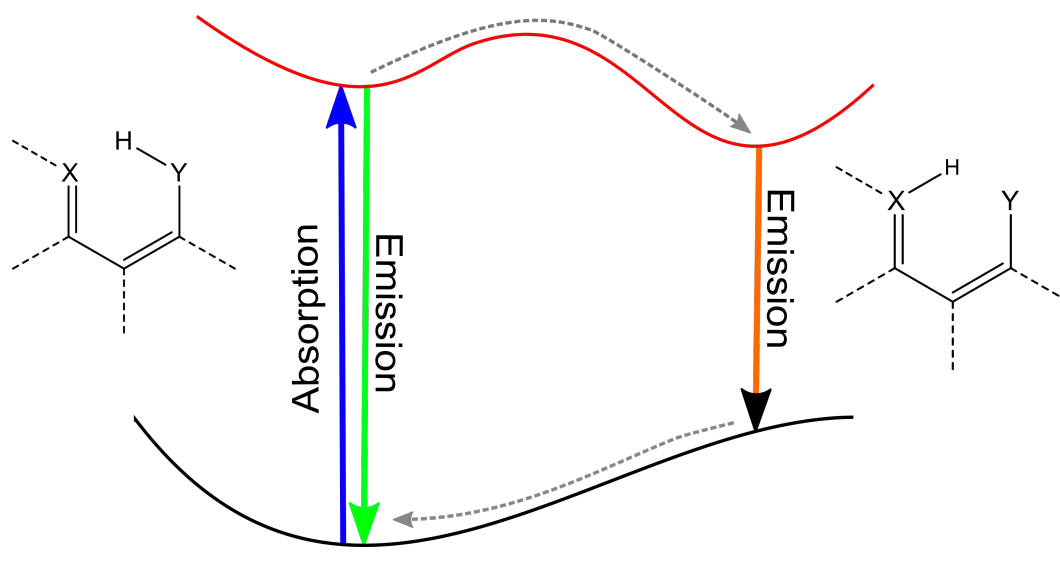


FIGURE 5.1: Generic four-level ESIPT mechanism. The proton transfer reaction is forbidden in the ground state but thermodynamically favorable in the excited state, resulting in an equilibrium between reactant (Y-H) and product (X-H) in the excited state each associated with a distinct emission wavelength.

At this point, there is a rich literature containing synthesis methods, [59] extensive photophysical studies, [71] and application studies of ESIPT in solution, [72] however solid state emitters which exhibit ESIPT behavior have been explored to a far lesser extent. When one considers that many reported ESIPT molecules are highly emissive in solution but weakly emissive in the solid state and suffer from notable shortcomings including low quantum yield and short fluorescence lifetimes, [65] this is unsurprising. The cause of the lower performance of ESIPT molecules in the solid state can be attributed to aggregation-caused quenching (discussed in detail in chapter 6) though, by considering certain design criteria during the synthesis of such chromophores, these effects may be minimized and the ESIPT properties enhanced. [65]

From a computational point of view, possessing a reliable tool able to quantitatively recover the absolute photophysical properties of ESIPT chromophores in solution and in the solid state as well as how these are subject to their environment would represent a potentially invaluable asset not only for post-synthesis understanding of ESIPT but at the molecular-design stage as well. Though the concept of modeling ESIPT in solution is well-established and has become routine, this is far from the case in the solid state. Difficulties arise from the directional nature of intermolecular interactions in the solid state as well as the proper account of long-range electrostatic interactions that could prove crucial to the understanding and prediction of the thermodynamic and photophysical processes at the core of ESIPT in the solid state. With this in mind, we aim to use a case study of a crystalline system exhibiting a (in this case double) proton transfer reaction yielding dual emission behavior to show that i) we can use the SC-Ewald algorithm to cheaply and easily incorporate these interactions into any crystalline model with 3D periodicity for the study of its photophysical properties and ii) their inclusion leads to a better reproduction of the environmental effects

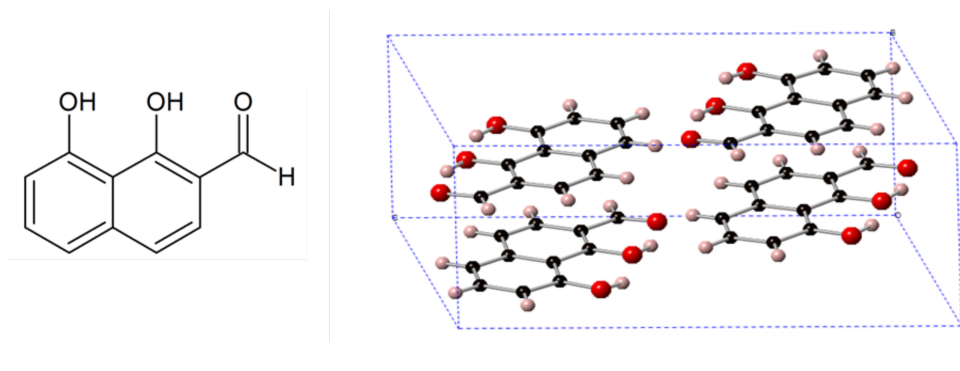


FIGURE 5.2: Left: structure of DHNA molecule considered in this chapter. Right: packing of crystalline DHNA (hydrogen: white; carbon: black, oxygen: red).

that are imposed by the crystalline environment and therefore better insight into how these might affect relevant photophysical processes. At this point we would like to stress the difference between this approach and more “conventional” approaches to charge embedding. While more traditional approaches indeed seek to incorporate effects of the surrounding crystalline medium with – often large – arrays of point charges fixed at predefined values obtained from cluster calculations, these do not reproduce the exact coulomb potential of a crystalline system. This is due to the charge array inevitably being truncated – regardless of its size – and the concomitant loss of the effect of infinite periodicity on the electrostatic potential. In contrast, this work seeks to use the fitting process outlined in chapter 4 which imposes the exact coulomb potential of the infinite crystal within a predefined area of interest. Indeed, this work represents the first application of SC-Ewald and serves as a proof of concept study before its further use in subsequent chapters.

In order to test our method effectively, it is desirable to select a system with excellent experimental data at hand - both photophysical and structural - as well as interesting, environment-sensitive excited-state properties. With this in mind, we selected the recently synthesized molecular crystal comprised of 1,8-Dihydroxy-2-naphthaldehyde (DHNA), [73] that is schematically depicted in figure 11.5. This molecule was strategically designed to directly probe the excited state intramolecular double proton transfer (ESIDPT) mechanism at the excited state, which in this case arises from two distinct intramolecular hydrogen bonds and results in clear dual emission. Peng and co-workers conducted a comprehensive experimental investigation of the photophysical properties of DHNA in cyclohexane solution and in single crystalline form with an accompanying theoretical analysis, [73] in the case of the solution, performed using DFT and TDDFT. In the case of DHNA in cyclohexane solution, using UV-vis spectroscopy and time-resolved femtosecond fluorescence upconversion techniques, they were able to attribute the observed dual emission to radiation from species that arose after the first ( $TA^*$ ) and second ( $TB^*$ ) proton transfer reaction. A general outline of the proposed mechanism is thus depicted in figure 5.3. Interestingly, going from solution to the solid state, the  $TA^*$  emission band undergoes a significant red shift – from 520 nm to 560 nm while the position of the  $TB^*$  emission band remains unchanged.

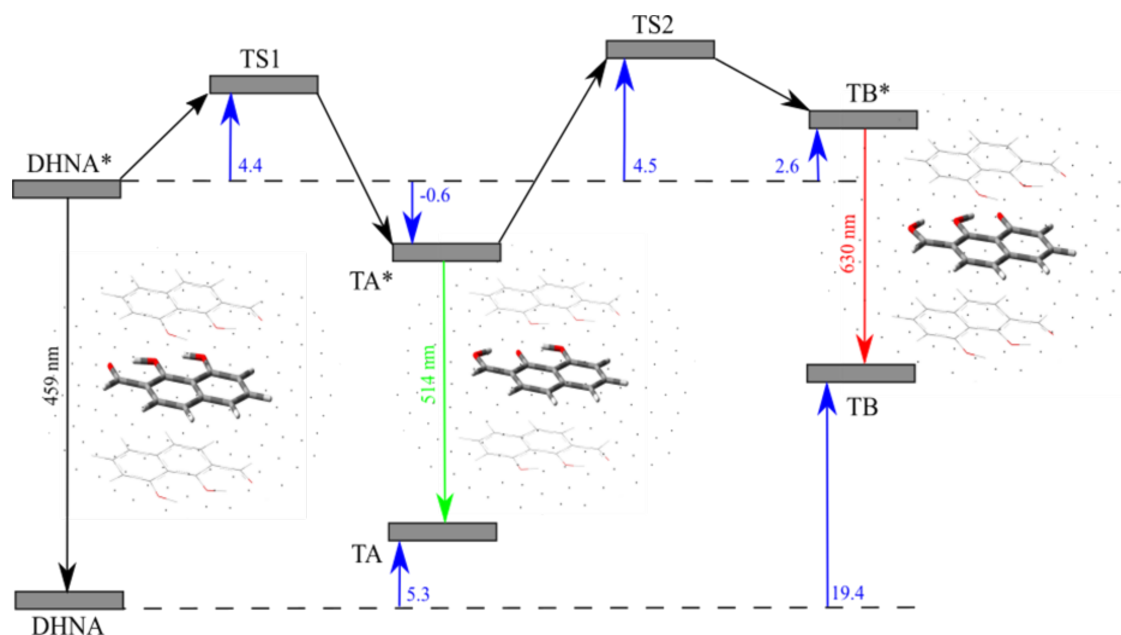


FIGURE 5.3: General reaction scheme for the excited double intramolecular proton transfer reaction taking place in crystalline DHNA. The values here are those computed using model  $T_{EMB}$  (see figure 5.4) with electronic embedding. Emission wavelengths (in nm) and relative energies with respect to DHNA (in kcal/mol) are given. Those shown for the ground state species correspond to points calculated on the ground state potential energy surface at the corresponding optimized excited state geometry.

Furthermore, insight into the thermodynamics of the ESIDPT processes in both the solution and the single crystal was gleaned from the study of variable temperature emission spectra, with interesting results. In the case of the solution, the TB\* state is thermodynamically favored while, in the solid, the TA\* state is prevalent. This stark difference between the thermodynamics of the ESIDPT reaction in solid state and in solution highlights the sensitivity of this reaction to environmental effects. These differences, associated with an environmental change from solution to solid state, make this system an ideal case study for the SC-Ewald approach.

This remainder of this chapter is structured as follows: following an outline of the computational details, a comparison of the different models used in this work is given. Next, the reproduction of the changes in the dual emission phenomenon between solvated and solid state DHNA is discussed, first for the simple charge embedding applied in a QM/QM' scheme and then for its self-consistent variant to simulate its emissive behavior. Finally, some concluding remarks are given.

## 5.2 Computational Details

The computational procedure involves calculations that make use of single molecules and molecular clusters which are predicated by calculations using periodic boundary conditions.

In this work, we employ only DFT for ground state calculations and TDDFT for those at the excited state.

All calculations using periodic boundary conditions were performed with the Crystal code, [74] which makes use of all-electron, atom-centered Gaussian basis sets. Energy convergence with respect to the number of k-points in the Monkhorst-Pack [75] grid was confirmed with the number of k-points in the irreducible Brillouin zone set to 30. The default settings for integral tolerances and convergence criteria were used throughout. A full geometry optimization was conducted at the B3LYP-D2 [76,77] level of theory - introducing empirical corrections to account for dispersion interactions - with a double zeta basis set including polarization and diffuse functions (i.e. the 6-31+G(d,p) Pople basis). For solid state calculations, diffuse functions were omitted from the basis set due to problems related to basis set linear dependence. As well as the geometry optimization, a population analysis was performed in order to determine the Mulliken charges for each atom in the unit cell.

Using this optimized geometry and the associated Mulliken Charges, the Ewald code [51] outlined in chapter 4 was used to construct and compute an array of background charges. This algorithm seeks to reproduce the Ewald potential felt by a predefined cluster within a 3D periodic lattice using only the knowledge of the positions and partial charges of the atoms within the crystallographic unit cell. An  $N_x \times N_y \times N_z$  supercell is formed which is then split into three zones: 1) the cluster of interest which will be given quantum mechanical treatment, 2) a spherical zone of point charges encasing the first zone with its partial charge values held constant and 3) all other point charges, which are allowed to vary (see chapter 4). In the charge-fitting process, the Ewald formula is used to compute the site potentials at all sites within zones 1 and 2 and, subsequently, a system of linear equations is solved to find charge values for zone 3 that allow the potential of all sites in zones 1 and 2 to be exactly equal to their Ewald values (and drives the overall dipole moment of the charge array to zero). This strategy is applied in both static and self-consistent schemes (see below).

In ref [52], general guidelines are given regarding the strategy for choosing the size of each zone for computing ground state potentials. Though their relative and absolute size appear to be system dependent, one essential constraint is that the root mean square (rms) of the discrepancy between the Ewald potential and the computed potential (after charge fitting) in zones 1 and 2 should be sufficiently small (see chapter 4, [78]). In the same study, it was also found that Ewald potentials in Zone 1 were improved both by increasing the number of atoms in Zone 2 and the overall size of the charge array (comprising Zones 1, 2 and 3). Keeping these general considerations in mind, in this work a  $6 \times 6 \times 4$  supercell was used in order to obtain a cube-like distribution of point charges resulting in a total of approximately 12000 point charges. For the quantum cluster (zone 1) both a DHNA monomer and a trimer were used, with the number of atoms in zone 2 set to 1500 in order to ensure that the central molecule(s) are not close to the outside 'wall' of the sphere comprising zone 2. Indeed, this gave an adequate root mean square (rms) error on the Ewald potential within zone 1 of  $0.17 \mu\text{V}$  for the monomer and  $6.5 \mu\text{V}$  for the trimer – deemed within the desired

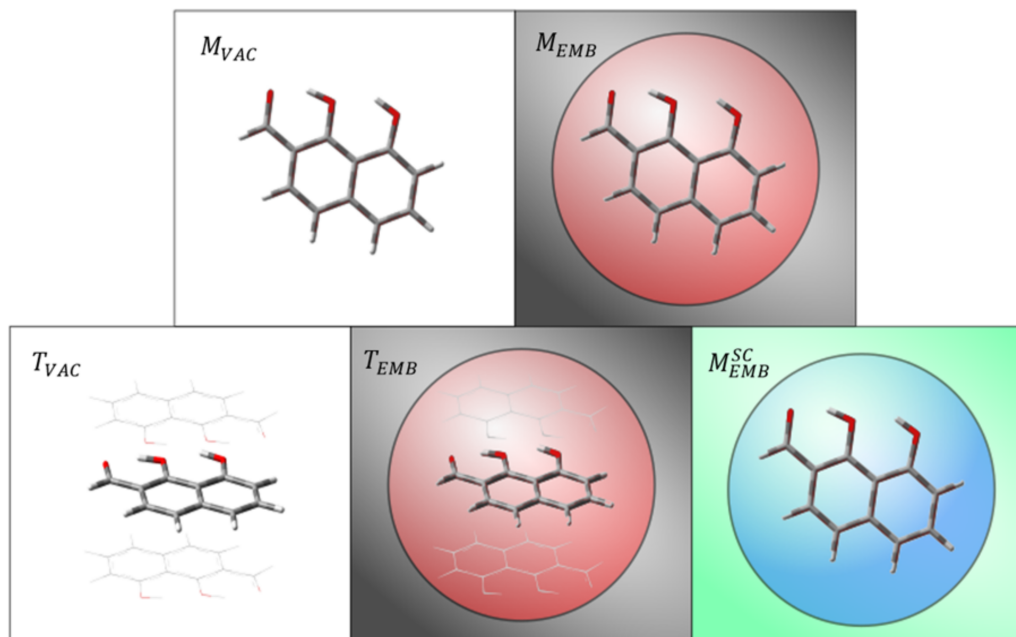


FIGURE 5.4: Schematic of models used in this work in which we have shown the optimized DHNA species. The coloured background signifies the presence of a background charge distribution generated by Ewald. Models include a single molecule in vacuum ( $M_{VAC}$ ), a single molecule embedded in the charge distribution generated by Ewald ( $M_{EMB}$ ), a trimer in vacuum ( $T_{VAC}$ ) and a trimer embedded in the charge distribution generated by Ewald ( $T_{EMB}$ ). The final model ( $M_{EMB}^{SC}$ ) involves the same initial setup as model  $M_{EMB}$ , although the charge background is determined self consistently with the excited state in question (indicated by different Zone 2 and 3 colour).

accuracy required for the calculation of absorption and emission spectra. Furthermore increasing the size of zone 2, with the total number of charges in the array fixed, lead to no appreciable variation.

All molecular calculations were performed using Gaussian 09 [79] and the same (6-31+G(d,p)) basis set. In the first approach, each of the species in the ESIDPT reaction were studied with four different models, specifically: using i) a single molecule in vacuum ( $M_{VAC}$ ), ii) a single molecule embedded in the charge distribution generated by Ewald ( $M_{EMB}$ ), iii) a trimer in vacuum ( $T_{VAC}$ ) and iv) a trimer embedded in the charge distribution generated by Ewald ( $T_{EMB}$ ) (see figure 5.4). For calculations involving a single molecule, the B3LYP [76] exchange-correlation functional was used to optimize the structure at the ground state for each of the species in the ESIDPT reaction. Subsequently, TD-DFT was used to optimize their structures at the excited state and calculate their respective emission energies. For calculations involving a trimer, the ONIOM QM/QM' method was employed using the B3LYP/6-31+G(d,p) level of theory for the high-layer and HF/STO-3G for the low-layer, with the atoms in the low layer held fixed during the geometry optimization procedure. As, in all cases, the point charge positions and low level ONIOM atoms are at the optimized ground state geometry provided by the periodic calculations, it is assumed that there is no cooperativity between molecules during the ESIDPT reaction.

In the second approach, charges were recomputed self-consistently - using the SC-Ewald approach introduced in chapter 4 - with respect to the electron density for a given excited state. This was done in order to attempt to recover the mutual polarization effect between the molecule of interest and the surrounding crystal due to the electronic rearrangement that occurs upon excitation. This was done using a convergence criterion of  $0.001 |e|$  with respect to the mean average deviation of the Mulliken charges of the central molecule, with tighter convergence criteria found to have a negligible effect on the computed emission energies. Note that, to avoid instabilities similar to those described previously, [80] the background charges were computed self-consistently using a smaller basis (6-31G(d,p)) and then the emission energies and new geometries calculated both using this basis set and by re-introducing the diffuse functions. Also it is to be noted that, in this case, the asymmetric unit of the crystal structure is equal to that of a single molecule of DHNA. Employing the Ewald code in a self-consistent manner with respect to charges computed quantum mechanically was done previously in the determination of ground state properties, such as NMR chemical shifts and indeed, other embedding programs capable of accounting for local defects in crystalline environments in a self-consistent manner exist.

All minima were verified by computing the harmonic frequencies either analytically (ground state) or semi-numerically (excited state) and checking that all frequencies were real. For transition states, one imaginary frequency, corresponding to the proton transfer reaction coordinate, was found.

## 5.3 Results and Discussion

### 5.3.1 Computed Emission Energies

With the focus of this work being the prediction of excited state properties in the solid state, we shall begin by discussing the performance of each model (figure 5.4) in attempting to reproduce the emission energy of each species observed via experiment. Table 5.1 shows all of the calculated emission wavelengths, in nm, for each model studied in this work alongside the experimental data from both a single crystal and cyclohexane solution.

Generally, at least at this level of theory, all models overestimate the emission energy of both the TA\* and TB\* species, with varying degrees of severity. Properties of molecular crystals are often approximated via the study of an isolated molecule in the gas phase, assuming all intermolecular forces are negligible. For this reason, we shall initially discuss the performance of each model with respect to this approximation - here designated  $M_{VAC}$ . In the case of  $M_{EMB}$ , the emission energy from TA\* is overestimated by a significant 0.31 eV. Furthermore, we were unable to achieve an excited state minimum for the TB\* species using only an isolated molecule and therefore were unable to calculate a meaningful emission energy. In turn, the absence of an excited state energy minimum for TB\* shows that this model fails to predict the inherent dual emission property of the DHNA molecular crystal observed experimentally. The rather large overestimation of the emission energy from TA\* together

with the lack of a stable energy minimum for  $TB^*$  is the first indication of the importance of intermolecular effects in the DHNA molecular crystal and that their inclusion in any model is crucial to the prediction of the photophysical properties.

For model  $M_{EMB}$ , it is clear that the inclusion of the ground state charge background offers a significant improvement. In the case of  $TA^*$  emission, the overestimation is reduced to 0.28 eV which, in any case, still represents a significant error. A more stark improvement can be found when analyzing the  $TB^*$  emission. Not only was it possible to locate an energetic minimum on the excited state potential energy surface, the emission wavelength was predicted to be 600 nm, in fairly good agreement with experiment, with an acceptable overestimation of 0.16 eV. In model  $M_{EMB}$  we have attempted to accurately capture long range electrostatic effects while ignoring other, likely influential, intermolecular forces. While the good agreement with the experimental  $TB^*$  emission is encouraging, the still rather poor agreement in the case of  $TA^*$  prompted us to further modify and refine the model in an attempt to capture other potentially important intermolecular effects.

This led to the introduction of models  $T_{VAC}$  and  $T_{EMB}$  (Figure 5), in which we have designated a trimer of DHNA molecules to be treated at the quantum level. This was done in order to more accurately capture closer-range electrostatic effects each of the species in the ESDIPT reaction and lead to lower, and so more accurate, excitation energies.

In the case of model  $T_{EMB}$ , the inclusion of both the trimer and the charge background improves the prediction of the  $TA^*$  emission wavelength to 514 nm (the best overall result, corresponding to an overestimation of an acceptable 0.20 eV with respect to experiment) while it has no effect on the calculated  $TB^*$  emission energy. Since this is the best performing model of those we have proposed with respect to experimental data, it highlights the effectiveness of both capturing the closer range electrostatic interactions while maintaining the longer-range electrostatic influence of the inherent periodicity of the crystal – here described in terms of the ground state Ewald background charge distribution. The remaining error observed with respect to the experimental data, other than the inherent error in the exchange-correlation functional, could be ascribed to the fixed nature of the charge distribution. In fact, if the surrounding charge field were somehow allowed to equilibrate with the electronic density of the central molecule upon excitation, it could be reasonable to assume that this would further enhance the quality of the calculated emission energy of each species – a point we shall return to later.

### 5.3.2 Emission Dependence on Environment: QM:QM' and Ewald

Experimentally, the behavior of the ESIDPT reaction was observed to be rather different depending on whether it takes place in cyclohexane solution or in a crystalline medium. Two major effects were observed: the apparent red shift of the  $TA^*$  emission peak by 0.17 eV (520 – 560 nm) going from the solution to the crystal and the inversion of relative emission band intensities of each species. Specifically, the emission band ascribed to the  $TB^*$  species

TABLE 5.1: Computed emission wavelengths (in nm) from the lowest lying excited state of each of the species involved in the ESDIPT reaction (in nm, with corresponding calculated oscillator strengths, in arbitrary units, given in brackets). Abbreviations signify the type of model used, according to figure 5.4.

| Species | $M_{VAC}$   | $M_{SOL}$   | $M_{EMB}$   | $T_{VAC}$   | $T_{EMB}$   | $M_{EMB}^{SC}$ | Solid State Exp. | Cyclohex. Exp. |
|---------|-------------|-------------|-------------|-------------|-------------|----------------|------------------|----------------|
| DHNA*   | -           | 459 (0.162) | 457 (0.093) | 461 (0.098) | 459 (0.089) | -              | -                | -              |
| TA*     | 492 (0.127) | 498 (0.174) | 498 (0.116) | 505 (0.122) | 514 (0.115) | 560 (0.085)    | 560              | 520            |
| TB*     | -           | 599 (0.183) | 600 (0.126) | 610 (0.124) | 630 (0.123) | 635 (0.100)    | 650              | 650            |

is far more intense than that of the TA\* band in cyclohexane solution, with the inverse being true in the case of the single crystal.

Regarding the first effect, Peng and co-workers already conducted DFT and TD-DFT studies of the ESIDPT reaction using a single DHNA molecule in cyclohexane solution (designated  $M_{\text{SOL}}$ ), taking advantage of a polarizable continuum model (see chapter 2) to account for solvent effects and so we will use their results in comparison with our calculated values of TA\* emission to assess each model's ability to reproduce the red shift (crystal shift) observed going from cyclohexane solution to the solid state.

It can be seen from table 5.1 that model  $M_{\text{EMB}}$  predicts no shift with respect to the calculated value in cyclohexane solution, showing that the charge distribution alone is insufficient to model this effect. Moving to the trimer ( $T_{\text{VAC}}$ ), we make a modest improvement, the crystal shift at least travelling in the correct direction, with a calculated red shift of 0.03 eV. Next, considering model  $T_{\text{EMB}}$ , we see an improvement with respect to  $T_{\text{VAC}}$  (crystal shift of 0.08 eV), bringing the calculated crystal shift into good agreement (within 0.1 eV) with the experimental value. However, in the same manner the TB\* emission was determined to be 0.1 eV lower in energy with respect to the solution - even greater than that of TA\* - while no shift was observed experimentally for TB\*. This shows that, at least for these models, the shift of the TA\* and TB\* emission in the solid state with respect to solution is not well reproduced. This point will be revisited within the context of the self-consistent charge scheme computed at the excited state.

### 5.3.3 Effect of the Environment on Reaction Thermodynamics

With respect to the second effect, namely the inversion of the relative intensities of the emission bands ascribed to TA\* and TB\* going from cyclohexane solution to the crystal, we will firstly discuss the calculated oscillator strengths determined alongside each emission wavelength for the first four models shown in figure 5.4, given in brackets in table 5.1. We can see that, whether in solution or crystalline form and regardless of the model used to describe the crystalline environment, the calculated oscillator strength is slightly greater for TB\* than for TA\*. This means that this information alone is insufficient to describe the intensity inversion phenomenon and points towards reaction thermodynamics as the root cause - as previously suggested by Peng and co-workers. [73]

To gain more insight, the excited state potential energy surface was mapped out along the ESIDPT reaction coordinate via interpolation between minimal energy structures at the excited state for models  $M_{\text{VAC}}$ ,  $M_{\text{EMB}}$ ,  $T_{\text{VAC}}$  and  $T_{\text{EMB}}$  and these are shown in figure 5.5 along with the corresponding relative ground state energies at the excited state geometry. In all cases, TB\* is higher in energy than TA\*, ranging from 2.66 kcal/mol in model  $T_{\text{VAC}}$  to 3.65 kcal/mol in model  $T_{\text{EMB}}$ . It is clear that any attempt to include the effects of the surrounding solid state environment destabilizes the TB\* form therefore making any emission from this species less likely. It is important to note that, as previously calculated by Peng and co-workers [73] in the case of the solution, B3LYP is known to overestimate the energy

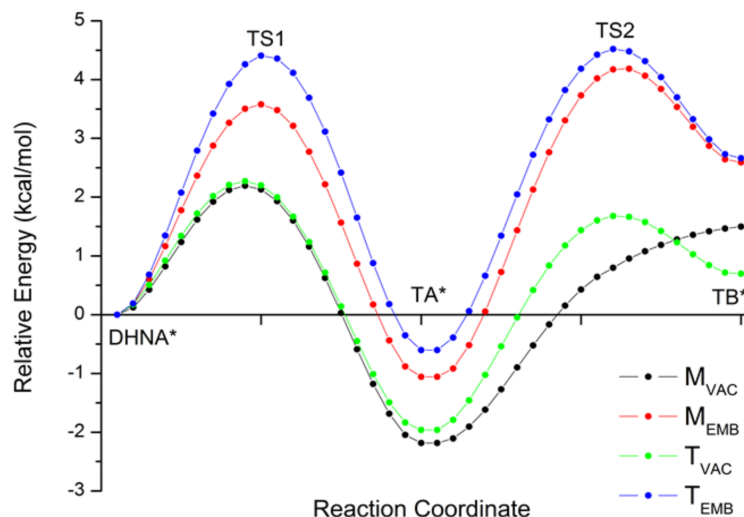


FIGURE 5.5: Excited state potential energy surfaces mapped along a reaction coordinate interpolating between each optimised excited state species. Each model, as outlined in figure 5.4, has been considered. As  $M_{VAC}$  did not produce an excited state minimum for  $TB^*$ , the structure for  $M_{EMB}$  was used for interpolation.

of the  $TB^*$  species giving results inconsistent with experimental data. In their work this was remedied through performing single point EOM-CCSD calculations on TD-DFT optimized structures which revealed the  $TB^*$  energy to be lower than  $TA^*$  in cyclohexane solution by 1.82 kcal/mol – contrary to what was observed with B3LYP. However, given that the most reliable model ( $T_{EMB}$ ) that we have investigated so far predicts that  $TB^*$  is 3.26 kcal/mol higher in energy than  $TA^*$ , it could be reasonable to conclude, despite the inherent overestimation of  $TB^*$  by B3LYP, that  $TB^*$  is indeed higher in energy than  $TA^*$  in the solid state. This is the inverse of what observed in cyclohexane solution and so the increased emission intensity of  $TA^*$  relative to  $TB^*$  in the solid state compared with in solution is a direct result of the destabilization of the  $TB^*$  species by the crystalline environment.

Analyzing the nature of the main molecular orbitals involved in the transition (figure 5.6), we can see that each step of the double proton transfer reaction results in visibly increased  $\pi$ -conjugation at the excited state which was previously cited as responsible for the reduced emission energy going from  $TA^*$  to  $TB^*$ . As we have established that  $TB^*$  is likely higher in energy than  $TA^*$  in the solid state, it follows that this observation alone is not sufficient to explain the lower emission energy measured experimentally for  $TB^*$ . Looking at the relative energies at the ground state for each species at the corresponding excited state geometry, it can be seen that the  $TB$  ground state is significantly destabilized relative to the  $TA$  ground state by the solid state environment in the non-equilibrium limit (by approximately 3.7 kcal/mol and 1.8 kcal/mol comparing models  $T_{VAC}$  and  $T_{EMB}$  for  $TB$  and  $TA$  respectively), which, in turn, reduces the emission energy. It can be seen that this effect is exaggerated upon the inclusion of the background charge distribution ( $T_{EMB}$ ) to the trimer, relative to the trimer alone ( $T_{VAC}$ ). Indeed, it is true that in all cases where the Ewald charges

TABLE 5.2: Computed emission wavelengths (in nm) from the lowest lying excited state TA\* and TB\* (in nm, with corresponding calculated oscillator strengths, in arbitrary units, given in brackets) using the  $M_{EMB}^{SC}$  model by self-consistently equilibrating first the charges only (Charges) and then charges and excited state geometry of the central molecule (Charges + Opt).

| Species | Charges     | Charges + Opt |
|---------|-------------|---------------|
| TA*     | 539 (0.097) | 541 (0.089)   |
| TB*     | 621 (0.107) | 619 (0.101)   |

are included, both TA\* and TB\* are destabilized - TB\* more profoundly so than TA\*.

To further support the idea that the TB\* emission is less likely in the solid state (and therefore less intense) than the TA\* emission, we will discuss the computed transition state barrier heights at the excited state. In agreement with experimental data (and in all solid state models tested) the TS2 barrier (corresponding to the TA\* $\rightarrow$ TB\* reaction) was computed to be slightly higher - ranging from 1.66 kcal/mol for model  $M_{EMB}$  to 0.72 kcal/mol for model  $T_{EMB}$  - than that of TS1 (corresponding to the DHNA\* $\rightarrow$ TA\* reaction).

### 5.3.4 Emission Dependence on Environment: SC-Ewald

Returning to the idea that the systematic underestimation of the TA\* and TB\* emission energies could be related to the absence of polarization of the charge embedding background, an attempt was made to alleviate this problem by using a single molecule of DHNA while calculating background charges self-consistently with respect to the first excited states of TA and TB. This model is hereafter designated as  $M_{EMB}^{SC}$  and corresponds to the SC-Ewald method introduced in chapter 4. This was done in order to mimic the mutual polarization between the central molecule and the surrounding crystalline environment after excitation of the central molecule. The results are shown in the bar graph in figure 11.6. It is clear that, for both TA\* and TB\* emission, the calculation of the emission energies is significantly improved, even when compared to the best model investigated previously ( $T_{EMB}$ ). For TA\*, the absolute error using model  $T_{EMB}$  is reduced from 0.198 eV (514 nm) to 0.001 eV (560 nm), providing excellent agreement with the experimental value. In the case of TB\* where the absolute error is reduced from 0.061 eV (630 nm) to 0.047 eV (634 nm), it is encouraging that SC-Ewald did not cause an emission energy that is already compatible with experiment to become significantly underestimated. Furthermore, when we compare the self-consistent result with that of  $M_{VAC}$  for TB\*, we observe a significant improvement (error decreases from 0.276 eV to 0.047 eV) while dealing with just a single molecule. These results show that the polarization of surrounding molecules in the molecular crystal upon the excitation of a given molecule should not be neglected when aiming to reproduce fine effects and that it could be intrinsically related to the overall photophysical properties of a molecular crystal.

From a more technical point of view, looking at both the ground state and excited state

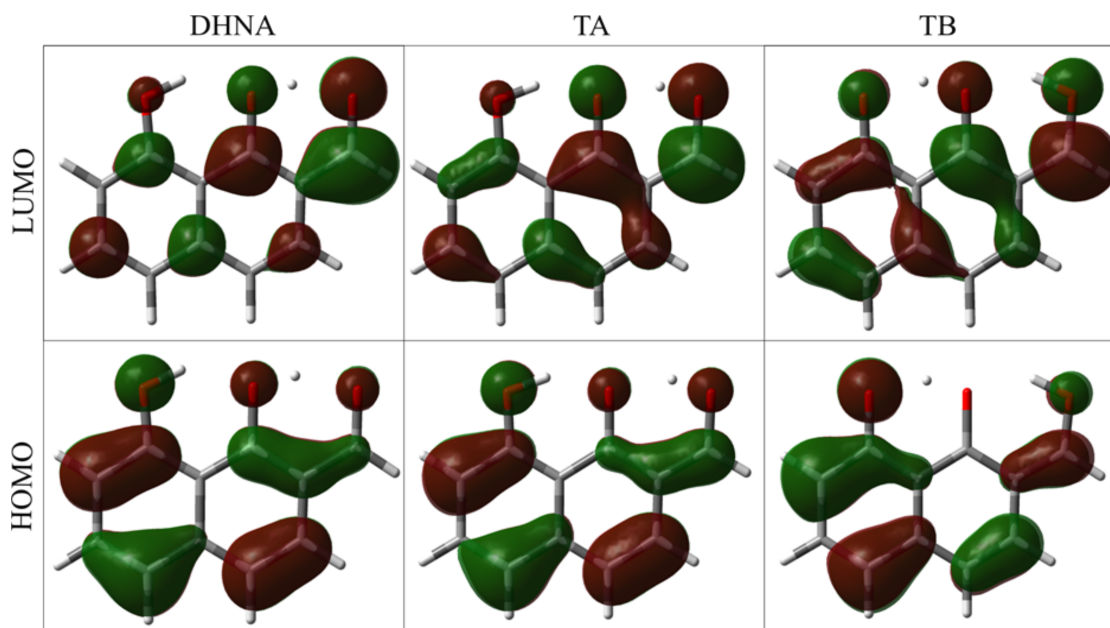


FIGURE 5.6: HOMO and LUMO molecular orbitals (surface isovalue 0.03 au) at the optimised excited state (model  $M_{EMB}$ ) geometries of each species in the ESDIPT reaction. Note that the orbital character does not change significantly depending on the model used.

dipole moments for the TA and TB species allows one to rationalize the difference in red shift between TA\* and TB\* emission with respect to solution, a phenomenon that was not recovered using the models discussed thus far. For TA, the dipole moment of the excited state (9.03 D) was calculated to be 3.27 D greater than that of the ground state (5.76 D), whereas the dipole moment for TB\* is only 1.08 D greater (7.46 and 8.54 D for the ground and excited states respectively). This explains the considerably lower energy obtained with respect to the non-self-consistent charges for TA\* emission relative to the far more modest reduction for TB\*. This can be rationalized through the idea of the greater ‘polarizing power’ of TA\* relative to TB\* on the surrounding molecules in the crystal. Indeed, the greater red shift for TA\* compared to TB\* going from solution to the solid state is now quantitatively reproduced. It can be concluded, then, that the greater dipole moment of TA\* relative to TB\* and thus the greater stabilization of TA\* in the solid-state gives rise to the apparent red shift observed experimentally for TA\* species only, going from solution in cyclohexane to the molecular crystalline environment.

In general, it is worth noting that the charge background reaches convergence relatively quickly with a typical number of cycles ranging from 3-8 in this case. Furthermore, it can be seen that, with respect to the self-consistent charges obtained for the geometry in  $M_{EMB}$ , the mutual optimization of the charges and the excited state geometry yields no significant improvement in calculated emission energies for either TA\* or TB\* table 5.2. This suggests that in future use of this method one iteration – that is to say one optimization of the charges with no subsequent geometry optimization - could be sufficient to describe the correction to the emission energies due to polarization of the surrounding crystal structure, although this

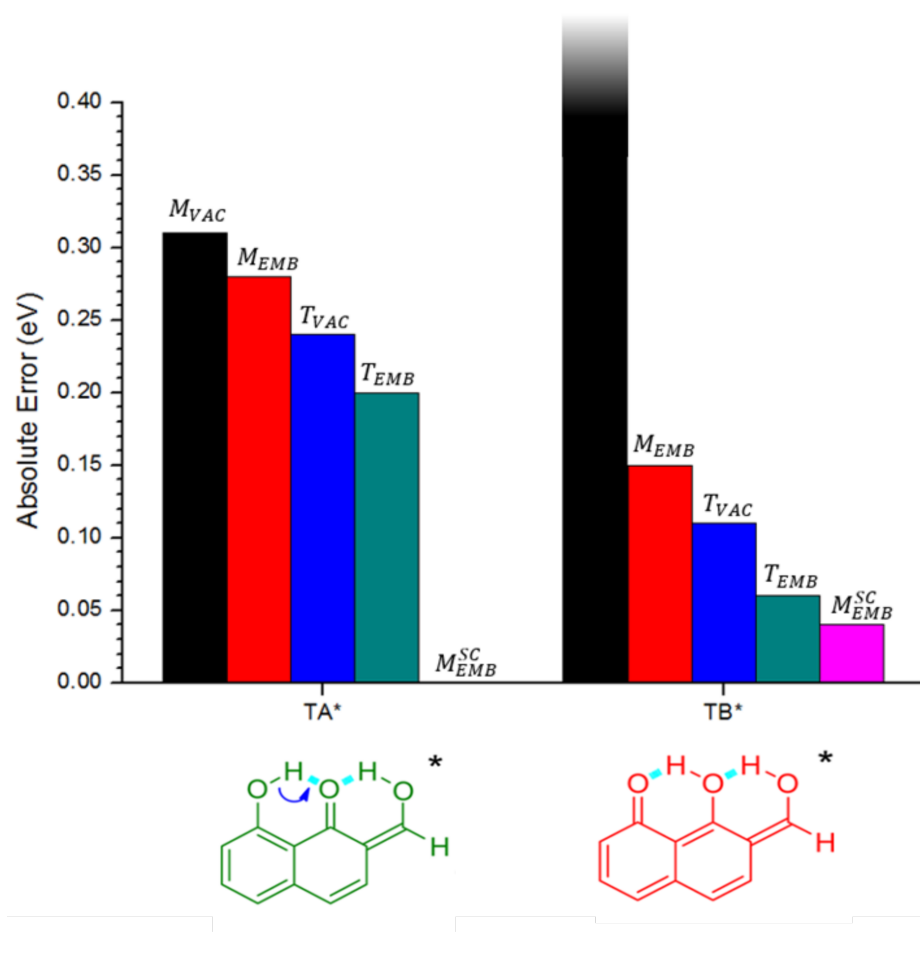


FIGURE 5.7: Absolute error in emission energies (eV) computed for each model considered in this chapter. Note that the error is considered infinite for TB\* emission using the  $M_{VAC}$  model as no minimum on the excited-state potential energy surface is obtained.

requires further testing. This good agreement with experiment also lends insight into the dynamics of the excited state process. Specifically, as all of the surrounding point charges are in the original DHNA positions and are frozen in place, this suggests that geometrical reorganization is sufficiently fast (and local) that it can be assumed to have no effect on that of the surrounding molecules. As a final point, it could be concluded that the stabilization of the excited states TA\* and TB\* by the polarization of the surrounding crystal lattice is in fact more important factor for the proper prediction of the emission energies than the accurate descriptions of closer-range electrostatic interactions, as in the QM/QM' ( $T_{EMB}$ ) approach.

## 5.4 Conclusions

The key conclusions of this chapter are summarized below:

- We have demonstrated that accounting for long-range electrostatic effects using the Ewald program offers improvement over the inclusion of only short-range electrostatic interactions introduced via an ONIOM QM:QM' model.
- As an initial application of the SC-Ewald approach, we have demonstrated that it can be used to cost-effectively account for local changes in electronic structure at the excited-state in the crystalline environment while, at the same time, explicitly accounting for long-range electrostatic effects inherent in periodic systems. The impact of these considerations on computed photophysical properties (in this case, emission) is compelling, with the model able to very accurately reproduce experimental observations, serving as a jumping-off point for further application in later chapters.
- As well as emission energies in the solid state, SC-Ewald is also able to recover the sensitivity of these properties to the environment, when changing from DHNA in solution to the crystalline phase.
- The state- and system-specific nature of SC-Ewald is evident in its behavior with respect to TA\* and TB\* emission, with each species exhibiting a different response to the self-consistent algorithm. This point is particularly encouraging for further applications to come.

This work has used a case study of a system (DHNA), exhibiting an excited state intramolecular double proton transfer reaction and whose complex photophysical properties are sensitive to environmental effects, to develop and demonstrate approaches which are capable of recovering the subtle yet profound effects of a crystalline environment on photophysical properties. Initially, a background charge distribution reproducing the exact Ewald potential of the crystal was used with improved results obtained using a QM/QM' approach alongside this charge distribution. In a second approach, results were found to be further improved (and indeed, in very good agreement with experiment) by using a self-consistent method to determine the values of the background point charges while considering only a single molecule explicitly at the QM level.

In this case, we demonstrate two different approaches that, while associated with very little additional computational cost, are able to retain the inherent effect of crystalline periodicity on the electrostatic potential felt by a central molecule and apply this in the context of photophysical property calculations. We have demonstrated that the inclusion of these effects can be crucial if one wishes to accurately describe and predict the result of photophysical processes at play in the solid state and, furthermore, to investigate how these may or may not differ from observed photophysical phenomena in other media, such as in solution. In the following chapters, we will see how SC-Ewald may be applied to other systems to study complex, environment-sensitive optical properties of organic molecules.

## Chapter 6

# Aggregation-Induced Emission: The case of Diphenyl Fluoronone

### 6.1 Introduction

Many organic luminophores exhibit very different photophysical behavior between dilute and concentrated solution. [81] Naturally, this difference in behavior is brought by the increased likelihood of inter-luminophore interactions in concentrated solutions. As a result, desirable properties observed from experimental measurements made in dilute solution are often (and indeed usually) not transferable to molecular aggregates or powders composed from the same organic molecule. More specifically, through what is often referred to as “concentration quenching”, the bright luminescence observed in dilute solutions for most organic luminophores is absent upon concentration of the solution. [82] Usually attributed to aggregate formation, the associated loss of intense luminescence properties is linked to the conventional design strategies that are used to construct such luminophores. [83] Specifically, the governance of organic molecular luminescence by the extent of molecular orbital conjugation leads to the ubiquitous presence of fused aromatic rings, resulting in increased  $\pi$ -conjugation and a flat, often rigid, molecular structure (as in the case of perylene, see figure 11.7) [84]. The resulting molecules can indeed demonstrate intense luminescence in dilute solution, though the increased opportunity for intermolecular  $\pi$ -stacking promotes the formation of excimers (two or more molecules which are weakly bound at the excited state by dissociation of an exciton across each molecule), the formation of which is a common source of aggregation-caused quenching (ACQ) [84]. From an applications point of view, the ACQ effect is considered undesirable for devices such as organic light-emitting diodes (OLEDs), for which the formation of solid-state crystalline material or films is crucial. [85,86] Furthermore, any application which requires contact with aqueous solution is made more difficult by the intrinsic hydrophobic nature of the  $\pi$ -conjugated backbone. Although this may be mitigated somewhat by the addition of polar functional groups, aggregate formation at sufficiently high concentrations is still prevalent. [87]

From these barriers to direct application, intense research effort has been devoted to circumvent the problem of ACQ and to provide organic molecular systems which are capable

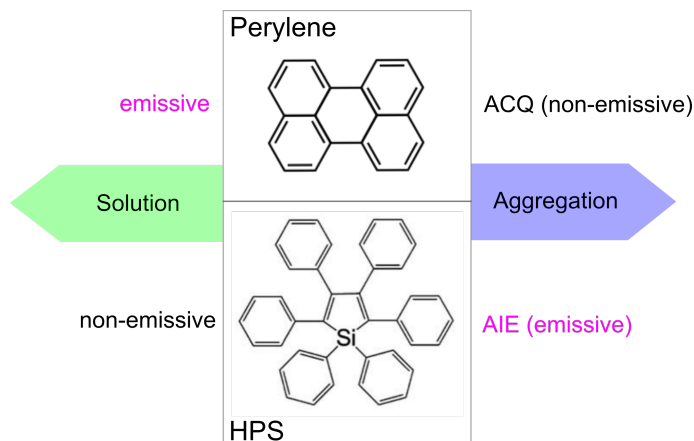


FIGURE 6.1: Typical organic molecules which exhibit aggregation-caused quenching (ACQ) and aggregation-induced emission (AIE).

of bright luminescence both in concentrated solution and in the solid state. Initially, attempts were made to obstruct the aggregation process through the addition of bulky substituents or to simply reduce the extent of conjugation for a given luminophore, though these strategies often lead to a drop in the luminescence efficiency. [87] In the last decade, systems which run counter to the ACQ paradigm were introduced - a series of silole derivatives, non-emissive in dilute solution yet highly fluorescent in aggregated or powdered forms. [88,89] This property, diametrically opposed to the destructive ACQ phenomenon, was termed “aggregation-induced emission” and has since resulted in the synthesis of many classes of such molecules. Though these observations spelled improvements in technological applications of organic luminophores, additional effort was required to understand the mechanisms behind AIE and how these may be exploited.

The vast majority of AIE behavior, including that of the silole derivative (HPS) shown in figure 11.7, is rationalized by the restriction of intramolecular rotation (RIR) paradigm. [88, 90–92] For HPS, there are six phenyl ring substituents linked to the silole core. These rings, which may rotate around their single bonds with the silole moiety, serve as an efficient rotational (or, more generally, vibrational) deactivation pathway, leading to non-radiative decay from an excited state to the ground state. In aggregates or in the solid state, this movement is severely restricted - removing this non-radiative deactivation pathway and conserving the otherwise brightly-emissive properties of the HPS molecule. This attribution of the RIR mechanism to the AIE phenomenon has also been investigated and verified by monitoring fluorescence as a function of solvent viscosity, system temperature, and by the application of pressure. [88]

From a theoretical point of view, attempts have been made to rationalize this process via the calculation of potential energy surfaces along rotational trajectories and the analysis of the non-radiative decay rates along these pathways. [93, 94] While this concept can readily explain AIE observed in chromophores such as HPS, in which the emission of the aggregate is of a similar wavelength to that of the molecule in solution, it is not sufficient to explain

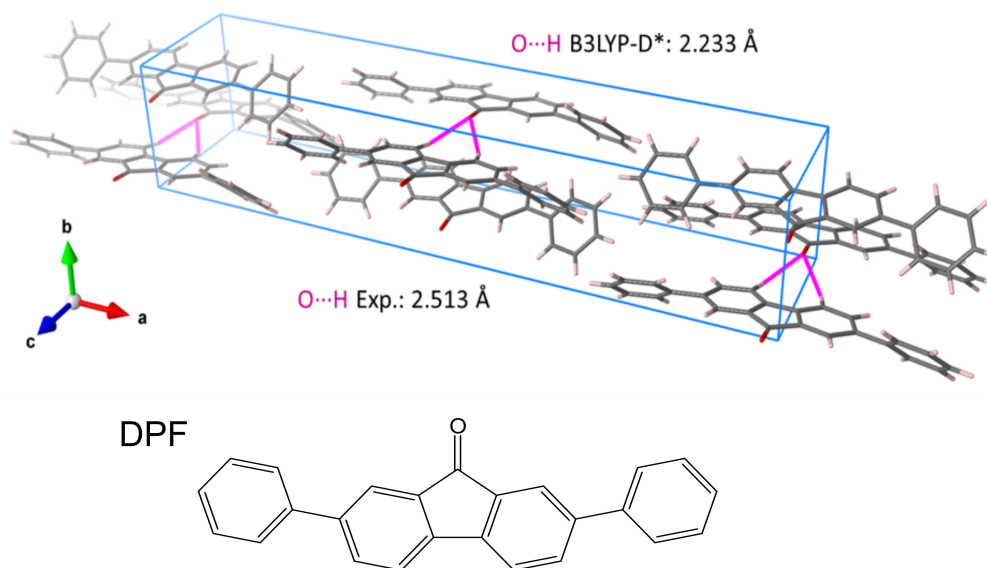


FIGURE 6.2: Top: Fully optimized B3LYP-D\*/6-31G(d,p) crystalline structure of DPF. The blue line represents the conventional unit cell, whereas the two equal intermolecular O-H hydrogen bonds are represented by purple sticks. The unit cell of the experimental structure ( $a = 34.84 \text{ \AA}$ ,  $b = 6.85 \text{ \AA}$ ,  $c = 7.21 \text{ \AA}$ ), is well-reproduced, with the resulting optimized lattice parameters  $a = 34.61 \text{ \AA}$ ,  $b = 6.48 \text{ \AA}$ ,  $c = 7.17 \text{ \AA}$ . Bottom: Structure of the DPF molecule.

large solvatochromic-like effects observed in some AIE chromophores. This apparent gap in understanding for this sub-set of AIE systems presents an opportunity for theoretical approaches to aid in their understanding through the application of excited-state methods such as TDDFT. Experimentally, the concomitant brightening and significant bathochromic shift of emission band maxima during the aggregation of such chromophores is often attributed to the formation of excimers, which is substantiated by an apparent broadening of the emission band itself, along with an increased excited state lifetime observed via time resolved fluorescence techniques. [95]

2,7-diphenylfluorenone (DPF) is one such chromophore, demonstrating more than a 150 nm red shift of the emission band after aggregation, which is attributed to excited state excimer formation. [95] This chromophore also readily forms powders, which exhibit very similar optical properties to the aggregates. In this chapter, we highlight an alternative root-cause for the AIE behavior of DPF and demonstrate that it arises from a single-molecule process rather than the formation of excimers. Using the SC-Ewald electrostatic embedding model (chapter 4) as an approximation of the solid state environment, it will be shown that the field induced by the crystalline environment can enhance the relative brightness of otherwise poorly emissive states in DPF, resulting in both enhanced fluorescence and a substantial bathochromic shift when compared with emission in dilute solution. [96]

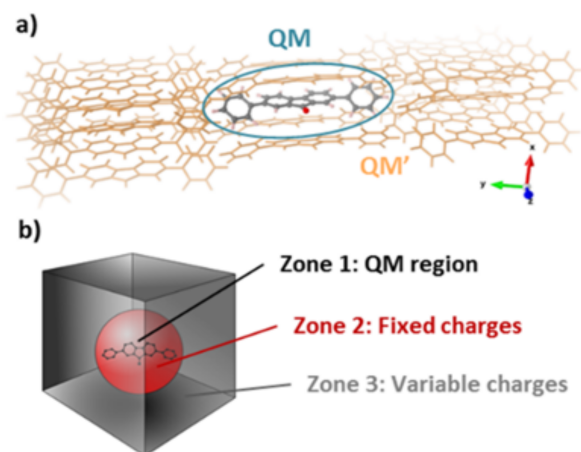


FIGURE 6.3: Schematic representation of the solid state models used in this work. (a) Solid state modeled using a two-level ONIOM QM/QM' scheme, with the low-level region including 20 nearest-neighbor molecules. (b) Solid state modeled using the ground (absorption) or excited state (emission) potentials generated by the SC-Ewald procedure, outlined in chapter 4. Fitted charges (grey cube, Zone 3) are used to reproduce the excited state infinite crystalline potential within a given zone (red ball, Zone 2). Within this zone, a quantum-mechanically treated cluster is placed (black molecule, Zone 1).

## 6.2 Computational Details

DFT and TDDFT calculations have been used to investigate the ground and excited state properties of a single DPF molecule in vacuum and in THF solution. The latter were described by using the Conductor-like Polarizable continuum solvation Model (C-PCM) [34] in the linear response formulation. Ground and excited state geometry optimizations and absorption/emission energies have been performed using both B3LYP [76] and CAM-B3LYP [97] functionals coupled with the 6-31+G(d,p) basis set. All calculations have been carried out with the Gaussian09 [79] suite of programs.

In order to determine the equilibrium atomic positions and unit cell parameters for subsequent embedding techniques, ground-state periodic calculations have been carried out on bulk DPF, employing the parallel version of the CRYSTAL09 [74] package. With the purpose of obtaining an electronic ground-state structurally as close as possible to the experimental one, we performed a dispersion-corrected B3LYP-D\* [98]/6-31G(d,p) optimization of the solid crystalline system, shown in 11.8. In such a case, diffuse functions were not utilized to avoid basis-set linear dependence issues. The Monkhorst-Pack [75] grid was set to 6 k-points within the Irreducible Brillouin Zone. In order to determine excited state properties of crystalline DPF, the QM/QM' ONIOM and the Self-Consistent Ewald embedding methods have been used.

For the ONIOM QM/QM' calculations, a sufficiently large cluster is cut from a crystalline supercell and treated at the QM/QM' level in which the high level region consists of the a single DPF molecule or a DPF dimer, as shown in figure 6.3. The low-level region

includes 20 DPF molecules for the monomer model (figure 6.3 a), whereas it includes 20 and 22 DPF molecules (the nearest-neighbor molecules, within a range of 3.8-4.0 Å) for the two dimer models considered, Dimer 1 and Dimer 2, respectively (figures 6.4 b and c).

Monomer and dimer vertical absorption energies have been computed at the TD-DFT/6-31+G(d,p):HF/STO-3G level of theory, at the optimized crystalline geometry (see above) whereas the emission spectra were computed by optimizing the lowest-energy bright singlet excited-states, S1 and S3, involved in the experimentally-observed fluorescence. The S2 state was not considered since, in every case, it was computed to be a dark (i.e. non-emissive) state (oscillator strength  $f=0.000$  a.u.). As DFT approximations, B3LYP and CAM-B3LYP functionals were considered for the high-level QM region. Following previous investigations, the low level region was treated at the Hartree-Fock (HF) level coupled with the Slater-type STO-3G minimal basis set which has been found to provide Mulliken charges similar to those obtained with more accurate calculations.

With the SC-Ewald approach, the solid state environment has also been modeled as is detailed in chapter 4. Briefly, this process seeks to approximate the excited state crystalline environment via a large array of point charges while, at the same time, performing a charge fitting process to reproduce the infinite electrostatic potential of the fully periodic system.

The charge array was composed of a  $5\times 5\times 5$  supercell, in order to obtain a cube-like distribution of point charges, giving a total of approximately 11000 point charges. For the charge fitting procedure, the fixed charge zone (Zone 2, see figure 6.3 b) was set to an origin-centered sphere containing 1500 atoms in order to ensure the QM region (Zone 1) is not close to the 'outside wall' of Zone 2. The resulting fitted charges in Zone 3 produced an adequate root mean square (RMS) error of the Ewald potential within Zone 1 of less than  $0.1 \mu\text{V}$ .

To model the crystalline environment at the excited state, this charge array was recomputed self-consistently using the Mulliken charges derived from the electronic density of the excited state of interest (S1 and S3 states in this case), applying a convergence criterion of  $0.001 |e^-|$  with respect to the mean average deviation of the computed charges in Zone 1. In order to avoid numerical instabilities, the SC-Ewald procedure was carried out using a reduced basis set (6-31G(d)), before reverting to the full basis set (6-31+G(d,p)) for the calculation of optical absorption and emission properties within the generated charge background.

## 6.3 Results and Discussion

### 6.3.1 Assessment of Dimer Coupling at the Excited State

Following the experimental interpretation of excimer formation as the root cause of AIE in DPF, [95] absorption features were first determined for two sets of dimers found in crystalline DPF. From figure 6.4, it can be clearly observed that, regardless of the dimer chosen, the effect on the calculated absorption spectrum - with respect to that of the monomer - is

negligible. This observation also holds when the solid state environment is approximated using the ONIOM method. Together, these results show that, at least in the vertical absorption regime, the intermolecular coupling is not sufficient to alter the observed photophysical properties either in terms of energy or absorption intensity. From these results, it is then necessary to consider alternative mechanisms to rationalize the AIE behaviour of DPF. In the following, starting from a monomer picture, it will be shown that both the absorption and emission spectra of aggregated DPF can be explained via a single-molecule process, facilitated by interactions with the crystalline environment at the excited state.

### 6.3.2 Assignment of Spectral Absorption Bands

Figure 6.5 shows the UV-Visible absorption spectra computed at B3LYP and CAM-B3LYP level for the DPF monomer in vacuum, THF solution and with the ONIOM QM/QM' and SC-Ewald embedding protocols. At first glance, a qualitative accuracy of both functionals for the overall spectral band shapes can be observed, with respect to the experimental counterpart in concentrated (60  $\mu\text{M}$ ) THF solution (figure 1g of the experimental paper [95]) – where DPF is said to be an emissive, aggregated form. Also, an almost quantitative spectral characterization is provided by B3LYP in terms of  $\lambda_{max}$  wavelengths, relative band intensities and band shapes. It should be noted that, to facilitate a comparison between isolated and aggregated properties of DPF, absorption spectra will be compared with those in concentrated THF solution (60  $\mu\text{M}$ ), whereas  $\lambda_{max}$  refers to experimental results obtained in mixed THF/water solutions (20  $\mu\text{M}$ ), though the optical transitions in each case are identical.

In more detail, the main transitions found experimentally (Table 1 of reference [95] – corresponding to 4.34 eV, 3.64 eV and 2.63 eV (286 nm, 341 nm, and 471 nm) – are quite well reproduced. A sizable bathochromic (hypsochromic) shift is observed with B3LYP (CAM-B3LYP) for the high energy/most intense  $\pi\text{-}\pi^*$  transition located experimentally at 4.34 eV, though this band is of little interest in the context of potential AIE mechanisms, due to the very low probability of populating the associated singlet excited state ( $S_0\rightarrow S_5$ ).

Moving towards lower energy transitions, a better description is given by B3LYP for the two convoluted bands at around 3.84 eV ( $S_0\rightarrow S_3$  and  $S_0\rightarrow S_2$  transitions with  $\pi\text{-}\pi^*$  character), whereas CAM-B3LYP predicts hypsochromically shifted transitions. It is worth noting here that the vibronic band shape observed in the experimental spectrum is not accounted for within the current computational protocol.

Though a weak absorption band at 2.63 eV (471 nm) is not explicitly discussed in the experimental work for the 20  $\mu\text{M}$  THF solution, it is consistent with a distinguishable non-negligible absorption band (figure 1c of reference [95]) present in the computed B3LYP spectra, corresponding to the HOMO-LUMO ( $S_0\rightarrow S_1$ ) transition, with charge transfer (CT) character. Here, the electronic effects from the use of different structural and environmental descriptions of DPF highlight that: i) as expected, B3LYP gives, in general, a better prediction of the  $S_0\rightarrow S_1$  wavelength, compared to experiment, but this could be due to the limited

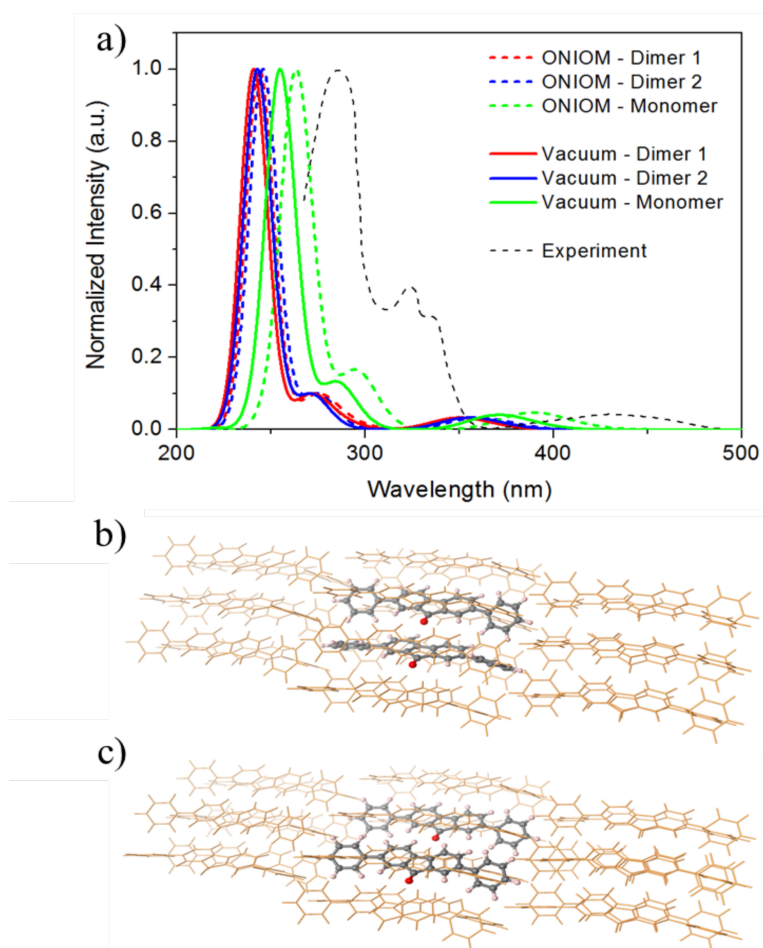


FIGURE 6.4: a) Absorption spectra of dimer clusters extracted from the crystalline structure of DPF, computed at the CAM-B3LYP level of theory for two different dimer configurations: Dimer 1 (b) and Dimer 2 (c). These spectra have been obtained both in vacuum (solid lines) and using the ONIOM QM/QM' cluster model (dotted lines). A FWHM value of 0.35 eV is used throughout. For comparison, analogous calculations performed on monomers and the experimental spectrum<sup>16</sup> are given.

through-space character of this transition, whereas ii) CAM-B3LYP, though underestimating the  $\lambda_{max}$  of all transitions, yields a systematic shift. Moreover, recalling that such functional is known to perform well in describing transitions with CT character, [26, 99] we expect it to provide reasonable values for emission with respect to B3LYP, which usually underestimates emission energies. iii) A bathochromic shift - from 376 nm to 397 nm - is associated with the changing electrostatic interactions when passing from vacuum to implicit solvation, to ONIOM QM/QM' and then to SC-Ewald embedding (CAM-B3LYP). Such a trend goes towards the experimental transition of 471 nm (though graphically, the  $\lambda_{max}$  is located even closer at ca. 440 nm). Note that the same magnitude of bathochromic shift is observed for B3LYP, going from 452 nm to 468 nm.

### 6.3.3 Solvated and Aggregated Fluorescence of DPF

In the following, it will be shown that the enhanced emission observed upon aggregation of DPF can be rationalized considering only a single molecule, with the condition that one must account for the influence of the solid state environment. Figure 11.9 shows the calculated and experimental emission spectra. Experimentally, [95] it is observed that concentrated solutions of DPF dissolved in tetrahydrofuran produce two distinct emission bands. The first band, at 360 nm (3.44 eV), is attributed to emission from isolated molecules of DPF in solution ( $E_{SOL}$ ) whereas the second band, at 534 nm (2.32 eV), is attributed to emission from the DPF aggregate ( $E_{AGG}$ ). Importantly,  $E_{AGG}$  is not observed in low concentration (20  $\mu$ M) THF solutions of DPF, due to the absence of aggregate formation. In the following, we approximate the aggregated form of DPF as a perfect crystal. Due to the near-identical emission behavior observed experimentally for powdered DPF and aggregated DPF and the precipitate-like nature of the aggregate, we deem this approximation to be viable.

From calculations performed on a single molecule of DPF, both in THF solution and by approximating the crystalline environment,  $E_{SOL}$  can be attributed to radiative emission from the S3 state, which corresponds to a  $\pi$ - $\pi^*$  excited state. From figure 11.9 it can be seen that, of all of the models tested  $E_{SOL}$  is best reproduced, albeit with a marginal blue shift, using the THF solvent model which results in a calculated emission energy approximately 0.2 eV from the experimental value. The solid-state models, however, yield a significantly blue shifted (by 0.5 eV) emission maximum relative to experiment. Given the superior performance of the THF model, these results support that  $E_{SOL}$  is indeed a result of emission from isolated monomers of DPF in solution. Additionally, it can be seen that both solid state models – ONIOM QM/QM' and SC-Ewald – produce similar emission bands. This is significant, as it is an indication that the close-range electrostatic interactions are well reproduced by the SC-Ewald approach, despite relying on simple point charges to approximate the crystalline environment. Furthermore, although SC-Ewald approximates the excited state crystalline potential while ONIOM approximates the ground state environment, due to the small spatial difference in density between the ground state and S3 excited state it is to be expected that the ground and excited state potentials – and thus the resulting emission energies – will be similar.

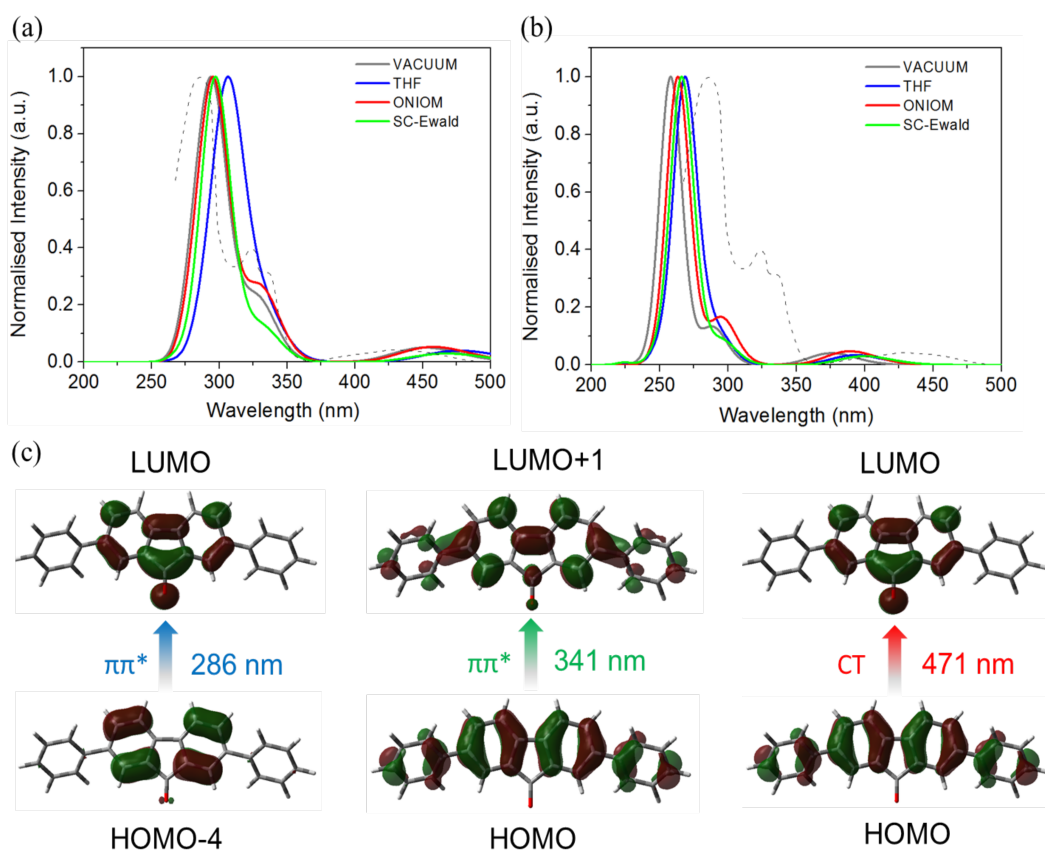


FIGURE 6.5: Calculated absorption spectra of DPF at the (a) B3LYP and (b) CAM-B3LYP level, adopting four different models to approximate the environment: i) in vacuum, ii) in THF, using implicit solvation, iii) in the solid state using an ONIOM QM/QM' model and iv) in the solid state using the ground state embedding potential as determined by the SC-Ewald procedure. A FWHM value of 0.35 eV is used throughout. The experimental absorption [?] is also shown (dashed lines). (c) Assignment and molecular orbitals involved in first three bright transitions ( $S_0 \rightarrow S_1$ ,  $S_0 \rightarrow S_3$ , and  $S_0 \rightarrow S_5$ ) of DPF (orbital isocontour value of 0.03 a.u.) along with the experimental absorption energies of the relevant bands.

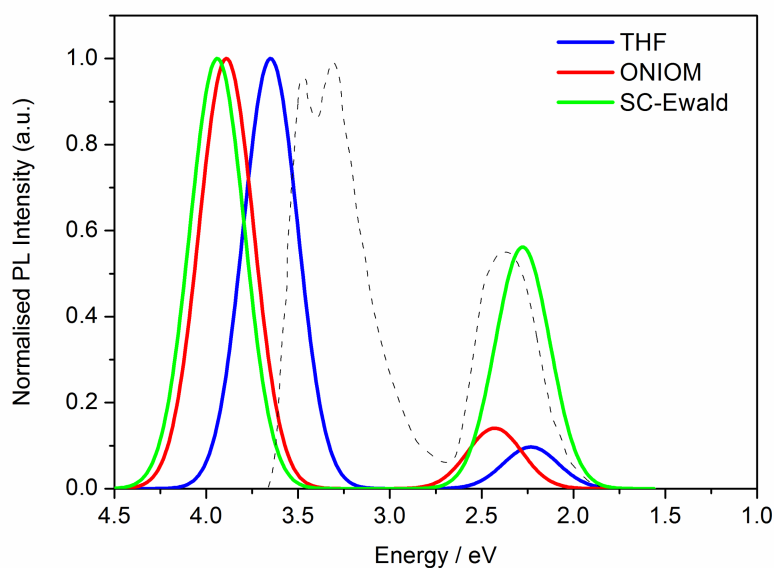


FIGURE 6.6: Calculated emission spectra of both  $S_0 \rightarrow S_1$  and  $S_0 \rightarrow S_3$  transitions at the CAM-B3LYP level: i) in THF (implicit solvation, C-PCM), ii) in the solid state using ONIOM QM/QM' and iii) in the solid state using the SC-Ewald embedding procedure. A FWHM value of 0.35 eV is used throughout. The experimental spectrum [95] is also shown (dashed lines).  $E_{SOL}$  and  $E_{AGG}$  indicate experimental emission bands attributed to dissolved and aggregated DPF respectively. All spectra are normalized with respect to  $E_{AGG}$ .

Now considering  $E_{AGG}$  – a result of emission from the  $S_1$  CT excited state ( $S_0 \rightarrow S_1$ ) – all models produce emission energies comparable with experiment, with errors of just 0.11, 0.12 and 0.05 eV for THF, ONIOM and SC-Ewald, respectively. In contrast to  $E_{SOL}$ , ONIOM and SC-Ewald yield somewhat different emission energies for  $E_{AGG}$ , with SC-Ewald producing an emission energy that is 0.15 eV red-shifted with respect to ONIOM. Again, this is significant and highlights the state-specific nature of the excited state crystalline potential generated by SC-Ewald. Naturally, the pronounced charge transfer character of the  $S_1$  excited state results in a marked rearrangement of the electronic density and, consequently, a non-negligible alteration to the surrounding embedding potential, which is reflected in the calculated emission energy.

Perhaps more interesting within the context of AIE is the difference in relative intensity between  $E_{SOL}$  and  $E_{AGG}$  produced by each model. In the case of THF, the weak emission from the  $S_1$  state relative to that of the  $S_3$  state is consistent with the lack of emission intensity observed experimentally for DPF in THF solution. Upon introducing the solid-state environment via the ONIOM model, a marginal enhancement of  $E_{AGG}$  can be noticed, in terms of brightness, although this is not of a sufficient magnitude to account for the experimentally measured enhanced emission of the aggregate. However, when accounting for the excited state crystalline potential as produced by SC-Ewald, a remarkable agreement with the experimental spectrum is observed, and the enhanced emission as a result of the

aggregation is recovered. In this way, the potentially non-negligible effects of not only the long-range electrostatic interactions but also the excited solid state potential are evident. Crucially, using this model it can be shown that both the large red-shift and enhanced emission intensity upon aggregation of DPF can be rationalized with a single molecule, without considering intermolecular electronically excited states or excimer formation. Notably, this is in contrast to the previous experimental interpretation, which relies on the formation of so-called “static excimers” – comprising dimers of DPF – to account for the 150 nm red-shift upon aggregation.

## 6.4 Conclusions

The key conclusions from this chapter are outlined below:

- In the modeling of AIE processes, we have demonstrated the potential importance of including environmental effects, and how different models (ONIOM and SC-Ewald) can lead to differences in the interpretation of the AIE mechanism.
- While the RIR paradigm is sufficient to rationalize AIE phenomena in many organic molecular systems, DPF highlights that this is not always the case.
- Our theoretical analysis demonstrates that the simultaneous enhancement and red-shifting of the emission maximum of DPF upon aggregation is a result of the electrostatic field induced by the crystalline environment, enhancing the intensity of otherwise poorly-emissive states (in solution).

Our results demonstrate how, generally, modelling different environmental effects to a sufficient quality is crucial for the understanding and reproduction of experimental observations within the context of AIE. More specifically, in the case of DPF, it has been shown that the often-cited restriction of intramolecular rotation paradigm provides an incomplete picture of the AIE process in this particular case. Instead, a theoretical analysis has shown that the concomitant red-shift and fluorescence-enhancement upon aggregation of DPF monomers in solution is due to an environmentally driven process, relying on both short- and long-range excited state electrostatic interactions between a single molecule and its surroundings within the aggregate. We therefore suggest that the excited-state field of the environment enables the enhanced emission of otherwise poorly emissive, low-lying excited states and leads to an observed intense aggregate emission at lower wavelength with respect to solution. Interestingly, this lies in contrast to the previous interpretation of experimental results, which cite the formation of so-called “static excimers”. We envisage that, for other reported cases of AIE accompanied by a significant changes in emission maxima, this protocol could be generally applied as a tool not only to understand, but to aid in the design of better-performing materials by providing a means of accommodating interaction with complex environments.



## Chapter 7

# Mechanochromic Fluorescence: Extending SC-Ewald to the Amorphous Phase

### 7.1 Introduction

The solid-state fluorescence of organic molecules strongly depends on the molecular structure and intermolecular interactions present in different morphologies. [100] In previous chapters, we have explored how fluorescence properties of organic molecular crystals can be altered by excited-state reactivity (proton transfer) and aggregation. These properties were also found to be highly sensitive to electrostatic interactions with the environment. In this chapter, we explore the sensitivity of solid-state fluorescence properties to both polymorphism and mechanical stress. In the context of material science, polymorphism is the ability of a given molecule to, when crystallized, assume different crystalline structures. [101] As a result, different polymorphs derived from the same parent molecule can exhibit distinctly different intermolecular interactions and, as a result, strikingly different optical properties. [102] Furthermore, by applying pressure through mechanical grinding and forming less-ordered polymorphs, some materials can exhibit a color change or a change in luminescence behavior, known as “mechanochromism”. [103] More recently, selective mechanochromism, sensitive to the type of mechanical pressure applied - be it anisotropic or isotropic - has been demonstrated for some materials. [104]

Although mechanochromism has become an intensively studied property of molecular materials, [103] the microscopic processes that lie at its origin remain poorly understood, prohibiting any kind of rational design strategy for real-world application. Opening up pathways towards design requires profound insight into the highly correlated structure-property relationships at the excited-state that govern mechanochromism. Up until this point, turning to theoretical approaches to study these connections has been impractical due to the inherent complexity related to the description and prediction of amorphous phase properties, particularly at the excited state. Indeed, theoretical description of absorption and

fluorescence requires sophisticated quantum chemical approaches which are often computationally demanding. Sampling a representative number of molecular configurations in the amorphous phase represents a tremendous computational investment, particularly for excited state calculations, and thus prevents any attempt at the reproduction or prediction of optical properties. With a dual experimental-theoretical approach, in this contribution we demonstrate that intelligent sampling of thermally accessible configurations in the crystalline phase, coupled with an understanding of the factors ruling local order in the amorphous phase, leads to a remarkable reproduction of experimental emission spectra and, in turn, provides vital understanding of the key processes behind mechanochromism and indeed the interpretation of amorphous-phase optical properties in general.

To do so, we introduce what shall be referred to as the DFB-X family of molecules - DFB-H, DFB-E and DFB-A - shown in figure 11.10. Taking DFB-A as an example, figure 7.2 highlights the effects of the environment (i.e. solution or crystalline), polymorphism and mechanical stress on fluorescence properties. In THF solution, DFB-A shows an emission maximum at around 425 nm and has two stable crystalline polymorphs (DFB-A1 and DFB-A2) with broader emission spectra at 480 and 520 nm, respectively. Interestingly, mechanical grinding (amorphization) of DFB-A crystals results in a global red-shift and significant broadening of the emission spectrum, with a maximum at 550 nm. DFB-A serves as an excellent example of how a change in intermolecular interactions brought by altering the relative conformations within the molecular material results in significant alterations of fluorescence behavior. Furthermore, DFB-H and DFB-E - due to the different potential intermolecular interactions brought by substitution of different donor groups - exhibit their own distinct polymorphism and response to mechanical perturbation. The complex response of this family of molecules to different environmental interactions and stimuli make it an ideal challenge for computational techniques which seek to account for such subtleties. Therefore, in this chapter we shall demonstrate how SC-Ewald - in conjunction with molecular dynamics (MD) techniques - is able to recover spectral changes due to polymorphism and uncover key physical concepts behind mechanochromic fluorescence.

## 7.2 Computational Details

As we are interested in the photophysical properties of the DFB-X family in solution, crystalline and amorphous phases, we rely on several different techniques, rooted in both density functional theory (DFT) and Molecular Dynamics (MD).

All calculations using periodic boundary conditions were performed with Crystal 14, [74] which permits the use of both hybrid density functionals and all-electron Gaussian-type basis sets. Starting from experimentally-resolved crystalline structures, using the B3LYP [76] functional and a 6-31G(d) basis set, optimization of the atomic positions and Mulliken population analyses for each member of the DFB-X family and their respective polymorphs were performed. In each case, a Monkhorst-Pack shrinking factor [75] of 4 is used, corresponding to 36 points in the irreducible Brillouin zone (IBZ) for DFB-H, DFB-E1, DFB-E2, and

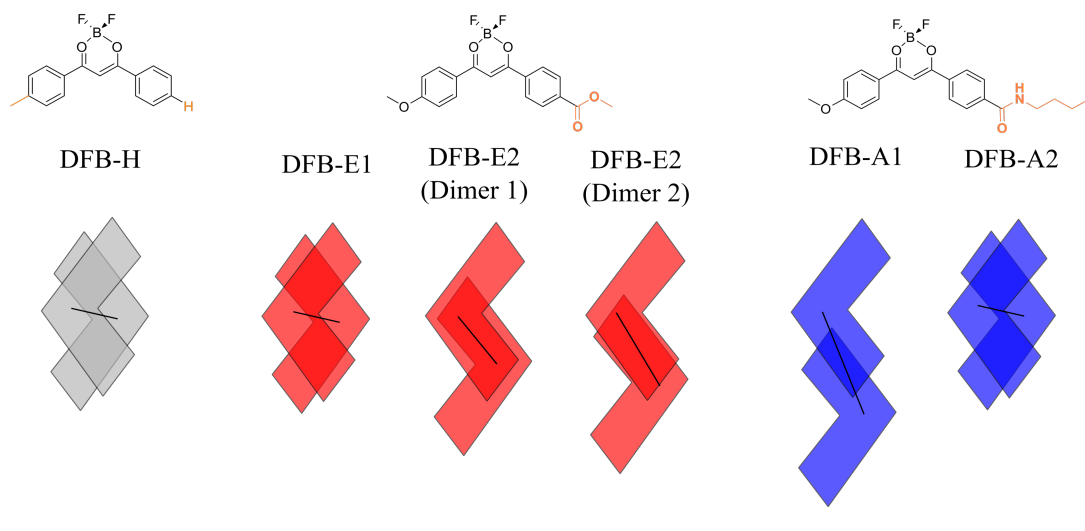


FIGURE 7.1: Molecular structures of molecules DFB-H, DFB-E and DFB-A. Colored kite shapes indicate the relative orientation and overlap of dimer pairs each of the experimentally resolved crystalline polymorphs, with a black line indicating the center of mass (COM) distance  $r$  in each case.

DFB-A1. As the crystalline structure of DFB-A2 could not be resolved experimentally, The Materials Studio package was used with the Dreiding force field, [105] considered the most reliable force field for molecular crystal prediction, [106,107] along with the RESP [108] partial charges calculated for the MD simulation. From the resulting polymorphs, the lowest-energy unique structure was selected and subsequently refined at DFT level in the same fashion as the other DFB-X polymorphs, again with a Monkhorst-Pack shrinking factor of 4, corresponding to 36 points in the IBZ. As it is not yet possible to directly compute electronic emission properties using periodic boundary conditions, these resulting structures and Mulliken population analyses are used as a starting point for the calculation of crystalline and amorphous emission, which are based on the SC-Ewald approach introduced in chapter 4.

### 7.2.1 Crystalline-Phase Emission

In doing so, we calculated the fluorescence properties of each polymorph in the DFB-X family in figure 11.10, using the Gaussian 09 [79] software suite. In each case, the charge array is formed of an  $8 \times 8 \times 8$  supercell, with the number of atoms in spherical Zone 2 kept constant at 2000, ensuring that each quantum-mechanically treated cluster is completely confined therein. The quality of the Madelung potential produced by the charge fitting process is assessed at 1000 check-points randomly distributed around the cluster. In all cases, the rms difference between the direct-sum and crystalline (Ewald) potentials was less than  $0.2 \mu\text{V}$ . In order to retain consistency with the guess charge values from periodic calculations and due to the well-known sensitivity of Mulliken charges to basis set size, [109] we used a 6-31G(d) basis set during the self-consistent procedure. For the excited state geometry optimisation and calculation of emission properties, this was extended to 6-31+G(d,p). Unless otherwise

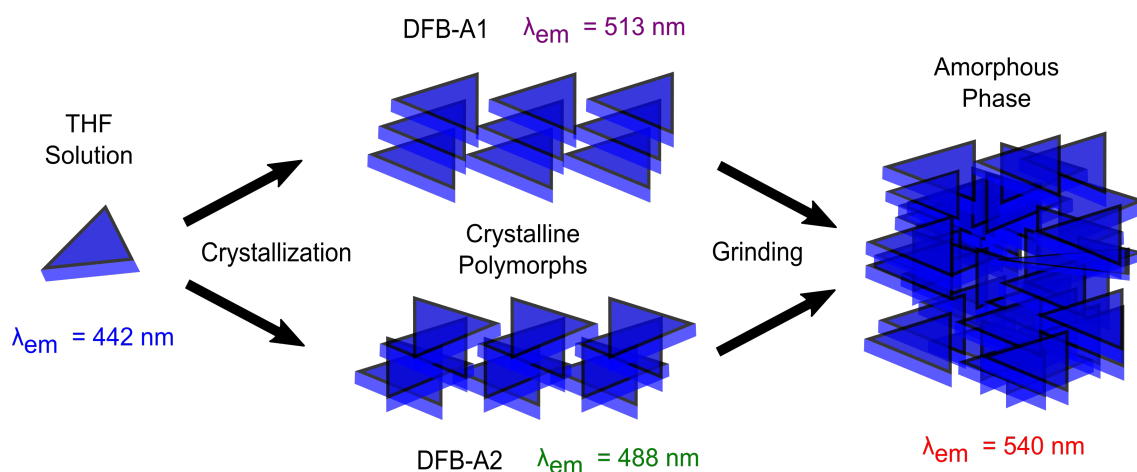


FIGURE 7.2: Illustration of how environmental differences between solvation (THF), crystallization and amorphization affect fluorescence properties of DFB-A (described by emission band maxima  $\lambda_{em}$ ).

stated all results were obtained with the range-separated hybrid density functional CAM-B3LYP [97] due to (i) its enhanced performance when modelling charge-transfer excitations over density functionals mixed with a fixed amount of Hartree-Fock exchange and those that rely solely on the generalized gradient approximation [99] and (ii) its stability with respect to the self-consistent charge adjustment procedure within SC-Ewald. From appendix 15, we see that both global hybrid functionals tested (B3LYP [76], PBE0 [22]) result in spurious charge transfer states as a result of the self-consistent procedure, leading to significantly underestimated emission energies. A schematic of the dimer clusters investigated in this work are shown in figure 7.1. Dimer clusters were selected as excimer formation is a frequently-suggested mechanism for fluorescence color changes upon crystallization of organic molecules. [102, 110, 111] The 10 lowest-energy excited states were calculated for each cluster, although in each case only the first excited-state (S1) geometry was optimized.

## 7.2.2 Amorphous-Phase Emission

The amorphous phases of DFB-H, DFB-E and DFB-A were reconstructed through Molecular Dynamics (MD) simulations. The starting configuration for each system was built by placing 500 molecules at random positions in a cubic, periodic box with an edge-length of  $150 \text{ \AA}$ . All systems were equilibrated in the NPT ensemble at atmospheric pressure and high temperature ( $P = 1 \text{ atm}$ ;  $T = 800 \text{ K}$ ) until the volume of the periodic box reached an equilibrium value. Following a further equilibration run at  $300 \text{ K}$ , a  $30 \text{ ns}$  trajectory in the NPT ensemble was obtained for each system. All MD simulations employed a time step of  $1 \text{ fs}$ . A cutoff of  $12 \text{ \AA}$  was applied to the van der Waals interactions through a switching function, whereas the particle mesh Ewald (PME) method was employed to calculate the electrostatic interactions. All simulations were performed using the NAMD2.11 package [112] with a Nose-Hoover Langevin barostat [113, 114] (oscillation period  $200 \text{ fs}$ , decay coefficient  $100 \text{ fs}$ ) and a Langevin thermostat [115] (damping coefficient  $1 \text{ ps}^{-1}$ ). The molecules were parametrized

using the CGenFF [116] force field along with accurate partial charges obtained through the restrained electrostatic potential (RESP) [108] procedure on the basis of HF/6-31G(d,p) calculations.

In order to create a link between the amorphous phase and crystalline defects, the frames extracted from the MD trajectories were used to calculate the probability  $p(r)$  of finding a dimer for which the constituent monomers lie on parallel planes. The planarity condition was satisfied when the four angles  $\theta_{ii} = 1, 2, 3, 4$  between the planes defined by the phenyl moieties were less than  $15^\circ$  or more than  $165^\circ$  (figure 7.3). This criterion was imposed due to the parallel nature of molecular planes in the crystalline phases. The probability was defined as the ratio between the number of parallel dimers with inter-monomeric distance  $r$  and the total number of parallel dimers. This probability is subsequently used to weight the emission signal calculated for a series of defects in the crystalline phase, based on their frequency in the amorphous phase.

Specifically, we perform a scan by projecting one of the monomer units along the directions parallel and perpendicular to the long-axis of the monomer, within its average plane. In doing so, we obtain emission energies, oscillator strengths and total energies of different structural defects in the crystal. Additionally, in order to combine with the MD simulations, the inter-monomeric distance  $r$  is measured for each defect. With this information in hand, the emission spectrum ( $F$ ) of the amorphous phase is calculated using a sum of weighted Gaussian functions:

$$F = \sum_i P_i \times g_i \times e^{-\frac{\Delta E_i}{kT}} \quad (7.1)$$

Where  $P_i$  is the probability of a given defect in the amorphous phase at inter-monomeric distance  $r$ ,  $g_i$  is a Gaussian function centred at the calculated emission energy of the defect, with an integrated area equal to the oscillator strength, and a full width at half maximum (FWHM) of 0.15 eV. Each contribution is also weighted using a Boltzmann factor calculated using the total excited-state energy of the defect relative to the equilibrium excited-state geometry in the crystalline phase ( $\Delta E_i$ ).

### 7.2.3 Emission in Solvent

For comparison with experimentally observed changes upon crystallisation, emission energies were obtained for each system in tetrahydrofuran (THF) solution, modelling the surrounding solvent using the conductor-like polarizable continuum model [34] (CPCM) applied within the state-specific paradigm [36]. Again, the range-separated exchange-correlation functional CAM-B3LYP [97] was used along with the 6-31+G(d,p) basis set.

## 7.3 Results and Discussion

In order to provide a complete picture of mechanochromic fluorescence from an ab-initio perspective, we naturally must provide a means of describing fluorescence from both the

crystalline and amorphous phases of a given molecular assembly. For the former, SC-Ewald enables the quantitative description of absorption and fluorescence events in molecular crystals. This scheme, described in detail in chapter 4, approximates the electrostatic (Madelung) potential of either the ground or excited state of the crystalline environment which acts on a preselected, quantum mechanically (QM) described part of the bulk solid (cluster). Due to previous reports of excimer formation in mechanochromic molecular crystals, we have considered QM clusters comprising both monomers and dimers (figure 7.1), although only results obtained using dimer clusters are discussed in the main text as these are able to consistently capture all relevant excited states for the description of the condensed-phase emission. As well as crystalline and amorphous emission, we further test the capabilities of our model by comparing with fluorescence properties calculated in THF solution.

### 7.3.1 Emission in DFB-X Crystalline Polymorphs

Table 7.2 shows the calculated change in emission energy for the DFB-X family in the crystalline (C) phase with respect to emission in solution (S). We shall refer to this quantity as  $\Delta E_S^C$ . In the case of DFB-H, crystallisation results in a red-shift of the emission maximum with an experimentally measured  $\Delta E_S^C$  value of -0.47 eV, the negative sign indicating a lower emission energy in the crystalline phase than in solution. The monomer model fails to qualitatively reproduce  $\Delta E_S^C$ , predicting a slight blue shift. The dimer model, for which the HOMO and LUMO orbitals are delocalized over both monomer units – indicating excimer formation – performs considerably better, correctly predicting  $\Delta E_S^C$  from a qualitative standpoint (-0.28 eV).

Crystallising DFB-E was found to result in two stable polymorphs, DFB-E1 and DFB-E2, with  $\Delta E_S^C$  values of -0.40 and -0.26 eV respectively. Calculations performed on DFB-E1 performed analogously to those of DFB-H, although the monomer model in this case was at least qualitatively correct, predicting a red-shift of -0.16 eV, with the dimer model considerably improving upon this result (-0.29 eV). Due to the “herringbone” structural motif present in DFB-E2, it was necessary to consider two different dimer models (Dimer 1, Dimer 2), as two unique dimers with slightly different stacking are present in the crystalline phase as opposed to the discrete dimer units found in DFB-H and DFB-E1. As for DFB-H, the monomer model yields a blue-shift, in contradiction with experiment. Interestingly, of the two dimer models tested, only Dimer 2 demonstrates true excimer behavior, with the HOMO and LUMO orbitals fully delocalized over both monomer sub-units. Analyzing the crystal structure of DFB-E2, we observed that Dimer 2 possesses a slightly greater intermolecular overlap with respect to Dimer 1. This is reflected in the distances between the centers of mass (COM) of each monomer sub-unit, equal to 5.5 and 6.3 Å in Dimers 1 and 2 respectively. This increased overlap lends itself to excimer formation, explains the lower emission energy calculated for Dimer 2 relative to Dimer 1 and highlights the potential impact of subtle structure-property relationships in the solid state.

TABLE 7.1: Computed emission energies for each member of the DFB-X family (in eV), computed with the SC-Ewald approach. In each case, different cluster models were tested, comprising monomers and dimers (see figure 11.10).

|                  | DFB-H | DFB-E1 | DFB-E2 | DFB-A1 | DFB-A2 |
|------------------|-------|--------|--------|--------|--------|
| Monomer<br>(vac) | 3.55  | 3.37   | 3.37   | 3.43   | 3.36   |
| Monomer (emb)    | 3.39  | 2.99   | 3.18   | 2.85   | 3.11   |
| Dimer 1 (vac)    | 3.26  | 3.05   | 3.31   | 3.12   | 3.09   |
| Dimer 1 (emb)    | 3.12  | 2.85   | 3.12   | 2.83   | 3.01   |
| Dimer 2 (vac)    | -     | -      | 3.17   | 3.41   | -      |
| Dimer 2 (emb)    | -     | -      | 2.98   | 2.82   | -      |
| Solution (THF)   | 3.40  | 3.15   | 3.15   | 3.19   | 3.19   |

TABLE 7.2: Differences in emission energy ( $\Delta E_S^C$ ) going from solution to the solid state (in eV) for each member of the DFB-X family, computed with the SC-Ewald approach. In each case, different cluster models were tested, comprising monomers and dimers (see figure 11.10). A negative (positive) value indicates a red (blue) shift with respect to emission in solution. Results were obtained both with Madelung field produced using SC-Ewald (emb) and in vacuum (vac).

|               | DFB-H | DFB-E1 | DFB-E2 | DFB-A1 | DFB-A2 |
|---------------|-------|--------|--------|--------|--------|
| Monomer (vac) | 0.15  | 0.22   | 0.22   | 0.24   | 0.17   |
| Monomer (emb) | -0.00 | -0.16  | 0.04   | -0.34  | -0.08  |
| Dimer 1 (vac) | -0.14 | -0.09  | 0.17   | 0.22   | -0.10  |
| Dimer 1 (emb) | -0.28 | -0.29  | -0.02  | -0.37  | -0.18  |
| Dimer 2 (vac) | -     | -      | 0.03   | -      | -      |
| Dimer 2 (emb) | -     | -      | -0.16  | -      | -      |
| Experiment    | -0.47 | -0.40  | -0.26  | -0.39  | -0.26  |

As for DFB-E, DFB-A also crystallises into two polymorphs (DFB-A1 and DFB-A2). Inspecting the molecular orbitals in appendix 15, we see that there is indeed excimer formation for DFB-A, with similar delocalisation over the second monomer unit as observed for the other polymorphs.

Although experimental emission spectra allude to two stable polymorphs of DFB-A, only DFB-A1 (space group P21/n) could be structurally resolved. We made use of a polymorph-prediction package to determine the structure of DFB-A2, imposing the space group  $P\bar{1}$  in keeping with DFB-H and DFB-E1. The resulting structure was refined at DFT level and, interestingly, was found to be only 2.1 kcal/mol higher in energy than the DFB-A1 polymorph. Unlike DFB-A1, the imposition of the  $P\bar{1}$  space group guarantees that DFB-A2 shares an analogous structure to DFB-H and DFB-E1 and, in turn, similar fluorescence properties. The DFB-A2 monomer model at least qualitatively predicts the experimental red-shift of -0.26 eV, although the dimer model (exhibiting excimer formation) provides a quantitatively accurate result (-0.18 eV).

We also note that the SC-Ewald approach was able to quantitatively predict the relative emission energies between different crystalline polymorphs. For example, the difference in emission energy measured experimentally between DFB-E1 and DFB-E2 is 0.14 eV, which we compare to the computationally determined value of 0.13 eV between excimer emission energies in each polymorph. We point to similar performance for DFB-A1 and DFB-A2, comparing the experimental and computational values of 0.15 and 0.13 eV respectively.

### 7.3.2 Emission in Amorphized DFB-X

To identify common structural features between the resulting crystalline and amorphous phases of the DFB-X family, we measured the distance between pairs of molecules in the amorphous phase (see figure 7.3). In figure 7.4, the resulting distances are plotted as a probability distribution and are compared with analogous distances computed for each of the corresponding crystalline polymorphs – shown as vertical dashed lines. It is striking that each polymorph possesses an inter-monomeric distance that lies very close to the peaks of the probability distribution for the corresponding amorphous phase. The number of peaks present in a given distribution appears linked to the number of stable crystalline polymorphs. DFB-H, which possesses one stable crystalline structure, produces a single distinct peak in the amorphous probability distribution while amorphous DFB-E and DFB-A yield two distinct probability peaks and each exhibit two stable crystalline polymorphs. While all of the polymorphs exhibit intermolecular  $\pi$ -stacking interactions, substitution of ester and amide groups in the case of DFB-E and DFB-A respectively introduces the potential for hydrogen-bonding interactions, leading to increased polymorphism and, subsequently, other distinct regions of crystalline-like local order in the amorphous phase. This indicates that a given amorphous material can inherit local structural properties from any available crystalline polymorphs, the structures of which are governed by the intermolecular interactions available to their constituent molecules. This serves as an indication that the design

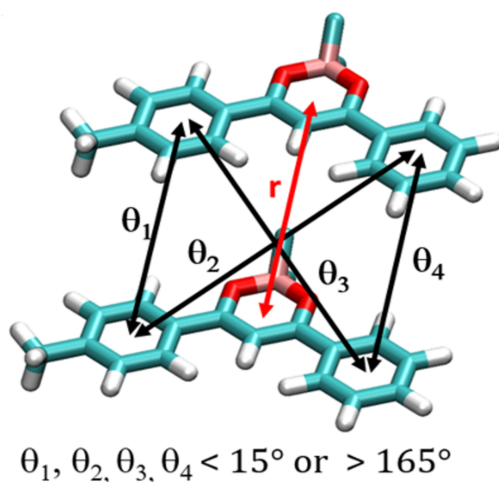


FIGURE 7.3: Criteria used to link amorphous and crystalline structures and generate probability distribution of parallel dimers in the amorphous phase separated by centre of mass (COM) distance  $r$ .

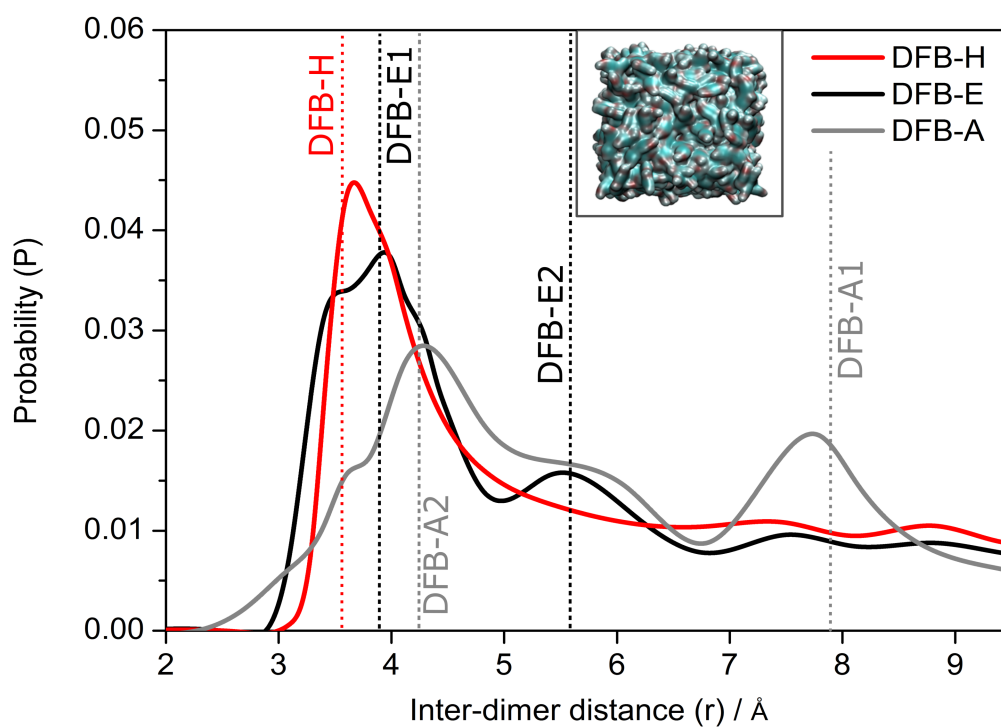


FIGURE 7.4: Probability distribution of (semi-)parallel dimers in the amorphous phase with a given intermolecular distance  $r$ . Vertical dashed lines indicate the same value computed for each crystalline polymorph. The inset shows an image of the computed amorphous phase for DFB-H.

of amorphous materials could be made possible through a consideration of potential intermolecular interactions in the crystalline phase.

From a computational point of view, these observations have significant consequences for the study of amorphous-phase photophysical properties, as a brute-force exploration of all possible excited-state molecular configurations is not feasible. Taking advantage of the local order present in the amorphous phase and its similarity to crystalline structural motifs, we model fluorescence properties using a hybrid approach employing ground-state MD simulations and excited-state calculations at TD-DFT level. For the latter, we approximate the amorphous phase as a series of “defects” in the crystalline phase, using the MD simulations to infer the probability of the presence of a given defect. Intuitively, this can be likened to an exploration of nearby higher-energy structures in the crystalline phase which are only accessible after the application of an external force (in this case, mechanical grinding). Though one can imagine many possible crystalline defects, we perform a simple scan limited only to two degrees of freedom, as shown in the inset of figure 11.11D. Specifically, we perform a geometrical scan by projecting a single molecule within each polymorph along its average plane in directions parallel ( $\Delta x$ ) and perpendicular ( $\Delta y$ ) to its long-axis. We expect the defect configurations within this scan to encompass those most relevant for the recovery of spectroscopic properties of the amorphous phase. In doing so, we obtain emission energies, oscillator strengths and total energies of different structural defects in the crystal. The starting point for each scan is the excited-state equilibrium geometry, the emission properties of which correspond to those of the crystalline phase itself. This technique relies on the interplay between various properties of these defects and how they are reflected in the computed emission spectrum. To introduce the application of this concept, we shall begin by discussing the amorphous phase of DFB-H. Here, we note that the lowest-lying excited state in crystalline DFB-H is a direct result of excimer formation, highlighted via the delocalization of the exciton over two monomer units. The formation of excimers is consistent with previous experimental interpretations of related systems. [102, 110, 111] To achieve coherence with experimental data, two monomer units have been included within the quantum-mechanically treated cluster throughout.

In figure 11.11, we show the results of this scanning procedure via a series of surface plots, where the emission energy is plotted for each scan coordinate to form a 3D surface. We use this to explain the origins of the color change observed upon amorphization of crystalline DFB-H. Figure 11.11A shows this 3D surface onto which we have mapped a color scheme depicting the probability of finding a pair of molecules in the amorphous phase - separated by distance  $r$  - with the same intermolecular distance as our crystalline defect. In line with figure 7.4, the highest-probability region is close to the excited-state equilibrium geometry of the crystalline phase. Figure 11.11B shows a similar plot. Here, the color map corresponds to the calculated oscillator strength for each dimer configuration. Positive displacement along the  $\Delta x$  direction (long axis) results in an increased oscillator strength, attributed to the reduced distance between donor and acceptor moieties of adjacent monomer units - promoting the charge transfer character of the transition. This effect is also reflected

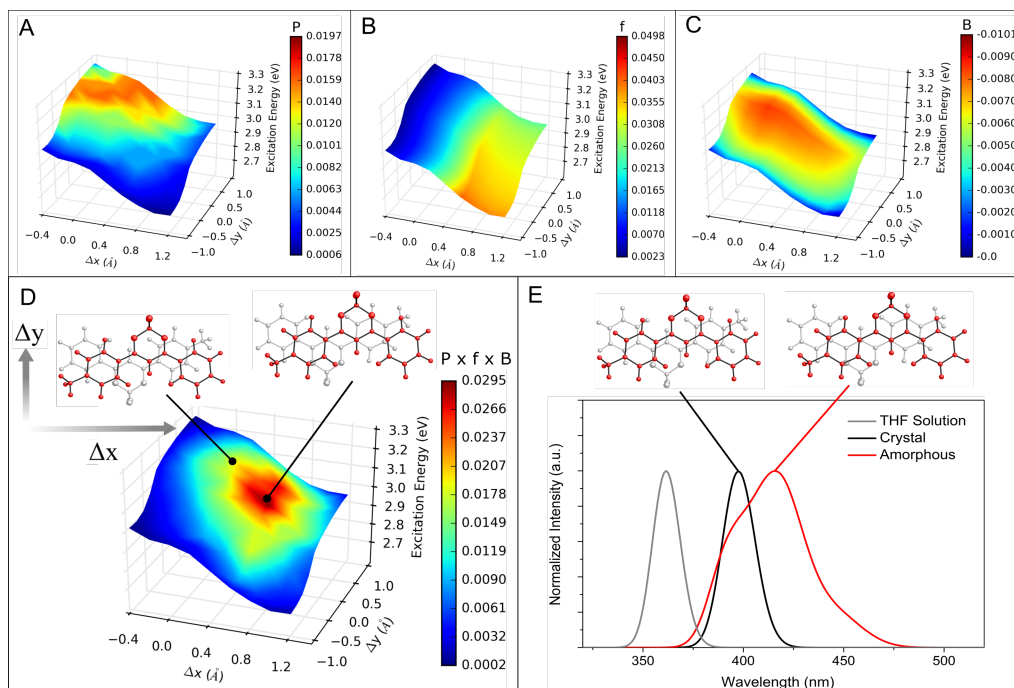


FIGURE 7.5: Surface plots of calculated emission energy with respect to the defect scan coordinates. For a given pair of molecules in the crystalline phase, one molecule (highlighted in red) is displaced along its average plane in directions parallel ( $\Delta x$ ) and perpendicular ( $\Delta y$ ) to its long axis. A color scheme is mapped onto this surface, representing A) the probability to find a particular configuration in the amorphous phase, B) the oscillator strength, C) the Boltzmann factor and D) the normalized product of each of these, yielding the weighted oscillator strength. Red (blue) regions represent a greater (lesser) contribution of a given scan coordinate to the overall computed emission spectrum in the amorphous phase. E) Computed emission spectra for solution (THF), crystalline and amorphous phases of DFB-H. Molecular structures shown indicate crystalline structure and maximum-contributing defect.

in the decreasing emission energy with increasing values of  $\Delta x$ . Figure 11.11C maps the relative probability (via the Boltzmann factor), of the existence of a given configuration at the excited state. This plot is crucial as the MD simulations are performed at the ground state and it is necessary to link the ground and excited state configurations of the amorphous and crystalline phases, respectively. As one might expect, the area of maximum probability surrounds the excited state equilibrium configuration in the crystal, although a distinct channel of higher-probability structures is evident along the  $\Delta x$  direction. The aforementioned plots are combined to form figure 11.11D, in which the product of the MD probabilities ( $P_i$ ), oscillator strengths ( $f_i$ ) and Boltzmann factors ( $B_i$ ) are mapped onto the emission energy surface. In this plot, red (blue) areas indicate a greater (lesser) contribution of a particular configuration to the overall amorphous-phase emission spectra. Remarkably, the area with greatest contribution does not lie at the excited state equilibrium configuration, but in a nearby region with lower emission energy. This represents the compensation of the reduced stability of excited-state configurations with slightly greater energy by a concomitant increase in oscillator strength – in this case stemming from increased charge-transfer character – resulting in a globally shifted emission maximum. We point to this counter-intuitive perturbation effect as the reason for the drastic change in emission color upon mechanical perturbation of the crystalline phase, which represents the first computational evidence for such a process that has indeed been previously suggested – for related polymorphs – based on results obtained using precise, directional mechanical perturbation techniques. [117] Additionally, mechanochromism resulting from the slipping of molecular columns by mechanical stimulus has been postulated for inorganic molecular systems. [118] To provide further support, we constructed the emission spectrum ( $F$ ) of the amorphous phase according to equation 7.1. This is essentially the same process used to generate the color map in figure 11.11D, replacing the oscillator strength with a Gaussian function. We show the resulting spectrum in figure 11.11E.

In figure 7.6, comparing with the corresponding experimental spectra reveals an impressive reproduction of the separation of the emission maxima in solution, crystalline and amorphous phases, especially given that the many potential configurations of the amorphous phase have been reduced to a simple two-dimensional scan. The amorphous experimental spectrum exhibits a shoulder at 396 nm which, due to its almost-perfect overlap with the crystalline emission spectrum, one might immediately attribute to left-over crystalline residue after smearing to form the amorphous phase. However, we show that the calculated emission spectrum of amorphous DFB-H captures this same feature, suggesting that this spectral shoulder is an intrinsic property of the amorphous phase and not a result of incomplete smearing of DFB-H crystals. Overall, despite the slight underestimation of the red-shift and the reduced broadening of the emission spectrum compared to experiment, this approach is able to recover all of the salient features of the amorphous emission spectrum.

From figure 7.6, the standard of the model is retained upon extension to DFB-E and DFB-A. Generally, the agreement with experimental differences between solution, crystalline and

amorphous emission maxima values is of an impressive quality. We note, however, that the SC-Ewald approach leads to an apparent systematic underestimation of the crystalline emission energy by approximately 0.1 eV with respect to the experimental measurements. This could be attributed to several factors, such as the neglect of any interactions with the environment other than electrostatics or the simplification of the environment to simple point charges.

For each amorphous (and indeed crystalline) model, the reproduction of experimental behaviour arises from an understanding of the formation of low-energy excited states through excimer formation. This echoes previous experimental hypotheses suggesting that low-energy, excimer-based exciton traps are responsible for mechanochromism, although, to our knowledge, this work represents the first clear foundation for such a mechanism based on both theoretical and experimental evidence. What we observe from our model suggests that small numbers of molecular configurations which are close to those of the crystalline materials themselves are responsible for mechanochromic fluorescence, rather than a complete phase change to a different solid state form. Moreover, the strength of the mechanochromic effect itself appears linked to the number of specific intermolecular interactions present in the solid state, with weaker slip planes bound mainly through van der Waals forces giving rise to more potent mechanochromic properties that are otherwise inhibited by specific intermolecular interactions such as hydrogen bonding. Naturally, this could lead to new concepts in the framework of molecular design, with the aim to influence the mechanochromic properties of materials by considering the balance between specific and non-specific intermolecular interactions and their subsequent effects on amorphous-phase fluorescence.

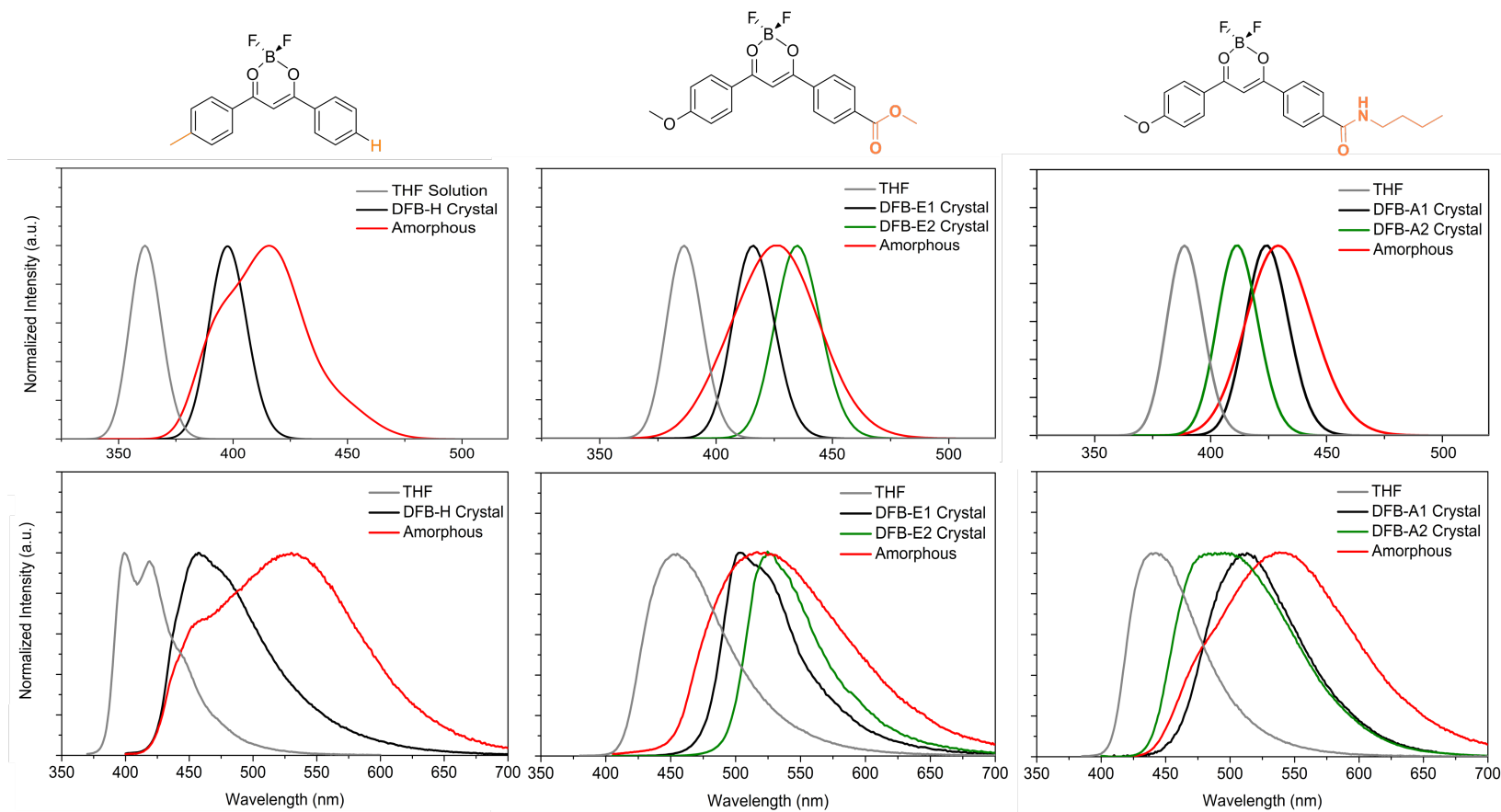


FIGURE 7.6: Computed (top) and experimental (bottom) emission spectra determined for solution, crystalline and amorphous phases for DFB-H (left), DFB-E (centre) and DFB-A (right).

## 7.4 Conclusions

The key conclusions of this chapter are outlined below:

- We have presented the first computational study of organic molecules in solution, crystalline and amorphous phases all together.
- Together, each phase model was able to quantitatively reproduce the changing fluorescence behavior of each member of the DFB-X family and recover the key polymorphism and mechanochromism properties.
- For the amorphous phase, complex band shape (in the case of DFB-H) and band broadening was also recovered.
- From a physical point of view, the computationally-observed, crystal-like local order in amorphous-phase DFB-X provides evidence for the presence of low-energy exciton traps which cause the global red-shift of emission maxima upon mechanical grinding.
- Overall, we have highlighted structure-property relationships which govern competition between low-energy excited states and how these influence the resulting emission spectra for given crystalline polymorphs and amorphous materials.

In this chapter, we have used the SC-Ewald approach introduced in chapter 4 to investigate changes in emission behavior of a family of molecules based on difluoroboron avobenzene brought by both polymorphism in the crystalline phase and amorphization via mechanical grinding. As well as a quantitative recovery of influence of polymorphism on fluorescence, using intelligent sampling of thermally-accessible molecular configurations in the amorphous phase, we have obtained a quantitative model which provides physical insight into the origins of mechanochromic luminescence and the optical properties of amorphous materials in general. Additionally, we have seen how the degree of polymorphism can be altered via the substitution of donor moieties which facilitate a wider array of potential intermolecular interactions, how this translates to regions of local order in the amorphous phase and the resulting influence on amorphous-phase fluorescence.



## Chapter 8

# Cluster Modeling of Luminescent Metal-Organic Frameworks

### 8.1 Introduction

MOFs are supramolecular solids composed of organic molecules (linkers) which link inorganic building units [119]. The enormous chemical space available for the design of these organic and inorganic moieties means the number of possible MOF structures that can be conceived is essentially infinite, promising tailored materials for specific purposes [120,121]. Although the structural properties of MOFs have been investigated extensively both from experimental and a theoretical points of view, the electronic properties of these materials have recently become an area of increasing interest - with particular attention paid to enhanced photoluminescence - with the idea of exploiting these properties in areas such as small molecule sensing [122], non-linear optics [123] and biomedical applications [124]. There is a particular interest in photoresponsive frameworks, which respond to light absorption by changes in their structure, or stimuli-responsive photoluminescent frameworks, whose optical properties are modified by external physical or chemical stimulations [125].

Luminescent properties of metal-organic frameworks (MOFs) have garnered attention for some time [126]. The flexibility offered by the building-block nature of MOFs translates to the design of functional luminescent materials, with different linkers and inorganic building units giving rise to different, often competing, modes of luminescence [127]. As an introduction, we shall outline different possible sources of luminescence for MOFs comprising transition metals [128], namely:

- Ligand-centered (LC)
- Metal-centered (MC)
- Metal-to-ligand Charge Transfer (MLCT)
- Ligand-to-Metal Charge Transfer (LMCT)
- Ligand-Ligand Charge Transfer (LLCT) or excimer formation

In the context of ligand-centered emission, as the linker moieties are typically conjugated organic compounds, they absorb in the UV and visible region. Linker excitation typically occurs via allowed singlet–singlet transitions and emission from the lowest singlet excited state, in line with Kasha’s rule. Situations where this is not the case include where there are efficient, non-radiative decay pathways to lower-lying states, which could either be the ground state or - when efficient intersystem crossing is possible - lower-lying triplet states. In the latter case, lower-energy luminescence from the triplet state to the ground state (phosphorescence) can be observed. Additionally, the increased rigidity offered by coordination to metal sites has been shown to reduce non-radiative decay rates and therefore increase the fluorescence intensity of otherwise poorly emissive organic linker molecules.

Depending on the metal’s electronic configuration and relative metal and linker orbital energies, a metal ion can have varying degrees of influence on emission properties. Where the transition metals within the inorganic building units do not have fully saturated valence shells, low-energy (albeit forbidden), metal-centered transitions can occur between these states. For appreciable intensity, however, significant distortion of the coordination environment is required in many cases. Alternatively, vacant orbitals in the outer shell of the metal can facilitate ligand-to-metal charge transfer. Conversely, for transition metals such as Cd(II) and Zn(II), fully saturated d10 valence shells render LMCT and MC transitions impossible, though, depending on the relative energy of ligand-centered orbitals relative to those in the d-shell of the transition metal, metal-to-ligand charge transfer may occur.

In cases where the density of a given MOF structure is high and there is significant inter-ligand  $\pi$ - $\pi$  interactions, charge transfer between ligands or the dissociation of excitons across several ligands becomes possible, resulting in lower-energy luminescence bands with broad, featureless shapes. Generally, as can be inferred from the above, the observed emission is governed by the interplay between the electronic structure of the inorganic building units and the structure of the MOF itself, which is dictated by linker orientation, geometry, and size. As a result, while several different luminescence mechanisms are possible, the potential for fine-tuning and competition between mechanisms is promising from an applications point of view.

While luminescence from MOF structures is a frequently observed phenomenon, little effort thus far has been invested to gain a complete understanding of these excited state processes. Furthermore, identifying emission routes and discerning between competing processes is usually difficult from an experimental point of view.

In this respect, gaining a more complete understanding of excited state behavior in MOFs from a theoretical perspective could be a powerful tool, aiding in the rational design of high-performance luminescent materials. With this in mind, this paper attempts to improve upon the current understanding of MOF luminescence via the design of a suitable quantum computational protocol, rooted in density functional theory (DFT) and its time-dependent counterpart (TD-DFT), for the characterization and prediction of MOF luminescence behavior. To this end, we have chosen an appropriate case study of a pair of MOF structures composed of a 4,4-bis((3,5-dimethyl-1H-pyrazol-4-yl)methyl)biphenyl ( $H_2$ DMPMB) ligand and

interchangeable metal cations of zinc and cadmium, recently characterised experimentally by Tabacaru and co-workers, [129] hereafter labelled M[DMPMB] ( $M = \text{Zn, Cd}$ ). With an orthorhombic structure, these two frameworks crystallise in near-identical structures (in the Pccn space group), depicted in figure 8.1 along with the protonated ligand structure. Each transition metal ion is coordinated by four ligand molecules in a distorted tetrahedral fashion. The nitrogen atoms of a pyrazole ring each bond to a different M atom by their lone pair, thus bridging between two metal ions. The biphenyl groups of neighboring ligands are oriented on perpendicular planes, giving rise to the possibility of T-shaped  $\pi$ - $\pi$  interactions. While other MOFs constructed using this linker were reported, the zinc and cadmium frameworks were specifically selected as they are isostructural – allowing one to directly probe the effects of changing the coordinating metal – and both exhibit interesting luminescence properties. Furthermore, the simple interchange of the coordinating metal from zinc to cadmium results in a 0.88 eV (that is, from 441 nm to 335 nm) blue shift and thus is an interesting and novel example of tuneable luminescence in metal-organic frameworks. Despite this, no explanation for this rather large change in emission wavelength was proposed in the literature.

First, a computational protocol is determined by screening the performance of various exchange–correlation functionals with respect to the prediction of important structural features including cell parameters and the coordination environment of the metal ions. Next, we investigate the excited state properties using DFT and TD-DFT approaches to characterize the emission behavior. The combined use of full periodic and cluster model approaches at appropriate levels of theory allows one to form a detailed picture of the excited state processes at play in these materials. [130]

## 8.2 Computational Details

Calculations were performed both on periodic and cluster models for each MOF structure. The computational setup used in each case is described below.

All calculations were carried out using the Crystal14 package [74] which uses atom-centred Gaussian basis sets. In order to strike a good balance between time and accuracy, the Pople double zeta basis set 6-31G(d) was used in all calculations for all but transition-metal atoms. Zinc and cadmium were described by the basis sets proposed by Pettinger [131] and Dou, [132] respectively. The number of k-points in the irreducible Brillouin zone was set to 8 via a shrinking factor of 2. A total of five exchange-correlation functionals were tested. This test set was composed of two GGA functionals (PBE [21] and BLYP [133, 134]), two hybrids (PBE0 [22] and B3LYP [76]) and a functional purposely optimized to yield accurate equilibrium structure properties in solids (bond lengths and lattice parameters) known as PBEsol [135].

Structural optimization of the MOFs and molecular crystal of the ligand ( $\text{H}_2\text{DMPMB}$ ) were performed. The Grimme [77] “D2” dispersion correction scheme was tested within the

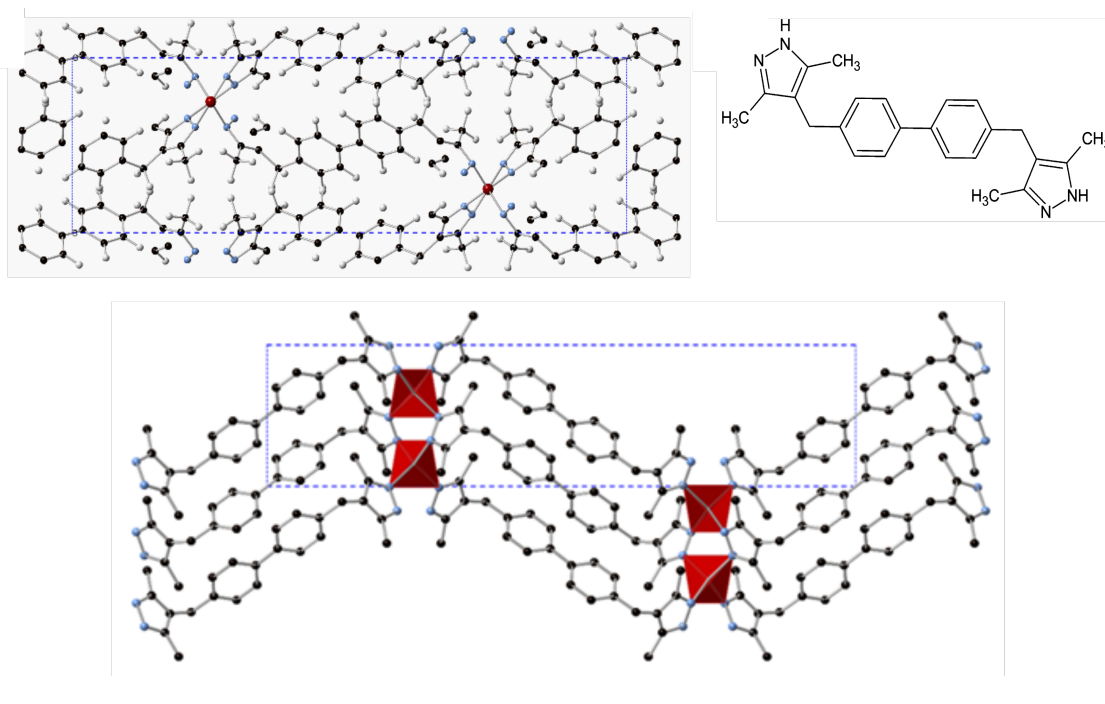


FIGURE 8.1: View along cell vector  $c$  showing unit cell; protonated H2DMPMB ligand structure; view along cell vector  $b$  showing metal coordination environment and infinite network

molecular crystal to better assess the extent of interligand interaction that arises from both  $\pi$ - $\pi$  stacking and hydrogen bonding interactions.

In order to qualitatively evaluate the emission energy from the triplet state, periodic calculations were also conducted using the SPINLOCK feature of Crystal14, allowing one to fix the difference between the number of alpha and beta electrons. This difference was set to 8 to simulate a triplet excited state centred on the 4 ligands present in the unit cell. After the optimisation of this excited state, a single point calculation was conducted for the singlet state while retaining the geometry of the triplet electron configuration in order to quantify the vertical energy gap between the singlet and triplet potential energy surfaces at this point.

All calculations on molecular clusters were conducted using Gaussian 09. [79] Calculations were performed on a cluster cut from the periodic structure of each of the M[DMPMB] ( $M = \text{Zn}, \text{Cd}$ ) systems previously optimized at PBE0 level of theory. Each cluster consists of two metal ions bridged by two DMPMB ligands, with an additional 4 ligands used to complete the metal coordination sphere and terminate the cluster. Hydrogen atoms were added to the uncoordinated pyrazole groups, as shown in figure 8.2. TD-DFT calculations were performed in order to calculate the vertical excitation energies and associated oscillator strengths of these clusters. All calculations were again performed with the 6-31G(d) Pople double zeta basis set for all non-metal atoms while the Los Alamos (LANL2) [136] effective core pseudopotential and corresponding double zeta valence basis set were used

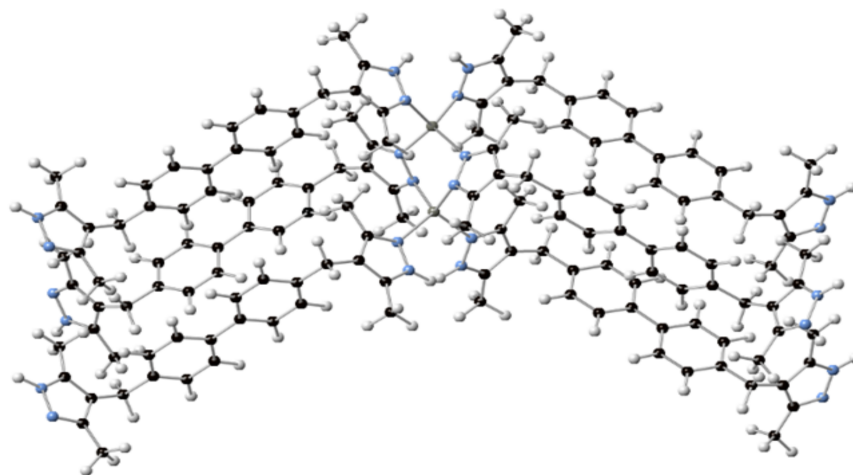


FIGURE 8.2: Cluster model taken along the 1D inorganic chain within M[DMPMB] used for TDDFT calculations showing metal cation (red), coordinating nitrogen atoms (blue) and organic linker with carbon (black) and hydrogen (white).

to describe the cadmium and zinc atoms. The same technique as described above for periodic calculations, while holding the uncoordinated (i.e. extended) nitrogen atoms fixed, was also used to assess the singlet-triplet energy gap and, in turn, validate the cluster model used to describe the solid state framework. Additionally, the  $S_1 \rightarrow S_0$  emission energies of the  $H_2DMPMB$  ligand were calculated by optimising its first singlet excited state geometry at TDDFT level for both the free ligand and with the nitrogen atoms constrained to the positions of the calculated MOF structures.

Absorption spectra have been presented as a combination of convoluted Gaussian functions with full width at half maximum height set to 0.3 eV centered at each excitation energy. Computed oscillator strengths are reported in the same figure as vertical lines.

## 8.3 Results and Discussion

### 8.3.1 Density Functional Performance

We first performed full energy-minimization of the  $Zn(DMPMB)$  and  $Cd(DMPMB)$  periodic structures, including both atomic coordinates and unit cell parameters, with our test set of functionals. Figure 8.3 shows the absolute error obtained for the  $a$ ,  $b$ , and  $c$  lattice parameters at the ground state for both  $Zn(DMPMB)$  (in blue) and  $Cd(DMPMB)$  (in green). While it is clear that, from the small absolute error relative to the experimental data, all functionals tested perform well in the description of the lattice geometry, the solid-state-tuned PBEsol functional performs best in the prediction of each lattice vector, followed by the PBE0 functional, for both materials.

Figure 8.4 shows the percentage error in the calculated metal coordination environment

relative to the experimental data, again using the functional test set mentioned above, at the ground state. The ability of a given functional to characterize the first coordination sphere of the metal centers was evaluated using two criteria: the error in i) nitrogen-metal-nitrogen coordination angles and in ii) the bond distance between the metal centres and coordinating nitrogen atoms. As with the lattice parameters, the data show that all functionals perform within a low margin of error for all parameters tested across both structures (maximum of 4.0% ( $4.4^\circ$ ) for BLYP GGA functional when calculating coordination angles). Surprisingly, given its remit, the PBEsol functional appears to give no appreciable increase in accuracy when calculating either bond lengths or angles and all functionals deliver a similar performance with no single level of theory standing out, in this case, as superior. Furthermore, there is no discernible difference in performance between hybrid and GGA functionals for the calculation of these structural features. From this it can be concluded that, for these MOF systems, the metal coordination environment is not very sensitive to the functional chosen given that GGAs, hybrids and a solids-optimised functional all performed similarly and were able to predict the coordination geometry of the metal sites with sufficient accuracy. Generally, hybrid functionals (such as PBE0 or B3LYP) slightly outperform GGAs. The lack of sensitivity of the coordination environment to the choice of functional and general good performance of all those tested rendered this an unimportant factor in the choice of functional and level of theory to be used in excited state calculations. For this reason, PBE0 was chosen for excited state calculations since it gave results of a similar quality to the PBEsol functional for structural parameters and as it is known to perform well on a broad range of systems within TD-DFT calculations [99, 137]. To test if charge transfer would play a significant role, vertical absorption energies for the Zn MOF were also calculated using the long-range corrected CAM-B3LYP functional, which is known to correctly treat both valence and charge transfer excitations [26]. Results shown in appendix 16 show no qualitative difference with respect to those calculated with PBE0 and we will thus only present and discuss the results obtained with PBE0 here. Given the importance of inter-ligand interactions in MOFs, significant dispersion interactions effects can be important in the prediction and characterization of luminescence phenomena. [109]

In light of this, the PBE0 functional was taken forward in order to investigate the effects of inter-ligand interaction of H<sub>2</sub>DMPMB, via the incorporation of dispersion interactions using an empirical pairwise potential as proposed by Grimme [77] (the corresponding results being labelled as PBE0-D2). The results are summarized in table 8.1. The H<sub>2</sub>DMPMB molecular crystal was chosen as a relevant test case as there are two potential inter-ligand interaction types within its structure: i) intermolecular hydrogen bonds between the hydrogen and nitrogen atoms located on the pyrazole moieties and ii)  $\pi$ - $\pi$  stacking between the biphenyl parts. Table 8.1 shows that the inclusion of the dispersion interactions roughly halves both the error in the hydrogen bond interaction, here monitored by the pyrazole nitrogen to nitrogen intermolecular distance (1.35% to 0.55%), and the  $\pi$ - $\pi$  stacking distance (5.06% to 2.88%), with a small increase in error with respect to the primitive cell volume (0.38% to 0.71%) and density (0.33% to 0.64%). This slight loss of accuracy with respect to the cell volume and density can be attributed to the tendency of the Grimme correction scheme to overestimate

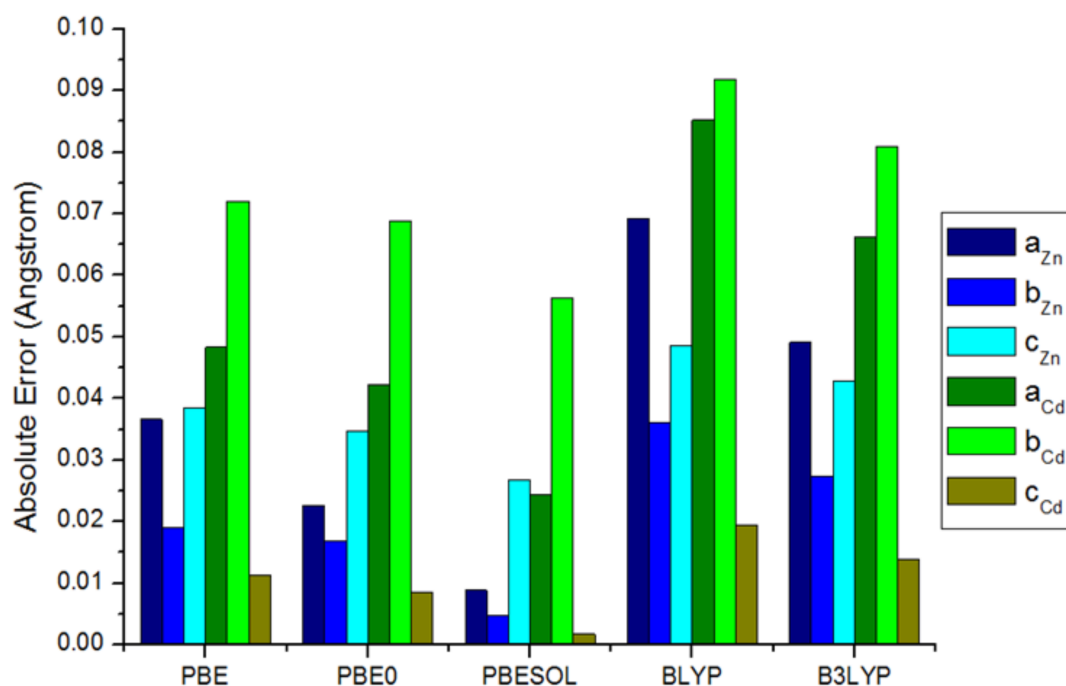


FIGURE 8.3: Histogram showing absolute error (in Å) in calculated lattice vectors relative to experimental data. Results obtained for Zn(DMPMB) and Cd(DMPMB) are represented as blue and green bars, respectively

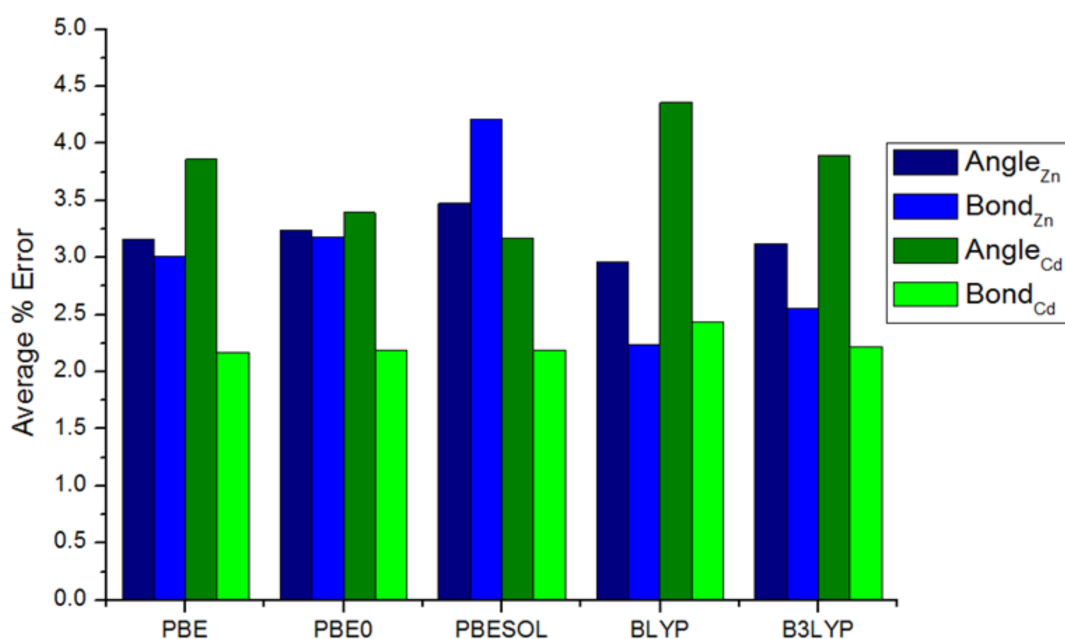


FIGURE 8.4: Histogram showing average percentage error in calculated coordination angles and coordination bond distances relative to experimental data. Results obtained for Zn(DMPMB) and Cd(DMPMB) are represented as blue and green bars, respectively.

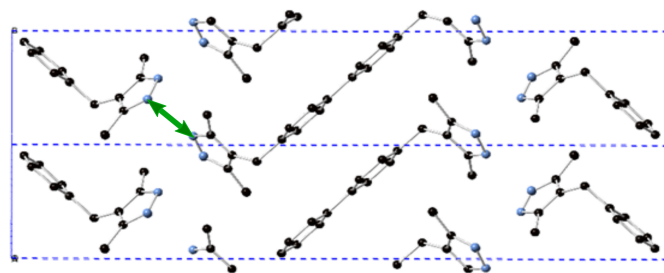


FIGURE 8.5: Structural view of 2 adjacent unit cells of  $H_2DMPMB$  ligand molecular crystal. Hydrogens are omitted for clarity. Green arrow indicates hydrogen bond distance defined via intermolecular nitrogen distance.

the long-range electron correlations that are responsible for intermolecular van der Waals forces. At first, it seems strange that the stacking distance is underestimated by the PBE0 functional alone (without dispersion correction) – suggesting that the PBE0 functional itself overestimates these interactions – but this is an indirect effect, due to the hydrogen bonding between ligands being poorly represented. Indeed, looking at the two-dimensional, layered structure of the molecular crystal figure 8.5, weaker hydrogen bonding interactions allow the coordinating pyrazole groups to spread further apart and, in turn, reduce the distance between biphenyl moieties. The introduction of the dispersion interactions better describes both the hydrogen bonding and  $\pi$ - $\pi$  stacking, pulling the ligands closer together at the pyrazole parts and further apart with respect to the biphenyl groups. This effect is rooted in the two-dimensional nature of the molecular crystal and is not a result of the PBE0 functional somehow overestimating the inter-ligand stacking interactions between biphenyl groups with respect to the addition of dispersion interactions.

### 8.3.2 Absorption and Fluorescence

Figure 8.6 shows the calculated vertical absorption spectra previously described using cluster models of the cadmium and zinc MOFs (as shown in figure 8.2) along with calculated absorption and emission spectra of the free ligand. The calculated absorption spectrum for the free ligand shows one, single band located at 259 nm. This band corresponds to a  $\pi$ - $\pi^*$  transition centred on the biphenyl moiety. All computed vertical transition energies are explicitly reported in the Supporting Information.

Overall, the spectra of the three compounds are actually dominated by this intense ligand centred (LC) transition which is only slightly tuned by the MOF environment. Importantly, at least for singlet-to-singlet transitions, no other “bright” transitions were computed within the energy range of interest. Here, a “bright” transition is deemed to be a transition with a calculated oscillator strength significantly greater than zero. As for the free ligand, for the zinc and cadmium MOF clusters an absorption band of  $\pi$ - $\pi^*$  character corresponding to the biphenyl-centred excitation of the ligand was determined and agrees well with the absorption band calculated for the free ligand itself at 264 nm.

TABLE 8.1: Calculated and experimental values of key structural parameters investigated on the H<sub>2</sub>DMPMB ligand molecular crystal. Nitrogen-to-Nitrogen intermolecular distance is defined as that between closest neighboring nitrogen atoms in the crystal and taken as a measure of intermolecular hydrogen bond features.

| Functional                         | PBE0   | PBE0-D2 | Experimental |
|------------------------------------|--------|---------|--------------|
| Nitrogen-Nitrogen distance (Å)     | 2.935  | 2.912   | 2.896        |
| Unit Cell Volume (Å <sup>3</sup> ) | 1017.3 | 1006.2  | 1013.4       |
| Density (g/cm <sup>3</sup> )       | 1.209  | 1.222   | 1.213        |
| Stacking Distance (Å)              | 3.658  | 3.742   | 3.853        |

Now we shall consider the emission properties of these materials. Experimentally, the photoluminescence has been ascribed to LC states, which is consistent with the fact that the LC computed transition is the only bright transition dominating the spectra of the compounds. Nevertheless, the origin of the large shift observed in emission going from the Zn to Cd based MOF it is not obvious or clear. To clarify this point - following the reasoning which supposes a LC emission - the emission energies for the M[DMPMB] clusters and H<sub>2</sub>DMPMB ligand were computed and they are reported, along with those derived from experiment [129], in Table 2 Note that the determination of the emission energy from the singlet excited state (S1→S0) (calculated via the full optimisation of the S1 excited state geometry) was undertaken for the free ligand only, while the energy of the phosphorescence (T1→S0) was determined as described in the computational details section.

The emission wavelength from the singlet  $\pi$ - $\pi^*$  excited state of the free ligand was calculated at 332 nm. Fixing the nitrogen atom positions constrained in the coordination geometry for both Zn[DMPMB] and Cd[DMPMB], the same calculations of the emission wavelength from the singlet  $\pi$ - $\pi^*$  excited state were undertaken to decouple any perturbative effects of the metal with those of the geometrical constraints imposed on the ligand by the metal within the MOF structures. It was found that this geometrical constraint had little effect as shown by both the calculated absorption and emission values for the ligand with constrained nitrogen on the pyrazole groups corresponding to the optimized solid-state structures for Zn[DMPMB] (4.44 eV -279 nm- absorption; 3.78 eV -328 nm- emission) and Cd[DMPMB] (4.48 eV -277 nm- absorption; 3.79 eV -327 nm- emission). Comparing the calculated emission energy for the free ligand or the ligand constrained at Cd[DMPMB] geometry (332 nm and 327 nm, respectively) and the experimentally observed emission value for the Cd[DMPMB] species (3.70 eV, 335 nm), it is clear that the emission from the cadmium based MOF can be ascribed confidently to a ligand centred transition, as previously predicted in the experimental work [129]. This is also shown pictorially in figure 8.6. Upon comparing the calculated emission energy from the singlet  $\pi$ - $\pi^*$  excited state of the free ligand or the ligand constrained at Zn[DMPMB] geometry (332 nm and 328 nm, respectively) and the experimental emission energy for Zn[DMPMB] (2.81 eV, 441 nm) it is clear that the

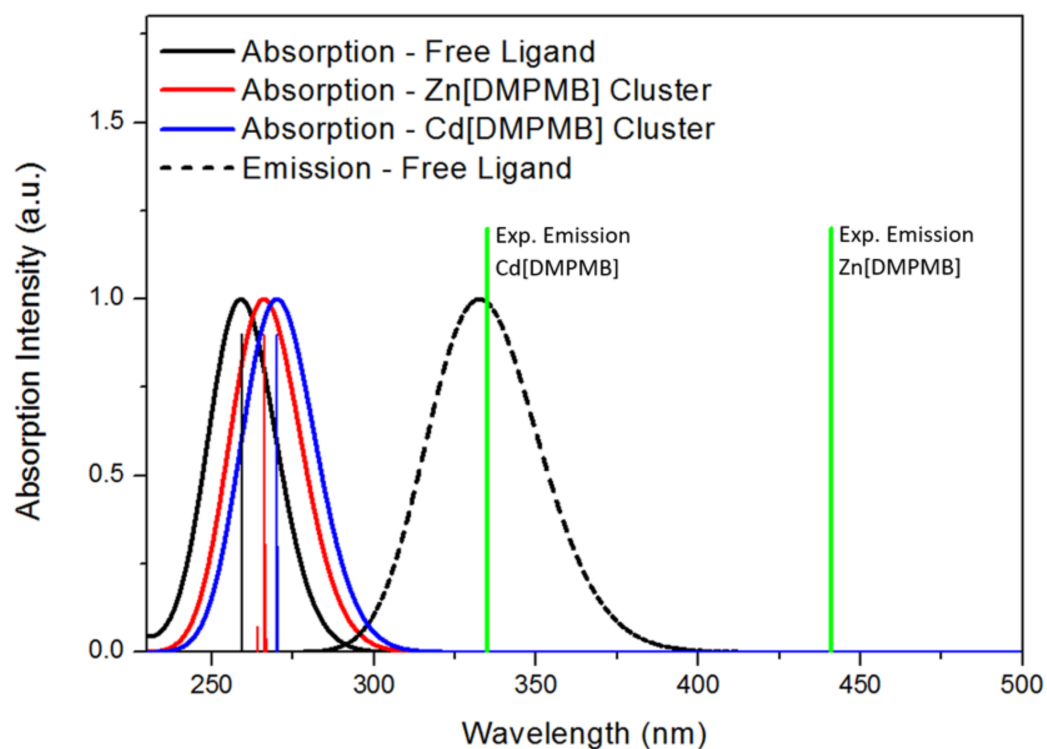


FIGURE 8.6: Calculated absorption spectra for clusters of Zn[DMPMB] and Cd[DMPMB] along with simulated absorption and emission spectra for the free H<sub>2</sub>DMPMB ligand. The wavelength of the experimentally observed emission maxima for both MOF species are also indicated. *a* and *b* indicate experimental excitation wavelengths of 254 and 365 nm, respectively.

emission shown by the zinc based MOF is not adequately explained by ligand centred emission from the singlet excited state. Furthermore, as seen above, accounting for the geometrical constraints imposed by coordination environment in Zn[DMPMB] does not account for this shift in emission energy with respect to the free ligand. Lastly, given the experimental excitation energy used in the case of Zn[DMPMB] (3.40 eV), it is unlikely that the emission observed in this MOF is a result of the same process as that observed for Cd[DMPMB] since the  $\pi$ - $\pi^*$  ligand centered excited state is predicted to be higher - vertically - than the excitation energy experimentally used (computed at 264 nm).

### 8.3.3 Phosphorescence in Zn[DMPMB]

If the Zn[DMPMB] emission does not stem from the ligand-centred singlet  $\pi$ - $\pi^*$  state, we are left with the option of this luminescence behaviour resulting either from another singlet excited state (fluorescence ( $S_1 \rightarrow S_0$ )) that can be accessed using the experimental absorption energy of 3.40 eV or from the triplet  $\pi$ - $\pi^*$  excited state (phosphorescence ( $T_1 \rightarrow S_0$ )) centred on the ligand.

As previously discussed for the absorption spectra of the Zn and Cd MOF clusters, there are no other singlet excited states with appreciable oscillator strength that lie within the required energy region and therefore are not likely to be at the origin of the intense photoluminescence properties observed for the Zn MOF. Therefore an emission from the triplet, which has been observed in other d10 metal-organic complexes [138, 139] could provide a reasonable explanation for the difference in fluorescence behavior between the zinc and cadmium based MOFs. Using the cluster approach, the triplet excited states were vertically computed from the ground state Zn and Cd MOF geometries at 378 and 371 nm, respectively. Therefore upon irradiation at 365 nm, as in experiment, this state can be populated. Indeed, although this type of transition is spin forbidden, the presence of metal ions allows their efficient population through spin-orbit coupling.

In addition to the emission energies from the singlet  $\pi$ - $\pi^*$  state, the emission energies from the triplet  $\pi$ - $\pi^*$  of the free ligand and Zn and Cd MOFs were also estimated using the previously described methodology, and these are shown, along with fluorescence data, in table 8.2. From an electronic density-difference plot ( $\rho_\alpha - \rho_\beta$ ) (figure 8.7), it can be seen that this triplet excited state is indeed centred on the biphenyl moiety of the ligand. The emission from the triplet excited state of the free ligand was found to be significantly red shifted (with respect to the singlet emission energy) at 554 nm (2.24 eV). The emission energies estimated from the triplet excited states of the constrained ligand geometries were found to be slightly blue shifted with respect to the free ligand (522 nm; 2.38 eV) for both Cd[DMPMB] and Zn[DMPMB]. Furthermore, phosphorescence wavelengths from the  $\pi$ - $\pi^*$  state were calculated using both cluster (figure 8.2) and periodic models. Beginning with the cluster model for Zn[DMPMB], a blue shift of 0.27 eV is observed relative to the free ligand phosphorescence from the  $\pi$ - $\pi^*$  state while a slightly smaller blue shift of 0.17 eV is determined via periodic calculations. For Cd[DMPMB], a smaller blue shift of 0.01 eV

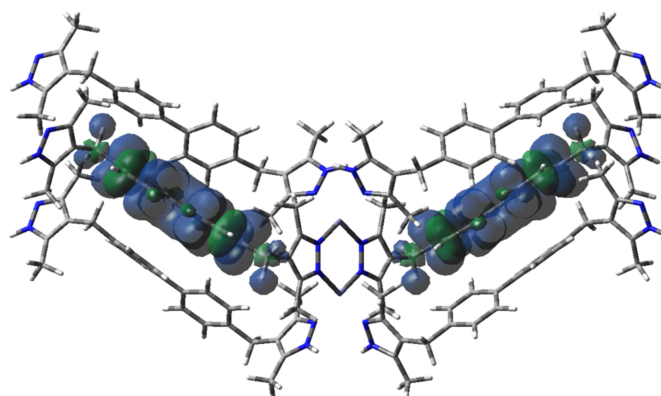


FIGURE 8.7: Spin density difference plot ( $\rho_{\alpha} - \rho_{\beta}$ ) computed for the first triplet state (T1) of the Zn[DMPMB] cluster.

is determined using the cluster model. From this, the effect of the environment is clearly observed on the emission energy from the triplet  $\pi$ - $\pi^*$  excited state.

Considering the emission energy observed in experiment and the calculated energy difference between the T1 and S0 surfaces for the Zn[DMPMB] cluster at the optimized T1 geometry, the results are comparable (2.50 eV calculated, 2.81 eV in experiment). This leads to the conclusion that the emission observed for the zinc compound could, indeed, also be a result of phosphorescence from a  $\pi$ - $\pi^*$  triplet excited state. It is also worth noting that, according to calculations conducted using PBE0, there is no appreciable change in coordination geometry between the optimised singlet ground state and triplet state of either MOF.

Finally, the small discrepancy between the T1  $\rightarrow$  S0 energy values calculated using the cluster model and periodic calculations (0.09 eV for Zn[DMPMB]; 0.059 eV for Cd[DMPMB]) allows one to conclude that the cluster model used to determine absorption energies via TDDFT calculations is sufficiently accurate. This also illustrates that these excitations are local processes in MOFs and could validate further use of similar cluster models to study excited state processes not only in metal-organic frameworks but in other photo-active materials.

TABLE 8.2: Calculated main absorption and emission energies for H<sub>2</sub>DMPMB, Zn[DMPMB] and Cd[DMPMB] along with experimental data. Calculations were also conducted holding the position of the nitrogen atoms of the ligand constrained to that computed at the ground state at PBE0 level for Zn[DMPMB] and Cd[DMPMB], labelled constrained N<sub>Zn</sub> and constrained N<sub>Cd</sub> respectively.

| Model   | Calculated           |                     |                     | Experimental        |
|---|----------------------|---------------------|---------------------|---------------------|
|   | $\lambda_{abs}$ (nm) | $\lambda_{em}$ (nm) | $\lambda_{em}$ (nm) | $\lambda_{em}$ (nm) |
|   | S0→S1                | S1→S0               | T1→S0               |                     |
| H <sub>2</sub> DMPMB (Free)                         | 285                  | 332                 | 554                 | -                   |
| H <sub>2</sub> DMPMB (Constrained N <sub>Zn</sub> ) | 279                  | 328                 | 522                 | -                   |
| H <sub>2</sub> DMPMB (Constrained N <sub>Cd</sub> ) | 277                  | 327                 | 522                 | -                   |
| Cd[DMPMB] (Cluster)                                 | 269                  | -                   | 520                 | 335 <sup>a</sup>    |
| Cd[DMPMB] (Periodic)                                | -                    | -                   | 515                 |                     |
| Zn[DMPMB] (Cluster)                                 | 266                  | -                   | 495                 | 441 <sup>b</sup>    |
| Zn[DMPMB] (Periodic)                                | -                    | -                   | 514                 |                     |

## 8.4 Conclusions

The key conclusions for this chapter are outlined below:

- We have outlined a cluster-based protocol for the computation of luminescence properties of metal organic frameworks, which has been used to discriminate between the different emission behavior of two iso-structural transition-metal based Zn and Cd MOFs.
- With this protocol, we were able to identify that Cd[DMPMB] emission results from ligand-centered emission from the first singlet excited-state, whereas Zn[DMPMB] emission likely results from ligand-centered emission from the first triplet excited-state.
- We observed that using periodic boundary conditions had a minimal effect on phosphorescence properties, suggesting that such properties may be modeled locally using clusters.

Rational design of useful optical properties within metal-organic frameworks is a subject of ever increasing attention in recent years with theoretical approaches poised to play a key role alongside experiment in the understanding further development of high performance materials. We have demonstrated a computational protocol rooted in quantum mechanical calculations at DFT and TD-DFT level able to successfully discriminate between subtle luminescence mechanisms in a pair of isostructural MOFs with interchangeable metal cations. This pair of systems is a novel example of tuneable luminescence in MOFs with an approximately 0.88 eV (441 nm to 335 nm) blue shift going from the zinc based to cadmium based structure. This method was able to confirm the higher energy emission seen from the cadmium-based structure is a result of a ligand-centred emission from the singlet  $\pi$ - $\pi^*$  excited state. The luminescence behavior resulting from the zinc-based structure was found to be more complex, with luminescence possibly resulting from both the triplet  $\pi$ - $\pi^*$  excited state (localised on the ligand). The effectiveness of this protocol in the discrimination of excited state processes in MOFs at relatively low computational cost can be a valuable tool in the design and understanding of high performance optical materials.

## Chapter 9

# Additional Concerns in Condensed-Phase Modeling: Spin-State Ordering in Transition Metal Complexes

### 9.1 Introduction

Up until this point, we have explored several examples of how excited-state phenomena can be influenced by environmental effects using density functional theory coupled with a charge embedding procedure. Generally, we have demonstrated how sensitivity to the environment can govern certain photophysical processes and that proper account of long-range electrostatics is crucial for their recovery. In this chapter, we move away from the concept that interactions in the condensed-phase are the primary concern, introducing challenging cases for DFT and how these may be modeled. In chapter 2, we introduced the concept of static electron correlation and how intrinsically single-reference (single-determinant) methods such as DFT can fail in the description of electronic structure when such concepts are important. Due to this inherent failure, the addition of an embedding method - however developed - cannot possibly improve upon computed properties.

One area where the incorporation of multi-reference methods can be crucial is the accurate description of bonding and spin state energetics in molecular complexes (and indeed metal-organic solids) containing transition metals with partially-filled d-shells. For the understanding and prediction of catalytic reactivity [140, 141], including biological reactions, and magnetic properties [142–144], accurate quantum-mechanical models are essential, yet these are often hindered by the near-degenerate nature of the metal-centered frontier orbitals which can introduce significant multi-reference character. As a result, the quantitative calculation of spin-state ordering in transition metal complexes has been repeatedly highlighted as a significant challenge for modern computational methods [145, 146]. Within this context, Density functional Theory, within the Kohn-Sham formalism (KS-DFT), suffers from its ever-present sensitivity to the chosen approximation of the exchange-correlation

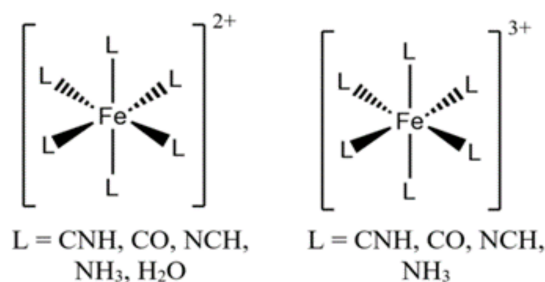


FIGURE 9.1: Model complexes considered in this study.

energy. Local approximations (LDA or GGA) are biased towards low-spin ground states due to their over-delocalisation of bonding molecular orbitals [147, 148]. This can be countered by the admixture of Hartree-Fock (HF) exchange present in hybrid density functionals, which are known to favor high-spin ground states [149, 150]. The optimal fraction of HF exchange, however, is case-dependent and has been shown to depend strongly on the ligand field [150], with commonly-used functionals, such as B3LYP [76] and PBE0 [22] regularly failing to predict the ground spin-state configuration of such compounds. Recently, an investigation into the effect of meta-GGA exchange, which depends on the Laplacian of the density, demonstrated that meta-GGA exchange favours high-spin states in strong-field ligands and low-spin states in weak-field ligands [151]. Additionally, due to the intrinsic multi-configurational nature of several of the spin states computed, a balanced and controlled description of static and dynamic correlation is required, which may be problematic for several of the approaches mentioned above.

More consistent results have been obtained with methods rooted in wave function theory (WFT), such as the complete active space self-consistent field [29] (CASSCF) approach. However, CASSCF energies usually require a correction to recover dynamic correlation energy not accounted for outside of the chosen active space, often added via multi-reference perturbation theory, such as CASPT2 [152]. Methods which approximate dynamic correlation based on multi-configurational reference functions are, however, generally limited to small- to medium-sized systems. A systematic application of these methods is conditional upon their ability to handle medium- to large-sized systems, and the computational expense required for this latter step often presents a significant bottleneck.

The recently-developed Multi-Configurational Pair Density Functional Theory [30] (MC-PDFT, see chapter 2) approach, which seeks to combine the advantages of WFT and DFT, presents a promising alternative to CASPT2 and requires significantly less computational effort [153]. The formulation of MC-PDFT exhibits two key differences with respect to KS-DFT: i) the reference wave-function is multi-configurational in nature and ii) a given density functional depends on both the total density and the on-top pair density. Furthermore, MC-PDFT has been recently extended to work with generalised-active-space multi-configurational wave functions [154], promising further reduced computational time and, in turn, access to yet larger and more complex systems.

TABLE 9.1: Basis sets used in MCSCF calculations.

| Atom            | Contraction    |
|-----------------|----------------|
| Fe              | [7s6p5d3f2g1h] |
| N, O, C (donor) | [4s3p2d1f]     |
| H               | [3s1p]         |

In this light, we decided to test the performance of MC-PDFT on the prediction of spin-state ordering and check if it offers any improvement over KS-DFT methods. To this end, we tested MC-PDFT on 9 model Fe(II) and Fe(III) complexes with five ligands of diverse ligand-field strength, shown in figure 9.1. We shall compare the performance of this method with both CASPT2 and KS-DFT results for a wide range of density functionals. Additionally, we investigated the dependence of CASPT2 and MC-PDFT on the size of the active-space. [155]

## 9.2 Computational Details

MC-PDFT calculations are performed using a set of four on-top density functionals, two of which are based on the PBE [21] exchange-correlation functional, which has no empirical parameters, with the other two based on revPBE [156], a modified form of PBE where one parameter is altered to improve agreement of atomic exchange energies with known exact results. In order to allow compatibility with MC-PDFT, PBE and revPBE are ‘translated’ in order to introduce a dependence on the on-top density. In the present paper, we test two translation procedures previously proposed in literature [32]. They are based on the on-top and spin densities for a broken-symmetry slater determinant [157] (hereafter labelled t) or on a ‘full’ translation (ft) which also introduces a dependence on the on-top density gradient. The resulting on-top density functionals are tPBE, ftPBE, trevPBE and ftrevPBE, where the prefixes ‘t’ and ‘ft’ indicate the method of translation from KS density functionals to on-top density functionals. These functionals represent the first-generation of on-top density functionals which, in principle, could be further optimized by considering exact theoretical constraints or optimisation against experimental data.

MC-PDFT, introduced in chapter 2 represents a post-SCF correction to the MCSCF energy and therefore a converged MCSCF wave function is a prerequisite for the calculation of MC-PDFT energies. In turn, MC-PDFT inherits the intrinsic drawbacks of MCSCF such as the case-dependent choice of the active space. The on-top energy, akin to the exchange-correlation energy in KS-DFT, includes a correction to the MCSCF kinetic energy plus the exchange and correlation energy.

We calculate the spin-state ordering of the above mentioned 9 complexes using a CASSCF wave function as the MCSCF method to which post-SCF energy corrections are applied using both CASPT2 and MCPDFT. We use basis sets analogous to those previously suggested by Pierloot and co-workers [158]. An exploratory investigation of the effect of active space

size was performed and we shall refer to these as (m/m-1,n), where m (m-1) is the number of active electrons in Fe(II) (Fe(III)) active spaces and n is the number of orbitals. 5 different active spaces are considered (figure 9.2):

- (6/5,5) – Fe(II) d-orbitals
- (10/9,7) – Fe(II) d-orbitals plus two  $\sigma$ -bonding Fe-ligand orbitals
- (6/5,10) – Fe(II) d-orbitals plus a second set d-orbitals of higher angular momentum
- (10/9,12) – (6,10) plus two  $\sigma$ -bonding, eg-like Fe-ligand orbitals
- (12/11,14) – (10,12) plus Fe 3s and its corresponding antibonding orbital

The largest of these is the active space proposed by Hauser [159]. For comparison, and to underline the effects of Hartree-Fock exchange on spin state ordering, we also conducted a representative benchmark of KS-DFT functionals comprising GGA, global-hybrid and meta-GGA exchange-correlation functionals. In all cases, a  $D_{2h}$  symmetry was imposed for both geometries and energy calculations (except for complexes 4 and 9, for which  $C_i$  symmetry was used). The use of symmetry, beside a trivial gain in computational time, is justified by two main arguments: i) we wish only to compare different theoretical methods and ii) it retains consistency in the active space across different complexes with ligands of varying ligand-field strength. Generally, we shall discuss results in terms of the energy difference between high- and low-spin forms of each complex ( $\Delta E_{H/L}$ ). Positive (negative) values of  $\Delta E_{H/L}$  indicate that the low (high) spin state is energetically favoured. Additionally, we refer to the difference in  $\Delta E_{H/L}$  computed for different ligands, with strong-field ligands expected to produce higher values of  $\Delta E_{H/L}$  than weak-field ligands. We consider 5 different ligands with the expected ordering  $H_2O < NH_3 < NCH < CO < CNH$ , in terms of  $\Delta E_{H/L}$ , inferred from the spectrochemical series. Additionally, based on previous diffusion Monte Carlo results from Droghetti [160] and ligand field theory, we expect Fe complexes with CNH and CO to have low-spin ground states and complexes with NCH,  $NH_3$  and  $H_2O$  to have high-spin ground states.

All KS-DFT calculations were conducted using Gaussian 09 [79]. Geometry optimisations were conducted using KS-DFT with the PBE0 exchange-correlation functional and TZVP basis set by Ahlrichs [161], with which vibrational frequency calculations were also performed to ensure the resulting geometries correspond to true minima. Using these geometries, single-point calculations for each density functional tested were conducted using the def2-QZVPP basis set previously suggested by Neese [162].

CASSCF, CASPT2 and MC-PDFT were conducted using a locally modified version of Molcas 7.9 [163]. We employ the default IPEA shift of 0.25 au and an imaginary level shifter of 0.10 au. All calculations made use of the ANO-RCC basis set – including relativistic effects via the standard second-order Douglas-Kroll-Hess Hamiltonian [164–167] – with the contraction schemes suggested by Pierloot [158] outlined in table 9.1. All MCSCF calculations

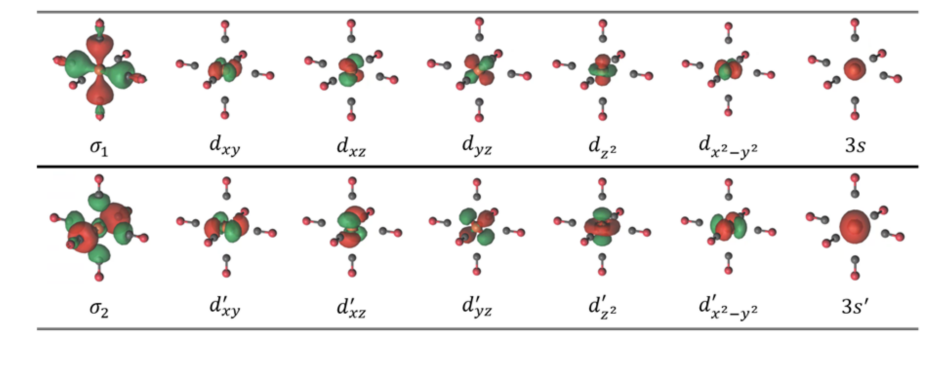


FIGURE 9.2: Example of the orbitals used in active spaces in this work, here shown using  $[\text{Fe}(\text{CO})_6]^{2+}$ . Five different active spaces, which represent various combinations of these orbitals, are used in total.

were performed at the PBE0 structures obtained at KS-DFT level – a strategy previously suggested by Pierloot and Vancoillie [158].

## 9.3 Results and Discussion

### 9.3.1 A Representative Benchmark with DFT

Figure 9.3 shows the results of the KS-DFT approaches, with CASPT2 (active space (12,11/14)) results shown as horizontal lines for comparison. Generally, for Fe(II) complexes, local functionals (i.e. with no explicit HF exchange) qualitatively reproduce the expected ordering of  $\Delta E_{H/L}$  with respect to the ligand-field strength. GGA functionals, such as BP86 [133, 168] and BLYP [133, 134], systematically overestimate  $\Delta E_{H/L}$  with respect to CASPT2, with the exception of OPBE which reduces the overestimation for all ligands and underestimates  $\Delta E_{H/L}$  for  $\text{H}_2\text{O}$  by 10 kcal/mol. For meta-GGA functionals, such as VSXC [169] and TPSS [170], we recall the trend recently outlined by Kulik [151], with a systematic underestimation (overestimation) of  $\Delta E_{H/L}$  for strong (weak) field ligands. M11-L [171] and MN15-L [172], despite being meta-GGA, represent outliers in this case. M11-L significantly overestimates  $\Delta E_{H/L}$  for all ligands, with the effect more severe for weak-field ligands. Conversely, MN15-L systematically underestimates  $\Delta E_{H/L}$  for all ligands, this time with strong-field ligands affected more significantly. No local functional is able to predict the correct ground state for every ligand, although M06-L returns the best performance, able to correctly predict a singlet ground state for CNH and CO ligands and a quintet ground state for  $\text{NH}_3$  and  $\text{H}_2\text{O}$  ligands. It incorrectly predicts a singlet ground state for NCH ligands, although only by a small margin ( $\Delta E_{H/L} = 1.0$  kcal/mol) and together these results represent a mean average error (MAE) of 11.8 kcal/mol with respect to CASPT2. Indeed,  $[\text{Fe}(\text{NCH})_6]^{2+}$  is arguably the only system in this work which can be considered a true spin-crossover complex, with a  $\Delta E_{H/L}$  value of -12.84 kcal/mol calculated at CASPT2 level. All other complexes indeed present, even at CASPT2 level, very high  $\Delta E_{H/L}$  values.

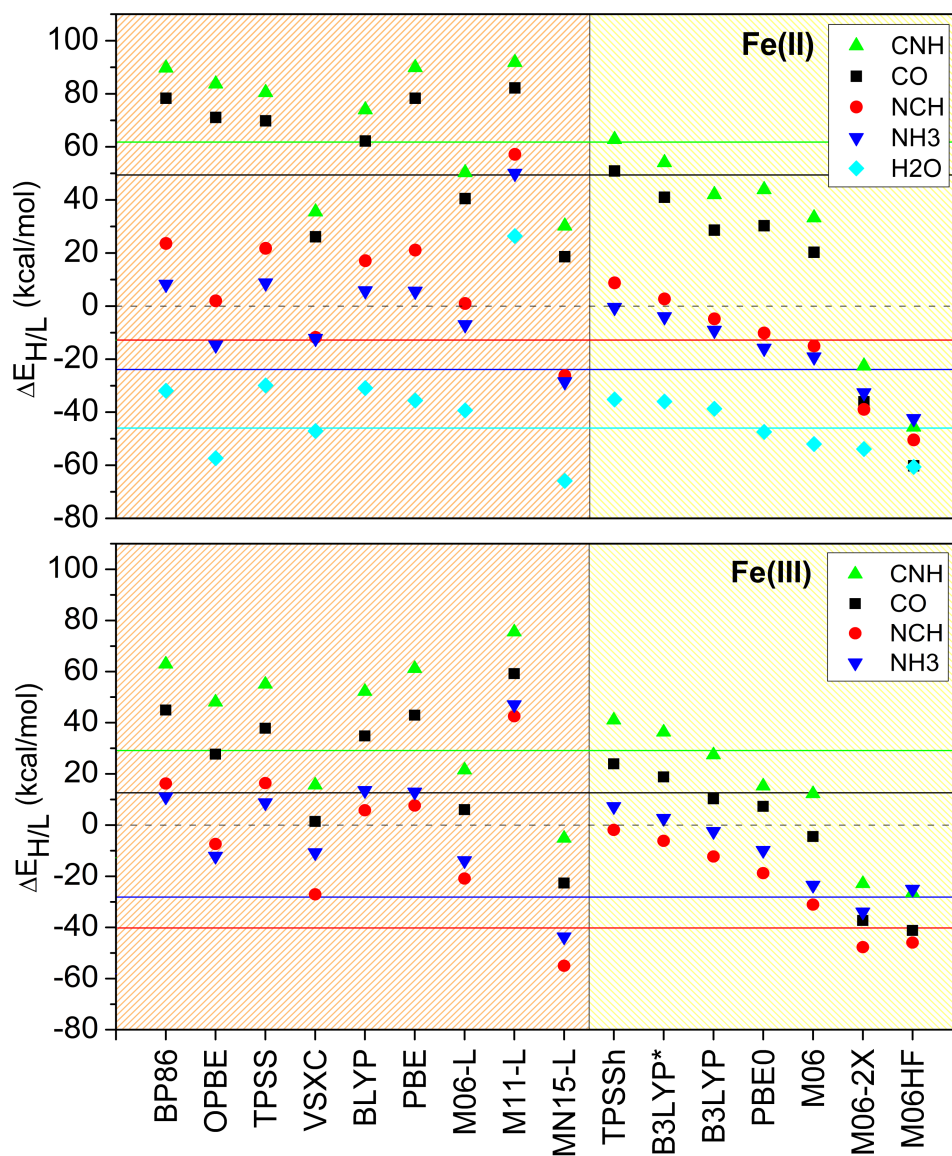


FIGURE 9.3:  $\Delta E_{H/L}$  calculated for Fe(II) (top) and Fe(III) (bottom) complexes. Region highlighted in orange includes only functionals with zero HF exchange, while the yellow region includes hybrid functionals with an ascending fraction of HF exchange (from left to right). Solid horizontal lines indicate  $\Delta E_{H/L}$  values calculated with CASPT2 (active space (12/11,14)) for each complex.

The section highlighted in yellow in figure 9.3 contains hybrid functionals ordered by ascending percentage of HF exchange. As expected, mixing HF exchange with otherwise pure functionals systematically reduces  $\Delta E_{H/L}$  as high-spin states are stabilised. This is exemplified in the comparison between the PBE and PBE0 functionals, the latter containing 25% HF exchange. We also note that the introduction of HF exchange induces greater high-spin stability in strong-field ligands than in weak-field ligands, echoing previous observations [150]. This can be rationalised via the different types of ligand-to-metal bonding present in each complex. Ligands which are good  $\pi$ -acceptors (CNH, CO) are most affected by introducing HF exchange. As the self-interaction error is reduced in orbitals of  $\pi$ -symmetry, the bonding metal-to-ligand  $\pi$ -orbitals are destabilized and the overall ligand-field strength is reduced, resulting in lower values of  $\Delta E_{H/L}$ . Conversely, ligands which are good  $\pi$ -donors (NCH, H<sub>2</sub>O) are less affected due to the increased population of more localized, antibonding d-orbitals upon ligand-to-metal donation. Lastly, ligands which only participate in  $\sigma$ -donation (NH<sub>3</sub>) are the least affected by the introduction of HF exchange, due to the more local nature of the  $\sigma$ -symmetry bonding orbitals.

Additionally, we note that the introduction of HF exchange seems to mostly override other contributing factors to  $\Delta E_{H/L}$ , with a clear trend towards high-spin stability observed in functionals with increasing HF exchange. The near-constant slope in  $\Delta E_{H/L}$  observed going from TPSSh [170] to PBE0 (representing an interval of 10-25% HF exchange in increments of 5%) is indicative of the near-insensitivity of this quantity to other parameters. For functionals with very high levels of HF exchange, such as M06-2X [173] and M06-HF [174], this relationship seems to break down. Not only do we observe the loss of the linear relationship between  $\Delta E_{H/L}$  and %HF, but the disproportionate stabilisation of high-spin states for strong-field ligands results in a different ordering of  $\Delta E_{H/L}$  for different ligands, when compared with both the spectrochemical series and calculations at CASPT2 level.

Moving on to Fe(III) complexes, we observe a similar overestimation of  $\Delta E_{H/L}$  for local GGA functionals with respect to CASPT2. This overestimation, particularly for weak-field ligands, is again minimised in OPBE, which correctly predicts the doublet (sextet) ground state for CNH and CO (NCH and NH<sub>3</sub>) ligands. The substitution of the PBE exchange functional for O [175] exchange, which constitutes an improvement over Becke's GGA exchange functional by a single-parameter optimisation against exchange energies of the first and second row atoms, provides a systematic improvement in  $\Delta E_{H/L}$  calculated for all ligands and for both Fe(II) and Fe(III) complexes. This is consistent with the strong dependence of  $\Delta E_{H/L}$  on exchange, as observed for hybrid functionals, and highlights the importance of this contribution to the overall energy. We note also that it is mirrored by the previous success of the OPBE functional for the calculation of spin-state ordering in spin-crossover compounds [176]. Again, M11-L and MN15-L are outliers within this test set, with analogous behaviour to what is observed for the Fe(II) complexes. The introduction of HF exchange via hybrid functionals has a similar effect as for Fe(II) complexes, again only showing an apparent linear dependence on %HF exchange, with a breakdown at very high levels of HF exchange. Another general observation, for both Fe(II) and Fe(III) complexes, is that the

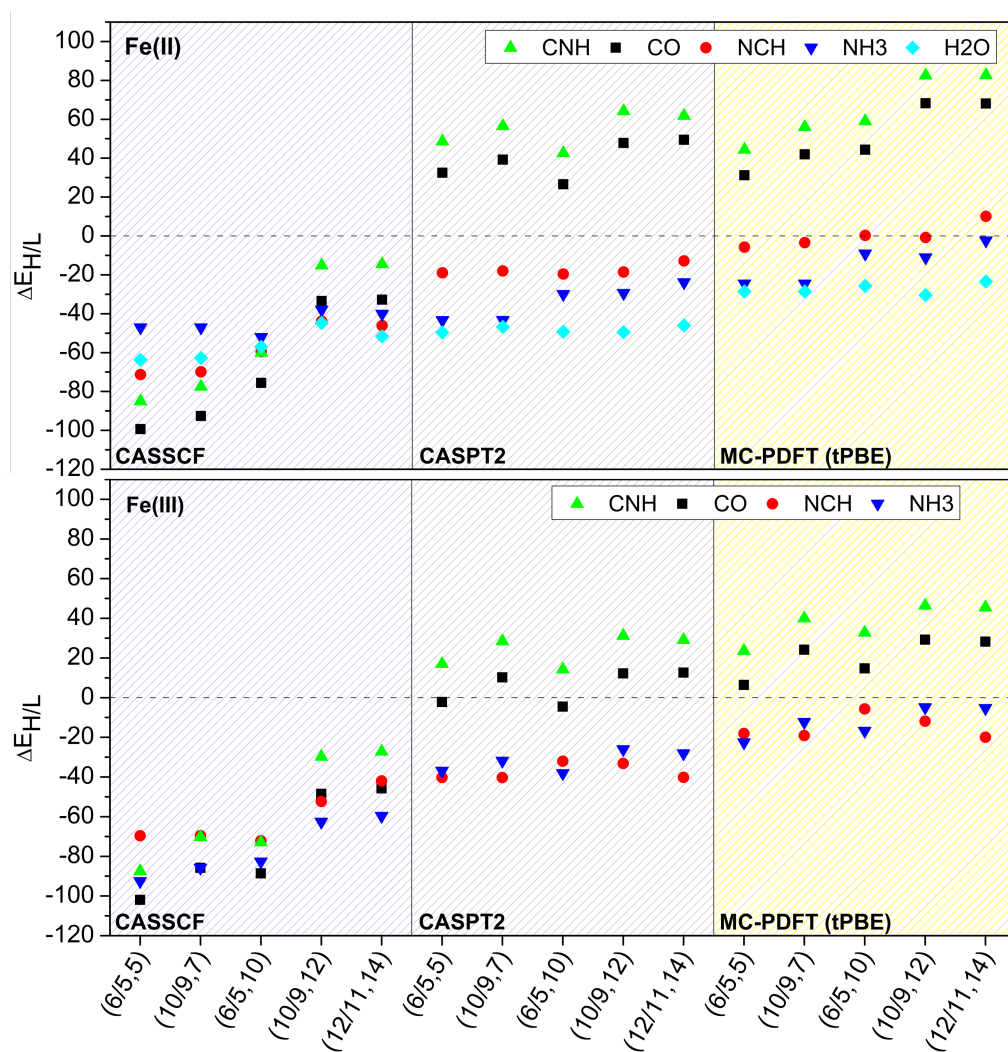


FIGURE 9.4:  $\Delta E_{H/L}$  calculated for Fe(II) and Fe(III) complexes as a function of active space size (in ascending order with respect to the number of orbitals used). Results computed with CASSCF, CASPT2 and MC-PDFT using the tPBE on-top density functional.

difference in  $\Delta E_{H/L}$  computed between each of the two strong-field ligands remains largely constant, irrespective of the functional used. The same holds true for weak-field ligands. This indicates that the true sensitivity with respect to the density functional approximation lies in the effective and balanced description of different types of metal-ligand bonding, highlighted in the ligand-dependent effect of HF exchange. These results establish that ligands which exhibit  $\pi$ -backbonding interactions with the metal (e.g. in strong-field ligands such as CO), are more affected by an increase in %HF exchange with respect to those which rely on ligand-to-metal  $\pi$ -donation or  $\sigma$ -bonding (e.g. in weak field ligands such as  $\text{NH}_3$ ). The cause for this lies in the greater tendency for orbital over-delocalisation in  $\pi$ -bonding orbitals with respect to  $\pi$ -antibonding or  $\sigma$ -bonding orbitals, which is at the heart of the apparent arbitrary performance of DFT with respect to functional formulation.

### 9.3.2 Performance of Wave Function Theory-Based Approaches

Based on these observations, the more consistent performance of WFT-based methods for the description of spin-state ordering could be attributed to a more balanced treatment of different metal-ligand bonding interactions. We expect this to hold true for CASSCF since the starting point for such calculations is the HF determinant, with the proviso that the dynamic correlation can be adequately recovered by some post-SCF procedure. For CASSCF calculations, this is usually accomplished via CASPT2 – a second order multi-reference perturbation method. CASPT2, however, is associated with a substantial computational investment which – for medium- to large-sized systems – can render this approach unfeasible. In this context, we shall now discuss the performance of the much more computationally affordable MC-PDFT approach and compare this to CASPT2. Figure 9.4 shows calculated  $\Delta E_{H/L}$  values for CASSCF, CASPT2 and MC-PDFT (with the tPBE functional) for 5 different active spaces. Straight away we note that CASSCF alone is insufficient to describe the expected spin-state ordering of both the Fe(II) and Fe(III) complexes for any active space tested. Interestingly, it appears that, while  $\Delta E_{H/L}$  is only modestly underestimated for weak-field ligands (with respect to CASPT2 values), the failure is much greater for strong-field ligands. Comparing the results of CASPT2 and MC-PDFT with respect to the active space size, we note that MC-PDFT reacts very similarly to CASPT2 upon changing the active space. Generally, introducing the eg-like  $\sigma$ -bonding orbitals stabilises low-spin states. As one might expect, this stabilisation is stronger for strong-field ligands than weak-field ligands. Interestingly, incorporation of the so-called ‘double shell’ effect [177] alone, by including Fe d-orbitals of higher angular momentum in the active space, has little effect on  $\Delta E_{H/L}$ . It is only when combined with the  $\sigma$ -bonding orbitals in the active space that a slight stabilisation of low-spin states is observed for strong-field ligands. Additionally, the inclusion of Fe 3s orbital and the corresponding antibonding orbital to the active space has little effect, with the exception of a modest stabilisation of Fe(II) complexes with weak-field ligands. This is to be expected, however, as the incorporation of these orbitals into the active space serves only to retain consistency of the active space across different systems, as outlined previously [159]. Despite minor variations, the general trend with respect to active

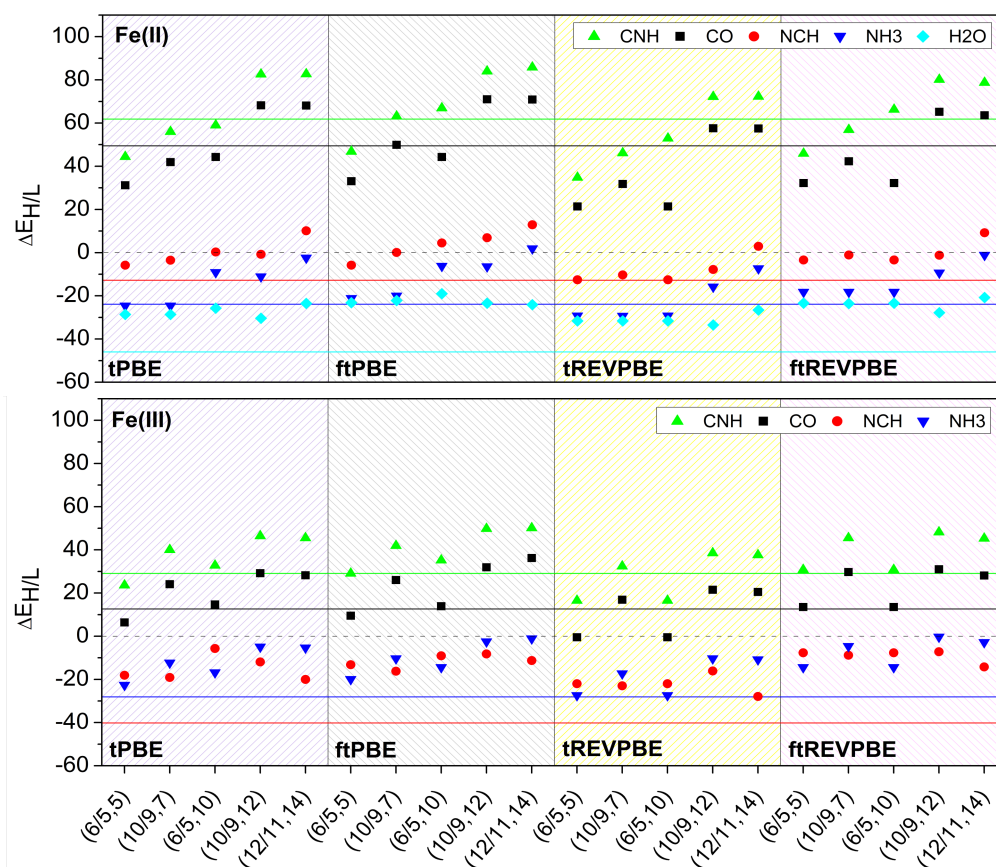


FIGURE 9.5:  $\Delta E_{H/L}$  (kcal/mol) calculated for Fe(II) and Fe(III) complexes as a function of active space size (in ascending order with respect to the number of orbitals used). In each case, four different formulations for the on-top density functional was used: tPBE, ftPBE, tREVPBE and ftREVPBE. Solid horizontal lines indicate  $\Delta E_{H/L}$  values calculated with CASPT2 (active space (12/11,14)) for each complex.

space size is that an increase in the active space size results in a stabilisation of low-spin states. This is consistent, as low-spin configurations are inherently more multi-reference in nature than high-spin configurations. Perhaps the most interesting result here is the qualitative similarity between  $\Delta E_{H/L}$  values calculated at MC-PDFT and CASPT2 level across all active spaces. Specifically, the differences in  $\Delta E_{H/L}$  between ligands calculated with CASPT2 are largely preserved when using MC-PDFT, demonstrating that this method benefits from the post-SCF nature of the correction to the energy and, although accomplished using an on-top density functional, does not compromise the balanced treatment of strong- and weak-field ligand bonding.

Figure 9.5 shows  $\Delta E_{H/L}$  calculated using each of the four on-top density functionals tested – again as a function of the active space size. In general, changing the translation method from ‘t’ to ‘ft’ results in a minor systematic increase in  $\Delta E_{H/L}$  for all ligands, whereas changing the base functional from PBE to revPBE yields a systematic decrease in  $\Delta E_{H/L}$ . This stabilisation of low-spin states going from PBE to revPBE echoes the replacement of PBE exchange with O exchange previously highlighted in the KS-DFT results. Interestingly, both revPBE and O make use of a fitting procedure based on atomic exchange energies. Crucially, a change in the functional formulation shows no difference in the treatment of strong- and weak-field ligands, underlining the even treatment of different bonding types by the CASSCF wave function. This is very encouraging, despite the systematic overestimation of  $\Delta E_{H/L}$  by MC-PDFT with respect to CASPT2 data, as MC-PDFT in its current implementation has much greater scope for improvement compared with CASPT2. In other words, having the possibility to improve the current first-generation functionals by taking into account known exact theoretical constraints or parametrisation against experimental data, MC-PDFT shows a flexibility similar to KS-DFT in functional formulation without suffering from the imbalanced treatment of different metal-ligand bonding modes. This point is further illustrated through figure 9.6, which demonstrates that MC-PDFT follows the trend set out by CASPT2, while PBE and PBE0 perform differently depending on the ligand-field strength of the ligand in the complex concerned. Additionally, the systematically improved performance of revPBE over tPBE echoes the improvement of exchange-tuned functionals investigated using KS-DFT (i.e. OPBE) and highlights the scope for improvement concerning on-top density functionals.

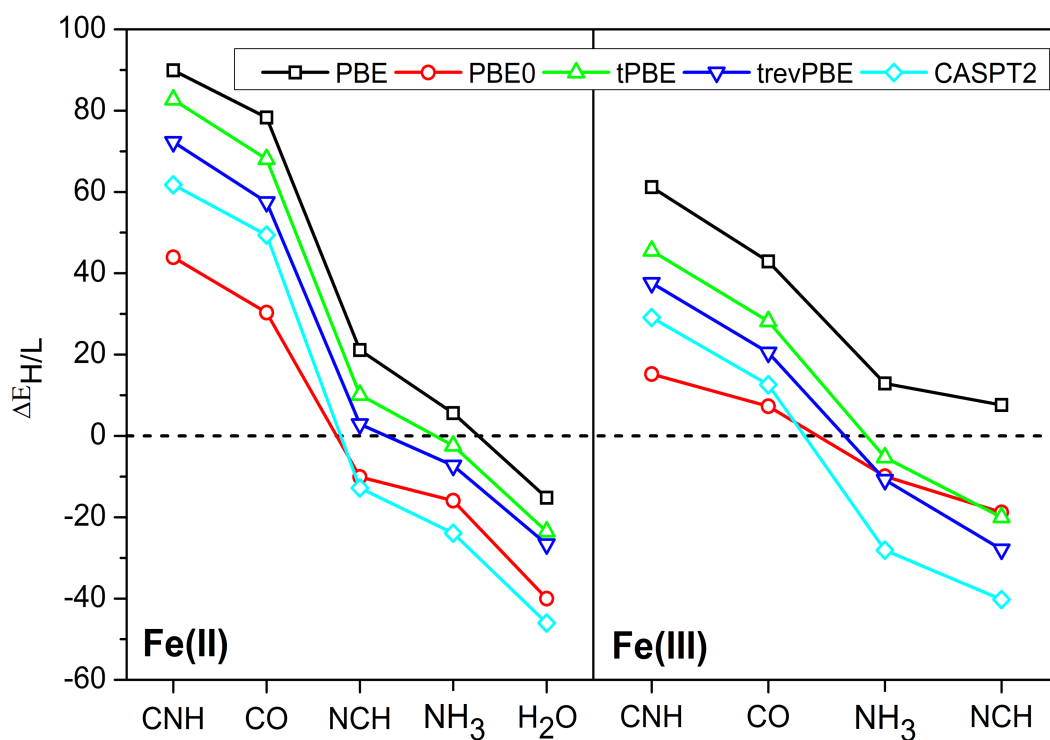


FIGURE 9.6:  $\Delta E_{H/L}$  (kcal/mol) calculated for Fe(II) (left) and Fe(III) (right) complexes in ascending order of computed ligand field strength. Results obtained using PBE, PBE0, MC-PDFT (with two different on-top functionals tPBE and trevPBE), and CASPT2 are shown, with the CASPT2 and MC-PDFT results based on the (12/11, 14) active space. Positive (negative) values of  $\Delta E_{H/L}$  correspond to a low-spin (high-spin) ground state.

## 9.4 Conclusions and Perspectives

By testing the performance of MC-PDFT in calculating the spin state ordering of nine Fe(II) and Fe(III) complexes, we find that, not only this method is able to qualitatively reproduce the spin-state ordering calculated at CASPT2 level, but that the treatment of ligands with diverse ligand field strengths is retained. We conclude that MC-PDFT is able to take advantage of the more even treatment of different ligand-metal bonding types by the underlying CASSCF wave function while at the same time benefiting from the reduced computational cost associated with calculating exchange and correlation energy using a density functional. MC-PDFT also reacts similarly to CASPT2 as a function of active space size and shows modest, yet consistent, sensitivity to the on-top density functional. We also emphasise that these results represent the application of first-generation on-top density functionals and are, in this respect, particularly encouraging.

This chapter serves as a type of perspective, so as to demonstrate that - regardless of the quality of a given environmental model - other problems related to the formulation of the underlying methodology can persist. Though not explored in this work, in principle it would be possible to couple findings from this chapter (i.e. the more consistent performance of multi-configurational wave function methods compared with DFT for the calculation of spin state ordering in Iron complexes) with those from previous chapters. Specifically, there is no reason why a methodology such as SC-Ewald could not be coupled with wave function theory methods such as CASSCF to account for environmental and static correlation effects. This could be a promising computational protocol for studying, for example, heterogeneous catalytic processes or magnetic properties in the solid state.



## Chapter 10

# General Conclusions and Perspectives

The objective of this thesis was to devise, construct and apply cost-effective approaches to calculate photophysical properties of crystalline media, specifically organic molecular crystals, by accounting for electrostatic interactions with the environment.

To do so, we made use of a self-consistent charge-adjustment procedure, SC-Ewald, which, through application of an excited-state embedding potential, attempts to recover both short- and long-range electrostatic contributions both from neighboring molecules and the long range, infinite potential (Madelung field). The resulting embedding procedure is then introduced into excited-state calculations based on time-dependent density functional theory. The resulting algorithm was tested on various molecular crystalline materials exhibiting interesting, and varied, optical properties.

Specifically, the first study, which was introduced as an effective proof-of-concept study for SC-Ewald applied to a dual-emissive molecular crystal exhibiting an excited-state dual proton transfer reaction, demonstrated that fluorescence properties calculated with SC-Ewald were superior to those calculated with other cost-mitigating methods, such as ONIOM. Indeed, emission properties calculated with SC-Ewald were of a remarkable quality when compared with experimental values.

In a second study, this time concerning the phenomenon of aggregation-induced emission observed in molecular crystalline diphenyl fluorone, revealed that the enhanced emissive properties of its aggregates and powders when compared with solution could be rationalized through a single-molecule process in which the radiative intensity of otherwise poorly-emitting states is enhanced by the electrostatic field produced by the excited-state embedding potential provided by SC-Ewald.

Extending the application of SC-Ewald to the study of fluorescent amorphous materials, we then studied a family of difluoroboron avobenzene derivatives which exhibit interesting structure-dependent fluorescent properties resulting from both polymorphism and mechanochromic fluorescence. As well as a quantitative recovery of the influence of polymorphism on fluorescence, using intelligent sampling of thermally-accessible molecular configurations in the amorphous phase, we obtained a quantitative model which provides physical insight into the origins of mechanochromic luminescence and the optical properties of amorphous materials in general. Additionally, through molecular dynamics simulations,

we have seen how the degree of polymorphism can be altered via the substitution of donor moieties which facilitate a wider array of potential intermolecular interactions, and how this translates to regions of local order in the amorphous phase and the resulting influence on amorphous-phase fluorescence.

The following study, actually completed earlier in the time-frame of the thesis, concerned a preliminary investigation into the luminescent properties of metal-organic frameworks, and how these may be studied using a combined cluster and periodic approach. Through this methodology, we postulated that the drastically different luminescence properties of a pair of iso-structural frameworks could arise through different radiative processes, be it fluorescence - in the case of the Cd-based framework, or phosphorescence - in the case of the Zn-based framework.

The final contribution to this thesis serves as a perspective and highlights the failings of density functional theory for the specific task of calculating spin-state ordering in transition metal complexes. Though application of wave function-based methods and the recently-developed multiconfiguration pair-density functional theory, we demonstrate that these methods can provide a more balanced treatment of strong- and weak-field ligands and their effects on spin-state ordering. Though this study does not concern the condensed phase, it is clear how these issues transfer to the solid state, and that special care - not only concerning environmental effects - must be taken.

With the development of SC-Ewald and the first three studies outlined in this thesis, it is clear that this represents a promising and cost-effective way of addressing the challenge of including environmental factors in the modeling of solid-state photophysical processes. Indeed, we have shown how this is often crucial for the understanding and prediction of such phenomena. Though these initial results are promising, further study into the behavior of SC-Ewald with respect to, for instance, functional choice and charge types is desirable, as well as further systematic study of the phenomena already presented in this work. Nevertheless, the performance and versatility of this model has thus far been rather remarkable, and should prompt further development into the study of other condensed-phase optical phenomena as well as lower-dimensional periodic systems such as surfaces and polymers.

## Chapter 11

# Résumé en français

### 11.1 Introduction

Les matériaux qui peuvent être considérés comme «photoactifs» sont ceux dont une réponse observable peut être provoquée par l'interaction avec la lumière. La réponse observable en question est, par exemple, une réaction chimique induite, un changement de couleur ou de luminescence, un changement de propriétés magnétiques.

A partir de ces matériaux, des dispositifs exploitant leurs propriétés pour une application donnée peuvent être fabriqués. Le développement constant de nouveaux matériaux photoactifs destinés à être utilisés dans des domaines tels que les dispositifs électroluminescents, médicaux et catalytiques résulte de la nécessité d'une plus grande efficacité, d'une performance améliorée et d'un coût réduit. Cependant, l'innovation repose actuellement sur des progrès incrémentaux, des essais, et une découverte parfois accidentelle où peu d'attention est portée à la conception de matériaux avant leur synthèse.

Compte tenu des moyens de calcul actuellement disponibles et des développements récents dans les méthodes de la fonctionnelle de la densité dépendant du temps, la modélisation peut permettre ce design pré-synthétique. Pour cela cependant, prendre en compte les changements induits par l'environnement en phase condensée sur les propriétés à l'état excité de ces matériaux est indispensable. Dans le cadre de la modélisation des processus photophysiques, au niveau moléculaire, les effets de la "phase condensée" sont ceux induits par les molécules de solvant d'une solution, alors qu'il s'agit de ceux d'autres molécules photoactives dans le cas de matériaux cristallins ou en phase amorphe.

Il est bien connu que les propriétés photophysiques d'un système moléculaire peuvent être fortement influencées par des interactions avec le milieu. Pour cette raison, des ressources considérables ont été consacrées à l'étude de l'influence environnementale afin de mieux comprendre et contrôler différents processus à l'état excité.

D'un point de vue expérimental et théorique, les méthodes d'étude des propriétés photophysiques de molécules photoactives en solution sont très bien développées, et la conception moléculaire guidée par la modélisation devient possible pour exploiter certaines propriétés. Malheureusement, l'état de l'art dans la modélisation de l'état solide est beaucoup moins développé par rapport à la modélisation des effets de solvant. En outre, à l'état

solide, les processus photophysiques sont plus difficiles à caractériser expérimentalement et les constats de comportement photophysique intéressant dans les systèmes périodiques, souvent faibles et subtils, sont beaucoup plus rares par rapport aux cas connus en solution. Décrire la photochimie complexe en phase solide représente donc un défi important pour les chimistes théoriciens. L'élaboration de modèles de qualité suffisante - à la fois capables de comprendre et de prédire l'influence d'un environnement sur les propriétés optiques, ainsi que leur modification par changement de l'environnement - constituent un élément nécessaire à la compréhension et à la conception de molécules et de matériaux fonctionnels.

Ce problème représente une tâche centrale de cette thèse, dans laquelle nous avons développé et appliqué un modèle d'embedding relativement peu coûteux - SC-Ewald - et capable de modéliser des interactions électrostatiques cruciales avec l'environnement à l'état solide. Cette approche, de type "embedded cluster" décrite dans le chapitre 4, améliore certains aspects des méthodes actuelles plus traditionnelles d'embedding telles que l'ONIOM.

## 11.2 Embedding à l'état excité: SC-Ewald

Nous présentons maintenant l'approche utilisée pour incorporer les effets électrostatiques d'environnement qui constitue la base de la majorité des travaux présentés plus loin dans cette thèse. Cette approche s'affranchit des problèmes liés à l'électrostatique à longue distance dans les systèmes périodiques infinis en utilisant la technique de sommation d'Ewald. Associée à une formulation auto-cohérente, cette approche produit un potentiel d'embedding dérivé de la densité d'état excité du cluster quantique. Dans la suite, nous introduisons tout d'abord le problème de l'électrostatique à longue distance dans les systèmes infinis et la façon dont Ewald l'a résolu, puis nous présentons la méthode d'embedding d'Ewald originale pour le calcul des propriétés à l'état fondamental. Enfin, nous décrivons la procédure auto-cohérente qui génère le potentiel d'embedding de l'état excité. Bien que l'on puisse supposer que ces interactions soient négligeables si les atomes concernés sont suffisamment éloignés du cluster quantique d'intérêt, démontrons dans la suite que ce n'est généralement pas le cas et comment cette hypothèse peut entraîner des erreurs importantes dans le potentiel de l'état fondamental.

Le potentiel électrostatique ressenti par un atome en un point donné dans un réseau périodique, connu sous le nom de potentiel de Madelung, [48] peut être représenté par une somme directe infinie qui n'est malheureusement que conditionnellement et lentement convergente. Ainsi, utiliser un jeu fini de charges ponctuelles pour décrire l'interaction avec le milieu peut entraîner de fortes erreurs.

Une solution intelligente à ce problème a été proposée par Ewald en 1921, [50] en utilisant une approche qui permet de contourner les propriétés de convergence conditionnelles de la somme directe. Dans cette approche, calculer l'énergie d'une charge ponctuelle  $q_i$  dans un réseau périodique infini nécessite trois quantités. La première est l'énergie de liaison

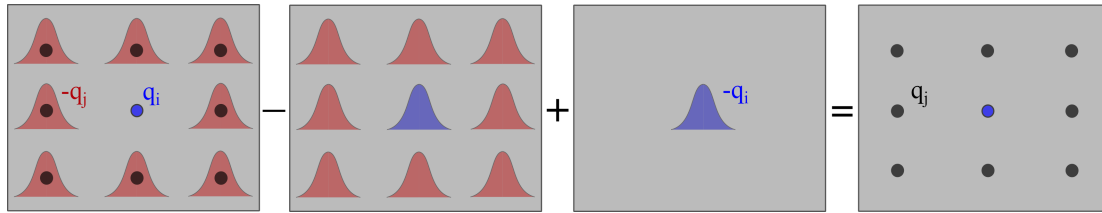


FIGURE 11.1: Représentation schématique de l'équation 4.2 - comment les termes intervenant dans la somme d'Ewald sont combinés pour reproduire le potentiel électrostatique au site  $q_i$  généré par tous les autres atoms  $q_j$  dans un réseau périodique.

de la charge  $q_i$  au milieu des autres charges  $q_j$ , chacune étant complétée par une distribution de charge Gaussienne fictive de charge totale de  $-q_j$ . Fondamentalement, cette fonction d'écrantage permet à cette somme de converger rapidement dans l'espace réel (direct). La deuxième quantité est l'énergie de liaison de la charge  $q_i$  avec les fonctions d'écrantage Gaussiennes décrites ci-dessus, plus une distribution gaussienne supplémentaire de charge totale  $-q_i$  centrée à la position de la charge  $q_i$ . Cette somme est réalisée sur un ensemble complet et périodique de distributions Gaussiennes identiques, et converge donc rapidement lorsqu'elle est effectuée dans l'espace réciproque. Le troisième terme est l'énergie de liaison de la charge  $q_i$  en raison de la fonction Gaussienne supplémentaire décrite précédemment. En combinant ces trois termes, l'énergie de liaison de la charge ponctuelle  $q_i$ , montré schématiquement en figure 11.1 est obtenue.

À partir de cette discussion, il est facile de comprendre que ce problème est général et se pose lors du traitement de clusters quantiques, où le milieu est habituellement représenté par un jeu fini de charges ponctuelles conçu pour reproduire le champ électrostatique du reste du cristal.

Nous introduisons maintenant une méthode [51, 52] - initialement conçue par Klintenberg et ses collègues en 1999 - qui cherche à résoudre certains des problèmes liés au potentiel électrostatique à longue distance dans les environnements cristallins, sans calculs périodiques au niveau quantique. Cette approche - et son extension aux potentiels d'états excités - constitue la base de la majorité de cette thèse. En résumé, originellement utilisée pour l'étude de défauts dans des systèmes périodiques ioniques, cette approche consiste ici à associer incorporation de charges ponctuelles à un processus d'ajustement de charges, produisant automatiquement un jeu de charges ponctuelles représentant exactement le potentiel de Madelung pour un système cristallin arbitraire. Un algorithme en cinq étapes, décrit schématiquement en Figure 11.2, est utilisé pour générer le jeu de charges ponctuelles.

Après la génération de charges ponctuelles ajustées, le potentiel électrostatique, calculé via une somme directe aux sites du cluster quantique, est maintenant égal à celui de l'approche d'Ewald et le problème des potentiels électrostatiques à longue distance erronés dans les méthodes de cluster fini est résolu. La somme totale est maintenant finie, bien que le potentiel électrostatique qu'elle produit soit dérivé avec précision de la somme d'Ewald. Dans le cadre de l'embedding d'Ewald, bien que les charges d'environnement permettent

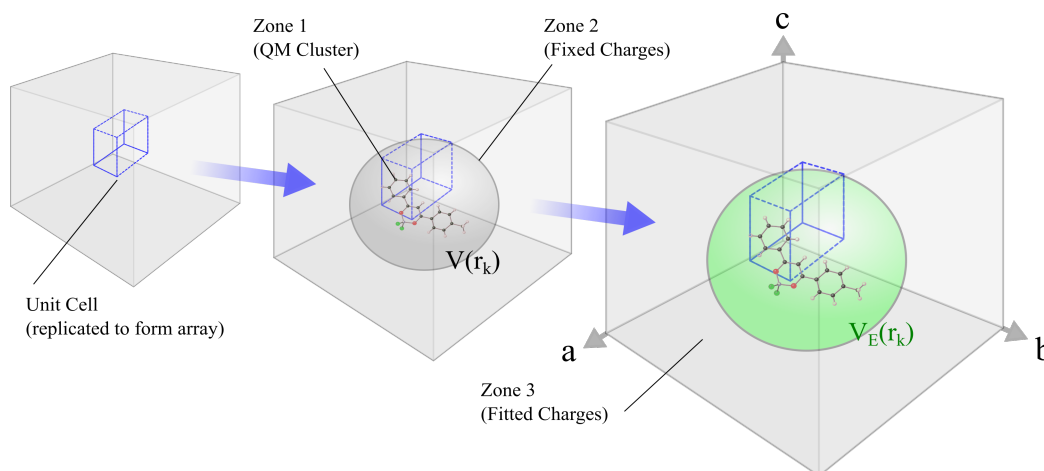


FIGURE 11.2: Représentation de la procédure d'embedding d'Ewald. Génération du jeu de charges comme supermaille de la maille cristallographique (gauche), division de ce jeu en trois zones (centre). Après ajustement de la valeur des charges en zone 3, le potentiel électrostatique d'Ewald est reproduit en tous points des zones 1 et 2 (intérieur de la sphère verte) (droite).

de polariser la fonction d'onde de l'état fondamental du cluster quantique, celles-ci restent fixes, rendant les effets de polarisation mutuelle impossible entre le cluster quantique de la Zone 1 et le reste du système. Ceci introduit potentiellement de graves approximations lors de l'étude de phénomènes à l'état excité - et en particulier pour les transferts de charge. Par conséquent, nous avons conçu une extension de l'embedding d'Ewald, capable de produire un potentiel électrostatique à l'état excité électriquement équilibré avec le cluster quantique. Ce faisant, nous utilisons Ewald comme point de départ pour produire un potentiel d'embedding à l'état excité généré par des charges de Mulliken. Les étapes impliquées dans ce processus sont décrites ci-dessous et sont montrées schématiquement en Figure 11.3. Maintenant que nous avons introduit les fondements théoriques nécessaires et l'approche SC-Ewald elle-même, la majeure partie du reste de cette thèse concerne l'application de cette dernière au calcul de divers phénomènes à l'état excité se produisant en phase cristalline. En particulier, on décrit ici une étude de type preuve de concept concernant le transfert de protons à l'état excité à l'état solide (chapitre 5), puis des phénomènes d'émission induite par agrégation (chapitre 6) ou encore de fluorescence mécano-chromique (chapitre 7).

### 11.3 Application au transfert de protons à l'état excité

Le transfert de proton intramoléculaire à l'état excité (ESIPT) est un processus photochimique qui produit un tautomère ayant une structure électronique différente de la forme excitée d'origine. [58] Généralement, cette réaction est décrite par un cycle à quatre niveaux, résultant du processus de tautomérisation de la forme énol (E) à kéto (K), qui est représenté schématiquement en figure 11.4.

Les propriétés de signature des fluorophores ESIPT incluent des déplacements de Stokes

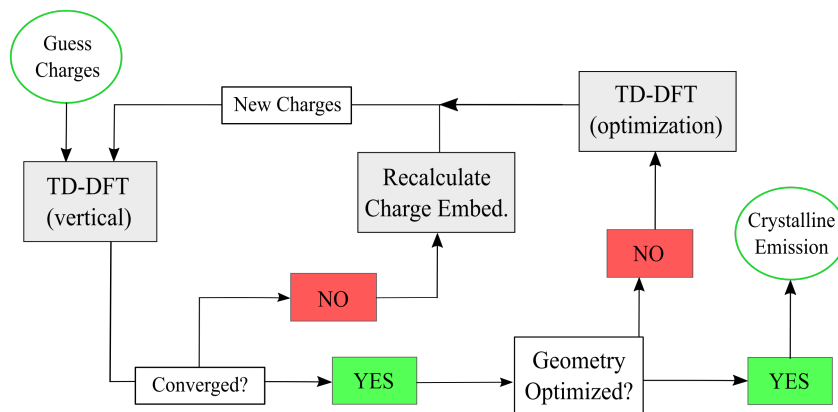


FIGURE 11.3: Procédure auto-cohérente utilisée pour obtenir le potentiel d'embedding à l'état excité de l'environnement cristallin, et pour optimiser la géométrie du cluster central à l'état excité afin d'obtenir les propriétés d'émission du cristal.

importants, des émissions duales et une sensibilité des propriétés optiques au milieu. [62, 63] La nature d'émissivité duale de ces chromophores provient de la longueur d'onde d'émission plus courte (plus longue) de la forme énol (kéto). La condition nécessaire au cycle à quatre niveaux à la base de l'ESIPT est la présence d'une liaison hydrogène intramoléculaire (liaison H) entre les donneurs de protons et les groupes accepteurs de protons. [60] La vitesse inhérente de l'ESIPT ( $k_{ESIPT} > 10^{12} s^{-1}$ ) est telle que ce processus peut avoir lieu même à très basse température, [61] bien que le taux de processus ESIPT dépende des groupes donneurs/accepteurs impliqués et du milieu, qu'il s'agisse de solvants ou d'autres chromophores ESIPT sous forme de cristaux moléculaires. [64, 65] Grâce aux propriétés de double émission des chromophores ESIPT et aux larges bandes d'émission résultantes capables de couvrir tout le domaine visible, ces systèmes ont gagné un intérêt considérable pour la production de lumière blanche. [62, 66, 67] De plus, les chromophores ESIPT ont été appliqués dans divers domaines comme celui des portes logiques moléculaires, [68] des dispositifs d'imagerie par fluorescence, [69] et encore d'absorbants d'UV. [70]

D'un point de vue informatique, posséder un outil capable de reproduire quantitativement les propriétés photophysiques de chromophores ESIPT en solution et à l'état solide ainsi que la façon dont ils sont soumis à leur environnement représenterait un atout potentiellement inestimable non seulement pour la compréhension de l'ESIPT mais aussi pour la conception moléculaire. Bien que le concept de modélisation de l'ESIPT en solution soit bien établi et devenu habituel, cela est loin d'être le cas à l'état solide. Les difficultés résultent de la nature directionnelle des interactions intermoléculaires à l'état solide ainsi que du bon rapport des interactions électrostatiques à longue distance qui pourraient être cruciales pour la compréhension et la prédiction des processus thermodynamiques et photophysiques à la base de l'ESIPT à l'état solide. Dans cet esprit, nous avons essayé d'utiliser une étude d'un système cristallin présentant deux réactions de transfert de proton résultant en une émission duale pour montrer que i) on peut utiliser l'algorithme SC-Ewald pour incorporer - à faible coût calculatoire et facilement - les interactions qui sont imposées par l'environnement

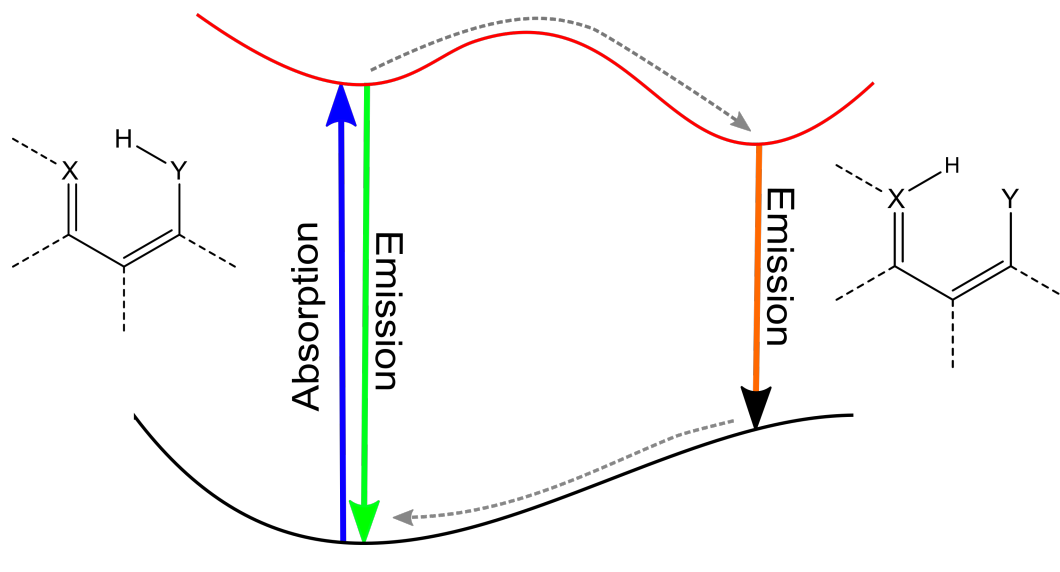


FIGURE 11.4: Mécanisme général d'ESIPT à quatre étapes. Le tautomérisme entre les formes énol et kéto est interdit à l'état fondamental mais thermodynamiquement favorisé à l'état excité, donnant lieu à un équilibre entre les formes énol et kéto à l'état excité associées à des longueurs d'onde d'émission distinctes.

dans n'importe quel modèle cristallin avec une périodicité 3D pour l'étude de ses propriétés photophysiques et ii) leur inclusion conduit à une meilleure reproduction des effets environnementaux et donc une meilleure compréhension de la façon dont ceux-ci pourraient affecter les processus photophysiques pertinents.

Ce travail s'est porté sur l'étude d'un système (DHNA, figure 11.5), présentant une réaction de transfert de proton intramoléculaire à l'état excité et dont les propriétés photophysiques complexes sont sensibles aux effets environnementaux, pour développer et tester des approches capables de reproduire des effets subtils mais significatifs. Les résultats principaux obtenus sont résumés en figure 11.6. Initialement, une distribution de charge reproduisant le potentiel Ewald de l'état fondamental exact du cristal a été utilisée avec des résultats améliorés obtenus en utilisant un cluster QM/QM' en plus de cette distribution de

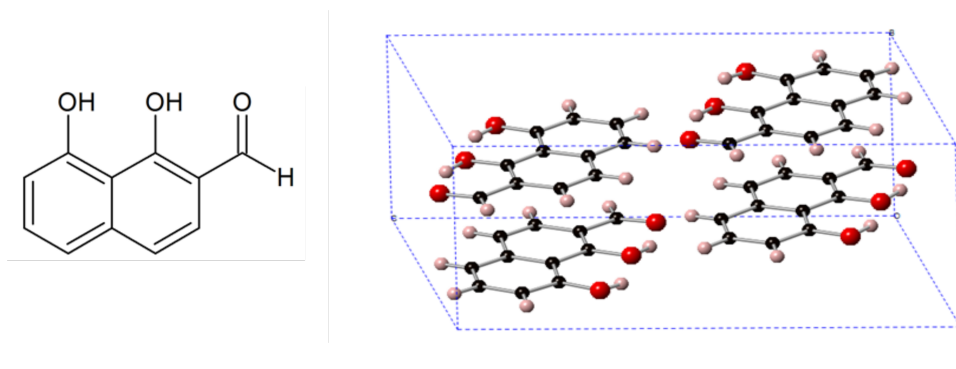


FIGURE 11.5: Gauche: structure de la molécule de DHNA considérée dans ce chapitre. Droite: packing de DHNA sous forme cristalline (hydrogène: blanc; carbone: noir; oxygène: rouge).

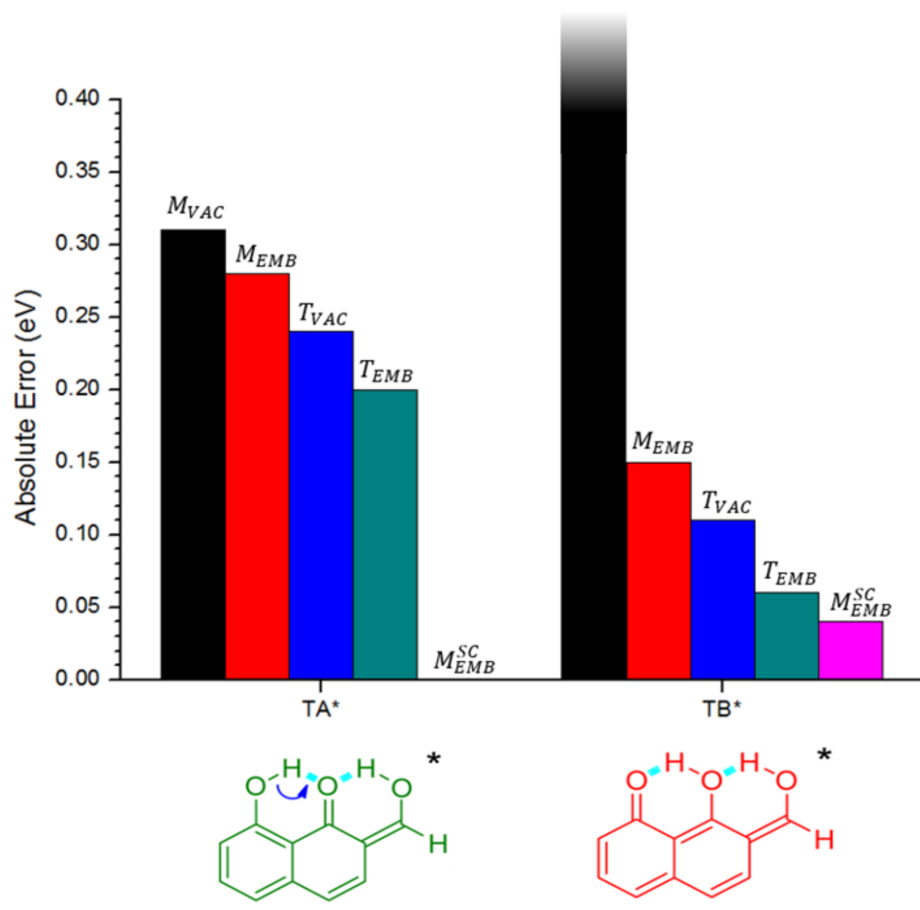


FIGURE 11.6: Erreurs absolues sur les énergies d'émission (eV) calculées pour chacun des modèles considérés dans ce chapitre. L'erreur est considérée comme infinie pour l'émission TB\* avec le modèle  $M_{VAC}$  puisqu'aucun minimum sur la surface d'énergie potentielle de l'état excité n'est obtenu.

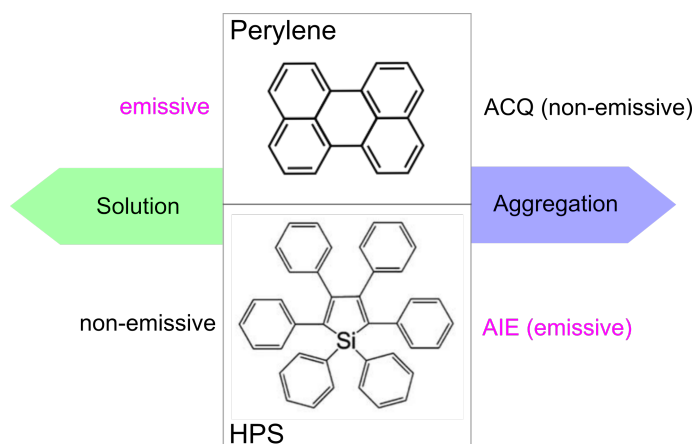


FIGURE 11.7: Molécules organiques typiques présentant des phénomènes d'aggregation-caused quenching (ACQ) et d'aggregation-induced emission (AIE).

charges. Dans une deuxième approche, les résultats ont été améliorés (et obtenus en très bon accord avec l'expérience) en utilisant notre méthode auto-cohérente (SC-Ewald) pour déterminer les valeurs des charges ponctuelles d'environnement tout en considérant uniquement une seule molécule explicitement au niveau QM.

Ici, nous avons présenté deux approches différentes qui, associées à un très faible coût de calcul supplémentaire, peuvent conserver l'effet de la périodicité cristalline sur le potentiel électrostatique ressenti par une molécule centrale et l'appliquer dans le contexte du calcul de propriétés photophysiques. Nous avons démontré que l'inclusion de ces effets peut être cruciale si on souhaite décrire ces effets avec précision et prédire le résultat de processus photophysiques à l'état solide. Dans les sections suivantes, nous verrons comment SC-Ewald peut être appliqué à d'autres systèmes pour étudier leurs propriétés optiques complexes et sensibles à l'environnement.

## 11.4 Application aux agrégats émissifs

Au cours de la dernière décennie, un groupe de molécules ne subissant pas l'effet d'«aggregation caused quenching» (ACQ), molécules émissives qui deviennent non-émissives après agrégation ou à l'état solide, ont été proposées - une série de dérivés du silole, non émissif en solution diluée mais fortement fluorescent sous forme agrégée ou en poudre. [88,89] Cette propriété, totalement à l'opposé du phénomène destructif de l'ACQ, nommée «émission induite par agrégation» (AIE) et a entraîné la synthèse de nombreuses classes de ces molécules. Bien que des améliorations dans les applications technologiques des luminophores organiques aient été constatées, des efforts supplémentaires sont nécessaires pour comprendre les mécanismes mis en jeu dans l'AIE et comment ceux-ci peuvent être exploités.

La grande majorité du comportement d'AIE, y compris celui des dérivés du silole (HPS) présenté en figure ??, est rationalisé par la restriction de rotation intramoléculaire (RIR).

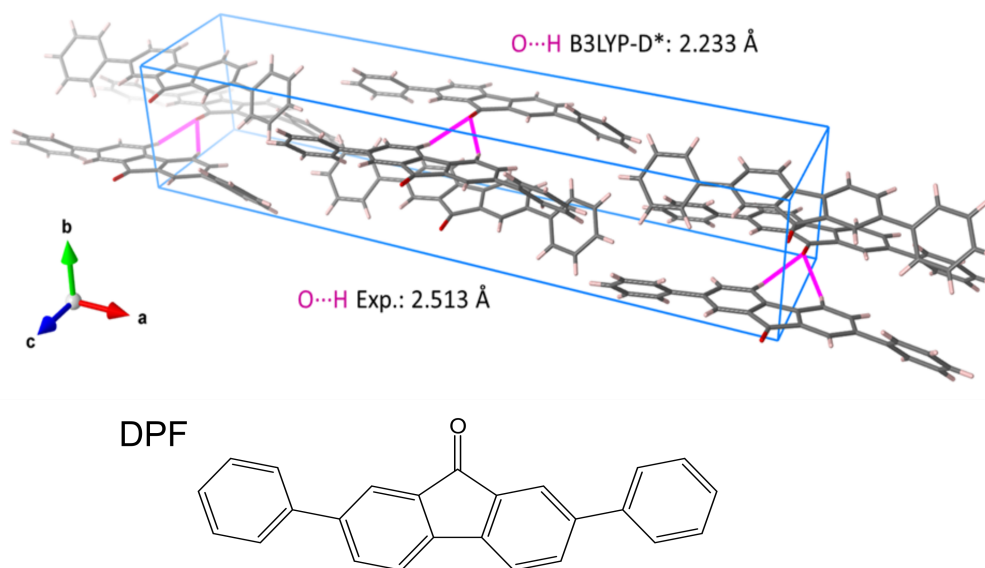


FIGURE 11.8: Structure cristalline complètement optimisée au niveau B3LYP-D\*/6-31G(d,p) du DPF. Le trait bleu représente la maille conventionnelle, et les deux liaisons hydrogènes O-H intermoléculaires sont en évidence à l'aide de segments violets. La maille de la structure expérimentale ( $a = 34.84 \text{ \AA}$ ,  $b = 6.85 \text{ \AA}$ ,  $c = 7.21 \text{ \AA}$ ), est bien reproduite, en comparaison des paramètres de maille optimisés ( $a = 34.61 \text{ \AA}$ ,  $b = 6.48 \text{ \AA}$ ,  $c = 7.17 \text{ \AA}$ )

[88,90–92] Pour HPS, il existe six substituants cycliques liés au cœur de silole. Ces fragments cyclique, qui peuvent tourner autour de leurs liaisons simples avec la fraction de silole, servent comme voies de désactivation rotative efficace (ou, plus généralement, vibrationnelle), conduisant à une désintégration non radiative d'un état excité à l'état fondamental. Dans les agrégats ou à l'état solide, ce mouvement est sévèrement restreint - en supprimant cette voie de désactivation non radiative et en conservant les propriétés hautement émissives de la molécule HPS. Cette attribution du mécanisme RIR au phénomène AIE a également été étudiée et vérifiée en observant la fluorescence en fonction de la viscosité du solvant, de la température du système et de l'application d'une pression. [88]

La 2,7-diphénylfluorénone (DPF) est un AIE chromophore, qui présente un déplacement vers le rouge de 150 nm de la bande d'émission après agrégation, attribué à la formation d'excimère à l'état excité. [95] Ce chromophore forme également facilement des poudres qui présentent des propriétés optiques très similaires aux agrégats. Dans ce chapitre, nous mettons en évidence une autre cause pour le comportement AIE de DPF et démontrons qu'il provient d'un processus à une seule molécule plutôt que de la formation d'excimères. En utilisant le modèle d'embedding SC-Ewald (chapitre ??) comme approximation de l'environnement à l'état solide, il est démontré (figure 11.9) que le champ induit par l'environnement cristallin peut améliorer la luminosité relative des états faiblement émissifs dans DPF, résultant à la fois en une fluorescence améliorée et un déplacement bathochrome substantiel par rapport aux émissions en solution diluée.

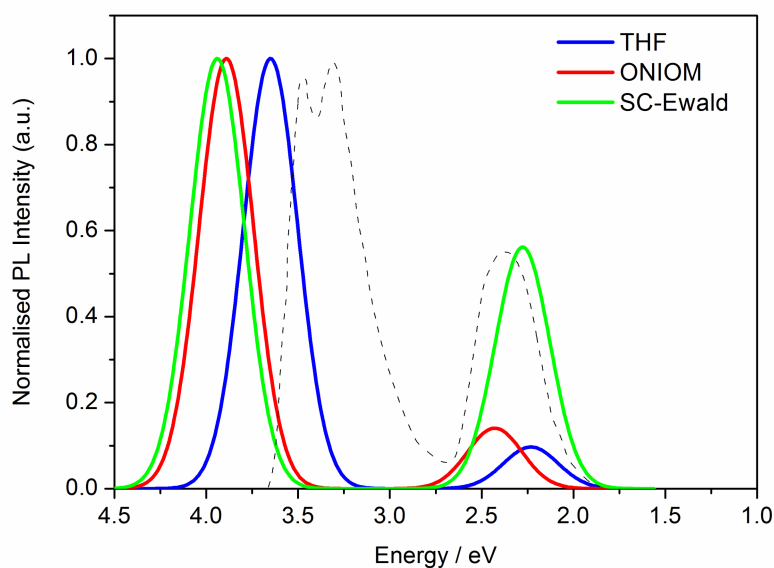


FIGURE 11.9: Spectres d'émission simulés pour les transitions  $S_0 \rightarrow S_1$  et  $S_0 \rightarrow S_3$  au niveau CAM-B3LYP: i) dans le THF (solvation implicite, C-PCM), ii) à l'état solide en utilisant une approche ONIOM QM/QM' et iii) à l'état solide en utilisant la procédure d'embedding SC-Ewald. Valeur de FWHM de 0.35 eV. Le spectre expérimental [?] est également reporté (pointillés).

Nos résultats démontrent comment, en général, la modélisation de différents effets environnementaux est cruciale pour la compréhension et la reproduction des observations expérimentales dans le contexte de l'AIE. Plus précisément, dans le cas de DPF, il a été démontré que la paradigme de la restriction de rotation intramoléculaire fournit une image incomplète du processus AIE dans ce cas particulier. Au lieu de cela, une analyse théorique a montré que l'augmentation simultanée de la fluorescence et de la longueur d'onde de fluorescence lors de l'agrégation des monomères de DPF en solution est due à un processus centré sur l'environnement, en s'appuyant sur des interactions électrostatiques à l'état excité à courte et à longue distance entre une seule molécule et son environnement. Nous suggérons donc que le champ de l'environnement à l'état excité permet une émission améliorée d'états excités et conduit à une émission intense d'agrégats observée à plus faible énergie par rapport à la solution. Il est intéressant de noter que cela diffère de l'interprétation antérieure des résultats expérimentaux, qui proposait la formation d'«excimères statiques». Nous prévoyons que, pour d'autres cas signalés d'AIE accompagnés d'un changement significatif dans les maxima d'émission, ce protocole pourrait généralement être utilisé comme outil non seulement pour comprendre, mais aussi pour faciliter la conception de matériaux performants en fournissant un moyen pour inclure des interactions avec des environnements complexes.

## 11.5 Extension aux matériaux amorphes

La fluorescence à l'état solide des molécules organiques dépend fortement de la structure moléculaire et des interactions intermoléculaires présentes dans différentes morphologies. [] Dans les chapitres précédents, nous avons étudié comment les propriétés de fluorescence des cristaux moléculaires organiques peuvent être modifiées par la réactivité à l'état excité (transfert de proton) et agrégation. Ces propriétés ont également été jugées très sensibles aux interactions électrostatiques avec l'environnement. Dans cette section, nous étudions la sensibilité des propriétés de fluorescence à l'état solide ainsi qu'au polymorphisme et au stress mécanique. Dans le contexte de la science des matériaux, le polymorphisme est la capacité d'une molécule à adopter différentes structures cristallines. En conséquence, différents polymorphes dérivés de la même molécule peuvent présenter des interactions intermoléculaires distinctement différentes et, par conséquent, des propriétés optiques remarquablement différentes. En outre, en appliquant une pression par broyage mécanique en formant des polymorphes moins ordonnés, certains matériaux peuvent présenter un changement de couleur ou un changement de comportement de luminescence, connu sous le nom de «mécanochromisme». Plus récemment, le mécanochromisme sélectif, sensible au type de pression mécanique appliquée - qu'il soit anisotropique ou isotrope - a été démontré pour certains matériaux.

Bien que le mécanochromisme soit devenu une propriété intensément étudiée des matériaux moléculaires [], les processus microscopiques qui sont au cœur de ces effets restent mal compris, interdisant toute sorte de stratégie de conception rationnelle pour l'application dans le monde réel. Envisager une voie de conception suppose une compréhension fine des relations structure-propriété fortement corrélées à l'état excité qui régissent le mécanochromisme. Jusqu'ici, se tourner vers des approches théoriques pour étudier ces relations a été difficile en raison de la complexité de la description et de la prédiction des propriétés de la phase amorphe, tout particulièrement à l'état excité. En effet, la description théorique de l'absorption et de la fluorescence nécessite des approches chimiques quantiques sophistiquées qui sont souvent exigeantes en termes de calcul. L'échantillonnage d'un nombre représentatif de configurations moléculaires dans la phase amorphe représente un énorme investissement de calcul, en particulier pour le calcul d'états excités, et empêche ainsi la reproduction ou la prédiction des propriétés optiques. En utilisant une double approche théorique-expérimentale, dans cette contribution, nous démontrons qu'un échantillonnage intelligent des configurations thermiquement accessibles en phase cristalline, couplé à une compréhension des facteurs qui régissent l'ordre local dans la phase amorphe, conduit à une reproduction remarquable des spectres d'émission expérimentaux et fournit non seulement une compréhension vitale des processus clés à la base du mécanochromisme mais aussi une interprétation des propriétés optiques des phases amorphes plus généralement.

Pour ce faire, nous présentons ce que l'on appellera la famille des molécules DFB-X - DFB-H, DFB-E et DFB-A - représentée en figure 11.10. En prenant DFB-A comme exemple, la figure ?? met en évidence les effets de l'environnement (c'est-à-dire solution ou milieu

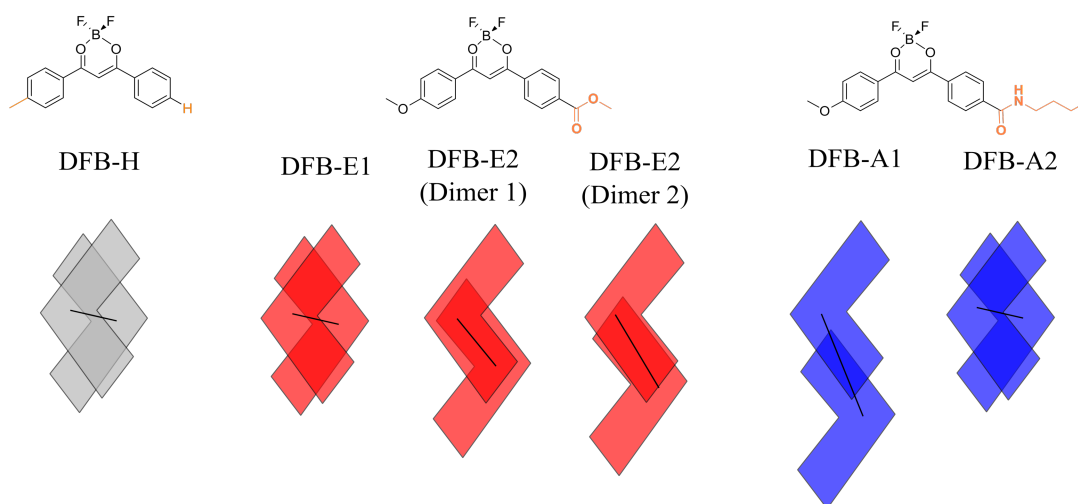


FIGURE 11.10: Structures moléculaires des molécules de DFB-H, DFB-E et DFB-A. Les motifs colorés indiquent les orientations relatives et le recouvrement entre paires de dimères pour les polymorphes cristallines résolus expérimentalement, le trait noir mettant en évidence la distance entre centre de masse  $r$  dans chaque cas.

cristallin), le polymorphisme et le stress mécanique sur les propriétés de fluorescence. Dans la solution de THF, le DFB-A présente un maximum d'émission à environ 425 nm et possède deux polymorphes cristallins stables (DFB-A1 et DFB-A2) avec des spectres d'émission plus larges à 480 et 520 nm, respectivement. Le broyage mécanique des cristaux DFB-A entraîne un décalage global vers le rouge et un élargissement significatif du spectre d'émission, avec un maximum à 550 nm. Le DFB-A constitue un excellent exemple de la façon dont une modification des interactions intermoléculaires apportées par la modification des conformations relatives dans les matériaux moléculaires entraîne des altérations importantes du comportement de fluorescence. En outre, DFB-H et DFB-E - en raison des interactions intermoléculaires différentes apportées par substitution de différents groupes de donneurs - présentent leur propre polymorphisme distinct et leur réponse à une perturbation mécanique. La réponse complexe de cette famille de molécules à différentes interactions et stimuli environnementaux en fait un candidat idéal pour tester et développer des approches de modélisation qui cherchent à expliquer de telles subtilités. Par conséquent, dans ce travail, nous avons démontré comment SC-Ewald - en conjonction avec les techniques de la dynamique moléculaire (MD) - est capable de reproduire les changements spectraux dus au polymorphisme et de mettre en évidence les concepts physiques à la base de la fluorescence mécanochromique. Dans ce travail, nous avons utilisé l'approche SC-Ewald introduite dans le chapitre ?? pour étudier les changements de comportement d'émission d'une famille de molécules dus à la fois au polymorphisme en phase cristalline et à l'amorphisation par broyage mécanique. Une reproduction quantitative de l'influence du polymorphisme sur la fluorescence a pu être obtenue, en utilisant un échantillonnage intelligent de configurations moléculaires accessibles thermiquement dans la phase amorphe, qui a pu fournir un aperçu physique des origines de la luminosité mécanochromique et des propriétés optiques des

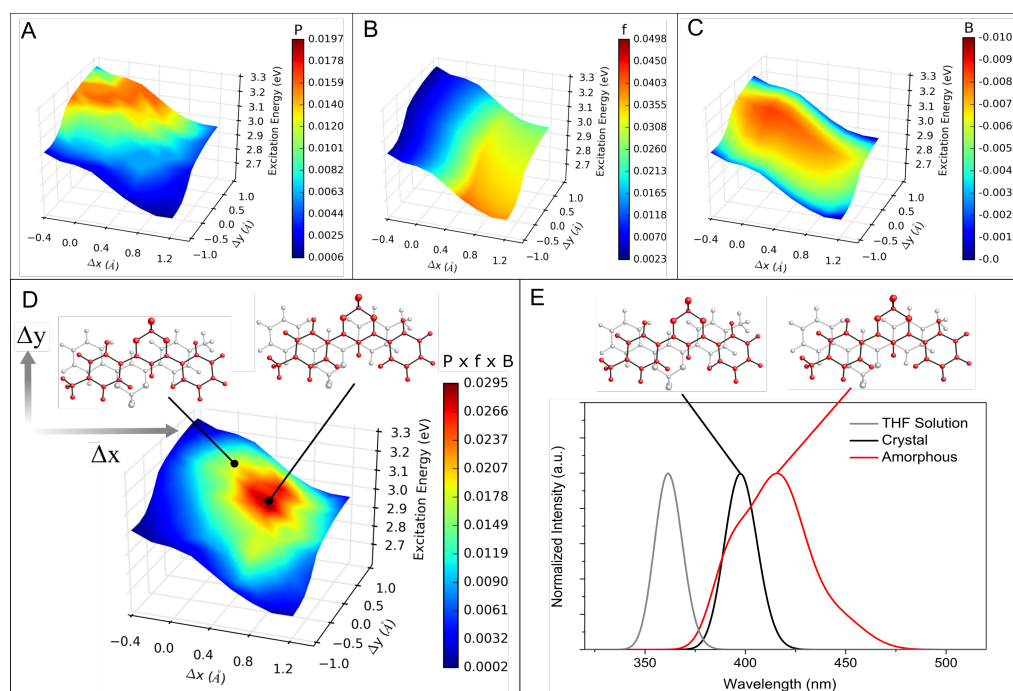


FIGURE 11.11: Tracés de surface des énergies d'émission calculées en fonction des coordonnées de scan du défaut. Pour une paire donnée de molécules en phase cristalline, une molécule (en rouge) est déplacée le long de son plan moyen parallèlement ( $\Delta x$ ) ou perpendiculairement ( $\Delta y$ ) de son axe. Une palette de couleurs est alors projetée sur cette surface, représentant A) la probabilité de trouver une configuration donnée en phase amorphe, B) la force d'oscillateur, C) le facteur de Boltzmann et D) le produit normalisé des termes précédents, donnant une force d'oscillateur pondérée. Les régions rouges (bleues) représentent une plus forte (faible) contribution d'une coordonnée de scan donnée au spectre d'émission calculé de la phase amorphe. E) spectre d'émission calculé en solution (THF), en phases cristalline et amorphe de DFB-H. Les structures moléculaires représentées indiquent les structures cristallines et le défaut contribuant le plus.

matériaux amorphes en général. En outre, nous avons vu comment le degré de polymorphisme peut être modifié par la substitution de fragments de donneurs qui facilitent une plus grande variété d'interactions intermoléculaires potentielles, comme cela se traduit par des zones localement ordonnées dans la phase amorphe et par l'influence sur la fluorescence en phase amorphe.

## Chapter 12

# Appendix to Chapter 4

This section outlines the file structure needed for a given calculation and the different modes that can be employed within SC-Ewald.

### Input Files

SC-Ewald requires several input files which constitute a combination of inputs for both Gaussian and Ewald. Note that the Ewald input files required to run SC-Ewald are different from the input files for the original Ewald code. Figure 12.1 schematically outlines all the input files required. In the following, an example of each input will be given for the

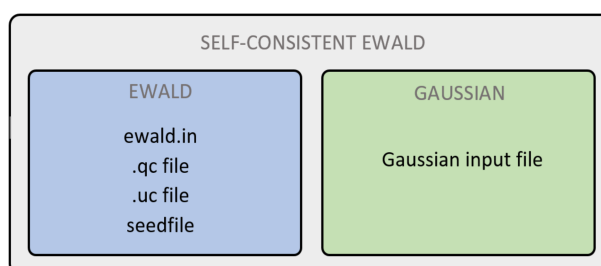


FIGURE 12.1: Summary of files required before running an SC-Ewald calculation.

molecular crystal of urea. Boxes highlighted in gray mark the input file lines which should be entered.

#### SC-Ewald Control File (`ewald.in`)

The main control file for Ewald. Here, specifics of the crystalline system under study, the method of producing QM-based charges and the geometrical specifications of the charge array are included.

#### Quantum Cluster File (`.qc`)

Specifies the Cartesian coordinates, symmetry constraints and initial charges of the quantum cluster (Zone 1). It is imperative that symmetrically equivalent atoms are placed one

|                       |   |
|-----------------------|---|
| urea                  | Enter general filename for the Ewald input/output files             |
| 1000                  | Enter number of random check points in zone 1:                      |
| 500                   | Enter # constraint atoms def. sphere containing zones 1 and 2:      |
| 0                     | Enter # atoms defining zone 1 sphere: 0=read from .qc file          |
| PATH/g09              | Enter Gaussian path including executable                            |
| PATH/Ewald            | Enter Ewald path including executable                               |
| P-1                   | Enter the space group of the system                                 |
| a b c                 | Enter the unit cell parameters a, b, c                              |
| $\alpha \beta \gamma$ | Enter the unit cell parameters $\alpha, \beta, \gamma$              |
| Mulliken              | Enter the charge-type to use (Mulliken or ESP implemented)          |
| opt=(settings)        | Enter the settings to use in the excited state optimisation routine |

after another in the .qc file and that their order matches that of the .uc file (see below). Specifying the number of equivalent atoms in the cluster ensures that the symmetry of the crystal itself is accounted for when the charge values are averaged and transferred to the external charge array.

| Atom Label | X         | Y        | Z         | Charge    | # of equivalent atoms in qc |
|------------|-----------|----------|-----------|-----------|-----------------------------|
| C          | 0.000000  | 2.795050 | 1.527640  | 0.956970  | 1                           |
| H          | 1.440570  | 4.235620 | 1.313870  | -0.383439 | 2                           |
| H          | -1.440570 | 1.354480 | 1.313870  | -0.383439 | 2                           |
| H          | 0.801620  | 3.596670 | -0.186700 | -0.241187 | 2                           |
| H          | -0.801620 | 1.993430 | -0.186700 | -0.241187 | 2                           |
| N          | 0.810560  | 3.605610 | 0.827060  | 0.100809  | 2                           |
| N          | -0.810560 | 1.984490 | 0.827060  | 0.100809  | 2                           |
| O          | 0.000000  | 2.795050 | 2.792970  | 0.090665  | 1                           |

### Unit Cell File (.uc)

Similar to the .qc file, here the fractional coordinates of the unit cell are specified along with symmetry constraints and initial charges. As for the .qc file, it is very important that symmetrically equivalent atoms are placed one after another in the .uc file and that the order of the atoms must match that of the .qc file. Careful attention must be paid to the total charge of the unit cell. Formally, it should be zero but numerical rounding in the guess charges can lead to a small non-zero total charge. If this residual charge is too large it can cause the charge fitting algorithm to explode, resulting in large, nonphysical charges. Matrix elements  $a_{ij}$  define the unit cell vectors and  $N_i$  defines the number of unit cells in the overall charge array (Zones 1, 2 and 3) which will have dimension  $2N_x \times 2N_y \times 2N_z$ .

### Seedfile

This file is just used to generate random numbers for use in the charge fitting process. Seed 1 should be in the range  $[1, 2^{31} - 86]$  and seed 2 in the range  $[1, 2^{31} - 250]$ .

### Gaussian Input File

Specifies parameters for excited state calculations on the quantum cluster. Note that – trivially – the atoms specified in the geometry of the Gaussian and .qc files should be the same. Pay attention also to the use of Charge and NoSymm in the Gaussian keyword commands. These are absolutely required and cannot be omitted. Charge ensures that Gaussian

| a <sub>1x</sub> | a <sub>1y</sub> | a <sub>1z</sub> | N <sub>x</sub> |            |                             |
|-----------------|-----------------|-----------------|----------------|------------|-----------------------------|
| a <sub>2x</sub> | a <sub>2y</sub> | a <sub>2z</sub> | N <sub>y</sub> |            |                             |
| a <sub>3x</sub> | a <sub>3y</sub> | a <sub>3z</sub> | N <sub>z</sub> |            |                             |
| 5.5901          | 0.0000          | 0.0000          | 6              |            |                             |
| 0.0000          | 5.5901          | 0.0000          | 6              |            |                             |
| 0.0000          | 0.0000          | 4.6674          | 6              |            |                             |
| X               | Y               | Z               | Charge         | Atom Label | # of equivalent atoms in uc |
| 0.500000        | 0.000000        | 0.672700        | 0.956970       | C          | 2                           |
| 0.000000        | 0.500000        | 0.327300        | 0.956970       | C          | 2                           |
| 0.257700        | 0.757700        | 0.281500        | -0.383439      | H          | 4                           |
| 0.742300        | 0.242300        | 0.281500        | -0.383439      | H          | 4                           |
| 0.757700        | 0.742300        | 0.718500        | -0.383439      | H          | 4                           |
| 0.242300        | 0.257700        | 0.718500        | -0.383439      | H          | 4                           |
| 0.143400        | 0.643400        | 0.960000        | -0.241187      | H          | 4                           |
| 0.856600        | 0.356600        | 0.960000        | -0.241187      | H          | 4                           |
| 0.643400        | 0.856600        | 0.040000        | -0.241187      | H          | 4                           |
| 0.356600        | 0.143400        | 0.040000        | -0.241187      | H          | 4                           |
| 0.855000        | 0.355000        | 0.177200        | 0.100809       | N          | 4                           |
| 0.645000        | 0.855000        | 0.822800        | 0.100809       | N          | 4                           |
| 0.355000        | 0.145000        | 0.822800        | 0.100809       | N          | 4                           |
| 0.145000        | 0.645000        | 0.177200        | 0.100809       | N          | 4                           |
| 0.500000        | 0.000000        | 0.401600        | 0.090665       | O          | 2                           |
| 0.000000        | 0.500000        | 0.598400        | 0.090665       | O          | 2                           |

|            |           |
|------------|-----------|
| seed 1     | seed 2    |
| 1474473010 | 704286502 |

knows to read the locations and values of the point charges that will be written to the input after the first Ewald run. NoSymm guarantees that the quantum cluster and point charges are positioned correctly and are not converted to the Gaussian standard orientation. Also note that density=current is required in order to obtain the charges of the excited state of interest, indicated by the root. It is important to note that an error will be returned if the 'opt' keyword is inserted in the Gaussian input file. If optimization of the geometry is required, SC-Ewald will automatically introduce the keyword at the appropriate moment in the algorithm. If specific actions during the optimization are required, these should be specified in the ewald.in control file.

|  |   |
|--|---|
| <pre>%chk=gau.chk %mem=8Gb %Nprocs=12 #P PBE1PBE/6-31g(d) NoSymm TD=(NStates=10,Root=1) #P density=current Charge  urea test of SC-Ewald  0 1 C 0.00000 2.79505 1.52764 O 0.00000 2.79505 2.79297 N 0.81056 3.60561 0.82706 N -0.81056 1.98449 0.82706 H 1.44057 4.23562 1.31387 H -1.44057 1.35448 1.31387 H 0.80162 3.59667 -0.18670 H -0.80162 1.99343 -0.18670</pre> | <p>Checkpoint<br/>Memory<br/>Processors<br/>Keyword Commands</p> <p>Title</p> <p>Charge, Multiplicity<br/>Atom, X, Y, Z</p> |
|--|---|

## Output Files

Aside from the standard Gaussian output file, Self-Consistent Ewald produces three additional outputs. Again these output files are for the test case of the urea molecular crystal.

### SC-Ewald Output (ewald.out)

This is the main output file of the program. It keeps track of the self-consistent procedure. The contents of the output are largely self-explanatory. The first statement outlines the mode

```
-----  
Welcome to the Self-Consistent Ewald program  
-----  
you have selected fully self-consistent excited state mode  
reading and checking input files...  
The path to Gaussian is : PATH/g09  
The path to Ewald is : PATH/Ewald  
-----  
Iteration : 0  
calculating new embedding charges with Ewald...  
writing Ewald charges to Gaussian input file...  
executing Gaussian...  
averaging charges according to symmetry...  
Convergence : NO  
-----  
Iteration : 1  
calculating new embedding charges with Ewald...  
writing Ewald charges to Gaussian input file...  
executing Gaussian...  
averaging charges according to symmetry...  
checking if charges have converged...  
Mean charge deviation = 0.0371816, Convergence threshold = 0.001  
Convergence : NO  
-----  
Iteration : 2  
calculating new embedding charges with Ewald...  
writing ewald charges to Gaussian input file...  
executing Gaussian...  
averaging charges according to symmetry...  
checking if charges have converged...  
Mean charge deviation = 0.0011019, Convergence threshold = 0.001  
Convergence : NO  
-----  
Iteration : 3  
calculating new embedding charges with Ewald...  
writing ewald charges to Gaussian input file...  
executing Gaussian...  
averaging charges according to symmetry...  
checking if charges have converged...  
Mean charge deviation = 0.0003159, Convergence threshold = 0.001  
Convergence : YES  
-----  
Successful termination of the Self-Consistent Ewald program!  
-----
```

that you have chosen for the SC-Ewald program to work with. The mode one uses is subject to the properties of interest and each of these is outlined below, in the next sub-section. It can be seen that the excited state potential converges in three iterations for urea, and this is indeed typical in general.

### Charge Fitting Output (filename.out)

Where, in this case, ‘filename’ is urea as was specified in the first line of ewald.in. This output file contains the results of the Ewald calculation and formation of the charge array. The key part of the output file is outlined below. The key values here are “rmspot” – the

```
(Ewald - direct sum) potential average 0.490918 rms 7.113251
dipole dx -2.930526 dy -2.930526 dz -0.000009 d2 17.175966 radmom 18.084128
unit cell: energy -7.180818

lapack...

Results after solving the system of linear eq.
q ranges: -1.028832 to 1.283388
rmspot = 0.000000

Not only the random chk points: rmspot=2.652796e-05
Only the random chk points: rmspot=3.253327e-05

Unit cell has 2 atoms of type C1
Unit cell has 4 atoms of type H1
Unit cell has 4 atoms of type H2
Unit cell has 4 atoms of type N1
Unit cell has 2 atoms of type O1
This gives Z=2

Madelung constant 0.421536 for R(H1-N1) 1.015281 Å
```

root mean squared deviation between the direct sum and Ewald sum potential at randomly checked points within Zone 1. These must be sufficiently small to ensure an accurate and reliable reproduction of the Ewald potential inside Zone 2. If these are deemed not to be small enough, the user can either increase the size of Zone 2 or Zone 3 or both.

### Compiled Output (output.log)

This file simply appends all of the Gaussian and Ewald inputs into one file so that the user has a detailed account of the whole process during the self-consistent procedure.

### Launching SC-Ewald Modes of Use

From the terminal, in the directory containing all of the above input files, SC-Ewald can be launched using the command:

```
./SCEwald.py natom ncell mode gau &
```

Where natom and ncell are the number of atoms in the quantum cluster (Zone 1) and the crystallographic unit cell, respectively. Parameter “gau” is the name of the relevant Gaussian input file. The mode corresponds to an integer - from 1 to 5 - and governs the actions SC-Ewald takes when executed. For each integer, these actions are:

1. An excited-state embedding potential fully equilibrated with the quantum-cluster excited state density is determined, along with the associated vertical excitation energies.
2. A single iteration is performed of the self-consistent cycle and the associated vertical excitation energies are computed.

3. The ground-state embedding potential is computed along with the associated vertical excitation energies. This should be considered the standard approach for the calculation of absorption energies.
4. Mode 1 is performed followed by an excited state optimization of the central cluster and a re-equilibration of the embedding potential with the newly acquired geometry and electronic density of the central cluster. This should be considered the standard mode for computing emission properties.
5. Mode 4 is performed self-consistently, producing an equilibrated set of point charge values, point charge positions and central cluster geometry.

When using the excited-state optimized geometry of the central cluster to reform the charge array, the Cartesian coordinates of the optimized central cluster are converted to fractional coordinates according to

$$\mathbf{r}_{cart.coord} = \bar{T}^{-1} \cdot \mathbf{r}_{fract.coord}, \quad (12.1)$$

where the transformation matrix  $\bar{T}$  is determined from the unit cell parameters:

$$\bar{T} = \begin{pmatrix} a & 0 & 0 \\ b\cos(\gamma) & b\sin(\gamma) & 0 \\ c\cos(\beta) & \frac{c(\cos(\alpha) - \cos(\beta)\cos(\gamma))}{\sin(\gamma)} & \frac{V}{a\sin(\gamma)} \end{pmatrix} \quad (12.2)$$

with the volume of the unit cell,  $V$ :

$$V = abc\sqrt{1 - \cos^2(\alpha) - \cos^2(\beta) - \cos^2(\gamma) + 2\cos(\alpha)\cos(\beta)\cos(\gamma)} \quad (12.3)$$

The symmetry operators of the selected space group are then applied and duplicate coordinates removed to yield the new atomic positions in the crystallographic unit cell, before reforming the overall charge array using this new unit cell.



## Chapter 13

# Appendix to Chapter 5

TABLE 13.1: Computed and experimental lattice parameters for the DHNA crystal.

| Parameter         | Experimental | Calculated | Error |
|-------------------|--------------|------------|-------|
| a Å               | 8.48         | 8.31       | 0.17  |
| b Å               | 6.76         | 6.29       | 0.46  |
| c Å               | 14.99        | 14.55      | 0.44  |
| $\beta$ (degrees) | 105.17       | 105.09     | 0.08  |

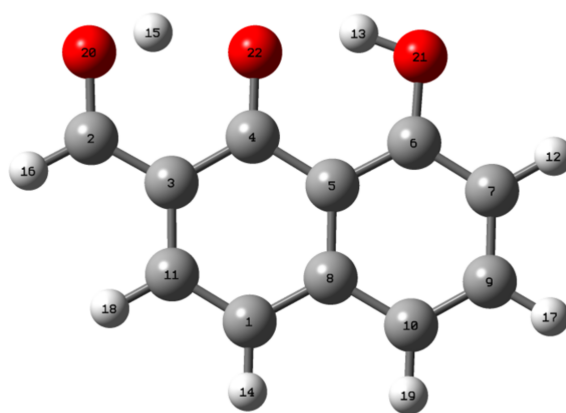


FIGURE 13.1: Molecule studied in this work with atom labels. The TA\* geometry is shown but atom labels are kept consistent throughout.

TABLE 13.2: Charges (in  $|e^-|$ ) computed for the central molecule (Zone 1) by Gaussian for each iteration during the generation of the self-consistent embedding potential. The procedure begins by using the Mulliken charges computed in the solid state as a guess. In this case, for TA\*, the charges reach convergence (mean average deviation  $\Delta_{MA} < 0.001|e^-|$ ) within 7 iterations.

| Atom          | Crystal | Iter. 1 | Iter. 2 | Iter. 3 | Iter. 4 | Iter. 5 | Iter. 6 | Iter. 7 |
|---------------|---------|---------|---------|---------|---------|---------|---------|---------|
| C 1           | -0.1650 | -0.1220 | -0.1234 | -0.1224 | -0.1228 | -0.1213 | -0.1206 | -0.1212 |
| C 2           | 0.2270  | 0.1461  | 0.1303  | 0.1139  | 0.1091  | 0.1056  | 0.1067  | 0.1082  |
| C 3           | 0.0400  | 0.0369  | 0.0354  | 0.0330  | 0.0315  | 0.0314  | 0.0308  | 0.0306  |
| C 4           | 0.2690  | 0.2113  | 0.1974  | 0.1891  | 0.1855  | 0.1842  | 0.1848  | 0.1858  |
| C 5           | 0.0560  | 0.0659  | 0.0659  | 0.0682  | 0.0684  | 0.0693  | 0.0691  | 0.0692  |
| C 6           | 0.2990  | 0.3078  | 0.2951  | 0.2989  | 0.2979  | 0.2986  | 0.2988  | 0.2999  |
| C 7           | -0.1420 | -0.1078 | -0.0967 | -0.0916 | -0.0903 | -0.0893 | -0.0886 | -0.0878 |
| C 8           | 0.0820  | 0.0557  | 0.0641  | 0.0695  | 0.0715  | 0.0736  | 0.0731  | 0.0726  |
| C 9           | -0.1070 | -0.1040 | -0.0708 | -0.0668 | -0.0626 | -0.0611 | -0.0590 | -0.0590 |
| C 10          | -0.1750 | -0.0925 | -0.0736 | -0.0695 | -0.0669 | -0.0649 | -0.0632 | -0.0644 |
| C 11          | -0.1370 | -0.1336 | -0.1432 | -0.1411 | -0.1436 | -0.1428 | -0.1435 | -0.1426 |
| H 12          | 0.1220  | 0.1321  | 0.1232  | 0.1260  | 0.1288  | 0.1345  | 0.1264  | 0.1219  |
| H 13          | 0.3720  | 0.3782  | 0.3839  | 0.3824  | 0.3823  | 0.3821  | 0.3838  | 0.3841  |
| H 14          | 0.1040  | 0.1374  | 0.1493  | 0.1467  | 0.1483  | 0.1469  | 0.1474  | 0.1481  |
| H 15          | 0.3850  | 0.3576  | 0.3529  | 0.3503  | 0.3500  | 0.3491  | 0.3508  | 0.3509  |
| H 16          | 0.1340  | 0.1208  | 0.1234  | 0.1230  | 0.1241  | 0.1225  | 0.1249  | 0.1247  |
| H 17          | 0.0920  | 0.0855  | 0.0948  | 0.0970  | 0.0978  | 0.0949  | 0.0901  | 0.0872  |
| H 18          | 0.1390  | 0.1953  | 0.1759  | 0.1773  | 0.1757  | 0.1748  | 0.1741  | 0.1763  |
| H 19          | 0.1010  | 0.1384  | 0.1432  | 0.1449  | 0.1458  | 0.1438  | 0.1422  | 0.1420  |
| O 20          | -0.5230 | -0.5951 | -0.6089 | -0.6111 | -0.6117 | -0.6151 | -0.6118 | -0.6108 |
| O 21          | -0.5620 | -0.5732 | -0.5743 | -0.5709 | -0.5714 | -0.5687 | -0.5700 | -0.5698 |
| O 22          | -0.6110 | -0.6409 | -0.6441 | -0.6470 | -0.6475 | -0.6481 | -0.6463 | -0.6459 |
| $\Delta_{MA}$ | -       | 0.0298  | 0.0096  | 0.0036  | 0.0016  | 0.0017  | 0.0017  | 0.0009  |

## Chapter 14

## Appendix to Chapter 6

| GAS-PHASE |               |             |        |                      |                  |       |         |        |        |                      |                  |
|-----------|---------------|-------------|--------|----------------------|------------------|-------|---------|--------|--------|----------------------|------------------|
| CAM-B3LYP |               |             |        |                      | B3LYP            |       |         |        |        |                      |                  |
| State     | Charac.       | coeff.      | E (eV) | $\lambda_{max}$ (nm) | Osc. Str. (a.u.) | State | Charac. | coeff. | E (eV) | $\lambda_{max}$ (nm) | Osc. Str. (a.u.) |
| S1        | H-L           | 0.67        | 3.30   | 375.97               | f=0.0751         | S1    | H-L     | 0.70   | 2.74   | 451.83               | f=0.0648         |
| S2        | H-5 -L        | 0.56        | 3.45   | 359.20               | f=0.0005         | S2    | H-2 -L  | 0.69   | 3.15   | 393.97               | f=0.0000         |
| S3        | H -L+1        | 0.54        | 4.29   | 288.75               | f=0.2404         | S3    | H-1 -L  | 0.70   | 3.73   | 332.74               | f=0.0059         |
| S4        | H-2 -L/H-6 -L | 0.47 / 0.37 | 4.66   | 265.92               | f=0.0001         | S4    | H -L+1  | 0.57   | 3.78   | 328.15               | f=0.2726         |
| S5        | H-4 -L/H -L+1 | 0.49 / 0.39 | 4.80   | 258.14               | f=1.8144         | S5    | H-3 -L  | 0.70   | 4.06   | 305.41               | f=0.0012         |

| THF (C-PCM) |         |        |      |        |          |       |               |             |      |        |          |
|-------------|---------|--------|------|--------|----------|-------|---------------|-------------|------|--------|----------|
| CAM-B3LYP   |         |        |      |        | B3LYP    |       |               |             |      |        |          |
| State       | Charac. | coeff. | (eV) | (nm)   | (a.u.)   | State | Charac.       | coeff.      | (eV) | (nm)   | (a.u.)   |
| S1          | H-L     | 0.67   | 3.15 | 393.54 | f=0.0734 | S1    | H -L          | 0.70        | 2.60 | 477.32 | f=0.0652 |
| S2          | H-7 -L  | 0.56   | 3.55 | 349.02 | f=0.0000 | S2    | H-5 -L/H-4 -L | 0.48 / 0.48 | 3.26 | 380.68 | f=0.0001 |
| S3          | H -L+1  | 0.53   | 4.24 | 292.14 | f=0.2338 | S3    | H-1 -L        | 0.70        | 3.58 | 345.88 | f=0.0112 |
| S4          | H-1 -L  | 0.51   | 4.56 | 271.75 | f=0.0015 | S4    | H -L+1        | 0.57        | 3.72 | 333.20 | f=0.2839 |
| S5          | H-4 -L  | 0.53   | 4.62 | 268.66 | f=2.1204 | S5    | H-2 -L        | 0.70        | 3.92 | 316.44 | f=0.0014 |

| MONOMER: ONIOM QM/QM' |         |        |      |        |          |       |              |             |      |        |          |
|-----------------------|---------|--------|------|--------|----------|-------|--------------|-------------|------|--------|----------|
| CAM-B3LYP/HF          |         |        |      |        | B3LYP/HF |       |              |             |      |        |          |
| State                 | Charac. | coeff. | (eV) | (nm)   | (a.u.)   | State | Charac.      | coeff.      | (eV) | (nm)   | (a.u.)   |
| S1                    | H-L     | 0.67   | 3.19 | 389.20 | f=0.0846 | S1    | H-L          | 0.70        | 2.65 | 467.52 | f=0.0480 |
| S2                    | H-5 -L  | 0.58   | 3.39 | 365.95 | f=0.0003 | S2    | H-5-L/H-2 -L | 0.40 / 0.41 | 3.26 | 379.86 | f=0.0000 |
| S3                    | H -L+1  | 0.56   | 4.20 | 295.32 | f=0.2921 | S3    | H-1-L+1      | 0.54        | 3.74 | 331.13 | f=0.1884 |
| S4                    | H-1 -L  | 0.50   | 4.57 | 271.58 | f=0.0010 | S4    | H-1-L        | 0.70        | 3.75 | 330.59 | f=0.0061 |
| S5                    | H-4 -L  | 0.50   | 4.70 | 263.52 | f=1.7570 | S5    | H-3-L        | 0.70        | 4.13 | 299.73 | f=0.0007 |

| MONOMER: SC-Ewald |               |             |      |        |          |       |         |        |      |        |          |
|-------------------|---------------|-------------|------|--------|----------|-------|---------|--------|------|--------|----------|
| CAM-B3LYP         |               |             |      |        | B3LYP    |       |         |        |      |        |          |
| State             | Charac.       | coeff.      | (eV) | (nm)   | (a.u.)   | State | Charac. | coeff. | (eV) | (nm)   | (a.u.)   |
| S1                | H-L           | 0.68        | 3.13 | 396.55 | f=0.0607 | S1    | H-L     | 0.70   | 2.70 | 457.80 | f=0.0663 |
| S2                | H-6 -L        | 0.52        | 3.57 | 347.19 | f=0.0000 | S2    | H-2-L   | 0.70   | 3.11 | 398.05 | f=0.0000 |
| S3                | H-4 -L/H -L+1 | 0.47 / 0.47 | 4.28 | 289.39 | f=0.0949 | S3    | H-1-L+1 | 0.70   | 3.69 | 335.77 | f=0.0068 |
| S4                | H-1 -L        | 0.47        | 4.62 | 268.64 | f=0.0006 | S4    | H-L+1   | 0.59   | 3.75 | 330.52 | f=0.3122 |
| S5                | H-4 -L/H -L+1 | 0.46 / 0.47 | 4.76 | 260.73 | f=2.0706 | S5    | H-3-L   | 0.70   | 4.04 | 306.79 | f=0.0010 |

FIGURE 14.1: Computed vertical excitations (the lowest five excited singlets are shown) at the B3LYP and CAM-B3LYP level in gas-phase and with implicit THF solvation (C-PCM). Results for monomer clusters employing the ONIOM QM/QM' approach and the SC-Ewald embedding model are also reported. The main character(s) of the transition (H-L stands for HOMO-LUMO), its coefficient(s), the related energy (E) and wavelength ( $\lambda_{max}$ ), and the oscillator strength (f) are shown.



## Chapter 15

# Appendix to Chapter 7

TABLE 15.1: Emission energies (in eV) calculated using SC-Ewald (emb) and in vacuum (vac) for monomer and dimer clusters of DFB-H. A test set of four density functionals are used comprising range separated hybrid (LC-PBE, CAM-B3LYP) and global hybrid (B3LYP, PBE0) functionals.

|               | B3LYP | CAM-B3LYP | PBE0 | LC-PBE |
|---------------|-------|-----------|------|--------|
| Monomer (vac) | 3.28  | 3.55      | 3.38 | 3.81   |
| Monomer (emb) | 3.10  | 3.39      | 3.18 | 3.60   |
| Dimer (vac)   | 2.39  | 3.26      | 2.46 | 3.61   |
| Dimer (emb)   | 2.15  | 3.12      | 2.24 | 3.45   |
| Monomer (sol) | 3.15  | 3.40      | 3.25 | 3.58   |

TABLE 15.2: Corresponding differences in emission energy ( $\Delta E_S^C$ ) going from solution to the solid state (in eV). A negative (positive) value indicates a red (blue) shift with respect to emission in solution.

|               | B3LYP | CAM-B3LYP | PBE0  | LC-PBE |
|---------------|-------|-----------|-------|--------|
| Monomer (vac) | 0.13  | 0.15      | 0.14  | 0.23   |
| Monomer (emb) | -0.05 | -0.00     | -0.07 | 0.02   |
| Dimer (vac)   | -0.76 | -0.14     | -0.79 | 0.03   |
| Dimer (emb)   | -1.00 | -0.28     | -1.02 | -0.13  |

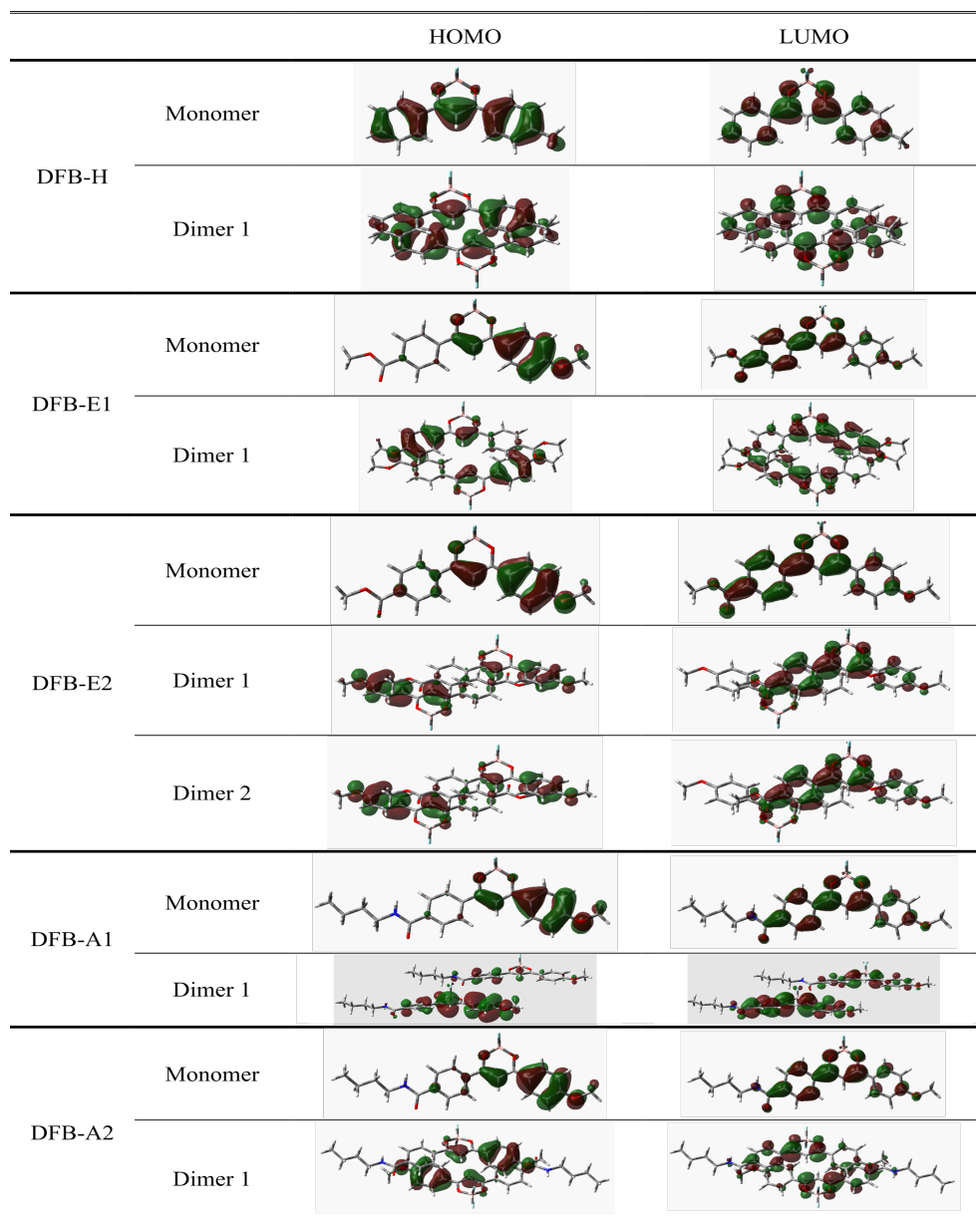


FIGURE 15.1: Computed molecular orbitals for each QM cluster used in this work. Orbitals shown were obtained with the CAM-B3LYP functional and an isovalue of 0.002 is used.

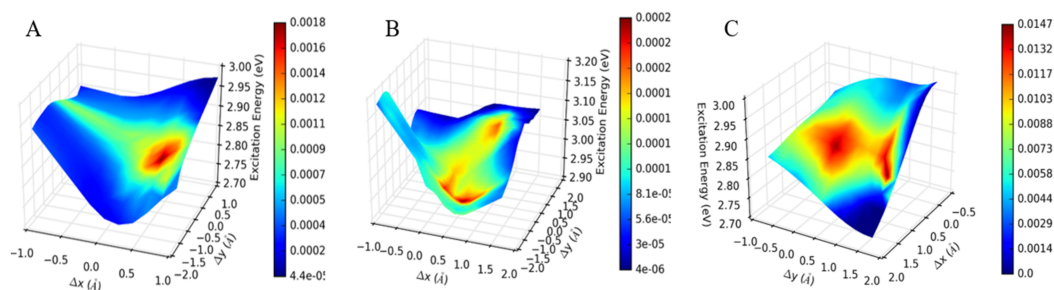


FIGURE 15.2: Surface plots of calculated emission energy for A) DFB-E1, B) DFB-E2 and C) DFB-A1 with respect to the defect scan coordinates. For a given pair of molecules in the crystalline phase, one molecule (highlighted in red) is displaced along its average plane in directions parallel ( $\delta x$ ) and perpendicular ( $\delta y$ ) to its long axis. A colour scheme is mapped onto this surface, representing the normalized product of each of these, yielding the weighted oscillator strength. Red (blue) regions represent a greater (lesser) contribution of a given scan coordinate to the overall computed emission spectrum in the amorphous phase.



## Chapter 16

# Appendix to Chapter 8

TABLE 16.1: Vertical excitation energies and associated oscillator strengths computed at PBE0 level for Zn[DMPMB].

| Transition | Wavelength (nm) | Oscillator Strength (a.u.) | Character           |
|------------|-----------------|----------------------------|---------------------|
| 1          | 264             | 0.235                      | $\pi\pi^*$ biphenyl |
| 2          | 266             | 2.995                      |                     |
| 3          | 267             | 1.020                      | $\pi\pi^*$ pyrazole |
| 4          | 266             | 0.128                      |                     |

TABLE 16.2: Vertical excitation energies and associated oscillator strengths computed at CAM-B3LYP level for Zn[DMPMB].

| Transition | Wavelength (nm) | Oscillator Strength (a.u.) | Character           |
|------------|-----------------|----------------------------|---------------------|
| 1          | 259             | 0.188                      | $\pi\pi^*$ biphenyl |
| 2          | 254             | 3.276                      |                     |
| 3          | 252             | 0.917                      | $\pi\pi^*$ pyrazole |
| 4          | 248             | 0.259                      |                     |

TABLE 16.3: Vertical excitation energies and associated oscillator strengths computed at PBE0 level for Cd[DMPMB].

| Transition | Wavelength (nm) | Oscillator Strength (a.u.) | Character           |
|------------|-----------------|----------------------------|---------------------|
| 1          | 269             | 0.195                      | $\pi\pi^*$ biphenyl |
| 2          | 269             | 2.995                      |                     |
| 3          | 270             | 0.998                      | $\pi\pi^*$ pyrazole |
| 4          | 270             | 0.224                      |                     |

TABLE 16.4: Vertical excitation energies and associated oscillator strengths computed at PBE0 for H<sub>2</sub>DMPMB ligand.

| Transition | Wavelength (nm) | Oscillator Strength (a.u.) | Character  |
|------------|-----------------|----------------------------|------------|
| 1          | 269             | 0.195                      |            |
| 2          | 269             | 2.995                      |            |
| 3          | 270             | 0.998                      | $\pi\pi^*$ |
| 4          | 270             | 0.224                      |            |
| 5          | 237             | 0.010                      |            |

## Chapter 17

## Appendix to Chapter 9

TABLE 17.1: MC-PDFT  $\Delta E_{H/L}$  splitting energies (in kcal/mol) calculated for 5 different active spaces and 4 different on-top density functionals: tPBE, ftPBE, trevPBE, ftrevPBE.

|          |            | Fe(II) |       |      |       |       | Fe(III) |       |      |       |  |
|----------|------------|--------|-------|------|-------|-------|---------|-------|------|-------|--|
|          |            | CO     | NCH   | CNH  | NH3   | H2O   | CO      | NCH   | CNH  | NH3   |  |
| tPBE     | (6/5,5)    | 31.2   | -5.8  | 44.4 | -24.6 | -28.6 | 6.4     | -18.1 | 23.6 | -22.6 |  |
|          | (10/9,7)   | 41.9   | -3.5  | 56.0 | -24.6 | -28.6 | 24.1    | -19.1 | 40.0 | -12.3 |  |
|          | (6/5,10)   | 44.3   | 0.3   | 59.0 | -9.1  | -25.7 | 14.7    | -5.7  | 32.8 | -16.8 |  |
|          | (10/9,12)  | 68.2   | -0.8  | 82.6 | -11.1 | -30.4 | 29.2    | -11.9 | 46.4 | -4.9  |  |
|          | (12/11,14) | 68.1   | 10.1  | 82.7 | -2.4  | -23.5 | 28.2    | -20.0 | 45.5 | -5.3  |  |
| ftPBE    | (6/5,5)    | 33.1   | -5.8  | 46.8 | -21.1 | -23.2 | 9.5     | -13.2 | 29.1 | -19.9 |  |
|          | (10/9,7)   | 49.9   | 0.1   | 63.1 | -20.0 | -22.2 | 26.0    | -16.2 | 41.9 | -10.3 |  |
|          | (6/5,10)   | 44.3   | 4.5   | 66.9 | -6.2  | -19.0 | 13.9    | -9.1  | 35.2 | -14.4 |  |
|          | (10/9,12)  | 71.0   | 6.9   | 84.0 | -6.4  | -23.4 | 31.9    | -8.2  | 49.8 | -2.5  |  |
|          | (12/11,14) | 70.9   | 12.9  | 85.8 | 1.9   | -24.1 | 36.2    | -11.3 | 50.1 | -1.1  |  |
| trevPBE  | (6/5,5)    | 21.4   | -12.6 | 34.8 | -29.2 | -31.6 | -0.5    | -22.0 | 16.5 | -27.4 |  |
|          | (10/9,7)   | 31.8   | -10.3 | 46.1 | -29.3 | -31.6 | 16.9    | -23.0 | 32.4 | -17.3 |  |
|          | (6/5,10)   | 21.4   | -12.6 | 52.9 | -29.2 | -31.6 | -0.5    | -22.0 | 16.5 | -27.4 |  |
|          | (10/9,12)  | 57.6   | -7.8  | 72.2 | -15.8 | -33.5 | 21.5    | -16.1 | 38.5 | -10.3 |  |
|          | (12/11,14) | 57.5   | 2.9   | 72.3 | -7.3  | -26.6 | 20.5    | -27.9 | 37.6 | -10.8 |  |
| ftrevPBE | (6/5,5)    | 32.2   | -3.4  | 45.9 | -18.2 | -23.4 | 13.5    | -7.7  | 30.8 | -14.4 |  |
|          | (10/9,7)   | 42.3   | -1.1  | 56.9 | -18.2 | -23.6 | 29.7    | -8.8  | 45.5 | -4.6  |  |
|          | (6/5,10)   | 32.2   | -3.4  | 66.3 | -18.2 | -23.4 | 13.5    | -7.7  | 30.8 | -14.4 |  |
|          | (10/9,12)  | 65.2   | -1.2  | 80.1 | -9.3  | -27.8 | 31.0    | -7.2  | 48.2 | -0.3  |  |
|          | (12/11,14) | 63.6   | 9.2   | 78.7 | -1.1  | -20.8 | 28.1    | -14.2 | 45.3 | -2.8  |  |

TABLE 17.2: CASSCF and CASPT2  $\Delta E_{H/L}$  splitting energies (in kcal/mol) calculated for 5 different active spaces.

|        |            | Fe(II) |       |       |       |       | Fe(III) |       |       |       |
|--------|------------|--------|-------|-------|-------|-------|---------|-------|-------|-------|
|        |            | CO     | NCH   | CNH   | NH3   | H2O   | CO      | NCH   | CNH   | NH3   |
| CASSCF | (6/5,5)    | -99.3  | -71.3 | -85.0 | -47.1 | -63.7 | -102.0  | -92.6 | -87.4 | -69.6 |
|        | (10/9,7)   | -92.6  | -69.9 | -77.5 | -47.1 | -62.7 | -85.9   | -85.8 | -70.2 | -69.6 |
|        | (6/5,10)   | -75.6  | -59.6 | -60.0 | -52.1 | -57.1 | -88.6   | -82.7 | -72.9 | -72.2 |
|        | (10/9,12)  | -33.5  | -43.9 | -15.1 | -38.0 | -44.8 | -48.5   | -62.6 | -29.8 | -52.4 |
|        | (12/11,14) | -32.8  | -46.2 | -14.5 | -40.1 | -51.7 | -45.8   | -59.7 | -27.2 | -42.0 |
| CASPT2 | (6/5,5)    | 32.4   | -19.0 | 48.6  | -43.4 | -49.7 | -2.2    | -37.0 | 17.0  | -40.3 |
|        | (10/9,7)   | 39.2   | -18.0 | 56.5  | -43.3 | -46.8 | 10.2    | -31.8 | 28.4  | -40.3 |
|        | (6/5,10)   | 26.6   | -19.6 | 42.6  | -29.9 | -49.3 | -4.6    | -38.1 | 14.3  | -32.0 |
|        | (10/9,12)  | 47.8   | -18.6 | 64.2  | -29.4 | -49.5 | 12.2    | -26.1 | 31.2  | -33.2 |
|        | (12/11,14) | 49.4   | -12.8 | 61.8  | -23.9 | -46.0 | 12.6    | -40.2 | 29.1  | -28.1 |

# Bibliography

- [1] Lei Ying, Cheuk-Lam Ho, Hongbin Wu, Yong Cao, and Wai-Yeung Wong. White polymer light-emitting devices for solid-state lighting: Materials, devices, and recent progress. *Advanced Materials*, 26(16):2459–2473, 2014.
- [2] Hisahiro Sasabe and Junji Kido. Recent progress in phosphorescent organic light-emitting devices. *European Journal of Organic Chemistry*, 2013(34):7653–7663, 2013.
- [3] Anyanee Kamkaew, Siang Hui Lim, Hong Boon Lee, Lik Voon Kiew, Lip Yong Chung, and Kevin Burgess. Bodipy dyes in photodynamic therapy. *Chemical Society Reviews*, 42(1):77–88, 2013.
- [4] ME Alberto, N Russo, and C Adamo. The contribution of computational studies to photodynamic therapy: Challenges and opportunities for the future of computational prediction. *Photodiagnosis and Photodynamic Therapy*, 17:A52, 2017.
- [5] Canan Acar, Ibrahim Dincer, and Greg F Naterer. Review of photocatalytic water-splitting methods for sustainable hydrogen production. *International Journal of Energy Research*, 40(11):1449–1473, 2016.
- [6] Wei Wang, Moses O Tadé, and Zongping Shao. Research progress of perovskite materials in photocatalysis-and photovoltaics-related energy conversion and environmental treatment. *Chemical Society Reviews*, 44(15):5371–5408, 2015.
- [7] AT Amos and BL Burrows. Solvent-shift effects on electronic spectra and excited-state dipole moments and polarizabilities. *Advances in Quantum Chemistry*, 7:289–313, 1973.
- [8] Martin Pope and Charles E Swenberg. *Electronic processes in organic crystals and polymers*. Oxford University Press on Demand, 1999.
- [9] Max Born and Robert Oppenheimer. Zur quantentheorie der molekeln. *Annalen der Physik*, 389(20):457–484, 1927.
- [10] Douglas R Hartree. The wave mechanics of an atom with a non-coulomb central field. part i. theory and methods. In *Mathematical Proceedings of the Cambridge Philosophical Society*, volume 24, pages 89–110. Cambridge Univ Press, 1928.
- [11] Douglas Rayne Hartree. The wave mechanics of an atom with a non-coulomb central field. part ii. some results and discussion. In *Mathematical Proceedings of the Cambridge Philosophical Society*, volume 24, pages 111–132. Cambridge Univ Press, 1928.

- [12] Clemens Carel Johannes Roothaan. New developments in molecular orbital theory. *Reviews of modern physics*, 23(2):69, 1951.
- [13] Christopher J Cramer. *Essentials of computational chemistry: theories and models*. John Wiley & Sons, 2013.
- [14] Pierre Hohenberg and Walter Kohn. Inhomogeneous electron gas. *Physical review*, 136(3B):B864, 1964.
- [15] Mel Levy. Universal variational functionals of electron densities, first-order density matrices, and natural spin-orbitals and solution of the v-representability problem. *Proceedings of the National Academy of Sciences*, 76(12):6062–6065, 1979.
- [16] Mel Levy. Electron densities in search of hamiltonians. *Physical Review A*, 26(3):1200, 1982.
- [17] John P Perdew and Mel Levy. Extrema of the density functional for the energy: Excited states from the ground-state theory. *Physical Review B*, 31(10):6264, 1985.
- [18] Walter Kohn and Lu Jeu Sham. Self-consistent equations including exchange and correlation effects. *Physical review*, 140(4A):A1133, 1965.
- [19] Seymour H Vosko, Leslie Wilk, and Marwan Nusair. Accurate spin-dependent electron liquid correlation energies for local spin density calculations: a critical analysis. *Canadian Journal of physics*, 58(8):1200–1211, 1980.
- [20] Paul AM Dirac. Note on exchange phenomena in the thomas atom. In *Mathematical Proceedings of the Cambridge Philosophical Society*, volume 26, pages 376–385. Cambridge Univ Press, 1930.
- [21] John P Perdew, Kieron Burke, and Matthias Ernzerhof. Generalized gradient approximation made simple. *Physical review letters*, 77(18):3865, 1996.
- [22] Carlo Adamo and Vincenzo Barone. Toward reliable density functional methods without adjustable parameters: The pbe0 model. *The Journal of chemical physics*, 110(13):6158–6170, 1999.
- [23] Erich Runge and Eberhard KU Gross. Density-functional theory for time-dependent systems. *Physical Review Letters*, 52(12):997, 1984.
- [24] Carsten A Ullrich. *Time-dependent density-functional theory: concepts and applications*. OUP Oxford, 2011.
- [25] Mark E Casida. Time-dependent density functional response theory of molecular systems: theory, computational methods, and functionals. 1996.
- [26] Andreas Dreuw, Jennifer L Weisman, and Martin Head-Gordon. Long-range charge-transfer excited states in time-dependent density functional theory require non-local exchange. *The Journal of chemical physics*, 119(6):2943–2946, 2003.

- [27] Tjalling Koopmans. Über die zuordnung von wellenfunktionen und eigenwerten zu den einzelnen elektronen eines atoms. *Physica*, 1(1-6):104–113, 1934.
- [28] Roi Baer, Ester Livshits, and Ulrike Salzner. Tuned range-separated hybrids in density functional theory. *Annual review of physical chemistry*, 61:85–109, 2010.
- [29] Bjorn O Roos, Peter R Taylor, Per EM Si, et al. A complete active space scf method (casscf) using a density matrix formulated super-ci approach. *Chemical Physics*, 48(2):157–173, 1980.
- [30] Laura Gagliardi, Donald G Truhlar, Giovanni Li Manni, Rebecca K Carlson, Chad E Hoyer, and Junwei Lucas Bao. Multiconfiguration pair-density functional theory: A new way to treat strongly correlated systems. *Accounts of Chemical Research*, 2016.
- [31] Giovanni Li Manni, Rebecca K Carlson, Sijie Luo, Dongxia Ma, Jeppe Olsen, Donald G Truhlar, and Laura Gagliardi. Multiconfiguration pair-density functional theory. *Journal of chemical theory and computation*, 10(9):3669–3680, 2014.
- [32] Rebecca K Carlson, Donald G Truhlar, and Laura Gagliardi. Multiconfiguration pair-density functional theory: A fully translated gradient approximation and its performance for transition metal dimers and the spectroscopy of re2cl82-. *Journal of chemical theory and computation*, 11(9):4077–4085, 2015.
- [33] Christopher J Cramer and Donald G Truhlar. Implicit solvation models: equilibria, structure, spectra, and dynamics. *Chemical Reviews*, 99(8):2161–2200, 1999.
- [34] Vincenzo Barone and Maurizio Cossi. Quantum calculation of molecular energies and energy gradients in solution by a conductor solvent model. *The Journal of Physical Chemistry A*, 102(11):1995–2001, 1998.
- [35] R Cammi, S Corni, B Mennucci, and J Tomasi. Electronic excitation energies of molecules in solution: State specific and linear response methods for nonequilibrium continuum solvation models. *The Journal of chemical physics*, 122(10):104513, 2005.
- [36] Roberto Improta, Vincenzo Barone, Giovanni Scalmani, and Michael J Frisch. A state-specific polarizable continuum model time dependent density functional theory method for excited state calculations in solution. *The Journal of chemical physics*, 125(5):054103, 2006.
- [37] Felix Bloch. Über die quantenmechanik der elektronen in kristallgittern. *Zeitschrift für Physik A Hadrons and Nuclei*, 52(7):555–600, 1929.
- [38] Roberto Dovesi. The language of band theory. In *Quantum-Mechanical Ab-initio Calculation of the Properties of Crystalline Materials*, pages 31–46. Springer, 1996.
- [39] André Severo Pereira Gomes and Christoph R Jacob. Quantum-chemical embedding methods for treating local electronic excitations in complex chemical systems. *Annual Reports Section "C" (Physical Chemistry)*, 108:222–277, 2012.

- [40] Keiji Morokuma. Oniom and its applications to material chemistry and catalyses. *Bulletin of the Korean Chemical Society*, 24(6):797–801, 2003.
- [41] Mats Svensson, Stephane Humbel, Robert DJ Froese, Toshiaki Matsubara, Stefan Sieber, and Keiji Morokuma. Oniom: a multilayered integrated mo+ mm method for geometry optimizations and single point energy predictions. a test for diels- alder reactions and pt (p (t-bu) 3) 2+ h2 oxidative addition. *The Journal of Physical Chemistry*, 100(50):19357–19363, 1996.
- [42] Hrant P Hratchian, Priya V Parandekar, Krishnan Raghavachari, Michael J Frisch, and Thom Vreven. Qm: Qm electronic embedding using mulliken atomic charges: Energies and analytic gradients in an oniom framework. *The Journal of chemical physics*, 128(3):034107, 2008.
- [43] Hai Lin and Donald G Truhlar. Qm/mm: what have we learned, where are we, and where do we go from here? *Theoretical Chemistry Accounts*, 117(2):185, 2007.
- [44] Mark A Thompson. Qm/mmpol: A consistent model for solute/solvent polarization. application to the aqueous solvation and spectroscopy of formaldehyde, acetaldehyde, and acetone. *The Journal of Physical Chemistry*, 100(34):14492–14507, 1996.
- [45] Chen Huang, Michele Pavone, and Emily A Carter. Quantum mechanical embedding theory based on a unique embedding potential. *The Journal of chemical physics*, 134(15):154110, 2011.
- [46] Asbjörn M Burow, Marek Sierka, Jens Döbler, and Joachim Sauer. Point defects in caF<sub>2</sub> and ceO<sub>2</sub> investigated by the periodic electrostatic embedded cluster method. *The Journal of chemical physics*, 130(17):174710, 2009.
- [47] Konstantin N Kudin and Gustavo E Scuseria. A fast multipole method for periodic systems with arbitrary unit cell geometries. *Chemical Physics Letters*, 283(1):61–68, 1998.
- [48] C Kittel. *Introduction to solid state physics*, 5th edn wiley. 1976.
- [49] HM Evjen. On the stability of certain heteropolar crystals. *Physical Review*, 39(4):675, 1932.
- [50] Paul P Ewald. Die berechnung optischer und elektrostatischer gitterpotentiale. *Annalen der Physik*, 369(3):253–287, 1921.
- [51] Mattias Klintonberg, SE Derenzo, and MJ Weber. Accurate crystal fields for embedded cluster calculations. *Computer physics communications*, 131(1-2):120–128, 2000.
- [52] Stephen E Derenzo, Mattias K Klintonberg, and Marvin J Weber. Determining point charge arrays that produce accurate ionic crystal fields for atomic cluster calculations. *The Journal of Chemical Physics*, 112(5):2074–2081, 2000.
- [53] Masaaki Kawata and Masuhiro Mikami. Rapid calculation of two-dimensional ewald summation. *Chemical physics letters*, 340(1):157–164, 2001.

- [54] DJ Langridge, JF Hart, and S Crampin. Ewald summation technique for one-dimensional charge distributions. *Computer physics communications*, 134(1):78–85, 2001.
- [55] Curtis W Hoganson and Gerald T Babcock. A metalloradical mechanism for the generation of oxygen from water in photosynthesis. *Science*, 277(5334):1953–1956, 1997.
- [56] James B Howard and Douglas C Rees. How many metals does it take to fix n<sub>2</sub>? a mechanistic overview of biological nitrogen fixation. *Proceedings of the National Academy of Sciences*, 103(46):17088–17093, 2006.
- [57] David R Weinberg, Christopher J Gagliardi, Jonathan F Hull, Christine Fecencko Murphy, Caleb A Kent, Brittany C Westlake, Amit Paul, Daniel H Ess, Dewey Granville McCafferty, and Thomas J Meyer. Proton-coupled electron transfer. *Chemical Reviews*, 112(7):4016–4093, 2012.
- [58] J Goodman and LE Brus. Proton transfer and tautomerism in an excited state of methyl salicylate. *Journal of the American Chemical Society*, 100(24):7472–7474, 1978.
- [59] Jianzhang Zhao, Shaomin Ji, Yinghui Chen, Huimin Guo, and Pei Yang. Excited state intramolecular proton transfer (esipt): from principal photophysics to the development of new chromophores and applications in fluorescent molecular probes and luminescent materials. *Physical Chemistry Chemical Physics*, 14(25):8803–8817, 2012.
- [60] Kew-Yu Chen, Cheng-Chih Hsieh, Yi-Ming Cheng, Chin-Hung Lai, and Pi-Tai Chou. Extensive spectral tuning of the proton transfer emission from 550 to 675 nm via a rational derivatization of 10-hydroxybenzo [h] quinoline. *Chemical communications*, (42):4395–4397, 2006.
- [61] Bernhard Dick and Niko P Ernstring. Excited-state intramolecular proton transfer in 3-hydroxyflavone isolated in solid argon: fluorescence and fluorescence-excitation spectra and tautomer fluorescence rise time. *Journal of Physical Chemistry*, 91(16):4261–4265, 1987.
- [62] Jinling Cheng, Di Liu, Lijun Bao, Kai Xu, Yang Yang, and Keli Han. A single 2-(2'-hydroxyphenyl) benzothiazole derivative can achieve pure white-light emission. *Chemistry—An Asian Journal*, 9(11):3215–3220, 2014.
- [63] Jinling Cheng, Di Liu, Wei Li, Lijun Bao, and Keli Han. Comprehensive studies on excited-state proton transfer of a series of 2-(2'-hydroxyphenyl) benzothiazole derivatives: Synthesis, optical properties, and theoretical calculations. *The Journal of Physical Chemistry C*, 119(8):4242–4251, 2015.
- [64] Ji Eon Kwon and Soo Young Park. Advanced organic optoelectronic materials: Harnessing excited-state intramolecular proton transfer (esipt) process. *Advanced Materials*, 23(32):3615–3642, 2011.
- [65] Vikas S Padalkar and Shu Seki. Excited-state intramolecular proton-transfer (esipt)-inspired solid state emitters. *Chemical Society Reviews*, 45(1):169–202, 2016.

- [66] Kuo-Chun Tang, Ming-Jen Chang, Tsung-Yi Lin, Hsiao-An Pan, Tzu-Chien Fang, Kew-Yu Chen, Wen-Yi Hung, Yu-Hsiang Hsu, and Pi-Tai Chou. Fine tuning the energetics of excited-state intramolecular proton transfer (esipt): white light generation in a single esipt system. *Journal of the American Chemical Society*, 133(44):17738–17745, 2011.
- [67] Hideaki Shono, Tatsuya Ohkawa, Haruhiko Tomoda, Toshiki Mutai, and Koji Araki. Fabrication of colorless organic materials exhibiting white luminescence using normal and excited-state intramolecular proton transfer processes. *ACS applied materials & interfaces*, 3(3):654–657, 2011.
- [68] Vandana Bhalla and Manoj Kumar. Fluoride triggered fluorescence “turn on” sensor for zn<sup>2+</sup> ions based on pentaquinone scaffold that works as a molecular keypad lock. *Organic letters*, 14(11):2802–2805, 2012.
- [69] Hao-Ming Lv, Yi Chen, Jian Lei, Chak-Tong Au, and Shuang-Feng Yin. An esipt-based ratiometric fluorescent probe for the imaging of nitroxyl in living cells. *Analytical Methods*, 7(9):3883–3887, 2015.
- [70] Dolores Santa María, Rosa M Claramunt, Vladimir Bobosik, M Carmen Torralba, M Rosario Torres, Ibon Alkorta, and José Elguero. Synthesis and structural study of 2-arylbenzotriazoles related to tinuvins. *Tetrahedron*, 69(14):3027–3038, 2013.
- [71] Vladimir I Tomin, Alexander P Demchenko, and Pi-Tai Chou. Thermodynamic vs. kinetic control of excited-state proton transfer reactions. *Journal of Photochemistry and Photobiology C: Photochemistry Reviews*, 22:1–18, 2015.
- [72] Cheng-Chih Hsieh, Chang-Ming Jiang, and Pi-Tai Chou. Recent experimental advances on excited-state intramolecular proton coupled electron transfer reaction. *Accounts of chemical research*, 43(10):1364–1374, 2010.
- [73] Chia-Yu Peng, Jiun-Yi Shen, Yi-Ting Chen, Pei-Jhen Wu, Wen-Yi Hung, Wei-Ping Hu, and Pi-Tai Chou. Optically triggered stepwise double-proton transfer in an intramolecular proton relay: a case study of 1, 8-dihydroxy-2-naphthaldehyde. *Journal of the American Chemical Society*, 137(45):14349–14357, 2015.
- [74] Roberto Dovesi, Roberto Orlando, Bartolomeo Civalleri, Carla Roetti, Victor R Saunders, and Claudio M Zicovich-Wilson. Crystal: a computational tool for the ab initio study of the electronic properties of crystals. *Zeitschrift fur Kristallographie-Crystalline Materials*, 220(5/6):571–573, 2005.
- [75] James D Pack and Hendrik J Monkhorst. "special points for brillouin-zone integrations"—a reply. *Physical Review B*, 16(4):1748, 1977.
- [76] FJ Devlin, JW Finley, PJ Stephens, MJ Frisch, et al. Ab-initio calculation of vibrational absorption and circular-dichroism spectra using density-functional force-fields—a comparison of local, nonlocal, and hybrid density functionals. *Journal of Physical Chemistry*, 99(46):16883–16902, 1995.

- [77] Stefan Grimme. Semiempirical gga-type density functional constructed with a long-range dispersion correction. *Journal of computational chemistry*, 27(15):1787–1799, 2006.
- [78] Liam Wilbraham, Carlo Adamo, Frédéric Labat, and Ilaria Ciofini. Electrostatic embedding to model the impact of environment on photophysical properties of molecular crystals: A self-consistent charge adjustment procedure. *Journal of chemical theory and computation*, 12(7):3316–3324, 2016.
- [79] MJ Frisch, GW Trucks, HB Schlegel, GE Scuseria, MA Robb, JR Cheeseman, G Scalmani, V Barone, GA Petersson, H Nakatsuji, et al. Gaussian 09 revision a.; 2009. *Gaussian Inc, Wallingford CT*.
- [80] Johannes Weber and Jörn Schmedt auf der Günne. Calculation of nmr parameters in ionic solids by an improved self-consistent embedded cluster method. *Physical Chemistry Chemical Physics*, 12(3):583–603, 2010.
- [81] G. v. Bunau. J. b. birks: Photophysics of aromatic molecules. wiley-interscience, london 1970. 704 seiten. preis: 210s. *Berichte der Bunsengesellschaft für physikalische Chemie*, 74(12):1294–1295, 1970.
- [82] AV Eltsov. Organic photochromes 1990.
- [83] BV Gemert, JC Crano, and RJ Guglielmetti. Topics in applied chemistry, organic photochromic and thermochromic compounds, vol. 1, chap. 3. 1999.
- [84] Yuning Hong, Jacky WY Lam, and Ben Zhong Tang. Aggregation-induced emission. *Chemical Society Reviews*, 40(11):5361–5388, 2011.
- [85] Ching W Tang and Steven A VanSlyke. Organic electroluminescent diodes. *Applied physics letters*, 51(12):913–915, 1987.
- [86] Zujin Zhao, Shuming Chen, Chunmei Deng, Jacky WY Lam, Carrie YK Chan, Ping Lu, Zhiming Wang, Bingbing Hu, Xiaopeng Chen, Hoi Sing Kwok, et al. Construction of efficient solid emitters with conventional and aie luminogens for blue organic light-emitting diodes. *Journal of Materials Chemistry*, 21(29):10949–10956, 2011.
- [87] Yuning Hong, Jacky WY Lam, and Ben Zhong Tang. Aggregation-induced emission: phenomenon, mechanism and applications. *Chemical communications*, (29):4332–4353, 2009.
- [88] Junwu Chen, Charles CW Law, Jacky WY Lam, Yuping Dong, Samuel MF Lo, Ian D Williams, Daoben Zhu, and Ben Zhong Tang. Synthesis, light emission, nanoaggregation, and restricted intramolecular rotation of 1, 1-substituted 2, 3, 4, 5-tetraphenylsiloles. *Chemistry of materials*, 15(7):1535–1546, 2003.
- [89] Zujin Zhao, Bairong He, and Ben Zhong Tang. Aggregation-induced emission of siloles. *Chemical Science*, 6(10):5347–5365, 2015.

- [90] Ju Mei, Nelson LC Leung, Ryan TK Kwok, Jacky WY Lam, and Ben Zhong Tang. Aggregation-induced emission: together we shine, united we soar! *Chem. Rev*, 115(21):11718–11940, 2015.
- [91] Michael Kasha. Energy transfer mechanisms and the molecular exciton model for molecular aggregates. *Radiation research*, 20(1):55–70, 1963.
- [92] Hai Qian, Morgan E Cousins, Erik H Horak, Audrey Wakefield, Matthew D Liptak, and Ivan Aprahamian. Suppression of kasha’s rule as a mechanism for fluorescent molecular rotors and aggregation-induced emission. *Nature Chemistry*, 2016.
- [93] Qunyan Wu, Chunmei Deng, Qian Peng, Yingli Niu, and Zhigang Shuai. Quantum chemical insights into the aggregation induced emission phenomena: A qm/mm study for pyrazine derivatives. *Journal of computational chemistry*, 33(23):1862–1869, 2012.
- [94] Qunyan Wu, Qian Peng, Yingli Niu, Xing Gao, and Zhigang Shuai. Theoretical insights into the aggregation-induced emission by hydrogen bonding: a qm/mm study. *The Journal of Physical Chemistry A*, 116(15):3881–3888, 2012.
- [95] Mao-Sen Yuan, Dong-En Wang, Pengchong Xue, Wenji Wang, Jian-Chun Wang, Qin Tu, Zhiqiang Liu, Yang Liu, Yanrong Zhang, and Jinyi Wang. Fluorenone organic crystals: two-color luminescence switching and reversible phase transformations between  $\pi$ - $\pi$  stacking-directed packing and hydrogen bond-directed packing. *Chemistry of Materials*, 26(7):2467–2477, 2014.
- [96] Davide Presti, Liam Wilbraham, Cecilia Targa, Frédéric Labat, Alfonso Pedone, Maria Cristina Menziani, Ilaria Ciofini, and Carlo Adamo. Understanding aggregation-induced emission in molecular crystals: Insights from theory. *The Journal of Physical Chemistry C*, 121(10):5747–5752, 2017.
- [97] Takeshi Yanai, David P Tew, and Nicholas C Handy. A new hybrid exchange–correlation functional using the coulomb-attenuating method (cam-b3lyp). *Chemical Physics Letters*, 393(1):51–57, 2004.
- [98] Bartolomeo Civalleri, Claudio M Zicovich-Wilson, Loredana Valenzano, and Piero Ugliengo. B3lyp augmented with an empirical dispersion term (b3lyp-d\*) as applied to molecular crystals. *CrystEngComm*, 10(4):405–410, 2008.
- [99] Denis Jacquemin, Eric A Perpète, Gustavo E Scuseria, Ilaria Ciofini, and Carlo Adamo. Td-dft performance for the visible absorption spectra of organic dyes: conventional versus long-range hybrids. *Journal of Chemical Theory and Computation*, 4(1):123–135, 2008.
- [100] Eugene Hadjoudis and Irene M Mavridis. Photochromism and thermochromism of schiff bases in the solid state: structural aspects. *Chemical Society Reviews*, 33(9):579–588, 2004.

- [101] Joel Bernstein, Roger J Davey, and Jan-Olav Henck. Concomitant polymorphs. *Angewandte Chemie International Edition*, 38(23):3440–3461, 1999.
- [102] Guoqing Zhang, Jiwei Lu, Michal Sabat, and Cassandra L Fraser. Polymorphism and reversible mechanochromic luminescence for solid-state difluoroboron avobenzene. *Journal of the American Chemical Society*, 132(7):2160–2162, 2010.
- [103] Yoshimitsu Sagara and Takashi Kato. Mechanically induced luminescence changes in molecular assemblies. *Nature chemistry*, 1(8):605, 2009.
- [104] Lu Wang, Kai Wang, Bo Zou, Kaiqi Ye, Hongyu Zhang, and Yue Wang. Luminescent chromism of boron diketonate crystals: distinct responses to different stresses. *Advanced Materials*, 27(18):2918–2922, 2015.
- [105] Stephen L Mayo, Barry D Olafson, and William A Goddard. Dreiding: a generic force field for molecular simulations. *Journal of Physical chemistry*, 94(26):8897–8909, 1990.
- [106] Anatoliy N Sokolov, Sule Atahan-Evrenk, Rajib Mondal, Hylke B Akkerman, Roel S Sánchez-Carrera, Sergio Granados-Focil, Joshua Schrier, Stefan CB Mannsfeld, Arjan P Zoombelt, Zhenan Bao, et al. From computational discovery to experimental characterization of a high hole mobility organic crystal. *Nature communications*, 2:437, 2011.
- [107] Domenico Alberga, Ilaria Ciofini, Giuseppe Felice Mangiatordi, Alfonso Pedone, Gianluca Lattanzi, Jean Roncali, and Carlo Adamo. Effects of substituents on transport properties of molecular materials for organic solar cells: a theoretical investigation. *Chemistry of Materials*, 2016.
- [108] Wenbo Yu, Xibing He, Kenno Vanommeslaeghe, and Alexander D MacKerell. Extension of the charmm general force field to sulfonyl-containing compounds and its utility in biomolecular simulations. *Journal of computational chemistry*, 33(31):2451–2468, 2012.
- [109] Davide Presti, Frederic Labat, Alfonso Pedone, Michael J Frisch, Hrant P Hratchian, Ilaria Ciofini, Maria Cristina Menziani, and Carlo Adamo. Computational protocol for modeling thermochromic molecular crystals: salicylidene aniline as a case study. *Journal of Chemical Theory and Computation*, 10(12):5577–5585, 2014.
- [110] Qiong Cao, Shuzhang Xiao, Miaofu Mao, Xiaohong Chen, Sa Wang, Ling Li, and Kun Zou. Structure–property correlation of solid-emissive boron–fluorine derivatives. *Journal of Organometallic Chemistry*, 717:147–151, 2012.
- [111] Samuel Guieu, Joana Pinto, Vera LM Silva, João Rocha, and Artur Silva. Synthesis, post-modification and fluorescence properties of boron diketonate complexes. *European Journal of Organic Chemistry*, 2015(16):3423–3426, 2015.

- [112] James C Phillips, Rosemary Braun, Wei Wang, James Gumbart, Emad Tajkhorshid, Elizabeth Villa, Christophe Chipot, Robert D Skeel, Laxmikant Kale, and Klaus Schulten. Scalable molecular dynamics with namd. *Journal of computational chemistry*, 26(16):1781–1802, 2005.
- [113] Glenn J Martyna, Douglas J Tobias, and Michael L Klein. Constant pressure molecular dynamics algorithms. *The Journal of Chemical Physics*, 101(5):4177–4189, 1994.
- [114] Scott E Feller, Yuhong Zhang, Richard W Pastor, and Bernard R Brooks. Constant pressure molecular dynamics simulation: the langevin piston method. *The Journal of chemical physics*, 103(11):4613–4621, 1995.
- [115] SA Adelman and JD Doll. Generalized langevin equation approach for atom/solid-surface scattering: General formulation for classical scattering off harmonic solids. *The Journal of chemical physics*, 64(6):2375–2388, 1976.
- [116] Xiaoping Wu, Zhiping Liu, Shiping Huang, and Wenchuan Wang. Molecular dynamics simulation of room-temperature ionic liquid mixture of [bmim][bf 4] and acetonitrile by a refined force field. *Physical Chemistry Chemical Physics*, 7(14):2771–2779, 2005.
- [117] Gamidi Rama Krishna, Mangalampalli SRN Kiran, Cassandra L Fraser, Upadrasta Ramamurthy, and Chilla Malla Reddy. The relationship of solid-state plasticity to mechanochromic luminescence in difluoroboron avobenzene polymorphs. *Advanced Functional Materials*, 23(11):1422–1430, 2013.
- [118] Hajime Ito, Tomohisa Saito, Naoya Oshima, Noboru Kitamura, Shoji Ishizaka, Yukio Hinatsu, Makoto Wakeshima, Masako Kato, Kiyoshi Tsuge, and Masaya Sawamura. Reversible mechanochromic luminescence of [(c6f5au) 2 ( $\mu$ -1, 4-diisocyanobenzene)]. *Journal of the American Chemical Society*, 130(31):10044–10045, 2008.
- [119] Hong-Cai Zhou, Jeffrey R Long, and Omar M Yaghi. Introduction to metal–organic frameworks. 2012.
- [120] Susumu Kitagawa et al. Metal–organic frameworks (mofs). *Chemical Society Reviews*, 43(16):5415–5418, 2014.
- [121] Junya Wang, Liang Huang, Ruoyan Yang, Zhang Zhang, Jingwen Wu, Yanshan Gao, Qiang Wang, Dermot O’Hare, and Ziyi Zhong. Recent advances in solid sorbents for co 2 capture and new development trends. *Energy & Environmental Science*, 7(11):3478–3518, 2014.
- [122] Zhichao Hu, Benjamin J Deibert, and Jing Li. Luminescent metal–organic frameworks for chemical sensing and explosive detection. *Chemical Society Reviews*, 43(16):5815–5840, 2014.
- [123] Samuel O Odoh, Christopher J Cramer, Donald G Truhlar, and Laura Gagliardi. Quantum-chemical characterization of the properties and reactivities of metal–organic frameworks. *Chemical reviews*, 115(12):6051–6111, 2015.

- [124] Amarajothi Dhakshinamoorthy, Abdullah M Asiri, and Hermenegildo Garcia. Catalysis by metal–organic frameworks in water. *Chemical Communications*, 50(85):12800–12814, 2014.
- [125] François-Xavier Coudert and Alain H Fuchs. Computational characterization and prediction of metal–organic framework properties. *Coordination Chemistry Reviews*, 307:211–236, 2016.
- [126] Johanna Heine and Klaus Müller-Buschbaum. Engineering metal-based luminescence in coordination polymers and metal–organic frameworks. *Chemical Society Reviews*, 42(24):9232–9242, 2013.
- [127] Yuanjing Cui, Yanfeng Yue, Guodong Qian, and Banglin Chen. Luminescent functional metal–organic frameworks. *Chemical reviews*, 112(2):1126–1162, 2011.
- [128] MD Allendorf, CA Bauer, RK Bhakta, and RJT Houk. Luminescent metal–organic frameworks. *Chemical Society Reviews*, 38(5):1330–1352, 2009.
- [129] Aurel Tabacaru, Claudio Pettinari, Fabio Marchetti, Simona Galli, and Norberto Masciocchi. Bis (pyrazolato)-based metal–organic frameworks fabricated with 4,4'-bis((3,5-dimethyl-1 h-pyrazol-4-yl) methyl) biphenyl and late transition metals. *Crystal Growth & Design*, 14(6):3142–3152, 2014.
- [130] Liam Wilbraham, François-Xavier Coudert, and Ilaria Ciofini. Modelling photophysical properties of metal–organic frameworks: a density functional theory based approach. *Physical Chemistry Chemical Physics*, 18(36):25176–25182, 2016.
- [131] Michael F Peintinger, Daniel Vilela Oliveira, and Thomas Bredow. Consistent gaussian basis sets of triple-zeta valence with polarization quality for solid-state calculations. *Journal of Computational Chemistry*, 34(6):451–459, 2013.
- [132] Y Dou, RG Egdell, DSL Law, NM Harrison, and BG Searle. An experimental and theoretical investigation of the electronic structure of cdo. *Journal of Physics: Condensed Matter*, 10(38):8447, 1998.
- [133] Axel D Becke. Density-functional exchange-energy approximation with correct asymptotic behavior. *Physical review A*, 38(6):3098, 1988.
- [134] Chengteh Lee, Weitao Yang, and Robert G Parr. Development of the colle-salvetti correlation-energy formula into a functional of the electron density. *Physical review B*, 37(2):785, 1988.
- [135] John P Perdew, Adrienn Ruzsinszky, Gábor I Csonka, Oleg A Vydrov, Gustavo E Scuseria, Lucian A Constantin, Xiaolan Zhou, and Kieron Burke. Restoring the density-gradient expansion for exchange in solids and surfaces. *Physical Review Letters*, 100(13):136406, 2008.

- [136] Lindsay E Roy, P Jeffrey Hay, and Richard L Martin. Revised basis sets for the lanl effective core potentials. *Journal of chemical theory and computation*, 4(7):1029–1031, 2008.
- [137] Denis Jacquemin, Valérie Wathelet, Eric A Perpète, and Carlo Adamo. Extensive tddft benchmark: singlet-excited states of organic molecules. *Journal of Chemical Theory and Computation*, 5(9):2420–2435, 2009.
- [138] Wai-Yeung Wong, Li Liu, and Jian-Xin Shi. Triplet emission in soluble mercury (ii) polyyne polymers. *Angewandte Chemie International Edition*, 42(34):4064–4068, 2003.
- [139] Hsiu-Yi Chao, Wei Lu, Yanqin Li, Michael CW Chan, Chi-Ming Che, Kung-Kai Cheung, and Nianyong Zhu. Organic triplet emissions of arylacetylide moieties harnessed through coordination to [au (pcy<sub>3</sub>)<sup>+</sup>]. effect of molecular structure upon photoluminescent properties. *Journal of the American Chemical Society*, 124(49):14696–14706, 2002.
- [140] Jeremy N Harvey, Rinaldo Poli, and Kevin M Smith. Understanding the reactivity of transition metal complexes involving multiple spin states. *Coordination Chemistry Reviews*, 238–239:347 – 361, 2003. Theoretical and Computational Chemistry.
- [141] Ingmar Bauer and Hans-Joachim Knölker. Iron catalysis in organic synthesis. *Chemical reviews*, 115(9):3170–3387, 2015.
- [142] Malcolm A Halcrow. Structure: function relationships in molecular spin-crossover complexes. *Chemical Society Reviews*, 40(7):4119–4142, 2011.
- [143] Jean-François Létard, Philippe Guionneau, and Laurence Goux-Capes. Towards spin crossover applications. *Spin Crossover in Transition Metal Compounds III*, pages 1–19, 2004.
- [144] S Zerdane, Liam Wilbraham, Marco Cammarata, Olga Iasco, Eric Rivière, M-L Boillot, Ilaria Ciofini, and Eric Collet. Comparison of structural dynamics and coherence of d–d and mlct light-induced spin state trapping. *Chemical Science*, 2017.
- [145] Kasper P Kepp. Consistent descriptions of metal–ligand bonds and spin-crossover in inorganic chemistry. *Coordination Chemistry Reviews*, 257(1):196–209, 2013.
- [146] Christopher J Cramer and Donald G Truhlar. Density functional theory for transition metals and transition metal chemistry. *Physical Chemistry Chemical Physics*, 11(46):10757–10816, 2009.
- [147] Georg Ganzenmüller, Nabil Berkaine, Antony Fouqueau, Mark E Casida, and Markus Reiher. Comparison of density functionals for differences between the high-(t 2 g 5) and low-(a 1 g 1) spin states of iron (ii) compounds. iv. results for the ferrous complexes [fe (l)(‘nhs 4’)]. *The Journal of chemical physics*, 122(23):234321, 2005.
- [148] Marcel Swart, André R Groenhof, Andreas W Ehlers, and Koop Lammertsma. Validation of exchange- correlation functionals for spin states of iron complexes. *The Journal of Physical Chemistry A*, 108(25):5479–5483, 2004.

- [149] Oliver Salomon, Markus Reiher, and Bernd Artur Hess. Assertion and validation of the performance of the b3lyp\* functional for the first transition metal row and the g2 test set. *The Journal of chemical physics*, 117(10):4729–4737, 2002.
- [150] Efthymios I Ioannidis and Heather J Kulik. Towards quantifying the role of exact exchange in predictions of transition metal complex properties. *The Journal of chemical physics*, 143(3):034104, 2015.
- [151] Efthymios I Ioannidis and Heather J Kulik. Ligand-field-dependent behavior of meta-gga exchange in transition-metal complex spin-state ordering. *The Journal of Physical Chemistry A*, 2017.
- [152] Kerstin Andersson, Per Aake Malmqvist, Bjoern O. Roos, Andrzej J. Sadlej, and Krzysztof Wolinski. Second-order perturbation theory with a casscf reference function. *The Journal of Physical Chemistry*, 94(14):5483–5488, 1990.
- [153] Andrew M Sand, Donald G Truhlar, and Laura Gagliardi. Efficient algorithm for multiconfiguration pair-density functional theory with application to the heterolytic dissociation energy of ferrocene. *The Journal of Chemical Physics*, 146(3):034101, 2017.
- [154] Samuel O Odoh, Giovanni Li Manni, Rebecca K Carlson, Donald G Truhlar, and Laura Gagliardi. Separated-pair approximation and separated-pair pair-density functional theory. *Chemical Science*, 7(3):2399–2413, 2016.
- [155] Liam Wilbraham, Pragma Verma, Donald G Truhlar, Laura Gagliardi, and Ilaria Ciofini. Multiconfiguration pair-density functional theory predicts spin-state ordering in iron complexes with the same accuracy as complete active space second-order perturbation theory at a significantly reduced computational cost. *The Journal of Physical Chemistry Letters*, 8(9):2026–2030, 2017.
- [156] Yingkai Zhang and Weitao Yang. Comment on “generalized gradient approximation made simple”. *Physical Review Letters*, 80(4):890, 1998.
- [157] John P Perdew, Andreas Savin, and Kieron Burke. Escaping the symmetry dilemma through a pair-density interpretation of spin-density functional theory. *Physical Review A*, 51(6):4531, 1995.
- [158] Kristine Pierloot and Steven Vancoillie. Relative energy of the high-(t 2 g 5) and low-(a 1 g 1) spin states of the ferrous complexes [fe (l)(nhs 4)]: Caspt2 versus density functional theory. *The Journal of chemical physics*, 128(3):034104, 2008.
- [159] Latevi Max Lawson Daku, Francesco Aquilante, Timothy W Robinson, and Andreas Hauser. Accurate spin-state energetics of transition metal complexes. 1. ccSD (t), caspt2, and dft study of [m (nch) 6] 2+(m= fe, co). *Journal of chemical theory and computation*, 8(11):4216–4231, 2012.

- [160] A Droghetti, D Alfè, and S Sanvito. Assessment of density functional theory for iron (ii) molecules across the spin-crossover transition. *The Journal of chemical physics*, 137(12):124303, 2012.
- [161] Florian Weigend and Reinhart Ahlrichs. Balanced basis sets of split valence, triple zeta valence and quadruple zeta valence quality for h to rn: Design and assessment of accuracy. *Physical Chemistry Chemical Physics*, 7(18):3297–3305, 2005.
- [162] Shengfa Ye and Frank Neese. Accurate modeling of spin-state energetics in spin-crossover systems with modern density functional theory. *Inorganic chemistry*, 49(3):772–774, 2010.
- [163] Francesco Aquilante, Luca De Vico, Nicolas Ferré, Giovanni Ghigo, Per-åke Malmqvist, Pavel Neogrady, Thomas Bondo Pedersen, Michal Pitoňák, Markus Reiher, Björn O Roos, et al. Molcas 7: the next generation. *Journal of computational chemistry*, 31(1):224–247, 2010.
- [164] Marvin Douglas and Norman M Kroll. Quantum electrodynamical corrections to the fine structure of helium. *Annals of Physics*, 82(1):89–155, 1974.
- [165] Bernd A Hess. Relativistic electronic-structure calculations employing a two-component no-pair formalism with external-field projection operators. *Physical Review A*, 33(6):3742, 1986.
- [166] Markus Reiher and Alexander Wolf. Exact decoupling of the dirac hamiltonian. ii. the generalized douglas–kroll–hess transformation up to arbitrary order. *The Journal of chemical physics*, 121(22):10945–10956, 2004.
- [167] Björn O Roos and Per-Åke Malmqvist. Relativistic quantum chemistry: the multiconfigurational approach. *Physical Chemistry Chemical Physics*, 6(11):2919–2927, 2004.
- [168] John P Perdew. Density-functional approximation for the correlation energy of the inhomogeneous electron gas. *Physical Review B*, 33(12):8822, 1986.
- [169] Troy Van Voorhis and Gustavo E Scuseria. A novel form for the exchange-correlation energy functional. *The Journal of chemical physics*, 109(2):400–410, 1998.
- [170] Viktor N Staroverov, Gustavo E Scuseria, Jianmin Tao, and John P Perdew. Comparative assessment of a new nonempirical density functional: Molecules and hydrogen-bonded complexes. *The Journal of chemical physics*, 119(23):12129–12137, 2003.
- [171] Roberto Peverati and Donald G Truhlar. M11-l: A local density functional that provides improved accuracy for electronic structure calculations in chemistry and physics. *The Journal of Physical Chemistry Letters*, 3(1):117–124, 2011.
- [172] Haoyu S Yu, Xiao He, and Donald G Truhlar. Mn15-l: A new local exchange-correlation functional for kohn–sham density functional theory with broad accuracy for atoms, molecules, and solids. *Journal of chemical theory and computation*, 12(3):1280–1293, 2016.

- [173] Yan Zhao and Donald G Truhlar. The m06 suite of density functionals for main group thermochemistry, thermochemical kinetics, noncovalent interactions, excited states, and transition elements: two new functionals and systematic testing of four m06-class functionals and 12 other functionals. *Theoretical Chemistry Accounts: Theory, Computation, and Modeling (Theoretica Chimica Acta)*, 120(1):215–241, 2008.
- [174] Yan Zhao and Donald G Truhlar. Density functional for spectroscopy: no long-range self-interaction error, good performance for rydberg and charge-transfer states, and better performance on average than b3lyp for ground states. *The Journal of Physical Chemistry A*, 110(49):13126–13130, 2006.
- [175] Nicholas C Handy and Aron J Cohen. Left-right correlation energy. *Molecular Physics*, 99(5):403–412, 2001.
- [176] Jeanet Conradie and Abhik Ghosh. Dft calculations on the spin-crossover complex fe (salen)(no): a quest for the best functional. *The Journal of Physical Chemistry B*, 111(44):12621–12624, 2007.
- [177] Manuela Merchán, Rosendo Pou-Amérigo, and Björn O Roos. A theoretical study of the dissociation energy of ni<sup>2+</sup> a case of broken symmetry. *Chemical physics letters*, 252(5-6):405–414, 1996.

## Résumé

L'objectif de cette thèse était de concevoir, de construire et d'appliquer des approches pour calculer les propriétés photophysiques des matériaux cristallins, en particulier les cristaux moléculaires organiques, en tenant compte des interactions électrostatiques avec l'environnement.

Pour ce faire, nous avons utilisé une procédure, SC-Ewald, qui, grâce à l'application d'un potentiel d'embedding d'état excité, tente de récupérer les contributions électrostatiques à courte et à longue distance. La procédure d'embedding résultante est ensuite introduite dans des calculs d'état excité basés sur la théorie fonctionnelle de la densité dépendant du temps. L'algorithme résultant a été testé sur différents matériaux cristallins présentant des propriétés optiques intéressantes et variées.

La première propriété étudiée était la réactivité de l'état excité, sous la forme d'une réaction de transfert des protons intramoléculaire à l'état excité, pour laquelle les bases de la méthode SC-Ewald étaient mise en place.

Dans une deuxième étude portant sur le phénomène des émissions induites par l'agrégation, nous avons démontré que l'amélioration de l'émission à l'état solide est influencée par l'environnement d'état excité, grâce à une amélioration des états faiblement émissifs.

Dans une troisième étude, nous avons exploré comment SC-Ewald peut être étendu pour étudier les propriétés à l'état excité dans la phase amorphe, par le phénomène de la méchanochromisme. Dans cette étude, nous avons révélé le caractère directionnel de cette propriété et introduit des lignes directrices pour la conception des matériaux à haute performance qui sont sensibles au stress.

## Mots Clés

État excité, cristaux moléculaires, DFT, AIE, méchanochromisme, transfert des protons

## Abstract

The objective of this thesis was to devise, construct and apply cost-effective approaches to calculate photophysical properties of crystalline media, specifically organic molecular crystals, by accounting for electrostatic interactions with the environment

To do so, we made use of a self-consistent charge-adjustment procedure, SC-Ewald, which, through application of an excited-state embedding potential, attempts to recover both short- and long-range electrostatic contributions both from neighboring molecules and the long range, infinite potential (Madelung field). The resulting embedding procedure is then introduced into excited-state calculations based on time-dependent density functional theory. The resulting algorithm was tested on various molecular crystalline materials exhibiting interesting, and varied, optical properties.

The first property studied was excited state reactivity, in the form of a excited state intramolecular double proton transfer reaction, for which the foundations for the SC-Ewald method were laid.

In a second study concerning the phenomenon of aggregation induced emission, we demonstrated that the emission enhancement in the solid state is driven by the excited state environment, through an enhancement of otherwise poorly emissive states.

In a third study, we explored how SC-Ewald may be extended to study excited state properties in the amorphous phase through the phenomenon of mechanochromic luminescence. In this study, we revealed the directional nature of this property and introduce guidelines for the design of high-performance, stress-sensitive materials

## Keywords

Excited states, molecular crystals, DFT, AIE, mechanochromism, proton transfer